学位論文

Classification of Shock Chemistry by Pre-shocked Conditions (衝撃波発生以前の分子雲の状態で分類する衝撃波化学)

平成 25 年 12 月博士 (理学) 申請

東京大学大学院理学系研究科物理学専攻

山口 貴弘

Abstract

Shocked regions ubiquitously exist in interstellar space as seen in star-forming regions, supernova remnants, and active galactic nuclei. These shocks deeply affect not only on physical conditions but also on chemcal compositions of the interstellar gas. So far, many spectral line surveys have been concucted in the millimeter- and submillimeter-wave regions toward high-mass or low-mass star-forming regions. These results revealed existences of various molecular species. It has often been claimed that some molecules would be produced through the shock. However, such star-forming regions generally have so complicated structures that it is difficult for us to distinguish the effect of shocks from their observational data.

In order to cope with this problem, we conducted a line survey in 3 mm wavelength (78-115 GHz) using the Nobeyama 45 m telescope toward L1157 B1, where is a shocked region caused by the interaction between the outflow from the low mass protostar IRAS 20386+6751 and the ambient gas. This region is apart from the protostar by $\sim 1'$, and hence, we can observe the pure shock chemistry without suffering from the protostar activities. In this region, we detected 130 lines of 29 species including some complex organic molecules such as $HCOOCH_3$, CH_3CHO, and NH_2CHO, and a phosphorus-bearing molecule PN, which is the first detection of this molecule in the low-mass star-forming region. We found that the shocked region of L1157 B1 is chemically rich. Evaporation of molecules from grain mantle plays an important role for the rich chemistry in the gas-phase.

To expand our understanding of the shock chemistry, we conducted a line survey toward L1448 B1/R1, which are shocked regions caused by internal bow shocks in the outflow from the protostar from L1448 mm. These regions are located in the vicinities from the protostar ($\sim$ 250 AU). In these shocked regions, we only detected SiO and SO, and found that the chemical composition of the shocked gas is different from that of L1157 B1.

Finally, we investigated the shocked region associated with the supernova shock toward a supernova remnant, IC 443. The supernova shock is considered to compress the diffuse and to form a shell-like structure. The pre-shocked gas in IC 443 is therefore considered to be a photodissociation region. In such a cloud, the UV radiation effect is important and the gas temperature is relatively high. In this region, we detected 44 lines of 14 species. We detected the CH_3OH lines in this region for the first time, but they are very weak.

Based on these results, we compared the characteristics of each shocked region. Some molecules such as CH_3OH show significant variation of their abundance. The absorption of CO onto the grain mantle is necessary for the production of CH_3OH. Hence, the lack of CH_3OH line in L1448 B1/R1 implies that the grain-mantle has already evaporated by the star-forming activity. Similarly, the low abundance ratio of CH_3OH in IC 443 may be due to the relatively high temperature of dust grains in the pre-shocked gas due to the UV heating. After all, we found that the shock chemistry is dominated by the grain mantle evaporation. It is determined by the pre-shocked conditions, more specifically the grain-mantle composition of the pre-shocked gas.

Contents

Chapter 1

Introduction

1.1 Interstellar Clouds

Interstellar space is not completely vacuum, but is filled with diffuse gas and dust called interstellar matter. The most abundant element is hydrogen and the next is helium. The second row elements such as C, N, and O have abundances of the order of 10^{-4} relative to hydrogen. The gas-to-dust mass ratio is about 100 around the solar neighborhood.

Interstellar matter is not uniformly distributed, but is more or less localized in interstellar clouds. The temperature and density of interstellar clouds are shown in Figure 1.1. Most of diffuse interstellar clouds are located on the straightline with constant pressure in Figure 1.1. This means that diffuse interstellar clouds are generally in pressure equilibrium. Apart from diffuse intercloud gas, interstellar clouds are classified into diffuse clouds and molecular clouds, depending on the major form of hydrogen. In diffuse clouds, 50 % or more hydrogen is in a form of atomic hydrogen, whereas molecular hydrogen is dominant in molecular clouds. When dense parts are formed in molecular clouds by gravitational instability and/or cloud-cloud collisions, they are subject to gravitational collapse. This leads to formation of new stars.

1.1.1 Diffuse Clouds

Diffuse clouds are defined as interstellar clouds with the density of 10-100 cm^{-3} and the total visual extinction of a few magnitude or less. In diffuse clouds, interstellar UV radiation well penetrates into the central part, and hence, hydrogen atoms and hydrogen molecules coexist. Since the photodissociation of molecules by the UV radiation is significant, only simple molecules such as CO, CN, CH, OH, and H_3^+ can exist there. The most important heating mechanism is the photoelectric heating, where electrons ejected from dust grains due to absorption of the UV radiation heat the gas. The cooling mechanism is mainly emission of fine structure lines of fundamental atoms and ions such as C_{II} and O_I. The temperature of diffuse cloud is thus 30 K - 100K.

1.1.2 Molecular Clouds

As the cloud density increases, the interstellar UV radiation is shielded in the central part of the clouds, and hence, hydrogen can be in molecular form. This is a molecular cloud. When the H_2 column density reaches a few times 10^{21} cm^{-3}, corresponding to the visual extinction, A_V of a few magnitude, the UV radiation cannot penetrate into the molecular cloud. In such a

condition, the cosmic-ray mainly contributes to the cloud heating. On the other hand, cooling processes are dominated by molecular line emissions and dust continuum emissions. Through the balance of the heating and cooling processes, the gas kinetic temperature in molecular clouds becomes 8-15 K as far as other heating mechanisms such as star formation inside the clouds do not contribute. A radiowave observation of molecules is an effective method to study such cold clouds. Since typical rotational energy level spacing of molecules is an order of a few K, the rotational levels are easily excited by the collision with H_2 molecule. Then, their emissions (mostly rotational transitions) can be observed by radiotelescopes.

Various molecules are formed by the gas-phase chemical reactions. In particular, ion-molecule reactions play a central role in production of molecules. Cosmic rays ionize the hydrogen molecules, which start chemical reactions as:

$$\mathrm{H_2 + c.r.} \rightarrow \mathrm{H_2^+ + e} \tag{1.1}$$

$$\mathrm{H_2^+ + H_2} \rightarrow \mathrm{H_3^+ + H} \tag{1.2}$$

$$\mathrm{H_3^+ + A} \rightarrow \mathrm{HA^+ + H_2} \tag{1.3}$$

$$\mathrm{HA^+ + B} \rightarrow \mathrm{AB^+ + H.} \tag{1.4}$$

In this way, various molecules are formed in interstellar clouds. It is also known that even in such a low temperature emvironment, chemical reactions on the dust grain proceed efficiently (Tielens 1982). Grain consists of grain core (silicate or graphite) and icy grain mantle (See Figure 1.2). In cold conditions, H_2O ice is produced by a reaction of O atom and H atom adsorbed on grain core, which makes grain mantle. Various molecules including complex organic molecules are also formed on the grain mantle by reactions of accreting atoms and molecules.

Star-forming regions harbor hot cores or hot corinos, which are hot and dense cores around newly born protostars (e.g. Blake et al. 1987; Herbst and van Dishoeck 2009). They show some chemical richness of complex organic molecules such as CH_3OH, $HCOOCH_3$, and CH_3CHO. These molecules are thought to be produced from CO by grain surface reactions (Herbst and van Dishoeck 2009). Since the sublimation temperature of CO is as low as 20 K, such complex molecules are thought to be produced mainly on dust grains in the starless core era, where the temperature is as low as 10 K.

1.2 Shock Physics

In space, supersonic motion of gas is ubiquitous, and it causes shock everywhere. We briefly discuss physics of the shock in this section. We here consider the ideal one-dimensional disturbance propagating a homogeneous medium with a constant velocity u_1 along the x axis. In this case, all quantities are determined by x and time (t).

Then, we introduce the frame of referece traveling with the velocity u_1. The undisturbed material enters the shock at x_1, where its velocity, density, and temperature are u_1, ρ_1, and T_1, respectively. On the other side of the front at x_2, these quantities are expressed as u_2, ρ_2, and T_2. Between x_1 and x_2, ρ and u are functions of x, and T may be irrelavant because the thermal equilibrium is not realized.

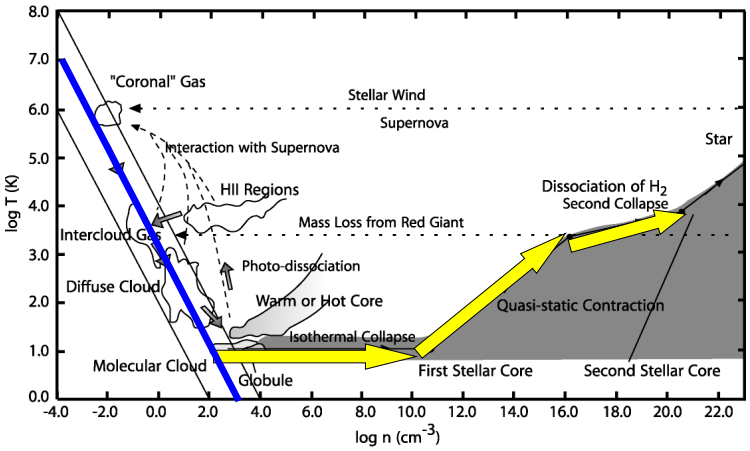

Figure 1.1: Temperature and the density of interstellar clouds.

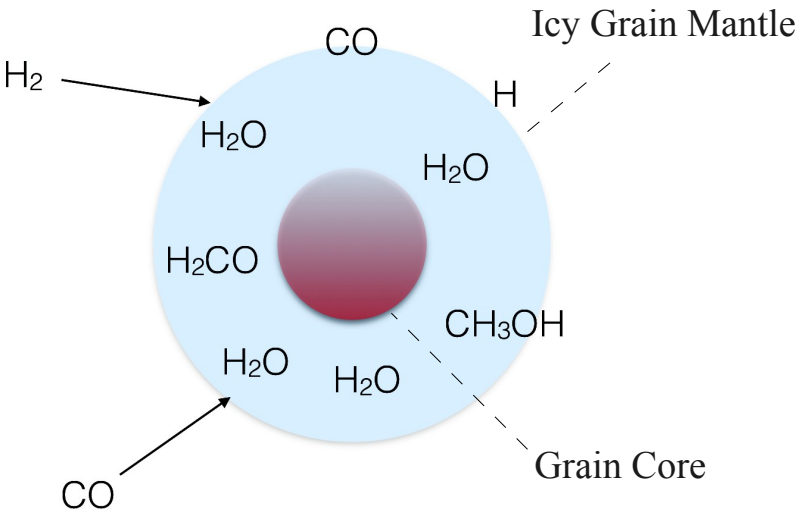

Figure 1.2: Grain Mantle Model

1.2.1 Adiabatic Process with $\boldsymbol{B} = 0$

By considering conservation of the mass and the momentum, the following equations hold;

$$\rho_1 u_1 = \rho_2 u_2 \tag{1.5}$$

$$p_1 + \rho_1 u_1^2 = p_2 + \rho_2 u_2^2. \tag{1.6}$$

In the adiabatic shock, the energy increase rate of the gas in unit area of the front per unit time equals the rate at which work is done on the gas by pressure forces. This can be represented as:

$$u_1\left(\frac{1}{2}\rho_1 u_1^2 + U_1\right) + u_1 p_1 = u_2\left(\frac{1}{2}\rho_2 u_2^2 + U_2\right) + u_2 p_2. \tag{1.7}$$

The U_i denotes the internal energy of the fluid per unit volume. If the gas on each side of the shock front is assumed to be the perfect gas, the internal energy is simply

$$U = \frac{p}{\gamma - 1}. \tag{1.8}$$

From equations (1.7) and (1.8), we obtain the following relation:

$$u_1\left(\frac{1}{2}\rho_1 u_1^2 + \frac{\gamma}{\gamma-1}p_1\right) = u_2\left(\frac{1}{2}\rho_2 u_2^2 + \frac{\gamma}{\gamma-1}p_2\right).$$

By using equation (1.5), we obtain:

$$u_1^2 + \frac{2\gamma}{\gamma-1}\frac{p_1}{\rho_1} = u_2^2 + \frac{2\gamma}{\gamma-1}\frac{p_2}{\rho_2}. \tag{1.9}$$

We eliminate p_2, by using equation (1.6) as:

$$u_2^2 + \left(\frac{2\gamma}{\gamma-1}\right)\left[\left(\frac{1}{\rho_2} - \frac{1}{\rho_1}\right)p_1 + \frac{1}{\rho_2}\left(\rho_1 u_1^2 - \rho_2 u_2^2\right)\right] = u_1^2$$

Then, it is represented as:

$$u_2^2 + \left(\frac{2\gamma}{\gamma-1}\right)\left[\left(\frac{\rho_2}{\rho_1} - 1\right)u_2^2 + c_{\mathrm{s}}^2\left(\frac{\rho_1}{\rho_2} - 1\right)\right] = u_1^2, \tag{1.10}$$

$$\tag{1.11}$$

where $c_{\mathrm{s}}^2 = \frac{p_1}{\rho_1}$. By using equation (1.5) again, this can be written as

$$\left(\frac{u_2}{u_1}\right)^2 + \left(\frac{2\gamma}{\gamma-1}\right)\left[\frac{u_2}{u_1} - \frac{u_2^2}{u_1^2} + \frac{1}{M^2}\left(\frac{u_2}{u_1} - 1\right)\right] = 1, \tag{1.12}$$

$$\tag{1.13}$$

where $M = \frac{u_1}{c_s}$. This is callsed as Mach number. When x is defined as $u_2/u_1 = x$, the equation (1.12) becomes:

$$(\gamma+1)x^2 - 2\gamma\left(1 + \frac{1}{M^2}\right)x + 2\gamma\frac{1}{M^2} + \gamma - 1 = 0. \tag{1.14}$$

The solutions of this equation are

$$x = 1,\ \frac{\gamma-1}{\gamma+1} + \frac{2\gamma}{\gamma+1}\frac{1}{M^2}.$$

Since the former solution does not generate the shock, we apply the latter to obtain:

$$\frac{u_2}{u_1} = \frac{\gamma-1}{\gamma+1} + \frac{2\gamma}{\gamma+1}\frac{1}{M^2}. \tag{1.15}$$

On the other hand, the following relation can be obtained from the equation (1.6):

$$\begin{aligned}\frac{p_2}{p_1} &= 1 + \frac{1}{p_1}(\rho_1 u_1^2 - \rho_2 u_2^2) \\ &= 1 + \frac{1}{c_\mathrm{s}}\left(u_1^2 - \frac{\rho_2}{\rho_1}u_2^2\right) \\ &= 1 + M^2\left(1 - \frac{u_2}{u_1}\right) \qquad (\because 1.5).\end{aligned}$$

We substitute u_2/u_1 by equation (1.15) to obtain the follwing relation:

$$\begin{aligned}\frac{p_2}{p_1} &= 1 + M^2\left(1 - \frac{\gamma-1}{\gamma+1} - \frac{2\gamma}{\gamma+1}\frac{1}{M^2}\right) \\ &= \frac{2}{\gamma+1}M^2 - \frac{\gamma-1}{\gamma+1} \qquad (1.16) \\ &= \frac{2M^2 - \gamma + 1}{\gamma+1}. \qquad (1.17)\end{aligned}$$

When u_1 is much higher than u_2, (i.e. $M \to \infty$), the equation 1.15 is simplified as:

$$\frac{u_2}{u_1} \sim \frac{\gamma-1}{\gamma+1}.$$

In the case of the atomic gas, $\gamma = 5/3$ can be applied, and we then obtain:

$$\frac{u_2}{u_1} \to \frac{1}{4}, \qquad \frac{\rho_2}{\rho_1} \to 4,$$

which means the density increse by a factor of 4 at maximum. From the equation (1.17), and the condition that $p_2 \gg p_1$, we obtain:

$$p_2 = p_1 + \rho_1 u_1^2\left(1 - \frac{u_2}{u_1}\right) \to \rho_1 u_1^2 \frac{2}{\gamma+1} \to \frac{3\rho_1 u_1^2}{4}.$$

If we denote the mass of a molecule as μ, $\rho V = \mu N$. From the equation of state,

$$\begin{aligned}kT_2 = \frac{p_2 V}{N} = p\frac{\mu}{\rho_2} &\to \frac{2}{\gamma+1}\rho_1 u_1^2 \frac{\mu}{\rho_2} \\ &\to \frac{2(\gamma-1)}{(\gamma+1)^2}\mu u_1^2 \to \frac{3}{16}\mu u_1^2.\end{aligned}$$

If we employ $u_1 = 10$ km s^{-1}, and $\mu = 1.3/N_\mathrm{A}$ g, T_2 becomes as high as 2970 K. Hence, the shock heating is significant in the adiabatic shock.

1.2.2 Isothermal Process

In the isothermal condition, equation (1.7) cannot be valid. On the other hand, we have:

$$\frac{p_1}{\rho_1} = \frac{p_2}{\rho_2} = \frac{kT}{\mu} = \frac{\partial p}{\partial \rho} = c_s^2. \qquad (1.18)$$

Thus, equation (1.6) becomes:

$$\begin{aligned}&\rho_1\left(c_s^2 + u_1^2\right) = \rho_2\left(c_s^2 + u_2^2\right) \qquad (1.19) \\ &\frac{\rho_2}{\rho_1}\left(\frac{c_s^2}{u_1^2} + \frac{u_2^2}{u_1^2}\right) = \frac{c_s^2}{u_1^2} + 1.\end{aligned}$$

For simplicity, we use the following relationship:

$$\frac{u_2}{u_1} = \frac{\rho_1}{\rho_2} = x \tag{1.20}$$

$$\zeta = \frac{c_s^2}{u_1^2} = \frac{1}{M^2}. \tag{1.21}$$

Then, we obtain

$$\frac{1}{x}\left(\zeta + x^2\right) = \zeta + 1. \tag{1.22}$$

The non-trivial solution of this equation is $x = \zeta$, and hence,

$$\frac{\rho_2}{\rho_1} = M^2 = \frac{u_1^2}{c_s^2}. \tag{1.23}$$

Therefore, in an isothermal shock, the dencity is enhanced by M^2 times, where M is the Mach number. If we assume $u_1 = 10\ \mathrm{km\ s^{-1}}$ and $c_s = 0.3\ \mathrm{km\ s^{-1}}$, the compression by a factor of 10^3 can occur. In actual situations, the intermidiate state between the adiabatic and isothermal shock is usually realized, and the enhancements of the temperature and the density are mitigated. If the magnetic field exists, the situation can be more complicated. Since the magnetic field efficiently propagates the energy, the shock front discontinuity is softened.

1.3 Shock Chemistry

1.3.1 Chemical Processes in Shocks

Shocks cause local and temporal raise of temperature and abrupt increase of density, and hence, they significantly affect the chemical compositions. Since interstellar clouds are in low temperature (10-30 K) and low density (10^2- 10^6 $\mathrm{cm^{-3}}$) conditions, chemical processes are usually restricted to exothermic reactions or reactions with small endothermicity. Furthermore, desorption from grain mantle is not efficient. However, shock allows chemical processes which cannot proceed in ordinary interstellar conditions, which realizes characteristic chemical compositions. One example is promotion of exothermic reactions and reactions with high activation barrier. For instance, the reaction

$$\mathrm{C^+ + H_2 \rightarrow CH^+ + H} \tag{1.24}$$

is exothermic by 0.4 eV (4600 K). This reaction can only proceed in adiabatic shocks, which enhances the abundance of $\mathrm{CH^+}$. A high abundance of $\mathrm{CH^+}$ in diffuse clouds is interpreted in this way (e.g. Sheffer et al. 2008). Another example is sublimation of grain mantle and disruption of grain cores. Dust grains consists of silicate and graphite materials, which are covered with the $\mathrm{H_2O}$ ice (mantle). In shocked regions, mantle species are released into the gas-phase thermally or non-thermally. In case of strong shock, the grain core is destroyed or eroded to liberate non-volatile species such as SiO into the gas-phase. In some cases, molecules are destroyed by shocks. Thermal dissociation as well as reactions with $\mathrm{H_2}$ and O, are responsible for destruction. These three are representative chemical processes in shocked regions.

In molecular clouds, the shock chemistry was historically invoked to account for rich chemical composition in high-mass star forming regions. For instance, the prototypical hig-mass star forming region Orion-KL shows rich spectral lines of various saturated complex organic molecules such as CH_3OH, $HCOOCH_3$, $(CH_3)_2O$, and C_2H_5CN as well as sulfur containing molecules such as SO and SO_2 (e.g. Blake et al. 1987; Schilke et al. 1997; Tercero et al. 2005). Since these molecules are not detected or very deficient in cold molecular clouds (Herbst and van Dishoeck 2009), they are thought to be formed in high temperature regions around the protostar, called hot cores. Although a heating mechanism of hot cores is still controversial, strong shock caused by stellar wind and/or energetic outflows from newly formed high-mass stars play an important role. Hence, the shock chemistry has often been discussed in relation to the hot core chemistry, where the above three characteristic chemical processes are considered (e.g. Nomura and Millar 2004). In the following sections, a few examples of shock chemistry are highlighted.

1.3.2 Sulfur Chemistry

Although SO and SO_2 are observed ubiquitously in interstellar clouds, they are extremely abundant in high-mass star-forming regions. Hence, the shock chemistry of sulfur-bearing molecules were extensively discussed. Pineau des Forêts et al. (1993) conducted two-fluid MHD models of shocks propagating in molecular clouds of $n_{\rm H}$ density ranging from 10^4 to 10^6 cm^{-3}, with velocity from 5 to 40 km s^{-1}. They focused on formation of sulfur-bearing moelcules such as SO, SO_2, CS, and H_2S in high-mass star-forming regions. They assumed that main form of sulphur is atomic, and suggested that SO is readily produced by the reaction of S and O_2. The reaction of SO and O_2 contributes to production of SO_2.

On the other hand, Charnley (1997) described the producution processes of sulfur-bearing species through grain mantle evaporation in high-mass star-forming region. He assumed the major form of the sulfur on the grain mantle is H_2S. In his model, S atom is formed through the abstraction reactions such as $H_2S \rightarrow SH \rightarrow S$, after H_2S is released into the gas-phase. Although these reactions are endothermic, endothermicity can be overcome in the high temperature conditions in shocks. Since it takes 10^4 yr or more for H_2S to be converted into SO and other molecules, abundance ratios, SO/H_2S and SO/SO_2, can be used as good indicators of the time elapsed after the grain mantle evaporation.

1.3.3 Silicon Chemistry

Another cases of molecules specific to shocked regions is silicon-bearing molecules including SiO and SiS. It is well known that silicon-bearing molecules including SiO is absent in the gas-phase of cold molecular clouds (Kaifu et al. 2004). This is interpreted as complete depletion of silicon onto dust grains. In fact, silicate is a main component of grain cores. In high-mass star-forming regions, strong spectral lines of SiO and SiS are observed (e.g. Blake et al. 1987). These species sometimes follow distribution of molecular outflows, and hence, they are thought to be sputtered out from grain cores in shocked regions. Later, the SiO emission was found in shocked regions caused by outflows from the low-mass protostar L1157 (Mikami et al. 1992). Now, SiO is widely used as an indicator of shocks.

1.3.4 Organic Chemistry

Various complex saturated organic molecules were detected in high-mass star-forming regions, and shock chemistry was thought to be responsible for them. Recently, a direct evidence of their relation to shock chemistry was found by sensitive radio astronomical observations. Arce et al. (2008) detected molecular lines of complex organic molecules such as $HCOOCH_3$, CH_3CN, HCOOH, and C_2H_5OH in the L1157 B1 shocked region. Sugimura et al. (2011) also detected additional complex organic molecules such as CH_3CHO, and a deuterated methanol CH_2DOH. They conducted a chemical model calculation for all above complex species and concluded that the grain surface chemistry is critical for the production processes of these complex organic molecules.

1.4 Aim of This Thesis

As mentioned above, the shock chemistry has mainly been investigated toward high-mass star-forming regions. However, it is difficult to extract the effect of shocks from other star-formation activities because of general structural complexity of high-mass star-forming regions. Because of this reason, our understanding of a role of shocks on chemical processes has still been limited. Shocks will enhance chemical reactions which do not occur in cold conditions, and at the same time, will heat up dust grains to supply various molecules formed there into the gas-phase. Although the latter contribution is strongly recognized by detection of organic molecules in the shocked region L1157 B1 (e.g. Arce et al. 2008; Herbst and van Dishoeck 2009; Sugimura et al. 2011), the former contribution has also been discussed for a long time (e.g. Blake et al. 1987; Nomura and Millar 2004; Brouillet et al. 2013). Hence, it is still important to explore their relative contributions by observations, in order to fully characterize the shock chemistry. This is the pricipal motivation of this thesis.

To cope with this problem, we focus on threee well-defined shocked regions with different characters. They are L1157 B1, L1448 B1/R1, and IC 443 G I. L1157 B1 is a shocked region caused by an interaction between a molecular outflow from the low-mass protostar L1157 mm and an ambient cloud. L1448 B1/R1 is a high velocity shock in a jet launched from the low-mass protostar L1448 mm. On the other hand, IC 443 G I is a shocked cloud associated with an old supernova remnant. Observations of these shocked regions require high sensitivity instruments, because their emissions are relatively faint in comparison with those from high-mass star-forming regions. For this reason, observations toward these shocked regions have been limited to fundamental and abundant species (Mikami et al. 1992; Avery et al. 1996; Bachiller et al. 1997; van Dishoeck et al. 1993). Such high-sensitivity observations are now possible, thanks to recent developments of receiver and backend technologies (e.g. Arce et al. 2008; Sugimura et al. 2011). By taking this advantage, we have conducted a spectral line survey which covers a whole 3 mm band (80-115 GHz) for the three target sources, and have characterized their chemical compositions without any preconception.

1.5 Outline of This Thesis

After describing the observational instrument, the Nobeyama 45 m telescope, we show the overall results of the line survery of L1157 B1 in Chapter 3. which is a shocked region caused by interactions between outflows from the protostar L1157 mm and the ambient gas. In Chapter

4, we report the detection of PN (Yamaguchi et al. 2011) in L1157 B1. This molecule is an important species as a biological molecule, although this is a first detectin in the low-mass star-forming region. In Chapter 5, we report the overall results of the line survey of L1448 B1/R1, which is a shocked region caused by outflows from the protostar L1448 mm. In Chapter 6, we present the overall results of the line survey of the supernova remnant, IC 443 G I. In Chapter 7, we compare the shock chemistry in the regions studied, especially, in L1157 B1 and IC 443 G I, and discuss what determines the characteristic of the shock chemistry.

Chapter 2

Observation

2.1 Nobeyama 45 m Telescope

The Nobeyama 45 m Telescope (Figure 2.1), which started its full operation in 1982, still has a top level performance in the 3 mm wavelength observation. Since the surface accuracy of the parabola antenna is required to be within 1/20 of the observation wavelength, the big telescope such as Nobeyama 45 m telescope has a problem of gravitational deformation. In order to cope with it, the frame structure supporting the main reflector is designed to have a homologous structure to keep the accuracy after the deformation. In addition, the main reflector consists of $\sim$ 600 panels, which can be remotely manuplated by actuators for the alignment. By the holography method using a satellite, the panel displacement from the paraboloide is measured, and the result is used for corrections. The sub-reflector is also operated automatically, according to the shift of the focal point caused by the deformation of the main reflector. The thermal deformation must also be taken care of because the radio telescope is also used in the exposed condition in daytime. The hanicomb-sandwitch panels, each of which is coverd with CFRP (carbon-fiber-reinforced-plastic, which has a lower thermal expansion coefficient than metal), are used for the main reflector. The backward of the main reflector is covered with sunshade panels, and the 70 fans circulate the air in the back structure.

The angular resolution of the antenna is usually described by the HPBW (half-power beamwidth) as:

$$\mathrm{HPBW} = K \times \lambda / D \tag{2.1}$$

K is a coefficient which depends on the illumination pattern of the main reflector, and is usually $\sim$ 1,2. D denotes the diameter of the aperture of the antenna, and λ is observation wavelength. Hence, the angular resolution of Nobeyama 45 m telescope ranges from $15''$ to $20''$ in the 3 mm band (80-115 GHz). In order to keep the tracking accuracy for this resolution, the master collimator is used, which stands on the center of the telescope isolated from the main reflector. The master collimator is first directed to the object. The main reflector then follows the direction of the master collimator. This mechanism realizes accurate tracking of the big telescope.

Figure 2.1: Nobeyama Radio Observatory 45 m Telescope.
http://www.nro.nao.ac.jp/ nro45mrt/pictures/photo/image/

2.2 Receiver

2.2.1 Heterdyne Receiver

The radiowave reflected by the sub-reflector is introduced into the receiver optimized for the required observation frequency. Since the thermal emission from molecular clouds, which is a target of our study, is not polarized, we can observe two orthogonal polarizations to improve sensitivity. Several receivers are prepared for observation of the frequency range from 22 to 150 GHz. Generally, there are two types of receivers. One directly amplifies the received radio-frequency signal (RF, hereafter), whereas the other amplifies the intermediate frequency which is down-converted from RF by mixing the local oscillator (LO) signal with a non-linear device (Figure 2.2). Since the conversion loss of the RF energy is inevitable, it is ideal to directly amplify RF. In the 45 m telescope, RF is directly amplified in the frequency range below 40 GHz. Since it is technically difficult to directly amplify RF in the frequency range above 40 GHz, the low-loss mixer is used for down-conversion (heterodyne receiver). A typical example of the heterodyne receiver is the SIS mixer receiver (See Section 2.2.3).

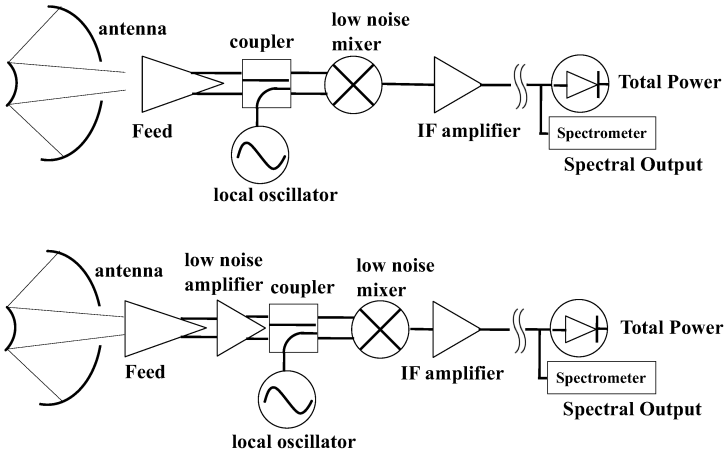

Figure 2.2: The basic schematic of the heterodyne receiver. Top: The receiver for the frequency range above 70 GHz, on which the low noise amplifier is not readily available. Bottom: The receiver for the frequency range below 50 GHz, on which the low noise amplifier is abailable. HEMT (High Electron Mobility Transistor) is used as the amplifier.

2.2.2 Frequency Convertor

In a heterodyne receiver, the most important part is the mixer for the RF and LO signals. For example, the non-linear semiconductor diode shows the following I-V characteristic;

$$I = I_0\left\{\exp\left(\frac{V}{V_0}\right) - 1\right\}, \tag{2.2}$$

where $V_0 = \dfrac{\eta kT}{e}$ and I_0, denotes the inverse saturation current, k Boltzmann constant, e electron charge, T the mixer temperature, η the coefficient which indicates the capability of the diode, respectively. The exponential part is expanded as follows:

$$I = I_0\left\{1 + \frac{V}{V_0} + \frac{1}{2}\left(\frac{V}{V_0}\right)^2 + \frac{1}{6}\left(\frac{V}{V_0}\right)^3 + \cdots - 1\right\}. \tag{2.3}$$

If the third or higher terms are ignored, this equation is approximated to be

$$I = I_0\left\{\frac{V}{V_0} + \frac{1}{2}\left(\frac{V}{V_0}\right)^2\right\}. \tag{2.4}$$

If we input the RF and LO signals, which are represented as:

$$V_{\rm s}(t) = V_{\rm s0}\cos\left(\omega_{\rm s}t + \phi_{\rm s}\right) \tag{2.5}$$

$$V_{\rm l}(t) = V_{\rm l0}\cos\left(\omega_{\rm l}t + \phi_{\rm l}\right), \tag{2.6}$$

respectively, the output current from the mixer is represented as

$$\begin{aligned} i_{\rm m} &= K\left[V_{\rm s}(t)+V_{\rm l}(t)\right]^2 \\ &= \frac{1}{2}\left(V_{\rm s0}^2+V_{\rm l0}^2\right)+\frac{1}{2}KV_{\rm s0}^2\cos 2\left(\omega_{\rm s}t+\phi_{\rm s}\right)+\frac{1}{2}KV_{\rm l0}^2\cos 2\left(\omega_{\rm l}t+\phi_{\rm l}\right) \\ &\quad +KV_{\rm s0}V_{\rm l0}\cos\left[\left(\omega_{\rm s}+\omega_{\rm l}\right)t+\left(\phi_{\rm s}+\phi_{\rm l}\right)\right] \\ &\quad +KV_{\rm s0}V_{\rm l0}\cos\left[\left(\omega_{\rm s}-\omega_{\rm l}\right)t+\left(\phi_{\rm s}-\phi_{\rm l}\right)\right]. \end{aligned} \tag{2.7}$$

The first, the second, and the third terms in the equation denote the DC component, the double frequency component for the RF signal, and the double frequency component for LO signal, respectively. The fourth and fifth terms describe the combination and difference frequency components, respectively. The heterodyne receiver outputs the difference frequency component by using an appropriate filter.

There are three types of heterodyne receivers, which are SSB (Single Side Band), DSB (Double Side Band), and 2 SB (Two Side Band). The frequency relation in the heterodyne receiver is

$$\nu_{\rm RF}=\nu_{\rm LO}\pm\nu_{\rm IF}$$

where $\nu_{\rm RF}$ is the radio frequency, $\nu_{\rm LO}$ the local oscillator frequency, and $\nu_{\rm IF}$ the intermediate frequency. Thus, the receiver has a sensitivity for the two RF frequencies for the given $\nu_{\rm IF}$ and $\nu_{\rm LO}$. The higher frequency, $\nu_{\rm LO}$ + $\nu_{\rm IF}$, is called Upper Sideband (USB), while the lower frequency, $\nu_{\rm LO}$ - $\nu_{\rm IF}$ is called Lower Sideband (LSB). The DSB receiver has a sensitivity efficiencies for both sidebands. SSB mixer chooses one from USB or LSB by an appropriate filter. In a DSB mixer, the one sideband only contributes to adding noise to the other sideband, which degrades the sensitivity. In case of the line observation, the contamination from the other side band makes confusion in the identification of the observed lines. Now, the waveguide type 2SB receiver is used in TZ1 HV receiver for the 45 m telescope. In this receiver, two polarization signals are separated, and each is converted by 2SB mixer. Thus, the observation efficiency is much enhanced.

A way to separate the two sidebands is to use two mixers driven by the LO signal with a phase shift of 90°. Then, the output IF signals are combined with the phase shift of 0° and 90° to derive the two side band signals (Figure 2.3). Here, we consider the situation where we obtain the USB component from IF 1.

We denote the USB and LSB components of the received signal as $\cos(\omega_{\rm U}t+\phi_{\rm U})$ and $\cos(\omega_{\rm L}t+\phi_{\rm L})$, respectively. The local oscillator signal is denoted as $\cos(\omega_{\rm LO}t)$. As shown in Figure 2.3, when the RF is introduced as 90° hybrid circuit → mixer 1 → 90° hybrid circuit, the USB component is given a phase shift, as

$$\begin{aligned} \cos(\omega_{\rm U}t+\phi_{\rm U}) &\rightarrow \cos(\omega_{\rm U}t+\phi_{\rm U}+90^\circ)\rightarrow\cos((\omega_{\rm U}-\omega_{\rm LO})t+\phi_{\rm U}+90^\circ) \\ &\rightarrow \cos((\omega_{\rm U}-\omega_{\rm LO})t+\phi_{\rm U}+90^\circ). \end{aligned} \tag{2.8}$$

Similarly, the LSB component becomes

$$\begin{aligned} \cos(\omega_{\rm L}t+\phi_{\rm L}) &\rightarrow \cos(\omega_{\rm L}t+\phi_{\rm L}+90^\circ)\rightarrow\cos((\omega_{\rm LO}-\omega_{\rm L})t-\phi_{\rm L}-90^\circ) \\ &\rightarrow \cos((\omega_{\rm LO}-\omega_{\rm L})t-\phi_{\rm L}-90^\circ)=\sin((\omega_{\rm LO}-\omega_{\rm L})t-\phi_{\rm L}). \end{aligned} \tag{2.9}$$

On the other hand, the USB component on the mixer 2 is given a phase shift, as

$$\begin{aligned} \cos(\omega_{\rm U}t+\phi_{\rm U}) &\rightarrow \cos(\omega_{\rm U}t+\phi_{\rm U})\rightarrow\cos((\omega_{\rm U}-\omega_{\rm LO})t+\phi_{\rm U}) \\ &\rightarrow \cos((\omega_{\rm U}-\omega_{\rm LO})t+\phi_{\rm U}+90^\circ). \end{aligned} \tag{2.10}$$

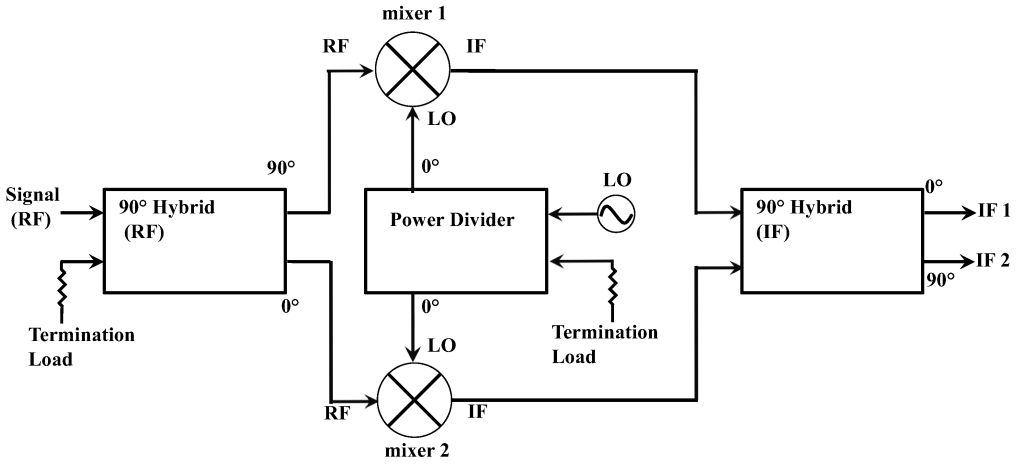

Figure 2.3: A block diagram of 2SB receiver.

The LSB component becomes

$$\begin{aligned}\cos(\omega_{\mathrm{L}}t+\phi_{\mathrm{L}}) &\to \cos(\omega_{\mathrm{L}}t+\phi_{\mathrm{L}}) \to \cos((\omega_{\mathrm{LO}}-\omega_{\mathrm{L}})t-\phi_{\mathrm{L}}) \\ &\to \cos((\omega_{\mathrm{LO}}-\omega_{\mathrm{L}})t-\phi_{\mathrm{L}}+90^{\circ}) = -\sin((\omega_{\mathrm{LO}}-\omega_{\mathrm{L}})t-\phi_{\mathrm{L}}). \end{aligned} \tag{2.11}$$

The signals from the mixer 1 and 2 are coupled to obtain the only USB component. In the same way, the LSB component is obtained at IF 2.

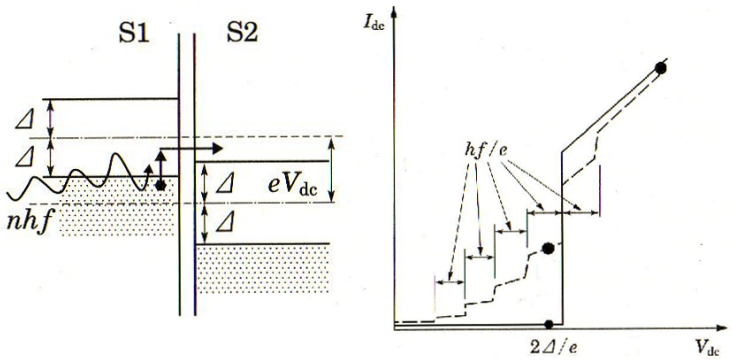

Figure 2.4: Left: The photon assisted tunneling model on the mixer. Right: The $V-I$ characteristic curve of the SIS mixer. The solid line indicates the case without the LO signal. The dashed line is the case with the local frequency.

2.2.3 SIS Super Conducting Mixer

For the Nobeyama T100 H/V and TZ1 H/V receivers, the SIS (Superconductor/Insulator/Superconductor) mixers are employed. The SIS device has a structure where a several nm of insulator is sandwiched by two superconducting electrodes. An SIS mixer works by the following two mechanisms,

(1) The $V - I$ characteristic has a strong non-linearity.
(2) The tunnel current on the SIS mixer varies at the difference frequency of the input RF and LO signals.

The left side of Figure 2.4 indicates the semiconductor model of the energy structure of SIS, and the shaded zone is in the superconducting condition, where electrons make Cooper-pairs. The superconducting electrons occupy these energy levels as many as possible, and almost no vacant level is left. This part corresponds to the valence band. The levels higher by more than twice the energy of the superconducting gap (2 Δ in Figure 2.4 left) is the conduction band, where only quasi-particles can exist. In Figure 2.4, $V_{\rm dc}$, $I_{\rm dc}$, e, and$f$ denote the difference in the electrical potential, the tunnel current, the charge of the electron, and the RF frequency, respectively. As indicated in Figure 2.4 (right), the tunnel current is almost negligible for $0 < V_{\rm dc} < 2\Delta/e$. However, when the electromagnetic wave with the energy hf is fed into the mixer, the tunneling current appears if $nhf + V_{\rm dc} > 2\Delta$, where n is integer. In this condition, the $V - I$ curve in Figure 2.4 (right) changes from the solid line to the dashed line causing the steps with the voltage interval of hf/e. This phenomenon is called photon assisted tunneling (PAT). When the RF signal (ν) is led into the mixer, the PAT current varies with the beat frequency of $|\nu - \nu_{\rm LO}|$. Hence, the IF frequency signal can be obtained by using the low-pass filter.

At Nobeyama Radio Observatory, the Nb/Al-AlO_x/Nb type of the SIS mixer is used. Since Nb has a relatively high transition temperature of 9 K and the large gap energy, it can be used up to the frequency of 700 GHz. The SIS mixer has a high conversion efficiency, because the differential resistance changes steeply compared with the traditional diode when the RF signal is input into it. In addition, since the SIS mixer has the low thermal noise due to the low operation temperature and the low shot noise due to the low operation current, it realizes the low receiver noise temperature of the several times of the quantum noise limit hf/k.

2.3 Spectrometer

2.3.1 Autocorrelator (AC)

The AC (Autocorrelator), which we used in the present thesis, is based on the Wiener-Khintchine theorem that the inverse Fourier transformation of a power spectrum equals the autocorrelation of the signal $x(t)$. The input signal $V(t)$ is multiplied with $V(t + \tau)$, which is the same signal delayed by τ, and the autocorrelation function is obtained as:

$$C(\tau) = \lim_{T\to\infty} \frac{1}{T} \int_{-T/2}^{T/2} V(t)V(t+\tau)dt. \tag{2.12}$$

It is Fourier-transformed to give the power spectrum as

$$P(\nu) = \frac{1}{2\pi} \int_{-\infty}^{\infty} C(\tau)e^{-2\pi i\nu\tau} d\tau. \tag{2.13}$$

In an autocorrelator, the input signals (IF signals) are first converted to the digital data at a certain sampling rate. After this conversion, a shift resister gives the signal a delay by the time of τ. After the AND operation with the non-delayed data, the autocorrelation is calculated. The maximum delay time is determined by the number of the shift registers, N, to be $N\tau$. By the sampling theorem, the full frequency range and the maximum frequency resolution can be estimated to be $\Delta\nu = 1/\tau$ and $\Delta\nu/N = 1/(2N\tau)$, respectively. Such a digital autocorrelator has some advantages over analogue spectrometers as AOS (Acousto-optical Spectrometer) that the filter can change the observable frequency range or the frequency resolution, and AC has little performance variation and low noise. Each autocorrelator at Nobeyama Radio Observatory has 2048 channels, and several frequency range modes from 2 GHz to 16 MHz, where the frequency resolution becomes higher in this order. In our line survey, we mainly used 2 GHz mode with two channels bind in order to cover as wide frequency ranges as possible. As a result, we obtained the frequency resolution of $\sim$ 1 MHz and the velocity resolution in 90 GHz of $\sim$ 3 km s^{-1} (Figure 2.5, Figure 2.6).

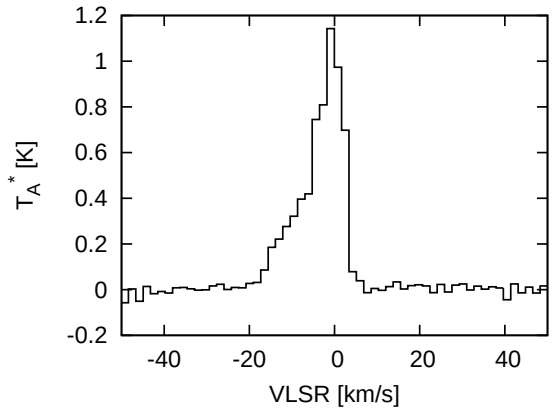

Figure 2.5: The SiO (2-1) spectrum obtained with the AC (autocorrelator).

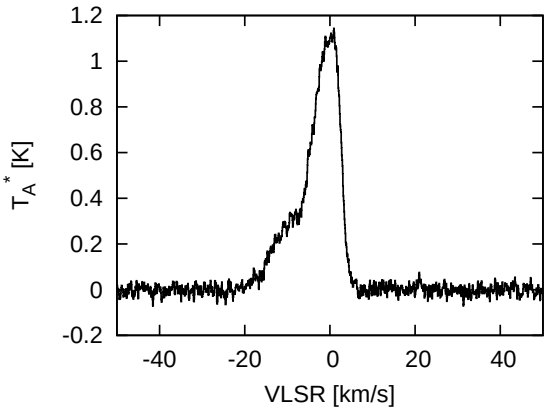

Figure 2.6: The SiO (2-1) spectrum obtained with the AOS (acousto-optical Spectrometer).

2.3.2 Acousto-optical Spectrometer (AOS)

The acousto-optical spectrometer (AOS) is a spectrometer utilizing the diffraction phenomenon of the ultrasonic sound wave propagating through a crystal. The IF is amplified, and is introduced into a piezoelectric device, which converts the electric signal to the supersonic sound wave. The ultrasonic sound wave propagates through the acousto-optical element, and is absorbed by the absorber. When the laser beam is irradiated into the crystal, it is diffracted by the compressional wave pattern of the ultrasonic sound wave. We can obtain the spectrum by detecting the diffracted laser with the CCD camera, where the diffraction angle and the diffraction intensity correspond to the frequency and the intensity of the signal, respectively.

At Nobeyama Radio Observatory, there are three types of AOS, which are AOS-H with the 40 MHz band width, AOS-W with the 250 MHz band width, and AOS-U with the 500 MHz band width. In each case, a Reticon with 2048 channels is used for the detection device. Thus, AOS-H and AOS-W have the frequency resolutions of 20 kHz (the velocity resolution of 0.07 km s^{-1} at 90 GHz) and 122 kHz (the velocity resolution of 0.07 km s^{-1} at 90 GHz), respectively.

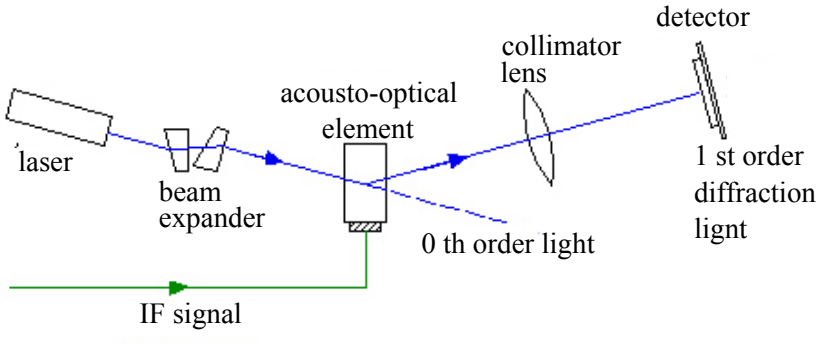

Figure 2.7: A block diagram of Acousto-optical spectrometer (AOS). Observatory. http://www.nro.nao.ac.jp/~nro45mrt/outreach/ov_spectr.html

Although almost all the spectral lines of molecules can be observed with the velocity resolution of 3 km s^{-1}, some molecular lines have the line width with 3 km s^{-1} or narrower. In this cases, we utilized the high AOS-H. For example, we show the line of N_2H^+ (1-0) (Figure 2.8

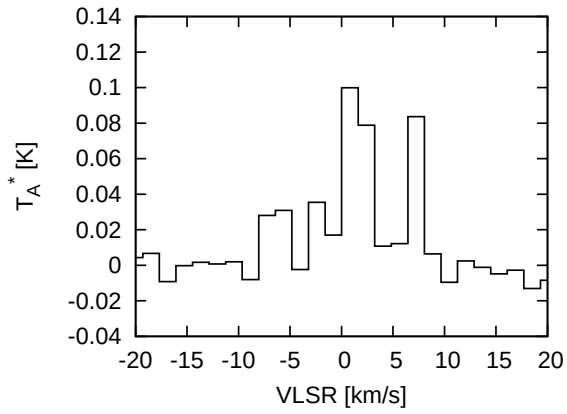

Figure 2.8: The spectrum of N_2H^+ (1-0) obtained with AC.

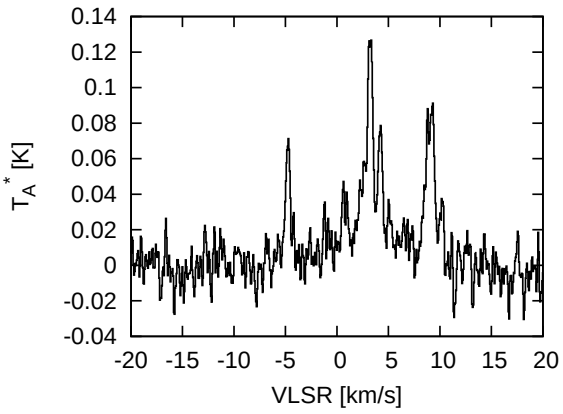

Figure 2.9: The spectrum of N_2H^+ (1-0) obtained with AOS-H

and 2.9). Although this molecule is observed in the line of the sight toward L1157 B1, it mainly exists in the ambient gas. Hence, the line profile has a line width narrower than 1 km s^{-1}, and the hyperfine structure due to the quadrupole moment of the N nuclei is resolved. In order to observe such a line profile, observations with AOS were sometime effective.

2.4 Calibration

In radio astronomy, the intensity is represented in the temperature scale by using the Rayleigh-Jeans law. We employed the chopper wheel method for intensity calibration. When we look at a source, the output from the receiver system is as

$$V_{\rm on} = C(T_{\rm source}e^{-\tau} + T_{\rm atm}(1 - e^{-\tau})). \tag{2.14}$$

On the other hand, the output voltage is as

$$V_{\rm off} = CT_{\rm atm}(1 - e^{-\tau}) \tag{2.15}$$

where an off-position (no-source position) is observed. Here, C, $T_{\rm source}$, $T_{\rm atm}$ and τ denote a constant specific to the device, the emission power from the source in the outer space, the atmospheric emission, and the opacity of the atmosphere, respectively. If we insert a radio-wave absorber (chopper) of temperature $T_{\rm abs}$ into the optical path of the telescope, the output is written as:

$$V_{\rm abs} = CT_{\rm abs}. \tag{2.16}$$

If we assume that the temperature of this absorber is equal to the atmospheric temperature, we obtain the emission power of the source as

$$T_{\rm source} = \frac{V_{\rm on} - V_{\rm off}}{V_{\rm abs} - V_{\rm off}} \times T_{\rm atm}. \tag{2.17}$$

$T_{\rm source}$ is the antenna temperature of the observed source outside the atmosphere, which is also indicated as T_A^*. If the weather condition is bad and the opacity of the atmosphere becomes high, the temperature difference between the absorber and the atmosphere cannot be ignored. Hence, this method empirically has error of ~ 20 %.

The beam-averaged radiative temperature of the source can be obtained by correcting the main beam efficiency as

$$T_{\rm mb} = \frac{T_A^*}{\eta_{\rm mb}} \tag{2.18}$$

where $\eta_{\rm mb}$, for example, of T100 H/V receiver used for the observation of L1157 B1 was 50 % at 80 GHz, 47% at 90 GHz, and 43 % at 100 GHz, respectively. The beam size also changes for these frequencies ranges to be $20''$, $18''$, and $17''$, respectively.

Chapter 3

L1157 B1

3.1 Outflow Shock in L1157 B1

L1157 B1 (d = 440 pc: Viotti 1969) is a famous shocked region caused by an interaction between bipolar outflow from the low-mass protostar IRAS 20386+6751 and the ambient gas. This bipolar outflow is well collimated (Figure 3.1), whose dynamical age is reported to be 1.8 $\times$ 10^4 yr (Umemoto et al. 1992). Mikami et al. (1992) detected a broad blue-shifted SiO (J = 2−1) line toward L1157 B1 (Figure 3.1), and suggested that SiO is liberated into gas-phase by disruption of silicate grains by the shock. The direct evidence of the shock was revealed by the detection of near-infrared H_2 emissions (Davis & Eislöffel 1995; Nisini et al. 2010b). Very recently, strong emission of H_2O liberated into the gas-phase by the shock was detected toward L1157 B1 with Herschel (Nisini et al. 2010a). The physical property of the shocked region was studied, for instance, by Hirano and Taniguchi (2001), Umemoto et al. (1999), and Bachiller & Pérez Gutiérrez (1997). The high kinetic temperature of 130-140 K is attributed to the shock heating (Umemoto et al. 1999), whereas the H_2 density is deduced to be $\sim 10^5$ cm^{-3} by observations of high density tracers such as CS and SiO (Mikami et al. 1992; Bachiller & Pérez Gutiérrez 1997). L1157 B1 is separated from the protostar by 1′ (0.13 pc), and hence, we can observe the 'pure' shocked region without being hampered by the complicated structure of the protostar core even with the single dish telescope.

Abundances of fundamental molecules in L1157 B1 were reported by Avery and Chiao (1996) and Bachiller and Pérez Gutiérrez (1997). These results clearly indicated that the abundances of some molecules such as SiO, CH_3OH, H_2CO, and SO are enhanced by the shock. The detailed distributions of molecules in L1157 B1 were obtained by interferometric observations (e.g. Benedettini et al. 2007), which demonstrated the clumpy nature of the shocked gas. Moreover, Arce et al. (2008) detected some complex organic molecules such as $HCOOCH_3$, HCOOH, and C_2H_5OH, whereas Codella et al. (2009) conducted a high resolution imaging of CH_3CN with PdBI. Nisini et al. (2010a) reported a line survey in the submillimeter-wave region toward L1157 B1 with Herschel, where the CH_3OH line emissions are found to be dominant.

As described above, L1157 B1 is one of the best objects for detailed studies on the shock chemistry. We therefore conducted an unbiased spectral line survey toward this source in the 3 mm band with the Nobeyama 45 m telescope (NRO 45 m), as a part of the legacy project of Nobeyama Radio Observatory. The initial result verifying the feasibility of the line survey was reported by Sugimura et al. (2011). They observed the frequency ranges of 88.6-91.0 GHz and 96.3-97.5 GHz, and detected several lines of complex organic molecules such as CH_3CHO

and $HCOOCH_3$, as well as a line of mono-deuterated methanol CH_2DOH. With the aid of the chemical model calculation for these complex organic molecules, they suggested the desorption of grain mantle species, which are formed by grain-surface reactions in the cold era, contributes to the abundances of some molecules such as $HCOOCH_3$ and HCOOH in L1157 B1. They also pointed out that gas-phase reactions could also be effective for production of a few species such as CH_3CHO even within the short dynamical timescale of the bipolar outflow (1.8×10^4 yr) (Umemoto et al. 1992). This result confirmed importance of the grain-surface production and the subsequent evaporation of complex organic molecules by the shock in L1157 B1. In other words, the composition of complex organic molecules in the gas-phase reflects that in grain mantles. The abundance ratios such as $[HCOOCH_3]/[CH_3OH]$, $[HCOOH]/[CH_3OH]$, and $[CH_3CHO]/[CH_3OH]$ are around 0.003-0.01, which are lower than those reported for a prototypical hot corino of the low mass star-forming region, IRAS 16293-2422, by more than one order of magnitude. Furthermore, the deuterium fractionation ratio $[CH_2DOH]/[CH_3OH]$ shows the similar difference: $[CH_2DOH]/[CH_3OH]$ is 0.01-0.03 toward L1157 B1, whereas it is 0.9 toward IRAS 16293-2422 (Parise et al. 2002). These results may suggest that the chemical composition of grain mantles is different between protostellar cores and ambient clouds (Sugimura et al. 2011).

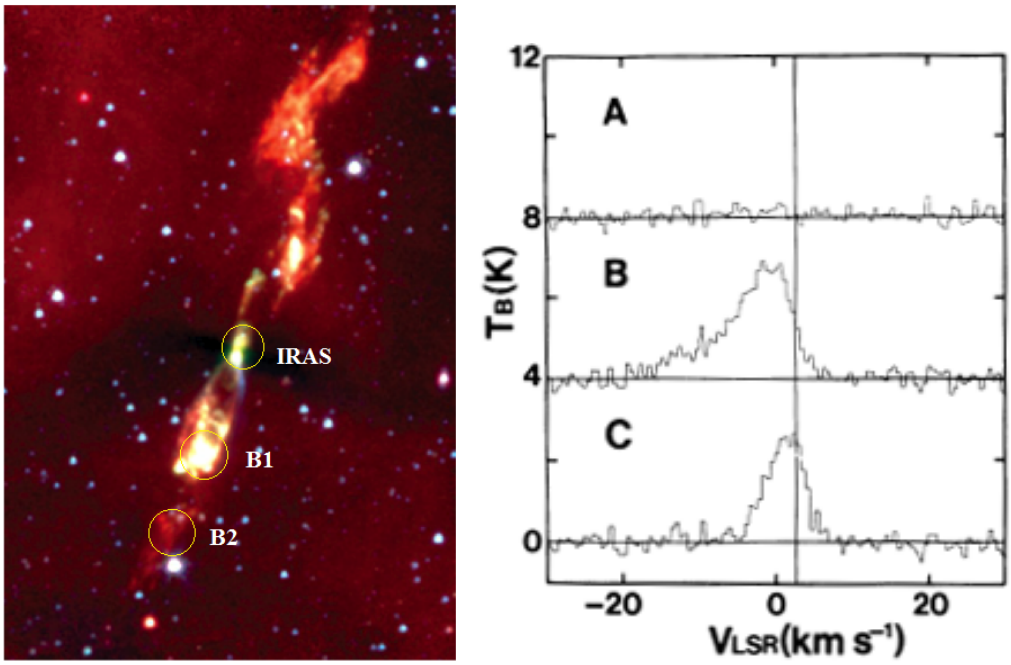

Figure 3.1: Left: L1157 star-forming region by Spitzer Space Telescope (NASA, http://www.spitzer.caltech.edu/images/1872-ssc2007-19a1-Baby-Picture-of-our-Solar-System). B1, where we focused on in our research, is formed through the interaction between the blue-shifted molecular outflow from L1157 and the ambient gas. L1157 B1 is separated from the protostar by (20″,-60″). B2 is separated by (35″,-95″) in the downstream of B1. We conducted an observation in this shocked region. Right: SiO (J = 2-1) spectrum detected by Mikami et al.(1992). B, C were obtained in B1, and in the position separated from the protostar by (45″,-105″), respectively. SiO was not detected toward the protostar (A). They detected SiO (J = 2-1 line) in regions where the interaction occurs between the outflow and the ambient gas.

Encouraged by the early results mentioned above, we extended the spectral line survey to the whole 3 mm band, covering the frequency range from 78.1 to 115.6 GHz. From this observation, a complete chemical composition of the L1157 B1 shocked region is revealed, whose general feature is presented in this chapter.

3.2 Observation

The observation of L1157 B1 was conducted with the NRO 45 m from March to May 2009, from December 2009 to May 2010, and from December 2010 to May 2011. L1157 B1 is the brightest CO clump located in the blue lobe of the bipolar outflow, whose coordinate is α(J2000) = $20^{\rm h}39^{\rm m}09^{\rm s}.75$, δ(J2000) = $68°01'15.9''$ ($\Delta\alpha = 20''$, $\Delta\delta = -60''$ from the protostar IRAS 20386+6751). The off-position is taken at α(J2000) = $20^{\rm h}39^{\rm m}09^{\rm s}.75$, δ(J2000) = $68°21'15.9''$. In this observation, we used the dual-polarization sideband-separating SIS receiver T100 H/V (Nakajima et al. 2008). The system temperatures ranged from 150 to 200 K in winter and about 250 K in spring. The intensity scale was calibrated by the chopper-wheel method, and is estimated to be accurate within 20 %. The image rejection ratio was measured by injection of artificial monochromatic signal, and was confirmed to be better than 10 dB for most cases. The main-beam efficiency ($\eta_{\rm mb}$) and the beam size are 0.41 and $18''$, respectively, at 90 GHz. The pointing of the telescope was checked by observing the nearby SiO maser source (T Cep), and was maintained to be better than $8''$.

The backend is a bank of auto-correlators (AC). Until May 2010, the bandwidth and the channel spacing were 512 MHz and 0.5 MHz, respectively in order to cover a wide-frequency range by sacrificing the spectral resolution. From December 2010, they were upgraded to 2 GHz and 0.488 MHz, respectively. In order to enhance the signal-to-noise ratio, two successive channels were summed up, yielding the frequency resolution of 1 MHz. This corresponds to the velocity resolution of $\sim$ 3 km s^{-1} at 90 GHz. Since the typical velocity width of the spectral line toward L1157 B1 is broader than 5 km s^{-1} except for a few molecules, this resolution is sufficient. Although the intermediate frequency (IF) output range of the side band separating SIS receiver was 2 GHz for LSB and USB each, the backend capability limited the actual instantaneous bandwidth to 1.2 GHz for each sideband until May 2010. From December 2010, the IF output range was extended to 4 GHz for LSB and USB each. Furthermore, we were able to obtain the LSB and USB data simultaneously, thanks to the upgrade of the backend. These significantly improved the efficiency of the survey. Note that we additionally used the high resolution spectrometer (AOS-H; 37 kHz resolution) for a few lines, although it has a band width of only 40 MHz. The total observation time was 300 hrs.

3.3 Results

3.3.1 Detected Molecules

Figure 3.2 is the overview of the observed spectrum toward L1157 B1 in the frequency range from 78.1 to 115.8 GHz, whereas Fig. Appendix A.1 shows its expansion. The rms noise level achieved is 4-10 mK at the frequency resolution of 1 MHz. With this sensitivity, we detected many weak lines in addition to strong lines such as HCO^+, CH_3OH, and CS. We assigned the observed lines by using the molecular spectral line databases, CDMS (Muller et al. 2005), JPL (Pickett et al. 1998), and NIST (Lovas et al. 2009). The spectral lines from the image side

band are indicated as 'image' in Fig. A.1. A basic criterion for detection is that the line has the integrated intensity with the confidence level higher than 4σ. However, we also picked up some lines even below this confidence level, if other lines of the same molecule are definitively detected. All the detected molecules are summarized in Table 3.1. In total, 130 lines of 29 species are detected. Table 3.2 lists the parameters of the detected lines, which are obtained by the Gaussian fitting. Almost all lines have broad velocity widths (FWHM) ranging from 5 to 9 km s^{-1}, indicating that these lines do not originate from the ambient gas but from the shocked region. However, the lines of some molecular ions (e.g. N_2H^+, $H^{13}CO^+$) and the isotopic species of CO exceptionally show narrow velocity widths ranging from 2 to 3 km s^{-1}. This suggests that they are emitted from the ambient gas. The peak velocities of most lines are blue-shifted with respect to the systemic velocity of the ambient gas of about 2.7 km s^{-1}. Exceptions are the lines of molecular ions and the isotopic species of CO, as in the case of the line widths. We will further discuss the relationship between the line width and the peak velocity in Section 3.4.2.

Complex Organic Molecules				
CH_3OH	$^{13}CH_3OH$	CH_2DOH	C_2H_5OH	CH_3CHO
NH_2CHO	HCOOH	$HCOOCH_3$		
Nitrile and Other Nitrogen-containing Molecules				
HCN	$H^{13}CN$	$HC^{15}N$	HNC	HNCO
HC_3N	CH_3CN			
Carbon Chain Molecules				
C_2H	CCS	CH_3CCH	H_2CCO	
Sulfur-containing Molecules				
CS	^{13}CS	$C^{33}S$	$C^{34}S$	OCS
SO	^{34}SO	SO_2	H_2CS	NS
CH_3SH ?				
Molecular Ions				
HCO^+	$H^{13}CO^+$	HCS^+	N_2H^+	
Other Molecules				
SiO	^{29}SiO	^{30}SiO	$Si^{18}O$?	SiS ?
CO	^{13}CO	$C^{18}O$	$C^{17}O$	c-C_3H_2
PN	CN	^{13}CN		

Table 3.1: Molecules Detected toward L1157 B1.

Table 3.2: Observed Line Parameters

Frequency (GHz)	Molecules	Transition	E_u (cm^{-1})	$T_{MB}{}^{\#}$ (K)	$V_{lsr}{}^{\#}$ (km/s)	$\Delta v^{\#}$ (km/s)	$\int T_{MB} dv$ (K·km/s)
79.0993132	CH_3CHO	4(1,3)-3(1,2) E	8.23	0.05±0.01	0.99±0.81	4.84±1.30	0.27±0.05
79.1501659	CH_3CHO	4(1,3)-3(1,2) A^{--}	8.18	0.06±0.01	0.52±0.68	7.57±1.41	0.51±0.06
80.076652	H_2CCO	4(1,4)-3(1,3)	15.7	0.03±0.01	1.36±0.62	5.56±0.95	0.20±0.03
80.832117	H_2CCO	4(0,4)-3(0,3)	6.74	0.01±0.01	1.29±1.64	5.53±2.72	0.08±0.03
81.50517	CCS	7(6)-6(5)	10.7	0.05±0.01	0.20±0.48	6.54±0.90	0.36±0.04
81.8814677	HC_3N	9-8	13.7	0.38±0.04	-0.88±0.23	7.56±0.81	2.98±0.05
83.688093	SO_2	8(1,7)-8(0,8)	25.5	0.21±0.02	-0.63±0.27	6.07±0.76	1.61±0.04
84.521169	CH_3OH	5(-1,5)-4(0,4) E	28.1	3.01±0.09	-0.55±0.03	5.78±0.19	18.69±0.04
84.5423295	NH_2CHO	4(0,4)-3(0,3)	7.06	0.03±0.01	-0.55±1.03	6.54±2.31	0.21±0.04
84.7461702	^{30}SiO	2-1	4.24	0.21±0.02	-1.37±0.32	6.48±0.58	1.73±0.04
84.97022	$^{13}CH_3OH$	8(0,8)-7(1,7) A^{++}	56.7	0.02±0.01	-0.93±1.33	10.40±2.71	0.24±0.06
85.139121	OCS	7-6	11.4	0.06±0.01	0.04±0.80	9.97±2.14	0.72±0.09
85.338893	c-C_3H_2	2(1,2)-1(0,1)	4.48	0.12±0.02	0.44±0.24	4.63±0.79	0.64±0.05
85.3479	HCS^+	2-1	4.27	0.05±0.01	0.35±0.41	4.69±1.11	0.26±0.05
85.568084	CH_3OH	6(-2,5)-7(-1,7) E	51.9	-0.04±0.01	-0.27±0.73	6.35±1.40	-0.30±0.07
85.759199	^{29}SiO	2-1	4.29	0.29±0.03	-1.52±0.34	7.31±0.70	2.72±0.06
86.054961	$HC^{15}N$	1-0	2.87	0.08±0.02	0.35±0.33	5.66±1.08	0.57±0.05
86.09395	SO	2(2)-1(1)	13.4	0.25±0.04	0.42±0.28	5.59±0.92	1.78±0.05
86.181413	CCS	6(7)-5(6)	16.2	0.02±0.01	-0.71±1.18	5.59±2.13	0.15±0.04
86.3399215	$H^{13}CN$	1-0	2.88	0.23±0.02	0.21±0.25	10.39±0.98	2.75±0.06
86.54681891	HCOOH	4(1,4)-3(1,3)	9.43	0.02±0.01	3.44±1.97	6.41±3.68	0.11±0.05
86.7542884	$H^{13}CO^+$	1-0	2.89	0.11±0.01	2.74±0.12	2.44±2.33	0.28±0.03
86.84696	SiO	2-1	4.35	2.08±0.19	-1.58±0.52	9.27±1.00	22.00±0.06
87.284105	C_2H	1-0, J = 3/2-1/2, F = 1-1	2.91	0.06±0.02	-0.02±0.79	6.00±1.62	0.43±0.07
87.316898	C_2H	1-0, J = 3/2-1/2, F = 2-1	2.91	0.44±0.07	-0.01±0.23	6.57±1.13	3.18±0.08
87.328585	C_2H	1-0, J = 3/2-1/2, F = 1-0	2.91	0.23±0.02	-0.20±0.20	5.68±0.52	1.52±0.08
87.401989	C_2H	1-0, J = 1/2-1/2, F = 1-1	2.92	0.21±0.04	-0.13±0.53	6.85±1.58	1.95±0.09
87.407165	C_2H	1-0, J = 1/2-1/2, F = 0-1	2.92	0.11±0.04	0.30±0.98	6.04±2.71	0.70±0.08
87.44647	C_2H	1-0, J = 1/2-1/2, F = 1-0	2.92	0.07±0.01	0.67±0.40	4.30±0.67	0.35±0.07
87.8488726	NH_2CHO	4(1,3)-3(1,2)	9.40	0.04±0.01	0.31±0.83	5.51±1.55	0.24±0.04
87.925237	HNCO	4(0,4)-3(0,3)	7.33	0.23±0.02	0.02±0.20	7.74±0.63	1.85±0.06
88.6316022	HCN	1-0	2.96	5.8±0.51	-1.21±0.76	12.68±1.40	74.37±0.05
88.843117	$HCOOCH_3$	7(1,6)-6(1,5) E	12.5	0.03±0.01	-0.04±0.71	3.85±1.55	0.11±0.03
88.851641	$HCOOCH_3$	7(1,6)-6(1,5) A	12.5	0.02±0.01	-0.44±0.60	5.22±1.03	0.11±0.03

Table 3.2: continued

Frequency (GHz)	Molecules	Transition	E_u (cm^{-1})	T_{MB} (K)	V_{lsr} (km/s)	Δv (km/s)	$\int T_{MB} dv$ (K·km/s)
89.188523	HCO^+	1-0	2.97	2.24±0.26	0.95±0.25	6.20±0.77	18.15±0.04
89.314589	$HCOOCH_3$	8(1,8)-7(1,7) E	14	0.03±0.01	3.01±0.60	8.16±1.20	0.32±0.05
89.316668	$HCOOCH_3$	8(1,8)-7(1,7) A	14				
89.40791	CH_2DOH	2(0,2)-1(0,1) e_0	4.5	0.03±0.01	0.20±0.62	6.88±1.15	0.27±0.04
89.5791785	HCOOH	4(0,4)-3(0,3)	7.48	0.03±0.01	0.72±0.63	5.05±1.09	0.18±0.03
90.663568	HNC	1-0	3.02	1.27±0.14	1.34±0.15	4.73±0.55	7.00±0.05
90.979023	HC_3N	10-9	16.7	0.69±0.08	-0.69±0.16	6.29±0.77	4.95±0.05
91.959206	CH_3CN	5(4)-4(4)	88.6	0.03±0.01[a]	-0.37±1.16[a]	7.54±1.91[a]	0.23±0.07[a]
91.971374	CH_3CN	5(3)-4(3)	53.9	0.10±0.01[a]	1.11±0.32[a]	4.71±0.54[a]	0.75±0.07[a]
91.980000	CH_3CN	5(2)-4(2)	29.1	0.09±0.01[a]	-0.13±0.56[a]	6.24±0.99[a]	0.70±0.07[a]
91.985284	CH_3CN	5(1)-4(1)	14.2	0.16±0.03[a]	0.99±0.50[a]	3.44±0.67[a]	0.78±0.07[a]
91.987054	CH_3CN	5(0)-4(0)	9.2	0.25±0.02[a]	0.59±0.37[a]	6.08±0.65[a]	1.67±0.08[a]
92.494308	^{13}CS	2-1	4.6	0.17±0.02	0.49±0.20	5.08±0.56	1.06±0.05
93.0983627	HCOOH	4(1,3)-3(1,2)	9.98	0.04±0.01	0.56±0.55	5.50±1.18	0.25±0.05
93.1733922	N_2H^+	1-0	3.11	0.17±0.03	1.46±0.61	4.47±0.92	1.16±0.07
93.580859	CH_3CHO	5(1,5)-4(1,4) A^{++}	10.9	0.10±0.01	0.63±0.26	5.21±0.62	0.79±0.04
93.595276	CH_3CHO	5(1,5)-4(1,4) E	11.0	0.08±0.02	0.75±0.46	7.14±1.49	0.76±0.05
93.870107	CCS	8(7)-7(6)	13.83	0.06±0.01	0.19±0.49	6.65±1.70	0.51±0.04
93.9797695	PN	2-1	4.7	0.04±0.01	-0.63±0.39	8.34±1.14	0.50±0.04
94.405163	$^{13}CH_3OH$	2(-1,2)-1(-1,1) E	8.62				
94.407129	$^{13}CH_3OH$	2(0,2)-1(0,1) A^{++}	4.72	0.09±0.01	1.80±0.61	9.76±1.35	1.01±0.06
94.411016	$^{13}CH_3OH$	2(0,2)-1(0,1) E	13.8				
95.169463	CH_3OH	8(0,8)-7(1,7) A^{++}	58.1	0.84±0.10	0.22±0.14	5.26±0.65	5.09±0.04
95.9143090	CH_3OH	2(1,2)-1(1,1) A^{++}	14.9	0.20±0.02	-0.25±0.17	5.51±0.68	1.23±0.04
95.94734	CH_3CHO	5(0,5)-4(0,4) E	9.68	0.06±0.01	0.18±0.22	5.40±0.38	0.35±0.04
95.96338	CH_3CHO	5(0,5)-4(0,4) A^{++}	9.62	0.07±0.01	0.57±0.28	4.49±0.65	0.39±0.04
96.2742	CH_3CHO	5(2,4)-4(2,3) A^{--}	15.9	0.02±0.01	-0.31±0.68	3.47±2.22	0.07±0.02
96.4129495	$C^{34}S$	2-1	4.82	0.26±0.02	-0.44±0.09	6.40±0.47	1.77±0.04
96.42562	CH_3CHO	5(-2,4)-4(-2,3) E	15.9	0.03±0.01	0.66±0.69	4.77±1.68	0.23±0.03
96.475523	CH_3CHO	5(2,3)-4(2,2) E	16.0	0.03±0.01	0.71±0.57	4.51±1.43	0.21±0.03
96.632668	CH_3CHO	5(2,3)-4(2,2) A^{++}	16.0	0.04±0.01	1.58±0.18	4.52±0.62	0.19±0.03
96.739362	CH_3OH	2(-1,2)-1(-1,1) E	8.71	3.04±0.31[a]	1.18±0.22[a]	3.45±0.16[a]	12.3±0.2[a]
96.741375	CH_3OH	2(0,2)-1(0,1) A^{++}	4.84	4.37±0.12[a]	0.79±0.16[a]	6.86±0.47[a]	32.8±0.1[a]
96.74455	CH_3OH	2(0,2)-1(0,1) E	14.0	0.85±0.09 [a]	0.06±0.45[a]	7.02±1.16[a]	5.3±0.1[a]

Table 3.2: continued

Frequency (GHz)	Molecules	Transition	E_u (cm^{-1})	T_{MB} (K)	V_{lsr} (km/s)	Δv (km/s)	$\int T_{MB} dv$ (K·km/s)
96.755511	CH_3OH	2(1,1)-1(1,0) E	19.5	0.22±0.02	-0.35±0.22	6.62±0.69	1.48±0.03
97.1720639	$C^{33}S$	2-1	4.86	0.04±0.01	0.81±0.87	10.31±1.55	0.49±0.06
97.3012085	OCS	8-7	14.6	0.07±0.01	-0.29±0.36	5.60±1.08	0.43±0.04
97.582804	CH_3OH	2(1,1)-1(1,0) A^{--}	15.0	0.45±0.01	-0.48±0.09	5.88±0.17	2.86±0.03
97.715317	^{34}SO	3(2)-2(1)	6.32	0.12±0.02	0.10±0.29	6.15±1.13	0.83±0.04
97.9809533	CS	2-1	4.90	3.38±0.29	-0.33±0.30	7.65±0.81	27.17±0.05
98.792289	$HCOOCH_3$	8(4,4)-7(4,3) A	22.2	0.02±0.01	0.22±0.81	4.95±1.40	0.15±0.05
98.863328	CH_3CHO	5(1,4)-4(1,3) E	11.5	0.12±0.01	0.44±0.19	5.67±0.33	0.80±0.04
98.900948	CH_3CHO	5(1,4)-4(1,3) A^{--}	11.5	0.11±0.02	0.68±0.28	5.69±0.91	0.72±0.04
99.29987	SO	3(2)-2(1)	6.41	2.53±0.22	0.06±0.17	5.80±0.55	17.71±0.03
100.076392	HC_3N	11-10	20.0	0.62±0.04	-0.99±0.16	6.84±0.48	4.55±0.05
100.094514	H_2CCO	5(1,5)-4(1,4)	19.1	0.05±0.01	0.27±0.35	4.20±0.51	0.21±0.04
100.681545	$HCOOCH_3$	9(0,9)-8(0,8) E	17.3	0.04±0.01	-2.49±0.52	6.17±0.93	0.30±0.04
100.683368	$HCOOCH_3$	9(0,9)-8(0,8) A	17.3				
100.990102	C_2H_5OH	8(2,7)-8(1,8)	24.4	0.02±0.01	0.63±1.11	4.48±1.82	0.12±0.04
101.4778095	H_2CS	3(1,3)-2(1,2)	15.9	0.24±0.02	-0.72±0.24	7.23±0.52	1.85±0.05
101.981429	H_2CCO	5(1,4)-4(1,3)	19.3	0.05±0.01	0.41±0.25	5.34±0.50	0.28±0.04
102.0642656	NH_2CHO	5(1,5)-4(1,4)	12.3	0.02±0.01	-0.66±0.31	4.74±0.86	0.15±0.03
102.5479844	CH_3CCH	6(0)-5(0)	12.0	0.03±0.01	0.66±0.36	11.1±1.0	0.33±0.04
103.0399065	H_2CS	3(2,2)-2(2,1)	43.5				
103.040452	H_2CS	3(0,3)-2(0,2)	6.87	0.13±0.01	-0.71±0.18	6.58±0.37	0.89±0.02
103.0518468	H_2CS	3(2,1)-2(2,0)	43.5	0.02±0.01	-1.17±0.43	6.46±0.92	0.14±0.02
104.0294183	SO_2	3(1,3)-2(0,2)	5.38	0.32±0.02	-0.69±0.15	6.09±0.34	2.21±0.05
104.2392952	SO_2	10(1,9)-10(0,10)	38.0	0.13±0.01	-0.36±0.32	6.54±0.63	0.97±0.05
104.48726	C_2H_5OH	7(0,7)-6(1,6)	16.2	0.03±0.01	1.21±1.00	5.45±1.82	0.15±0.03
104.61704	H_2CS	3(1,2)-2(1,1)	16.1	0.17±0.01	-0.86±0.15	6.53±0.60	1.15±0.04
104.808632	C_2H_5OH	5(1,5)-4(0,4)	9.31	0.03±0.01	0.57±0.47	5.67±1.00	0.20±0.03
105.4642181	NH_2CHO	5(0,5)-4(0,4)	10.6	0.04±0.01	0.19±0.37	6.04±0.81	0.22±0.03
106.347726	CCS	9(8)-8(7)	17.4	0.07±0.01	-0.18±0.24	5.97±0.47	0.49±0.03
107.01377	CH_3OH	3(1,3)-4(0,4) A^{++}	19.7	-0.17±0.01	0.22±0.19	6.22±0.37	-1.13±0.02
108.1267202	HCOOH	5(1,5)-4(1,4)	13.0	0.02±0.01	-0.26±0.55	6.22±1.15	0.12±0.02
108.780201	^{13}CN	$J = 3/2$-1/2, F = 3-2, $F_1 = 1, F_2 = 2 - 1$	3.65	0.02± 0.01	1.26±0.77	5.99±1.62	0.12±0.02
108.893963	CH_3OH	0(0,0)-1(-1,1) E	9.12	0.38±0.06	-0.02±0.22	6.20±1.01	2.69±0.03
109.173634	HC_3N	12-11	23.7	0.59±0.03	-0.83±0.08	6.41±0.41	4.11±0.03
109.25222	SO	2(3)-1(2)	14.6	0.35±0.04	-0.02±0.21	6.10±0.75	2.67±0.03
109.463063	OCS	9-8	18.3	0.07±0.01	-0.45±0.14	6.08±0.52	0.47±0.04
109.7821734	$C^{18}O$	1-0	3.66	0.42±0.01	3.02±0.04	2.26±0.25	1.32±0.02

Table 3.2: continued

Frequency (GHz)	Molecules	Transition	E_u (cm^{-1})	T_{MB} (K)	V_{lsr} (km/s)	Δv (km/s)	$\int T_{MB} dv$ (K·km/s)
109.905749	HNCO	5(0,5)-4(0,4)	11.0	0.22±0.03	0.48±0.28	5.91±0.89	1.77±0.05
110.2013543	^{13}CO	1-0	3.68	1.69±0.09	3.31±0.06	3.09±0.23	6.04±0.03
110.3494703	CH_3CN	6(4)-5(4)	92.3	0.04±0.01	0.55±0.45	3.11±0.60	0.14±0.03
110.3643537	CH_3CN	6(3)-5(3)	57.6	0.08±0.01	0.30±0.21	5.22±0.49	0.51±0.04
110.374989	CH_3CN	6(2)-5(2)	32.8	0.08±0.01	-0.26±0.29	5.29±0.70	0.47±0.04
110.381372	CH_3CN	6(1)-5(1)	17.9				
110.3834999	CH_3CN	6(0)-5(0)	12.9	0.17±0.01	2.17±0.30	9.47±0.58	1.68±0.05
110.880447	$HCOOCH_3$	9(5,5)-8(5,4) A	30.0	0.03±0.01	1.28±0.73	4.17±1.27	0.18±0.03
112.248728	CH_3CHO	6(1,6)-5(1,5) A^{++}	14.7	0.05±0.02	0.49±0.97	4.38±1.66	0.23±0.04
112.254524	CH_3CHO	6(1,6)-5(1,5) E	14.7	0.05±0.02	0.65±0.95	4.92±1.98	0.27±0.04
112.358982	$C^{17}O$	1-0	3.75	0.06±0.01	2.18±0.35	3.34±0.69	0.24±0.04
112.8914435	HCOOH	5(2,3)-4(2,2)	20.1	0.03±0.01	0.36±0.84	5.84±1.57	0.15±0.03
113.1233701	CN	1-0, J = 1/2-1/2, F = 1/2-1/2	3.77	0.06±0.02	0.78±0.68	4.47±1.51	0.34±0.04
113.1441573	CN	1-0, J = 1/2-1/2, F = 1/2-3/2	3.77	0.28±0.02	0.22±0.18	5.40±0.34	1.65±0.05
113.1704915	CN	1-0, J = 1/2-1/2, F = 3/2-1/2	3.78	0.32±0.01	0.31±0.11	5.58±0.26	1.94±0.05
113.1912787	CN	1-0, J = 1/2-1/2, F = 3/2-3/2	3.78	0.36±0.02	0.27±0.14	5.28±0.38	2.20±0.04
113.4101860	CCS	8(9)-7(8)	23.3	0.02±0.01	2.00±1.06	8.09±1.89	0.22±0.05
113.4881202	CN	1-0, J = 3/2-1/2, F = 3/2-1/2	3.79	0.40±0.03	0.67±0.17	4.26±0.41	1.95±0.04
113.4909702	CN	1-0, J = 3/2-1/2, F = 5/2-3/2	3.79	0.96±0.03	0.19±0.08	5.86±0.21	6.19±0.04
113.4996443	CN	1-0, J = 3/2-1/2, F = 1/2-1/2	3.79	0.25±0.01	0.21±0.16	5.83±0.31	1.60±0.04
113.5089074	CN	1-0, J = 3/2-1/2, F = 3/2-3/2	3.79	0.29±0.03	0.45±0.15	5.31±0.67	1.77±0.05
113.5204315	CN	1-0, J = 3/2-1/2, F = 1/2-3/2	3.79	0.02±0.01	-0.22±1.00	6.94±2.25	0.20±0.04
113.75661	$HCOOCH_3$	9(3,6)-8(3,5) A	22.8	0.03±0.01	-0.28±0.64	5.36±1.41	0.20±0.03
114.94019	CH_3CHO	6(0,6)-5(0,5) E	13.5	0.08±0.01	0.10±0.32	5.08±0.76	0.44±0.05
114.959911	CH_3CHO	6(0,6)-5(0,5) A^{++}	13.5	0.07±0.01	0.31±0.42	5.10±0.91	0.42±0.05
115.153935	NS	J = 5/2-3/2, F = 7/2-5/2 e	6.14	0.05±0.01	2.20±0.54	3.73±1.13	0.19±0.04
115.156812	NS	J = 5/2-3/2, F = 5/2-3/2 e	6.60	0.04±0.01	2.84±1.06	8.79±2.36	0.38±0.04
115.2712018	CO	1-0	3.85	7.83±0.36	0.89±0.15	5.64±0.29	51.17±0.06
115.556253	NS	J = 5/2-3/2, F = 7/2-5/2 f	6.19	0.07±0.01	-0.00±0.30	4.80±0.60	0.42±0.05
115.570763	NS	J = 5/2-3/2, F = 5/2-3/2 f	6.18	0.06±0.02	-0.71±0.58	4.34±1.13	0.39±0.05

[a]Obtained from the data taken with the high resolution spectrometer ($\Delta\nu$ = 37 kHz).

Table 3.3: Possibly Detected Molecules and Unidentified Lines

Frequency (GHz)	Molecules	Transition	E_u (cm^{-1})	T_{MB} (K)	V_{lsr} (km/s)	Δv (km/s)	$\int T_{MB} dv$ (K·km/s)
Tentative							
80.704938	$Si^{18}O$	2-1	4.04	0.02±0.01	-0.79±0.73	5.02±1.25	0.11±0.03
86.22378	$(CH_3)_2O$	2(2,0)-2(1,1) AE	5.81	0.02±0.01	-2.59±0.90	5.47±1.61	0.14±0.04
88.166832	$H^{13}CCCN$	10-9	16.2	0.03±0.01	1.81±0.97	5.57±1.60	0.18±0.04
89.861484	HCOOH	4(2,3)-3(2,2)	16.3	0.02±0.01	0.12±2.32	6.28±3.92	0.16±0.05
90.145634	$HCOOCH_3$	7(2,5)-6(2,4) E	13.7	0.02±0.01	0.74±0.80	4.58±1.99	0.09±0.04
90.156511	$HCOOCH_3$	7(2,5)-6(2,4) A	13.7	0.02±0.01	-0.09±1.79	8.32±3.75	0.21±0.05
90.771564	SiS	5-4	9.08	0.03±0.01	4.74±0.71	3.24±2.34	0.10±0.03
91.75132	HSCN	8(0,8)-7(0,7)	13.8	0.03±0.01	1.40±0.76	2.41±9.74	0.08±0.03
101.13916	CH_3SH	4(0)-3(0) A	9.0	0.04±0.01	0.82±1.07	14.3±2.3	0.32±0.04
101.13965	CH_3SH	4(0)-3(0) E	9.0				
106.743244	^{34}SO	2(3)-1(2)	14.5	0.02±0.01	-0.03±0.62	4.95±1.39	0.10±0.04
108.9242772	SiS	6-5	12.7	0.01±0.01	-1.96±0.45	11.8±1.0	0.15±0.03
Unidentified*							
80.5350	U			0.02		5.90±1.43	0.13±0.03
88.0313	U			0.03		5.75±1.51	0.25±0.05
92.8078	U			0.06		5.67±1.06	0.39±0.05
96.6038	U			0.03		5.66±0.79	0.21±0.03
100.0581	U			0.05		4.10±0.56	0.26±0.04
107.2141	U			0.02		7.22±1.27	0.19±0.03
115.0794	U			0.02		5.70±2.54	0.19±0.05

#Obtained from the Gaussian fit.

*Frequencies are based on the peak positions of the observed spectral profile, assuming the V_{lsr} of 2.7 km s^{-1}.

Molecules	N ($T_{\rm rot}$ = 12 (K)) ($\rm cm^{-2}$)	N ($T_{\rm rot}$ = 30 (K)) ($\rm cm^{-2}$)	N ($T_{\rm rot}$ = 50 (K)) ($\rm cm^{-2}$)
CH_3OH	$(1.7\pm0.5)\times10^{15}$	$(2.8\pm0.9)\times10^{15}$	$(5.1\pm1.9)\times10^{15}$
$^{13}CH_3OH$	$(3.5\pm0.7)\times10^{13}$	$(1.1\pm0.2)\times10^{14}$	$(2.2\pm0.5)\times10^{14}$
C_2H_5OH	$(3.7\pm2.2)\times10^{13}$	$(4.7\pm2.7)\times10^{13}$	$(9.2\pm5.6)\times10^{13}$
CH_3CHO	$(2.6\pm0.9)\times10^{13}$	$(3.2\pm1.3)\times10^{13}$	$(5.2\pm2.3)\times10^{13}$
NH_2CHO	$(2.4\pm1.1)\times10^{12}$	$(3.5\pm1.7)\times10^{12}$	$(5.9\pm3.1)\times10^{12}$
HCOOH	$(1.9\pm1.0)\times10^{13}$	$(2.1\pm1.1)\times10^{13}$	$(3.3\pm1.9)\times10^{13}$
$HCOOCH_3$	$(9.7\pm5.1)\times10^{13}$	$(6.6\pm3.8)\times10^{13}$	$(9.2\pm5.6)\times10^{13}$
HCN	$(1.3\pm0.3)\times10^{14}$	$(2.6\pm0.5)\times10^{14}$	$(4.0\pm0.8)\times10^{14}$
$H^{13}CN$	$(4.9\pm1.0)\times10^{12}$	$(9.9\pm2.0)\times10^{12}$	$(1.6\pm0.3)\times10^{13}$
$HC^{15}N$	$(1.0\pm0.2)\times10^{12}$	$(2.1\pm0.5)\times10^{12}$	$(3.3\pm0.7)\times10^{14}$
HNC	$(1.7\pm0.5)\times10^{13}$	$(2.4\pm0.8)\times10^{13}$	$(3.4\pm1.3)\times10^{13}$
HNCO	$(2.8\pm0.7)\times10^{13}$	$(3.8\pm1.2)\times10^{13}$	$(6.4\pm2.4)\times10^{13}$
HC_3N	$(4.2\pm1.0)\times10^{13}$	$(1.9\pm0.6)\times10^{13}$	$(2.0\pm0.8)\times10^{13}$
CH_3CN	$(3.1\pm1.4)\times10^{15}$	$(1.7\pm0.8)\times10^{13}$	$(8.4\pm3.8)\times10^{12}$
C_2H	$(2.3\pm0.9)\times10^{14}$	$(3.8\pm1.7)\times10^{14}$	$(5.8\pm2.8)\times10^{14}$
CCS	$(6.8\pm2.8)\times10^{12}$	$(4.8\pm2.1)\times10^{12}$	$(5.9\pm2.9)\times10^{12}$
CH_3CCH	$(2.5\pm1.0)\times10^{13}$	$(2.6\pm1.2)\times10^{13}$	$(4.0\pm1.9)\times10^{13}$
CS	$(2.2\pm0.7)\times10^{14}$	$(2.4\pm0.8)\times10^{14}$	$(3.3\pm1.3)\times10^{14}$
^{13}CS	$(6.3\pm1.6)\times10^{12}$	$(8.3\pm2.7)\times10^{12}$	$(1.2\pm0.5)\times10^{13}$
$C^{33}S$	$(2.8\pm1.0)\times10^{12}$	$(3.6\pm1.5)\times10^{12}$	$(5.1\pm2.3)\times10^{12}$
$C^{34}S$	$(1.2\pm0.3)\times10^{13}$	$(1.5\pm0.5)\times10^{13}$	$(2.1\pm0.8)\times10^{13}$
OCS	$(7.9\pm2.4)\times10^{13}$	$(5.1\pm1.9)\times10^{13}$	$(6.0\pm2.5)\times10^{13}$
SO	$(2.2\pm0.6)\times10^{14}$	$(2.4\pm0.8)\times10^{14}$	$(3.3\pm1.3)\times10^{14}$
^{34}SO	$(1.2\pm0.5)\times10^{13}$	$(1.4\pm0.6)\times10^{13}$	$(2.1\pm1.0)\times10^{13}$
SO_2	$(3.1\pm0.7)\times10^{14}$	$(1.3\pm0.4)\times10^{14}$	$(1.8\pm0.7)\times10^{14}$
H_2CS	$(1.0\pm0.5)\times10^{14}$	$(3.1\pm1.2)\times10^{13}$	$(4.0\pm1.7)\times10^{13}$
NS	$(1.3\pm0.5)\times10^{13}$	$(1.4\pm0.6)\times10^{13}$	$(1.9\pm0.9)\times10^{13}$
HCO^+	$(2.5\pm0.8)\times10^{13}$	$(3.5\pm1.2)\times10^{13}$	$(5.0\pm2.0)\times10^{13}$
$H^{13}CO^+$	$(4.4\pm4.4)\times10^{11}$	$(6.8\pm6.8)\times10^{11}$	$(9.9\pm10.0)\times10^{11}$
HCS^+	$(1.9\pm0.7)\times10^{12}$	$(2.6\pm1.1)\times10^{12}$	$(3.7\pm1.7)\times10^{12}$
N_2H^+	$(3.0\pm0.7)\times10^{10}$	$(4.5\pm1.3)\times10^{10}$	$(6.5\pm2.3)\times10^{10}$
SiO	$(6.8\pm1.9)\times10^{13}$	$(8.5\pm2.8)\times10^{13}$	$(1.2\pm0.5)\times10^{14}$
^{29}SiO	$(6.8\pm1.7)\times10^{12}$	$(9.2\pm2.9)\times10^{12}$	$(1.3\pm0.5)\times10^{13}$
^{30}SiO	$(4.4\pm1.1)\times10^{12}$	$(6.0\pm1.9)\times10^{12}$	$(8.6\pm3.2)\times10^{12}$
CO	$(1.7\pm1.4)\times10^{17}$	$(1.0\pm0.3)\times10^{17}$	$(1.3\pm0.5)\times10^{17}$
^{13}CO	$(8.7\pm2.1)\times10^{15}$	$(1.1\pm0.3)\times10^{16}$	$(1.6\pm0.6)\times10^{16}$
$C^{17}O$	$(1.1\pm0.4)\times10^{14}$	$(1.5\pm0.6)\times10^{14}$	$(2.2\pm0.9)\times10^{14}$
$C^{18}O$	$(1.5\pm0.3)\times10^{15}$	$(2.0\pm0.6)\times10^{15}$	$(2.8\pm1.0)\times10^{15}$
c-C_3H_2	$(3.6\pm1.1)\times10^{12}$	$(7.7\pm2.8)\times10^{12}$	$(1.4\pm0.6)\times10^{13}$
PN	$(1.2\pm0.4)\times10^{12}$	$(1.6\pm0.6)\times10^{12}$	$(2.2\pm1.0)\times10^{12}$
CN	$(1.5\pm0.5)\times10^{14}$	$(1.9\pm0.7)\times10^{14}$	$(2.7\pm1.1)\times10^{14}$
^{13}CN	$(4.4\pm2.7)\times10^{12}$	$(6.3\pm4.0)\times10^{12}$	$(9.3\pm6.2)\times10^{12}$
H_2CCO (ortho)	$(9.9\pm3.3)\times10^{12}$	$(9.6\pm3.8)\times10^{12}$	$(1.3\pm0.6)\times10^{13}$
H_2CCO (para)	$(1.2\pm1.4)\times10^{12}$	$(1.4\pm1.7)\times10^{12}$	$(2.0\pm2.3)\times10^{12}$

Table 3.4: Column Densities of Detected Molecules.

Molecules	N ($T_{\rm rot}$ = 12 (K)) ($\rm cm^{-2}$)	N ($T_{\rm rot}$ = 30 (K)) ($\rm cm^{-2}$)	N ($T_{\rm rot}$ = 50 (K)) ($\rm cm^{-2}$)	Transition
$(CH_3)_2O$	$< 4.8\times10^{12}$	$< 9.4\times10^{12}$	$< 1.7\times10^{13}$	4(1,4)-3(0,3) (99.325 GHz)
C_2H_3CN	$< 1.2\times10^{11}$	$< 6.4\times10^{10}$	$< 8.0\times10^{10}$	11(1,10)-10(1,10) (101.637 GHz)
C_2H_5CN	$< 3.5\times10^{12}$	$< 3.4\times10^{12}$	$< 4.9\times10^{12}$	9(1,9)-8(0,8) (93.949 GHz)
HDO	$< 8.5\times10^{12}$	$< 2.4\times10^{12}$	$< 2.6\times10^{12}$	1(1,0)-1(1,1) (85.78GHz)
C_4H	$< 2.9\times10^{13}$	$< 1.2\times10^{13}$	$< 1.2\times10^{13}$	11-10, J = 23/2-21/2
C_3H	$< 1.1\times10^{12}$	$< 1.1\times10^{12}$	$< 1.4\times10^{12}$	$^2\Pi_{1/2}$ J = 9/2-7/2, F = 5-4 e (97.995 GHz)
l-C_3H_2	$< 2.1\times10^{11}$	$< 1.9\times10^{11}$	$< 2.3\times10^{11}$	5(1,5)-4(1,4) (102.99 GHz)
l-C_4H_2	$< 3.5\times10^{11}$	$< 2.0\times10^{11}$	$< 2.3\times10^{11}$	10(1,9)-9(1,8) (89.687 GHz)
C_3S	$< 7.7\times10^{11}$	$< 2.8\times10^{11}$	$< 2.7\times10^{11}$	15-14 (86.708 GHz)
HC_5N	$< 1.1\times10^{13}$	$< 8.5\times10^{11}$	$< 5.7\times10^{11}$	31-30 (82.539 GHz)
HNCS	$< 6.4\times10^{11}$	$< 6.8\times10^{11}$	$< 1.0\times10^{12}$	8(0,8)-7(0,7) (93.83 GHz)
HSCN	$< 7.4\times10^{11}$	$< 8.0\times10^{11}$	$< 1.2\times10^{12}$	8(0,8)-7(0,7) (91.75 GHz)
PO	$< 5.5\times10^{11}$	$< 6.1\times10^{11}$	$< 8.2\times10^{11}$	J, F = 5/2, 3-3/2, 2 (109.206 GHz)

Table 3.5: Upper Limits to Column Densities for Undetected Molecules.

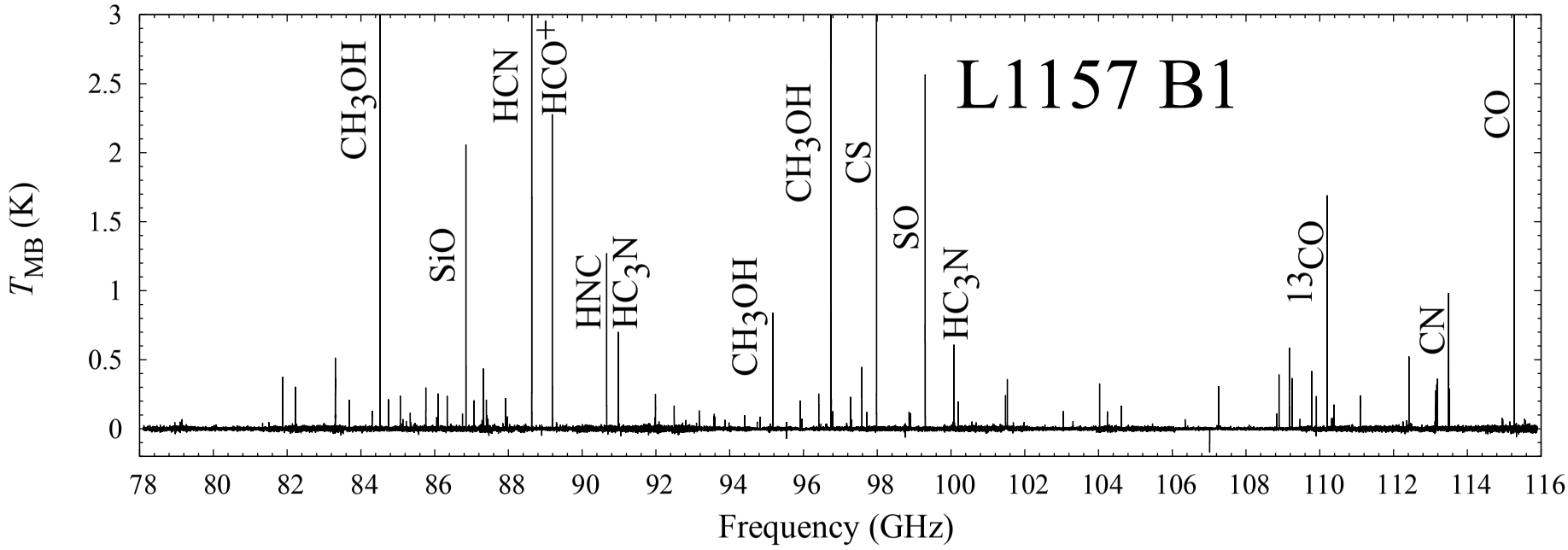

Figure 3.2: The total spectrum of L1157 B1

3.3.2 Column Densities of Molecules

Rotation Temperature and Column Density

For the molecules detected in multiple transitions, we calculated rotational temperatures. The conventional formula,

$$\int T_{\rm mb} dv = \frac{8\pi^3 \mu^2 S_{\rm ul} N \nu}{3U} \exp\left(-\frac{E_{\rm u}}{kT_{\rm rot}}\right) \tag{3.1}$$

is not a good approximation for a low rotational temperature case, because it assumes that the rotational temperature is much higher than the cosmic microwave background temperature, $T_{\rm b}$. Hence, we employed the following rigorous equation,

$$T_{\rm mb} = \frac{h\nu}{k}\{\frac{1}{\exp(h\nu/kT_{\rm rot})-1} - \frac{1}{\exp(h\nu/kT_{\rm b})-1}\}(1-e^{-\tau_\nu}) \tag{3.2}$$

$$\tau_\nu = \frac{8\pi^3 \mu^2 S_{\rm ul} N}{3h\Delta v U}\{\exp\left(\frac{h\nu}{kT_{\rm rot}}\right)-1\}\exp\left(-\frac{E_u}{kT_{\rm rot}}\right). \tag{3.3}$$

Here, $T_{\rm mb}$ is defined in eq. 2.18. Results are summarized in Table 3.6. Overall, the rotation temperatures are below 40 K except that for CH_3CN, which corresponds to the gas kinetic temperature. Although these molecules reside in the shocked region, these rotation temperatures are significantly lower than the kinetic temperature of 130-140 K estimated by Umemoto et al. (1999). As shown by the shock model of Bergin et al. (1998), the cooling timescale of the shocked gas is a few hundred years, which is much shorter compared with the dynamical timescale of the outflow (1.8×10^4 yr). The rotation temperatures seem to reflect this cooling effect. Since the H_2 density is about 10^5 cm^{-3}, the rotational level population are not always thermalized (non-LTE effect). This also contributes to the low rotation temperature.

However, the rotation temperatures have large uncertainties, and also show significant scattering from molecule to molecule. This is probably due to the limited range of the upper state energy of the transitions employed in the analysis. Hence, we fixed the rotation temperature to be 12 K, 30 K, and 50 K in order to derive the column densities of the molecules. The range of the temperature is set by referring to the result of the rotation temperature. The results are shown in Table 3.4. The upper limits to the column densities for non-detected molecules are also derived in the same way, as summarized in Table 3.5.

3.3.3 Complex Organic Molecules

Sugimura et al. (2011) reported the lines of the oxygen-bearing organic molecules such as CH_3OH, CH_3CHO, HCOOH, and $HCOOCH_3$. We detected other transitions of these molecules as well as three new lines of C_2H_5OH, which was first found in this source by Arce et al. (2009). These results confirm rich organic chemistry in L1157 B1.

We detected five emission lines of CH_3OH in addition to the four lines reported by Sugimura et al. (2011). Since CH_3OH is very abundant in the L1157 B1 shocked region, the b-type transitions were observed with moderate intensities in addition to the a-type transitions. Here, the a-type and b-type transitions mean that they are caused by the dipole moment projected on the a and b principal axes. More importantly, we detected the $6_{-2,5}-7_{-1,7}$ E and $3_{1,3}-4_{0,4}$ A^{++} lines in absorption, as shown in Fig. 3.3. Since there is no strong millimeter-wave continuum source toward L1157 B1, these are absorptions mainly against the cosmic microwave background. This indicates a non-LTE condition for the rotational level population of CH_3OH in this source.

Molecules	$T_{\rm rot}$
CH_3OH (A+E)	6.9±4.1
C_2H_5OH	32.3±0.6
CH_3CHO (A+E)	11.8±3.9
NH_2CHO	9.1±5.2
HC_3N	39.2±18.5
CH_3CN	64.2±17.0
C_2H	4.8±2.2
CCS	20.6±10.1
OCS	14.0±7.4
SO	6.8±6.5
SO_2	22.7±1.4
H_2CS	21.3±9.3

Table 3.6: LTE Rotation Temperatures and Column Densities.

Usually, these lines are observed in emission in star-forming regions. For instance, Goldsmith et al. (1983) reported the $3_{1,3} - 4_{0,4}$ A^{++} line in emission toward the Orion KL hot core, and the TIMASS survey toward the low-mass hot corino source IRAS 16293-2422 (Caux et al. 2011) also shows emissions of these two lines. We evaluated the brightness temperature of the $3_{1,3} - 4_{0,4}$ A^{++} line to be -0.19 K with the non-LTE radiative transfer code, RADEX (van der Tak et al. 2007), assuming a kinetic temperature of 50 K, an H_2 density of 10^5 cm^{-3}, a line width of 6.5 km s^{-1}, and a column density of 3×10^{15} cm^{-2}. The negative brightness temperature means absorption against the cosmic microwave background. For the kinetic temperature of 100 K and the H_2 density of 10^6 cm^{-3}, typical values for hot core sources, it appears to be emission of 0.71 K, because the rotational level population becomes close to the LTE condition. Therefore, this line is sensitive to the physical condition. A more detailed analysis will be presented in section 3.4.1.

CH_3CHO is detected toward high-mass star-forming regions (e.g. Gottlieb 1973; Ikeda et al. 2001) and hot corino sources of low-mass star forming regions such as IRAS 16293-2422 (Cazaux et al. 2003). Although this molecule is detected toward cold dark clouds such as TMC-1 and L134N (Matthews et al. 1985), the fractional abundance relative to H_2 tends to be higher in hot cores and/or hot corinos than in cold dark clouds. Sugimura et al. (2011) detected three lines of this molecule, and evaluated the fractional abundance to be (1.3-2.6) $\times 10^{-8}$. This value is higher by two orders of magnitude than that in TMC-1 (6×10^{-10}; Matthews et al. 1985), which suggests that CH_3CHO in L1157 B1 does not originate from the ambient component simply compressed by the shock but is related to the shock chemistry. In the present survey, we newly detected 13 lines of this molecule.

Arce et al. (2008) detected 9 lines of $HCOOCH_3$ toward L1157 B1 in the 3 mm and 1.3 mm bands with the IRAM 30 m telescope. Sugimura et al. (2011) detected additional two transitions ($7_{1,6} - 6_{1,5}$ and $8_{1,8} - 7_{1,7}$) with NRO 45 m. In the present line survey, we detected the $8_{4,4} - 7_{4,3}$ A, $9_{0,9} - 8_{0,8}$ (A+E), $9_{5,5} - 8_{5,4}$ A, and $9_{3,6} - 8_{3,5}$ A lines. This further confirms the existence of $HCOOCH_3$ in L1157 B1. So far, $HCOOCH_3$ had been thought to be specific to hot cores/hot corinos (e.g. Cazaux et al. 2003; Kuan et al. 2004; Bottinelli et al. 2004; Sakai et al. 2006), and had never been detected toward cold dark clouds (Requena-Torres et al. 2007). Sugimura

et al. (2011) reported on the basis of the chemical model calculation that it is impossible to explain the abundance of $HCOOCH_3$ obtained for L1157 B1 by the gas-phase production within the dynamical time scale of 1.8×10^4 yr. They concluded that it is more reasonable to invoke the grain-surface reactions for production of $HCOOCH_3$ (e.g. Garrod and Herbst 2006). It is therefore likely that $HCOOCH_3$ detected toward L1157 B1 is evaporated from grain mantles by the shock.

Arce et al. (2008) also detected two lines of HCOOH. Sugimura et al. (2011) also found the $4_{0,4} - 3_{0,3}$ line. We newly detected the $4_{1,4} - 3_{1,3}$, $4_{1,3} - 3_{1,2}$, $5_{1,5} - 4_{1,4}$, and $5_{2,3} - 4_{2,2}$ lines. This molecule is known to exist in the high-mass star-forming regions such as Ori KL (e.g. Liu et al. 2002), low-mass star-forming regions such as IRAS 16293-2422 (Cazaux et al. 2003), and cold dark clouds such as L183 (Requena-Torres et al. 2007). Now the existence of this molecule in the shocked region is well established.

In the present line survey, we detected four lines of NH_2CHO ($4_{0,4} - 3_{0,3}$, $4_{1,3} - 3_{1,2}$, $5_{1,5} - 4_{1,4}$, and $5_{0,5} - 4_{0,4}$). This is the first detection of this molecule in L1157 B1. Although this molecule contains the nitrogen atom unlike the other organic molecules mentioned above, it is also suggested to be produced through grain-surface reactions including CO, N and H (Tielens and Hagen 1982). So far, NH_2CHO was detected toward high-mass star-forming regions (e.g. Bisschop et al. 2007), but was not found in low-mass star-forming regions or cold dark clouds. Recently, Kahane et al. (2013) reported the detection of NH_2CHO in IRAS 16293-2422. They suggested that the abundance of NH_2CHO ($\sim 10^{-10}$) in IRAS 16293-2422 can be achieved by the exothermic neutral-radical reaction between H_2CO and NH_2. They also pointed out the similarity of abundances of this molecule among SgrB2, Orion-KL, IRAS 16293-2422, and the comet Hale-Bopp. They concluded that the energetic radiative processes in massive star-forming regions may not be necessary for the production of this molecule. The abundace of NH_2CHO in L1157 B1 is calculated to be 1.4×10^{-9}, which is no less than that in IRAS 16293-2422. It is controversial whether NH_2CHO originates from the gas-phase reaction in the shocked region, or comes from the grain mantle evaporated by the shock. However, the time scale of the H_2CO + NH_2 reaction should be longer than 10^4 yr for NH_2, and hence, the gas-phase production may be difficult in L1157 B1, considering the lifetime of the outflow (1.8×10^4 yr). This supports the grain mantle origin of NH_2CHO in L1157 B1.

Arce et al. (2008) further detected C_2H_5OH ($4_{1,4} - 3_{0,3}$) toward L1157 B1. We newly detected the $8_{2,7} - 8_{1,8}$, $7_{0,7} - 6_{1,6}$, and $5_{1,5} - 4_{0,4}$ lines, confirming the existence of C_2H_5OH. According to Charnley et al. (1992), this molecule has the origin of grain surface chemistry, since it is difficult to reproduce the abundances of C_2H_5OH in the compact ridge of Orion KL (10^{-6}) and some hot core sources such as W51 (10^{-8}, Turner 1991) by gas-phase production process because of the slow radiative association of H_3O^+ and C_2H_4. In fact, C_2H_5OH is not observed toward dark clouds (Irvine et al. 1987). The abundance ratio relative to H_2 in L1157 B1 is 2.2×10^{-8}. Since this abundance ratio is comparable to the value obtained toward hot cores by Millar et al. (1988), and Bisschop et al. (2008), it seems that C_2H_5OH in L1157 B1 is produced on the grain surface, and evaporated by the shock as in the case of other complex organic molecules.

In addition to above oxygen-containing complex organic molecules, we detected the CH_3CN ($J_K = 5_K - 4_K$, $6_K - 5_K$; K = 0-4) lines. This molecule is known to exist in hot cores/hot corinos (e.g. Churchwell et al. 1992), and is regarded as an useful tracer to study the dense part near the protostars (e.g. Beltrán et al. 2004). Note that Arce et al. (2008) detected the $J_K = 14_K - 13_K$ (K = 0-3) lines toward L1157 B1, and Codella et al. (2009) conducted

a high resolution mapping observation of the $J_K = 8_K - 7_K$ (K = 0-4) line with the PdBI interferometer to trace the bow shock structure.

In the present survey, four lines of H_2CCO ($4_{1,4} - 3_{1,3}$, $4_{0,4} - 3_{0,3}$, $5_{1,5} - 4_{1,4}$, and $5_{1,4} - 4_{1,3}$) were detected. This is the first detection of H_2CCO in L1157 B1. This molecule is known to exist in cold dark clouds such as TMC-1 and L134N as well as high-mass and low-mass star-forming regions (Kaifu et al. 2004; Blake et al. 1987; van Dishoeck et al. 1995). The broad line width in L1157 B1 indicates that this molecule also resides in the shocked region.

3.3.4 Carbon-Chain Molecules

We detected five lines of CCS ($J_N = 7_6 - 6_5$, $6_7 - 5_6$, $8_7 - 7_6$, $9_8 - 8_7$, and $8_9 - 7_8$) and six hyperfine component lines of C_2H ($N = 1 - 0$). Carbon-chain molecules are known to be abundant in young starless cores such as TMC-1 and Lupus-1 A (e.g. Suzuki et al. 1992; Kaifu et al. 2004; Sakai et al. 2010) as well as in low-mass star-forming regions exhibiting the warm carbon-chain chemistry such as L1527 and IRAS 15398-3359 (Sakai et al. 2008; 2009). The CCS lines in L1157 B1 have broad line widths of 5-6 km s^{-1} and blue-shifted peak velocities of ($-$0.2-2.3) km s^{-1}, which are similar to those of other lines emitting from the shocked region. Similarly, the C_2H lines have the line widths of 4-7 km s^{-1}, and peak velocities of ($-$0.2-0.7) km s^{-1}. These results indicate that both CCS and C_2H mainly reside in the shocked region. So far, C_2H and HC_3N have been detected in shocked regions (Bachiller and Pérez Gutiérrez 1997). The present detection of CCS gives rise to an interesting problem of the formation of these carbon-chain molecules in the shocked region.

The column density of C_2H (2.3×10^{14} cm^{-2}) in L1157 B1 is comparable to that in L1527 (5×10^{14} cm^{-2}) where is known as a nursery for various carbon-chain molecules. In addition, the abundance ratio of CCS to C_2H in L1157 B1 is 3×10^{-2}, which is similar to that in L1527 (1.0×10^{-2}). However, other longer carbon-chain molecules such as C_3H, and C_4H were not detected in L1157 B1. These results indicate that although short carbon-chain molecules, C_2H, and CCS, can be produced in L1157 B1, the chemical process is different from the warm carbon-chain chemistry (WCCC; Sakai et al. 2008, 2009, 2010), and is inefficient to produce other longer carbon-chain molecules.

3.3.5 Sulfur-bearing Molecules

As for sulfur-bearing species, we detected CS ($J = 2 - 1$), ^{13}CS ($J = 2 - 1$), C^{34}S ($J = 2 - 1$), C^{33}S ($J = 2 - 1$), OCS ($J = 7 - 6$, $8 - 7$, and $9 - 8$), SO ($J_N = 2_2 - 1_1$, $3_2 - 2_1$, and $2_3 - 1_2$), ^{34}SO ($J_N = 3_2 - 2_1$), SO_2 ($8_{1,7} - 8_{0,8}$, $3_{1,3} - 2_{0,2}$, and $10_{1,9} - 10_{0,10}$), H_2CS ($3_{1,3} - 2_{1,2}$, $3_{0,3} - 2_{0,2}$, $3_{2,1} - 2_{2,0}$, and $3_{1,2} - 2_{1,1}$) , and four hyperfine components of NS ($\Omega = 1/2$, $J = 5/2 - 3/2$) in addition to CCS, further confirming the rich sulfur chemistry in the L1157 B1 shocked region. In contrast to SiO, which is considered to be produced through the disruption of silicate grains by the shock (Mikami et al. 1992), Charnley et al. (1997) suggested that many sulfur-containing molecules can be produced through the gas-phase reactions from H_2S evaporated from grain mantles. According to the mapping observation toward L1157 by Bachiller et al. (2001), the distribution of SiO is concentrated to the shock front such as B1 and B2, whereas that of SO is more extended. This seems consistent with the grain-mantle origin of the sulfur-bearing molecules in contrast to SiO which requires the disruption of silicate grains by strong shock. We will compare the spectral line profiles of the sulfur-bearing molecules with that of SiO to see

such differences in Section 3.4.2.

Charnley (1997) suggested that the SO/H_2S and SO/SO_2 abundance ratios could be an indicator of the time elapsed since the grain mantle evaporation, since the sulfur-bearing molecules are produced from H_2S through gas-phase reactions in such a process as $H_2S \rightarrow SO \rightarrow SO_2$. Abundance ratios of SO_2, H_2CS, CS, and OCS relative to SO in L1157 B1 range from 0.45 to 1.4 (Table 3.9). Massive star-forming regions tend to indicate much wider ranges of abundance ratios of these sulfur bearing molecules, which may result from the complexity of those regions. It seems that only abundance ratio of $N(SO_2)/N(SO)$ in Table 3.9 are comparable among sources. The $N(SO_2)/N(SO)$ ratio of 1.4 in L1157 B1 is attainable in the dynamical timescale of 1.8×10^4 yr of L1157 B1 as indicated by Charnley (1997). Since his chemical model assumes high temperature conditions (100-300 K) of the hot core, and the shocked gas cools down quickly as shown in Section 3.3.2, it seems difficult to directly apply this model to the L1157 B1 case. Therefore, sulfur-bearing molecules would not be produced with enough abundances through gas-phase reactions, and hence, we cannot deny the grain-mantle origin of these sulfur-bearing molecules in L1157 B1.

3.3.6 Other Molecules

In addition to above-mentioned molecules, we detected the spectral lines of fundamental molecules such as SiO ($J = 2-1$), $Si^{18}O$ ($J = 2-1$), ^{30}SiO ($J = 2-1$), ^{29}SiO ($J = 2-1$), HC_3N ($J = 9-8$, $10-9$, $11-10$, and $12-11$), 9 fine and hyperfine components of CN ($N = 1-0$), HCN ($J = 1-0$), $H^{13}CN$ ($J = 1-0$), $HC^{15}N$ ($J = 1-0$), HNC ($J = 1-0$), CO ($J = 1-0$), ^{13}CO ($J = 1-0$), $C^{17}O$ ($J = 1-0$), $C^{18}O$ ($J = 1-0$), HCO^+ ($J = 1-0$), $H^{13}CO^+$ ($J = 1-0$), HCS^+ ($J = 2-1$), and N_2H^+ ($J = 1-0$). Owing to the high sensitivity of the present survey, we were able to detect the spectral lines of the rare isotopic species. The isotope ratios will be discussed in Section 3.3.9.

Iglesias and Silk (1978) reported a chemical model indicating a substantial decrease of HCO^+ behind a 10 km s^{-1} shock propagating into a dense molecular cloud. This model suggests that the large density increase behind the shock front destroys ions. In a few thousand years after the shock, the HCO^+ abundance drops by two orders of the magnitude from that in the pre-shocked gas. However, the fractional abundance of HCO^+ relative to H_2 in L1157 B1 is 1.5×10^{-8}, which is comparable to that in a dark cloud, TMC-1 (Ohishi et al. 1992). In addition, this ratio in the protoster, L1157 mm, is 1.5×10^{-9}. The line profile of HCO^+ ($1-0$) in L1157 B1 exhibits the broad line width and the blue-shifted peak velocity (6.2 km s^{-1}, 0.95 km s^{-1}), which indicate existence of this molecule in the shocked region. Hence, it seems that the significant destruction of HCO^+ does not occur in L1157 B1, where the shock velocity is as high as 20 km s^{-1}. However, another molecular ion, N_2H^+, has a lower abundance in L1157 B1 than in L1157 mm. The column density ratio $N(N_2H^+)_{L1157B1}/N(N_2H^+)_{L1157mm}$ is ~ 0.1. The line profile of N_2H^+ ($1-0$) in L1157 B1 indicates very narrow line width (1 km s^{-1}), and the peak velocity is comparable to the systemic velocity of 2.7 km s^{-1}, which evidence the ambient cloud origin of the line. Therefore, on the contrary to the case of HCO^+, N_2H^+ may significantly be destructed in the shock.

Chemical models predict that the high temperature reaction increases the abundance ratio, $N(HCN)/N(HNC)$, although HCN and HNC originate from the common precursor, $HCNH^+$ (Allen et al. 1980, Herbst 1978). For example, Schilke et al. (1992) reported the ratio of ~ 80 in the vicinity of Orion KL, while Hirota et al. (1998) found that the ratios are similar to one

another, and are lower than 1 in dark clouds. The column density ratio, N(HCN)/N(HNC), in L1157 B1 is $\sim$ 25. The high temperature condition caused by the shock would enhance this ratio.

3.3.7 Possible Detections

Possible detections are summarized in Table 3.3. First, we possibly detected the $8_{0,8} - 7_{0,7}$ (3σ) line of HSCN. This molecule was identified as an interstellar molecule toward Sgr B2(N) by Halfen et al. (2009). However, more stable geometrical isomer, HNCS, was not detected in L1157 B1 with the rms noise level of 5 mK ($T_{\rm A}^*$) for the $7_{0,7} - 6_{0,6}$, $8_{0,8} - 7_{0,7}$, and $9_{0,9} - 8_{0,8}$ lines, although they are detected with similar intensities to HSCN in Sgr B2 (Frerking et al. 1979). Second, we can see the SiS ($J = 6 - 5$) line at $V_{\rm lsr}$ of -2.0 km s^{-1} with the confidence level of 5σ. Sugimura et al. (2011) reported the tentative detection of SiS ($J = 5 - 4$) with the confidence level of 6σ, though the peak velocity is red-shifted ($\sim$ 4.7 km s^{-1}). Hence, the detection of SiS in L1157 B1 is still controversial. Furthermore, we noticed the CH_3SH ($4_0 - 3_0$) line with the confidence level of 8σ. Several other lines of CH_3SH around this line have weaker intrinsic intensities, and hence, they were not detected. Although we are fairly confident on the detection of this species, we still need to observe the other lines with higher sensitivity for confirmation.

Sugimura et al. (2011) reported non-detections of $(CH_3)_2O$ toward L1157 B1, which are typically seen toward hot cores of high-mass star-forming regions along with $HCOOCH_3$ and CH_3CHO (e.g. Bisschop et al. 2007). Within our observational frequency range, many lines of $(CH_3)_2O$ are included. Although we have a hint for the $(CH_3)_2O$ line ($2_{2,0} - 2_{1,1}$), other lines with stronger intrinsic intensities were not detected. Hence, we still need more sensitive observations to claim detection of this species.

3.3.8 Important Non-detections

We did not detect C_2H_3CN, though several lines with reasonable intrinsic intensities are included in our observational frequency range. Moreover, we did not detect the NH_2CN ($4_{1,4} - 3_{1,3}$) and CH_2CN ($4_{0,4} - 3_{0,3}$) lines, which have been detected toward Sgr B2(M) (Wannier and Linke 1978; Irvine et al. 1988).

Although we detected a few short carbon-chain molecules, CCS and C_2H, and HC_3N, as well as carbon-chain related species, c-C_3H_2, we could not detect longer carbon-chain molecules such as C_3H, C_4H and HC_5N. The carbon-chain chemistry in L1157 B1 seems to be different from that in young starless cores, where various long carbon-chain molecules such as C_4H and HC_5N are detected (Sakai et al. 2008).

Sugimura et al. (2011) detected CH_2DOH by observing the $2_{0,2} - 1_{0,1}$ e_0 line (Quade and Suenram 1980). Although some other lines of deuterated molecules such as HDO ($1_{1,0} - 1_{1,1}$), NH_2D ($1_{1,1} - 1_{0,1}$) and HDCS (e.g. $3_{0,3} - 2_{0,2}$) were included in our observational frequency range, we did not detect them in the present survey. Since Bachiller and Gutiérrez (1997) could not detect the DCO^+ and DCN lines toward L1157 B1, our non-detection of above deuterated molecules is not surprising.

In spite of our effort, 7 lines are still unidentified, as listed in Table 3.3. A criterion for the U line is that the line has an integrated intensity with the confidence level higher than 4σ and is not assigned to known spectral lines in the databases (CDMS, JPL, and NIST). It is also

confirmed that they do not come from the image band. Their line widths suggest that they are emitted from the shocked region.

3.3.9 Isotopic Species

The integrated intensity ratio between $C^{34}S$ and $C^{33}S$ ($J = 2-1$) (hereafter denoted as $I(C^{34}S)/I(C^{33}S)$) is 5.9 (Sugimura et al. 2011), which is similar to the $^{34}S/^{33}S$ isotope ratio in interstellar clouds (6.27±1.01, Chin et al. 1996). Similarly, the $I(C^{34}S)/I(^{13}CS)$ ratio is evaluated to be 1.67, which is close to the $I(C^{34}S)/I(^{13}CS)$ ratio in interstellar clouds (1.87-2.92, Chin et al. 1996). If the isotopic ratios in L1157 are assumed to be similar to those in nearby interstellar clouds, these results mean that the $C^{34}S$, $C^{33}S$ and ^{13}CS lines are optically thin. On the other hand, the $I(^{12}CS)/I(^{13}CS)$ ratio is found to be 26.6, which is about a half of the $^{12}C/^{13}C$ isotopic ratio in interstellar clouds (60; Lucas and Liszt 1998). Hence, the ^{12}CS line is slightly optically thick toward L1157 B1. In addition, the $I(^{32}SO)/I(^{34}SO)$ ratio for the 3_2-2_1 lines is derived to be 21.3. Since this value is similar to that reported for interstellar clouds by Chin et al. (1996) (24.4±5.0), we can conclude that the ^{32}SO and ^{34}SO lines are optically thin.

The $I(^{28}SiO)/I(^{29}SiO)$ and $I(^{28}SiO)/I(^{30}SiO)$ ratios for the $J = 2-1$ lines are evaluated to be 8.1 and 12.7, respectively. These are 0.41 and 0.43 times of the terrestrial isotopic $^{28}Si/^{29}Si$ and $^{28}Si/^{30}Si$ ratios (19.7 and 29.8), respectively. On the other hand, $I(^{29}SiO)/I(^{30}SiO)$ ratio (1.57) is consistent with the terrestrial isotopic ratio (1.51). Hence, the ^{28}SiO line is optically thick, whereas the ^{29}SiO and ^{30}SiO lines are optically thin.

The $I(H^{12}CN)/I(H^{13}CN)$ ratio for the $J = 1-0$ lines is derived to be 27, which is lower than the standard $^{12}C/^{13}C$ ratio in interstellar clouds (60) by a factor of 0.45. The $I(HC^{14}N)/I(HC^{15}N)$ ratio is 130, while the interstellar value of $^{14}N/^{15}N$ is 237 (Lucas and Liszt 1998). Hence, the HCN line is slightly optically thick. On the other hand, $I(H^{13}CN)/I(HC^{15}N)$ is determined to be 4.8. If we calculate the $[H^{13}CN]/[HC^{15}N]$ ratio by assuming $[H^{13}CN]/[H^{12}CN]$ of 1/60 and $[HC^{15}N]/[HC^{14}N]$ of 1/237, this ratio should be 4.0. Since this value is close to the observed value, the $H^{13}CN$ and $H^{15}CN$ lines can be regarded as optically thin.

We evaluated the $I(^{12}CH_3OH)/I(^{13}CH_3OH)$ ratio to be 51.4 for the sum of the $2_{-1,2} - 1_{-1,1}$, $2_{0,2} - 1_{0,1}$ A^{++} and $2_{0,2} - 1_{0,1}$ E lines. On the other hand, the ratio is 21.2 for the $8_{0,8} - 7_{1,7}$ A^+ lines. Since the latter ratio suffers from the possible maser effect of this line (e.g. Plambeck and Menten 1990), we employ the former value for comparison. The $I(^{12}CH_3OH)/I(^{13}CH_3OH)$ ratio is close to the standard interstellar $^{12}C/^{13}C$ ratio of 60, and hence, we can say that the $^{12}CH_3OH$ lines are not optically thick.

3.4 Discussion

3.4.1 Excitation Calculation

Absorption Lines of CH_3OH

We detected two absorption lines of CH_3OH ($6_{-2,5} - 7_{-1,7}$ E, $3_{1,3} - 4_{0,4}$ A^{++}; Yamaguchi et al. 2012; Figure 3.3) in L1157 B1. This result means that the excitation temperatures of these two lines are lower than the cosmic microwave background temperature (2.7 K). This result clearly indicates the non-LTE condition for the rotational level population of CH_3OH in this source. Then, we applied the non LTE radiative transfer code, RADEX (van der Tak et al. 2007), to

$3_{1,3} - 4_{0,4}$ A^{++} line. We found that this line is sensitive to the physical condition of clouds, and the absorption feature well reflects that in L1157 B1.

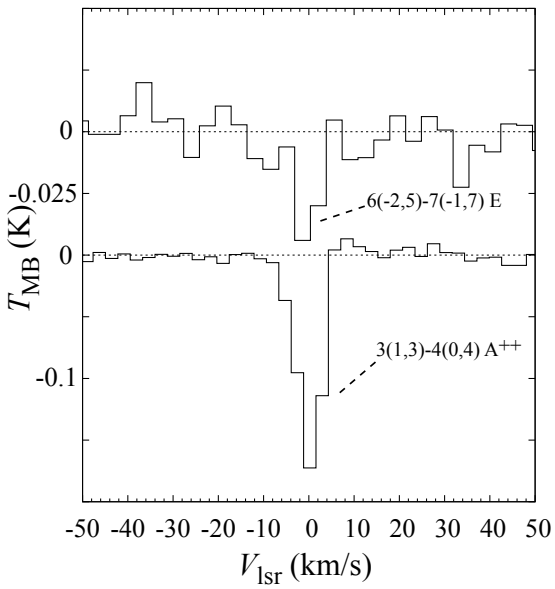

Figure 3.3: The absorption lines of CH_3OH ($6_{-2,5} - 7_{-1,7}$ E and $3_{1,3} - 4_{0,4}$ A^{++})

Statistical Equilibrium Calculation

We employed the statistical equilibrium calculation in order to analyze the observed intensities. This method calculates the rotational level population by considering excitation and de-excitation processes by collision, absorption, and emission. We used the code 'RADEX' (van der Tak et al. 2007), in our calculation. The outline of the RADEX program is described in Appendix C.

First, we applied this method to all CH_3OH transitions, and compared the observed values using the minimum χ^2 method. We assumed three column densities of CH_3OH, 10^{14} cm^{-2}, 10^{15} cm^{-2}, and 10^{16} cm^{-2} for simplicity. We found that only 10^{15} cm^{-2} can well reproduce the observed intensities (Figure **??**). We fixed the kinetic temperature to be 64 K which is derived from the CH_3CN rotation temperature. Then, the H_2 density is determined to be 2×10^5 cm^{-3} (Figure 3.5).

Next, we calculated column densities of some simple species by use of the chi-square method, assuming the H_2 density derived for CH_3OH, and the kinetic temperature. The results are listed in Table 3.7. The statistical equilibrium calculation is more preferable for interstellar clouds, because it employs the different excitation temperatures for the different transitions. However, the collisional cross section data are not available, and hence, we practically use the LTE method. The difference between these two methods are confirmed to be small in our case.

3.4.2 Comparison of V_{lsr}-Δv Diagram

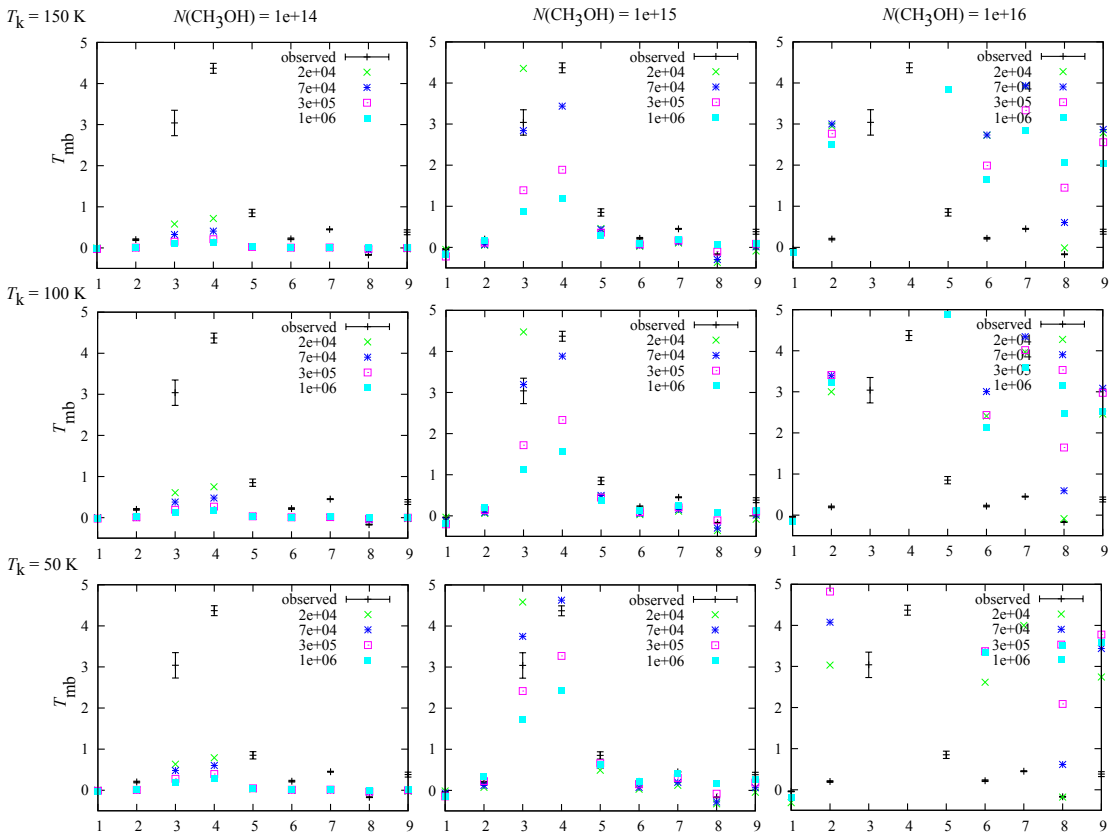

Figure 3.4: Statistical equilibrium calculation for the CH_3OH lines. The vertical axis indicates the radiation temperature, and numbers on horizontal axis correspond to the transitions of $6_{-2,5}$-$7_{-1,7}$ E, $2_{1,2}$-$1_{1,1}$ A^{++}, $2_{-1,2}$-$1_{-1,1}$ E, $2_{0,2}$-$1_{0,1}$ A^{++}, $2_{0,2}$-$1_{0,1}$ E, $2_{1,1}$-$1_{1,0}$ E, $2_{1,1}$-$1_{1,0}$ A^{--}, $3_{1,3}$-$4_{0,4}$ A^{++}, and $0_{0,0}$-$1_{-1,1}$ E. The cross, star, open square, and closed square represent the H_2 density of 2×10^4, 7×10^4, 3×10^5, and 1×10^6 cm^{-3}, respectively.

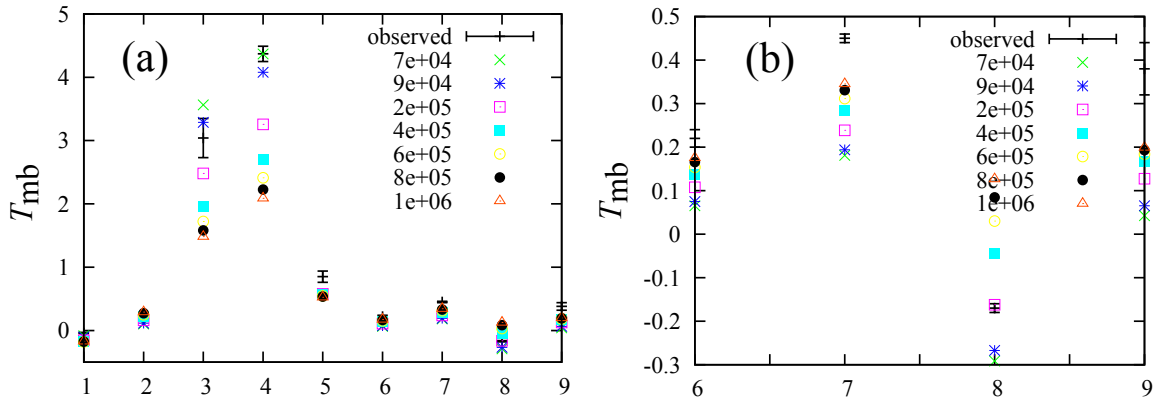

Figure 3.5: (a): Statistical equilibrium calculation of CH_3OH radiation temperatures with the kinetic temperature of 64 K, and the column density of 10^{15} cm^{-2} with the same method as in Figure 3.4. The minimum χ^2 method indicates that the H_2 density of 2×10^5 cm^{-3} is the best fit. (b): The enlarged part of (a) shows that higher excitation lines show the best fit with the H_2 density of $2{\times}10^5$ cm^{-3}.

Molecules	N ($T_{\rm rot}$ = 12 (K)) (cm^{-2})	Radex (cm^{-2})
CH_3OH	$(1.7{\pm}0.5){\times}10^{15}$	$1{\times}10^{15}$
HCN	$(1.1{\pm}0.5){\times}10^{14}$	$2{\times}10^{14}$
$H^{13}CN$	$(2.3{\pm}0.6){\times}10^{12}$	$4{\times}10^{12}$
$HC^{15}N$	$(1.3{\pm}0.5){\times}10^{12}$	$7{\times}10^{11}$
HNC	$(1.7{\pm}0.5){\times}10^{13}$	$9{\times}10^{12}$
HNCO	$(2.8{\pm}0.7){\times}10^{13}$	$2{\times}10^{13}$
HC_3N	$(4.2{\pm}1.0){\times}10^{13}$	$1{\times}10^{13}$
CH_3CN	$(3.1{\pm}1.4){\times}10^{15}$	$7{\times}10^{12}$
CS	$(2.2{\pm}0.7){\times}10^{14}$	$1{\times}10^{14}$
OCS	$(7.9{\pm}2.4){\times}10^{13}$	$6{\times}10^{13}$
SO	$(2.2{\pm}0.6){\times}10^{14}$	$1{\times}10^{14}$
SO_2	$(3.1{\pm}0.7){\times}10^{14}$	$8{\times}10^{13}$
H_2CS	$(1.0{\pm}0.5){\times}10^{14}$	$2{\times}10^{13}$
HCO^+	$(2.5{\pm}0.8){\times}10^{13}$	$2{\times}10^{13}$
HCS^+	$(1.9{\pm}0.7){\times}10^{12}$	$3{\times}10^{12}$
N_2H^+	$(3.0{\pm}0.7){\times}10^{10}$	$2{\times}10^{11}$
SiO	$(6.8{\pm}1.9){\times}10^{13}$	$4{\times}10^{13}$
^{29}SiO	$(6.8{\pm}1.7){\times}10^{12}$	$4{\times}10^{12}$
CO	$(1.7{\pm}1.4){\times}10^{17}$	$2{\times}10^{17}$
^{13}CO	$(4.4{\pm}1.1){\times}10^{15}$	$2{\times}10^{16}$
c-C_3H_2	$(3.6{\pm}1.1){\times}10^{12}$	$2{\times}10^{12}$
CN	$(1.5{\pm}0.5){\times}10^{14}$	$1{\times}10^{14}$

Table 3.7: Column Densities of Simple Molecules Calculated by the LTE Method (left) and Statistical Equilibrium Method (right).

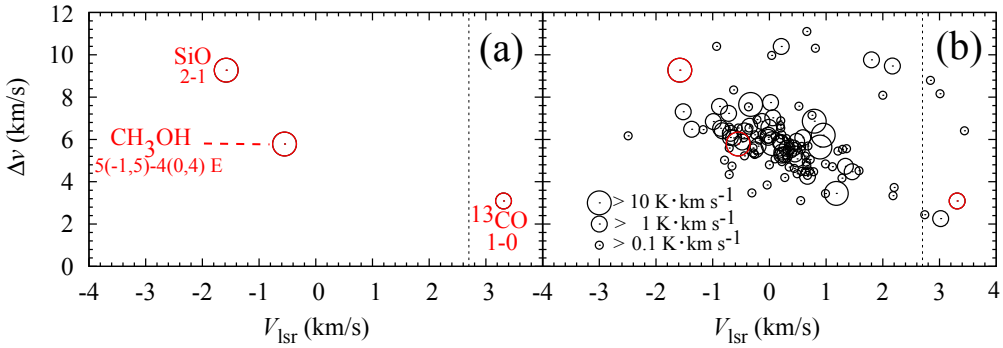

Figure 3.6: (a): $V_{\rm lsr}$-Δv plots for SiO ($J = 2 - 1$) CH_3OH ($5_{-1,5} - 4_{0,4}$), and ^{13}CO (1-0). (b): Those for all spectra. The size of the circle approximately represents the intensity. The vertical dotted line at $V_{\rm lsr} = 2.7$ km s^{-1} shows the systemic velocity of the L1157 cloud.

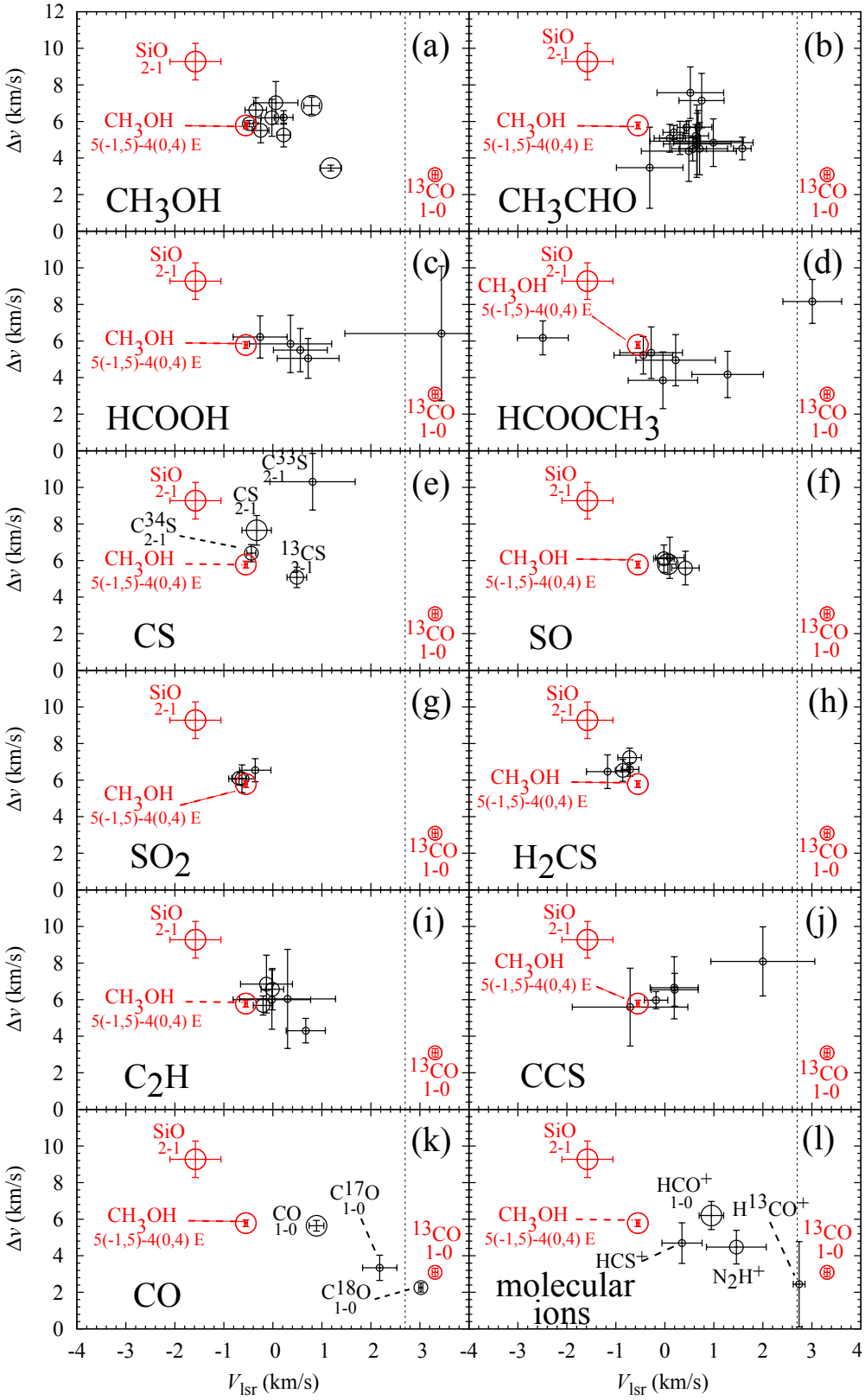

Figure 3.7: $V_{\rm lsr}$-Δv plots for various molecules. See Figure 3.6(b) and its caption for the size of the circle. The vertical dotted line at $V_{\rm lsr} = 2.7$ km s^{-1} shows the systemic velocity of the L1157 cloud.

Since L1157 B1 is a shocked region impacted repeatedly by the blue lobe of the molecular outflow, typical line profiles tend to be blue-shifted with respect to the systemic velocity of the quiescent gas ($\sim$ 2.7 km s^{-1}). Furthermore, they show broad line widths from 5 to 9 km s^{-1}. The peak velocity ($V_{\rm lsr}$) and the line width (Δv) are approximately determined by assuming the Gaussian profile, although the actual profile is slightly asymmetric. The results are given in Table 3.2 with the fitting errors. Although the spectral resolution is about 3 km s^{-1}, we can determine the $V_{\rm lsr}$ value much more precisely by the fit, as shown in Table 3.2. The $V_{\rm lsr}$ and Δv values thus determined should reflect differences of the distributions of molecules to some extent. In this section, we discuss the relation between $V_{\rm lsr}$ and Δv for various kinds of molecules.

For this purpose, we employ the SiO ($J = 2-1$), CH_3OH ($5_{-1,5} - 4_{0,4}$ E) and ^{13}CO (J = 1-0) lines as the standard lines (Fig. 3.6(a)). Among many CH_3OH line, we choose this line, because it is relatively strong and is free from blending of other lines. SiO is considered to be released into the gas-phase through disruption of silicate grains by strong shocks (Mikami et al. 1992). Hence, the distribution of this molecule is concentrated around the shock front of the outflow (e.g. Bachiller et al. 2001). As the result, the SiO ($J = 2 - 1$) line shows the most blue-shifted peak velocity and the broadest line width. Namely, it has $V_{\rm lsr}$ of -1.6 ± 0.5 km s^{-1} and Δv of 9$\pm$1 km s^{-1}, which is located near the upper-left corner of the $V_{\rm lsr}$-Δv plot (Fig. 3.6(a)). On the other hand, CH_3OH is produced in grain mantles, and is released into the gas-phase by the sputtering. The mapping observation by Bachiller et al. (2001) indicates that the distribution of CH_3OH is more extended than that of SiO, although the emission peak is close to that of the SiO emission. Since CH_3OH is evaporated more easily than SiO, the evaporation of CH_3OH can occur even under weaker shocks. Hence, the peak velocity is less blue-shifted than the SiO line, and the line width is narrower. For example, the line profile of the $5_{-1,5} - 4_{0,4}$ E line has $V_{\rm lsr}$ of -0.55 ± 0.03 km s^{-1} and Δv of 5.8$\pm$0.2 km s^{-1}. In contrast, the ^{13}CO (J =1$-$0) line is mainly emitted from the quiescent ambient gas, and hence, the peak velocity and the line width ($V_{\rm lsr}$ = 3.3$\pm$0.1 km s^{-1}, Δv = 3.1$\pm$0.2) are much different from those of the SiO and CH_3OH lines. This is also true for the $C^{18}O$ (J = 1$-$0) line. The $V_{\rm lsr}$ values of the ^{13}CO (J = 1$-$0) and $C^{18}O$ (J = 1$-$0) are 3.3 and 3.0 km s^{-1}, respectively, which are close to the systemic velocity ($\sim$ 2.7 km s^{-1}). If the line profile reflects the distribution of molecule as seen in the above representative molecules, the line width will systematically decrease as the peak velocity becomes closer to the systemic velocity. In fact, the correlation diagram of $V_{\rm lsr}$-Δv for all the detected lines indicates such a trend, as shown in Fig. 3.6(b). In the following subsections, we will discuss the $V_{\rm lsr}$-Δv plot for each class of molecules.

Organic Molecules

Figures 3.7(a)-(d) indicate the $V_{\rm lsr}$-Δv diagrams of CH_3OH, CH_3CHO, HCOOH and $HCOOCH_3$. As mentioned above, the CH_3OH lines have redder $V_{\rm lsr}$ and narrower Δv than the SiO (J = 2$-$1) line (Fig. 3.6(a)), although the plots are scattered considerably. As mentioned above, the difference between the two molecules reflects the difference of their distributions, and then the difference of their production processes. The averaged position in the diagram is ($V_{\rm lsr}$, Δv) = (0.1 km s^{-1}, 5.9 km s^{-1}). Figure 3.8 (a) and (b) show the correlation plots between the $V_{\rm lsr}$ values and the upper-state energies (E_u) of the CH_3OH lines and between the line widths and E_u, respectively. No apparent correlations are found, indicating that the emitting region is almost the same for these lines.

The CH_3CHO lines show a similar trend as shown in Fig. 3.7(b). The averaged position

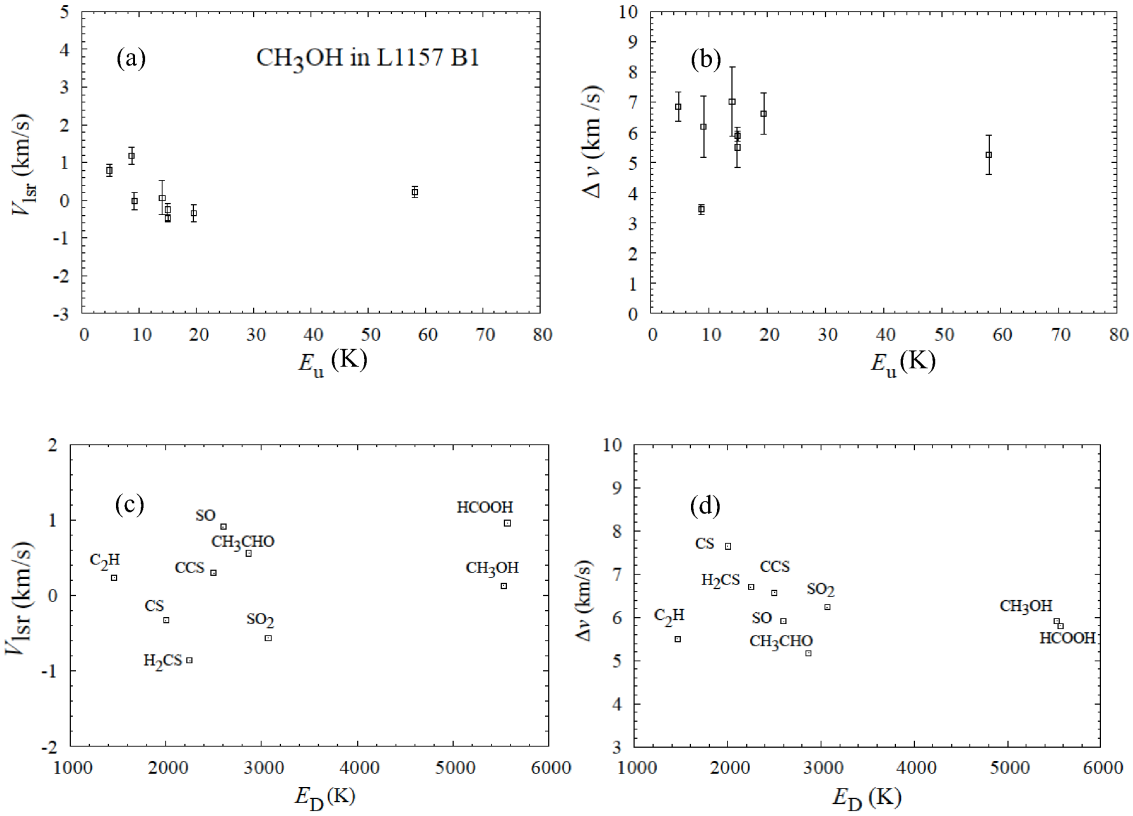

Figure 3.8: Top: For CH_3OH line profiles, (a) is the $V_{\rm lsr}$-E_u diagram, and (b) is Δv-E_u diagram. Here, E_u denotes the upper state energy of the transition. There seems no apparent correlation in both diagrams. Bottom: For fundamental molecules, (d) is the $V_{\rm lsr}$-$E_{\rm D}$, and (d) is the Δv-$E_{\rm D}$ diagram, respectively, where $E_{\rm D}$ denotes the desorption energy. There seems no apparent correlation.

in the diagram is ($V_{\rm lsr}$, Δv) = (0.6 km s^{-1}, 5.2 km s^{-1}) for the CH_3CHO lines, although the individual data of the CH_3CHO lines are scattered due to a low signal-to-noise ratio. A slight difference of the averaged $V_{\rm lsr}$ between CH_3OH and CH_3CHO might indicate the difference of production processes between them. Sugimura et al. (2011) suggested a possibility of the gas-phase production of CH_3CHO in the shocked region in contrast to the CH_3OH case. A more extended (higher $V_{\rm lsr}$) nature of CH_3CHO looks consistent with their suggestion. However, this argument apparently requires more statistics. Similarly, the averaged positions for the HCOOH and $HCOOCH_3$ lines seem to have higher peak velocities and narrower line widths in comparison with those of the SiO ($J = 2 - 1$) line (Figure 3.7(c) and (d), respectively). Nevertheless, the line profiles of CH_3CHO, HCOOH, and $HCOOCH_3$ still have lower peak velocities and broader line widths than those of ^{13}CO, which means that they do not mainly come from the ambient gas.

Sulfur-containing Molecules

Figures 3.7(e)-(h) are the $V_{\rm lsr}$-Δv diagrams for CS and its isotopomers, SO and its isotopomer, SO_2, and H_2CS. The averaged positions for these molecules in the diagram are also shifted toward the lower-right direction in comparison with that of SiO ($J = 2-1$). Mikami et al. (1992) pointed out that the SiO ($J = 2-1$) line is detected only toward shocked regions such as L1157 B1 and L1157 B2, whereas CS ($J = 2-1$) can also be seen toward the protostar position (L1157 mm). The mapping observations of L1157 by Bachiller et al. (2001) indicated that the distribution of CS ($J = 3-2$) is more extended than that of SiO ($J = 3-2$), although the distributions of both the CS and SiO emissions have a peak around the shocked regions. The same situation holds for SO (Bachiller et al. 2001). The difference of the averaged positions in the $V_{\rm lsr}$-Δv diagram reflects the difference of the distributions between these sulfur containing molecules and SiO. As mentioned in section 3.3.5, these sulfur-containing molecules are thought to be produced by the gas-phase reactions in the high temperature gas from H_2S evaporated from grain mantles (Charnley 1997). If so, the sulfur-containing molecules in L1157 B1 originate from the grain mantle as in the case of the organic molecules, and hence, the averaged positions in their $V_{\rm lsr}$-Δv diagrams are expected to be similar to each other. However, the data for the sulfur-containing molecules tend to be located in the lower $V_{\rm lsr}$ (average = -0.27 km s^{-1}) in comparison with those for organic molecules such as CH_3CHO, HCOOH and $HCOOCH_3$ (average = 0.43 km s^{-1}) in Figure 3.7. This systematic trend may indicate that the distributions of the sulfur-containing molecules are different from those of the organic molecules in the shocked region.

Carbon-chain Molecules

Figures 3.7(i) and (j) are the $V_{\rm lsr}$-Δv diagrams of C_2H and CCS, respectively. As in the case of organic molecules and the sulfur-containing molecules, the averaged positions in the $V_{\rm lsr}$-Δv diagrams for these carbon-chain molecules are shifted toward the lower-right direction in comparison with that of the SiO ($J = 2 - 1$) line. Namely, they have higher peak velocities and narrower line widths than the SiO ($J = 2 - 1$) line. The averaged line widths are from 5 to 7 km s^{-1}. This feature suggests that the lines of carbon-chain molecules mainly come from the shocked regions. It seems likely that the production of these carbon-chain molecules is triggered by the grain mantle evaporation, not by the disruption of grain cores.

Recently, production of carbon-chain molecules through the evaporation of CH_4 is reported for some low-mass star-forming regions (Sakai et al. 2008). This is called warm carbon-chain

chemistry (WCCC). In WCCC, carbon-chain molecules are produced in a lukewarm region ($T \sim$ 25 K) around the protostar, where H_2O is still frozen-out. The evaporated CH_4 reacts with C^+ to form $C_2H_3^+$, which is a precursor ion for C_2H and C_2H_2. The similar process may be possible in the shocked region. However, H_2O is also evaporated from dust grains and can be a main destructor for C^+ in L1157 B1 unlike in L1527. Hence, the production efficiency of carbon-chain molecules would not be very high. Our result will be useful for further studies of the carbon-chain chemistry in the shocked region.

Other Molecules

Figures 3.7(k) and (l) are the $V_{\rm lsr}$-Δv diagrams of CO with its isotopomers and molecular ions, respectively. The ^{12}CO line shows the exceptionally lower peak velocity and broader line width than the other CO isotopomers, because it well traces the outflow and the shocked region due to its high optical depth. On the other hand, the rare CO isotopomers mainly trace the ambient gas. A similar situation can be seen for the molecular ions (HCO^+ and $H^{13}CO^+$) and CS (CS, ^{13}CS, and C^{33}S). The optically thick HCO^+ line tends to trace the outflow and the shocked region, whereas their rare isotopomer lines trace the ambient gas. The N_2H^+ line has the peak velocity approximately close to the systemic velocity of the ambient gas and the narrow line width of 1.14 km s^{-1}, and hence, the N_2H^+ ion mainly exists in the ambient gas.

In the above subsections, we have compared the $V_{\rm lsr}$-Δv plots for some classes of molecules. Such a plot is found to be useful to study the distribution of each molecule qualitatively from the single dish data. However, our results have to be confirmed eventually by high spatial resolution observations with interferometers. It should be noted that the $V_{\rm lsr}$-Δv plots are not the consequence of the different desorption energies of molecules. This is confirmed by the absence of correlation of $V_{\rm lsr}$-Δv with the desorption energies, as shown in Figure 3.8 (c) and (d). Once the icy grain mantle is sublimated, all the molecular species contained in the mantle are liberated into the gas-phase.

3.4.3 Comparison with Star-forming Regions

We have detected several organic molecules such as HCOOH, $HCOOCH_3$, CH_3CHO, and C_2H_5OH in L1157 B1. They are typically found in hot-core/corino sources. Because of energetic star-forming activities, their chemical compositions are different from those in cold quiescent dark clouds such as TMC-1 and L134N. The chemical composition in L1157 B1 is also significantly different from that in dark clouds in that these dark clouds are rich in carbon-chain molecules rather than saturated organic molecules. Therefore, we employed the representative star-forming regions, IRAS 16293-2422, Sgr B2, and Orion KL for comparison.

IRAS 16293-2422 is a famous low-mass hot corino source, which involves a binary protostar system. The chemical composition of this source is much different from that in cold dark clouds in that various saturated complex organic species and some shock tracers such as SiO are detected. These characteristics are considered to originate from the high gas density and energetic star-forming activities. Thus, we think that IRAS 16293-2422 can be a good source for comparison with L1157 B1 shocked region.

The Orion-KL is a gigantic and complex high-mass star-forming region including several components, which are distinguished by their chemical and physical natures. The "extend ridge" position corresponds to a peak in molecular and dust emission about 24″ northeast of IRc2.

Its kinematic signature is characterized by a relatively undisturbed gas of $\Delta v \sim 3$ km s^{-1} and $V_{\rm lsr} \sim 10$ km s^{-1}. The "hot core" position is almost centered at IRc2. This region indicates somewhat active traits with the dense and warm material, the higher velocity dispersion of Δv $\sim$ 5-10 km s^{-1}, and a $V_{\rm lsr} \sim 5$ km s^{-1}, which is blue-shifted with respect to the ambient cloud. The "compact ridge" position is located about 8″ southwest of IRc2, which also shows warm and dense physical conditions, though relatively quiescent compared with the "hot core". The "plateau" is formed by a high-velocity bipolar outflow originating from the vicinity of IRc2, and is traced by CO, SiO and vibrationally excited H_2. Hence, we choose "hot core", and "compact ridge" for comparison because of their rich chemistry.

Sgr B2 mainly consists of three parts, which are denoted as N, M, and NW. In Sgr B2(N), spectral lines of complex organic molecules are conspicuous, and the rotation temperatures of molecules often exceed 200 K, while SO_2 is the dominant source of emission in Sgr B2(M). Sgr B2(NW) traces the cloud envelope, where rotation temperatures range from 15 to 50 K. Here, we choose Sgr B2(N) for comparison because it seems to represent the organic chemistry in the cloud.

In Table 3.8, we summarize the molecular abundance ratios relative to CH_3OH in the above sources and L1157 B1. Since CH_3OH is the most fundamental saturated organic molecule, we employed this as a reference molecule. By taking the abundance ratios, we can escape from the beam dilution problem which is essentially different from source to source. In L1157 B1, the abundance ratios of organic molecules range from 10^{-3} to 10^{-2}. This tendency is similar to those in massive star-forming regions. On the other hand, those abundances in IRAS 16293-2422 seem higher by one or two orders of magnitudes.

In Figure 3.9 and 3.10, we plot the abundances of various molecules relative to CH_3OH for Orion KL hot core, compact ridge, SgrB2(N), and IRAS 16293-2422 against that for L1157 B1. Overall, IRAS 16293-2422 shows higher abundance ratios than L1157 B1, especially in complex organic molecules such as HCOOH, $HCOOCH_3$, and CH_3CHO. On the other hand, Sgr B2(N), and Orion KL (Hot Core, Copact Ridge) tend to have comparable or lower abundance ratios of HCOOH, CH_3CHO, and C_2H_5OH, although CH_3CN is more abundant by one to two orders of magnitude than in L1157 B1. These result may indicate that production processes of oxygen-containing organic molecules are different from that of CH_3CN.

The molecular abundances in L1157 B1 are rather similar to those in high-mass star-forming regions in spite of significant differences in physical conditions. As discussed by Sugimura et al. (2011), complex organic molecules in L1157 B1 are considered to originate mainly from grain mantle. If this is also the case for high-mass star-forming regions, the grain mantle compositions in L1157 B1 would be similar to those in Ori KL and Sgr B2. In contrast, the grain mantle compositions in L1157 B1 are much different from those in the low-mass protostar, IRAS 16293-2422. The grain mantle of IRAS 16293-2422 should be very rich in complex organic molecules.

In general, the grain mantle compositions vary along the physical evolution of clouds. In the starless core phase, when the cloud temperature is as low as 10 K, hydrogenation processes are dominant, because heavy species such as C, N, O, OH, CO, and H_2CO cannot move around the surface. Hence, formation of complex species is not very efficient. If grain mantle is evaporated by shocks or sudden protostellar heatings at this stage, the abundances of complex organic molecules in the gas-phase would not be very high. This seems to be the situation for L1157 B1 and probably for Ori KL and Sgr B2. Since the evolutionary speed of high-mass stars is very fast, chemical processes on dust grains during the warm-up phase do not work efficiently. On

the other hand, low-mass protostars such as IRAS 16293-2422 evolve slowly, and warm-up the surrounding region gradually. In this case, heavy species can move around the surface, and have a chance to react with other heavy species, although this process competes with hydrogenation (Garrod and Herbst 2006). However, the H atom abundance on the surface becomes lower for higher grain temperature, and hence, the hydrogenation is suppressed in the warm-up phase. Because of these reasons, the complex organic molecules are produced efficiently on grain surface of low-mass starforming regions to give their high gas-phase abundances.

The abundances of sulfur-bearing molecules in L1157 B1 are compared with those in other regions. For this purpose, we employ SO as a standard molecule, and calculated the abundances relative to SO (Table 3.9). The abundances are generally higher than those in the cold quiescent dark cloud L134N. For OCS, CS, and H_2CS, the ratios in L1157 is higher than those in Ori KL (hot core and compact ridge) and Sgr B2(M). This reflects higher abundance of SO in these regions. Ori KL and Sgr B2 are very active high-mass star-forming regions, and hence, much more sulfur is supplied from dust grains there than in L1157 B1. Since carbon is mostly fixed to CO, SO is expected to be produced efficiently. This picture is consistent with the result that the SO/SO_2 ratio does not vary very much among the sources.

Molecule	L1157 B1	IRAS 16293	Sgr B2(N)	Orion KL(HC)	Orion KL(CR)
C_2H_5OH	0.022(14)	-	0.0055^e	0.02^f	0.004^f
CH_3CHO	0.015(7)	0.17^a	0.0064^e	-	0.00051^g
NH_2CHO	0.0014(8)	0.0007^b	0.002^e	0.001^f	0.0008^f
HCOOH	0.011(7)	0.21^a	0.00084^e	0.0055^f	0.0037^f
$HCOOCH_3$	0.057(34)	1.3^a	0.0091^e	0.1^f	0.083^f
CH_3CN	0.003(11)	0.033^a	0.13^e	0.028^f	0.013^f
HNCO	0.016(6)	0.039^c	0.00034^e	0.14^f	-
OCS	0.046(20)	0.22^d	0.0013^e	0.079^f	0.073^f
SO	0.13(5)	0.35^d	0.07^e	1.4^f	0.67^f
SO_2	0.18(7)	0.33^d	0.16^e	0.85^f	0.43^f
H_2CS	0.059(34)	0.42^d	0.096^e	0.0061^f	0.0033^f
SiO	0.04(16)	0.007^d	0.000014^e	0.043^f	0.02^f

[a]Cazaux et al. (2003) [b]Kahane et al. (2013) [c]van Dishoeck et al. (1995) [d]Blake et al. (1994) [e]Nummelin et al. (2000) [f]Sutton et al. (1995) [g]Ikeda et al. (2001)

Table 3.8: The molecular abundance ratios to CH_3OH compared with other sources.

Source	N(SO) (cm^2)	$N(H_2S)/N$(SO)	$N(SO_2)/N$(SO)	N(OCS)/N(SO)	N(CS)/N(SO)	$N(H_2CS)/N$(SO)
Sgr B2(N)[a]	3.5×10^{17}	-	2.3	0.019	-	1.4
Sgr B2(M)[a]	6.2×10^{17}	-	8.1	0.0082	-	0.0012
Hot Core[b]	1.5×10^{17}	-	0.63	0.058	0.033	0.0045
Compact Ridge[b]	2.0×10^{17}	-	0.65	0.11	0.04	0.0049
Extended Ridge[b]	1.1×10^{15}	-	0.42	<0.9	3.0	0.31
L134N[c]	2.0×10^{14}	0.04	0.2	0.1	0.05	0.03
L1157 B1	2.2×10^{14}	0.8-1.3[d]	1.4	0.36	1.0	0.45

[a]Nummelin et al. (2000). [b]Sutton et al. (1995). [c]Ohishi et al. (1992). [d]Bachiller and Peréz Gutiérrez (1997).

Table 3.9: Abundace ratios to SO of sulfur-baring molecules.

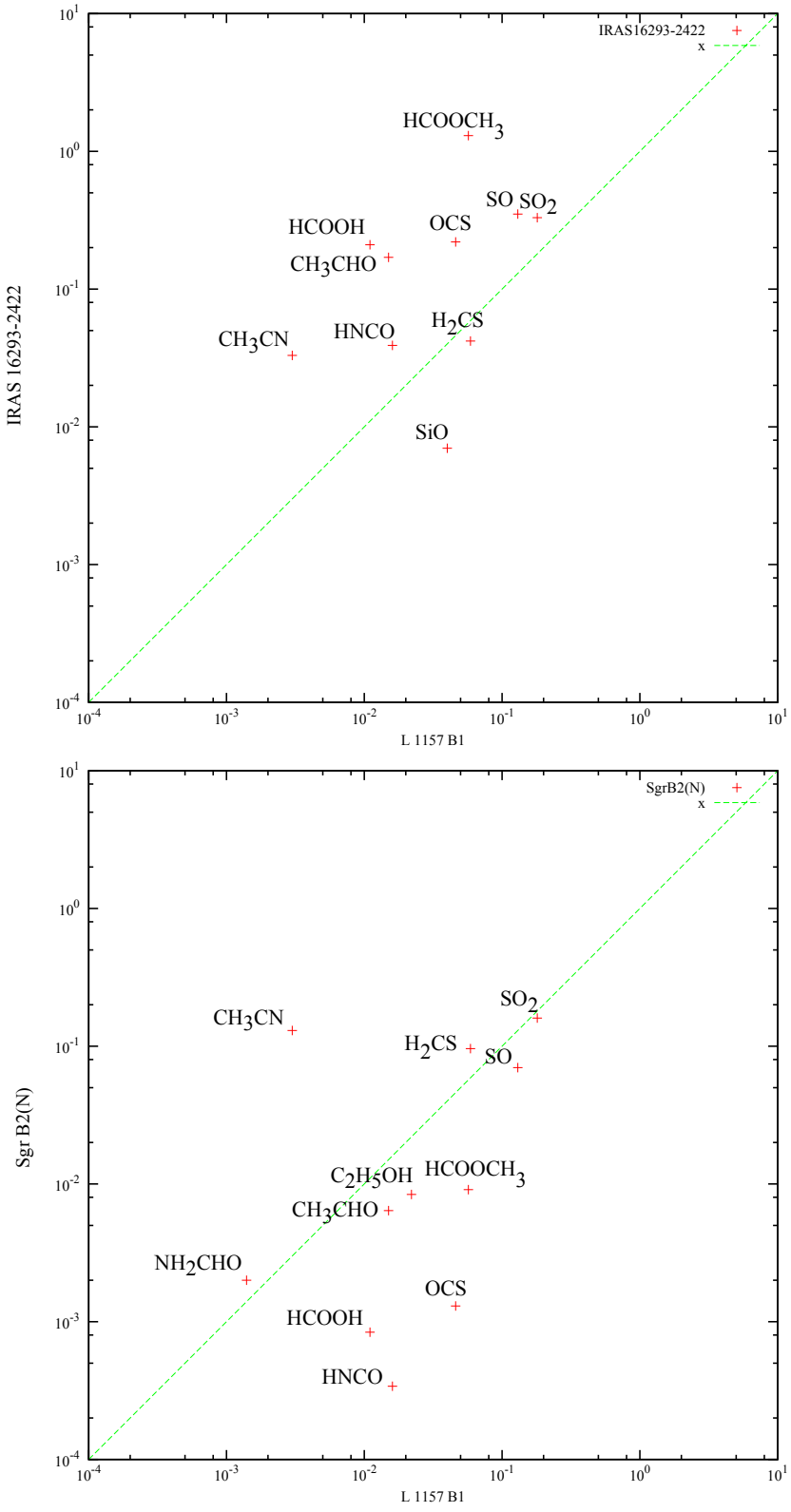

Figure 3.9: Comparison of molecular abundance ratios relative to CH_3OH between L1157 B1 and other sources. Top: The comparison for IRAS 16293-2422. Bottom: The comparison for Sgr B2(N).

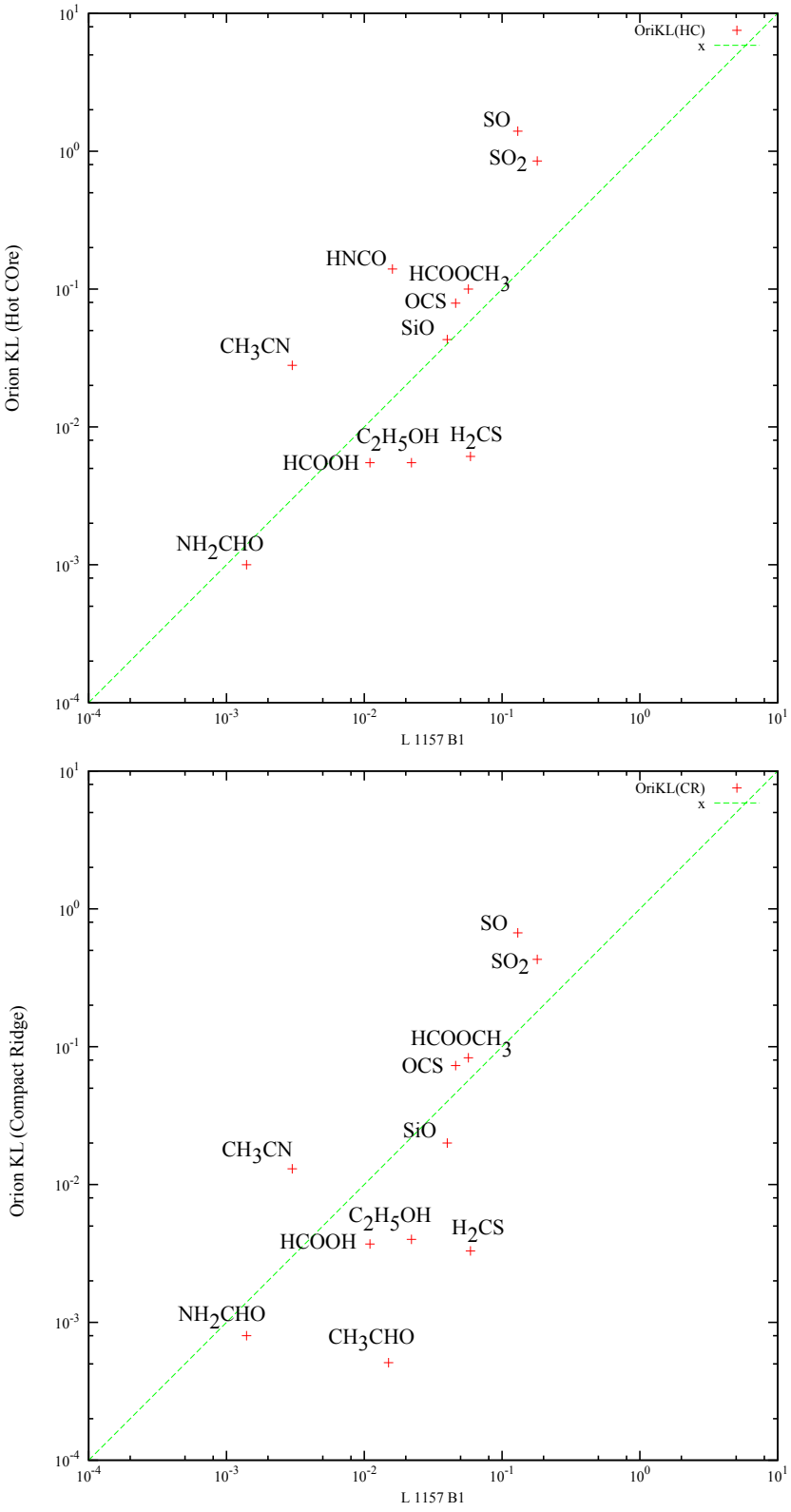

Figure 3.10: Comparison of molecular abundance ratios relative to CH_3OH between L1157 B1 and other sources. Top: The comparison for Orion KL Hot Core. Bottom: The comparison for Orion KL Compact Ridge.

Chapter 4

Phosphorus-containing Molecules

4.1 Interstellar Phosphorus-containing Molecule

Phosphorus is a relatively abundant element, whose cosmic abundance relative to H is 4×10^{-7}. Although it is lower by two orders of magnitude in abundance than those of the other third-row elements like Si and S, six phosphorus-containing molecules have been identified in space. They are PN (Turner and Bally 1987; Ziurys 1987; Turner et al. 1990), CP (Guélin et al. 1990), PO (Tenenbaum et al. 2007), HCP (Agúndez et al. 2007), CCP (Halfen et al. 2008), and PH_3 (Agúndez et al. 2008; Tenenbaum and Ziurys 2008), where the detection of PH_3 is tentative. Among them, PN is the only phosphorus-containing molecule found in molecular clouds, while all of them are detected toward the envelopes of evolved stars like IRC+10216. So far, PN has been detected toward high-mass forming regions such as Orion KL, W51, and Sgr B2, whereas it has not been found in cold starless cores (Turner and Bally 1987; Ziurys 1987; Turner et al. 1990). Hence, high temperature chemistry is thought to be important for its production (Turner and Bally 1987; Ziurys 1987).

A theoretical model for the gas-phase phosphorus chemistry in molecular clouds was first discussed by Thorne et al. (1984) on the basis of the laboratory experiment of the reaction rates for phosphorus-containing molecules. Later, Millar and Herbst (1987) and Millar et al. (1991) presented the chemical model simulations including phosphorus-containing molecules, and indicated that PN is the most stable phosphorus-containing molecule in the gas-phase of molecular clouds. Charnley and Millar (1994) considered the phosphorus chemistry in hot cores, and proposed that PN is formed from PH_3 evaporated from grain mantles. However, this scheme has not been confirmed because of limited observations, and hence, the phosphorus chemistry is still poorly understood.

L1157 B1 is a famous shocked region in the L1157 molecular cloud, which is formed by the interaction between the ambient gas and the blue lobe of the outflow from the low-mass protostar IRAS 20386+6751 (Umemoto et al. 1992; Mikami et al. 1992). In the course of the spectral line survey with the Nobeyama 45 m telescope, we fortuitously detected the $J = 2$-1 line of PN toward L1157 B1. In this chapter, we present the detection of PN, and discuss the phosphorus chemistry in the shocked region.

4.2 Observations

Observations were conducted with the 45 m radio telescope at Nobeyama Radio Observatory from 2010 February to May. Frequencies and line strengths of the PN (J = 2-1) line and the other shock tracer lines (SiO and CH_3OH) are listed in Table 4.1. The 2SB SIS receiver, T100 H/V, was used in the observations, whose system temperature ranged from 150 to 250 K (Nakajima et al. 2008). The image rejection ratio is typically higher than 13 dB. The main-beam efficiency ($\eta_{\rm mb}$) is 0.45, and the half power beam width (HPBW) of the telescope is 18″. We used autocorrelation spectrometers (ACs) and acousto-optical radio spectrometers (AOS-Hs) as the backend, whose velocity resolutions are 1.6 km s^{-1} and 0.118 km s^{-1}, respectively, at 94 GHz. We checked the telescope pointing by observing the nearby SiO maser source (T Cep) every hour, and maintained the pointing accuracy to be better than 8″. We observed the spectral lines listed in Table 4.1 toward the B1 and B2 positions (Bachiller and Pérez Gutiérez 1997), as well as toward the protostar position of IRAS 20386+6751. The observed positions in L1157 are given in Table 4.2. The offsets of the B1 and B2 position from the protostar position are (20″, -60″) and (45″, -105″), respectively. The position-switching mode was employed for all the observations, where the off position was taken at ($\alpha_{2000.0}$, $\delta_{2000.0}$) = ($20^{\rm h}39^{\rm m}9.75^{\rm s}$, 68°21′15.9″).

4.3 Results

4.3.1 Detection of PN

We detected the J = 2-1 line of PN toward the position B1 in the course of the spectral line survey. The line profile is shown in Figure 4.1, where AC is used as the backend. The systemic velocity of the quiescent gas is 2.7 km s^{-1}, whereas the molecular lines observed toward B1 show a slightly blue-shifted feature. The $V_{\rm lsr}$ value for the PN (J = 2-1) line is -0.66 km s^{-1}, which is reasonable for the line at the B1 position. Here we employ the rest frequency of the PN (J = 2-1) line without the hyperfine structure (93979.7695 MHz) taken from CDMS. We carefully checked the available molecular line databases (CDMS and JPL), and found no accidentally overlapping lines of molecules known toward this source either in the signal or image bands. In fact, we find no line emission in the corresponding image frequency according to our line survey observation. Furthermore, no coincidence of other molecular transitions with PN (J = 2-1) was reported in the Ori KL spectrum by Turner and Bally (1987). Based upon these results, we conclude that the detected line is the J = 2-1 line of PN.

The J = 2-1 line of PN splits into the hyperfine components due to the nuclear quadrupole interaction of the N nucleus (I = 1), as shown in Table 4.1. The F = 3-2 and 2-1 components have the frequencies which are close to the above frequency without the hyperfine structure, whereas the F = 1-0 and F = 2-2 components appear at the slightly red-shifted velocity by 4.9 km s^{-1} (Table 4.1). The F = 1-0/2-2 components were not detected clearly in this study, because of its weak intrinsic intensity (0.27 times of the F = 3-2/2-1 components), although a little hump marginally seen at the high velocity side in the AC spectrum may be a sign of the F = 1-0/2-2 components.

After the detection of PN toward B1, we conducted observations toward the B2 (see Figure 3.1 for its position) and protostar positions as well as the B1 position with the higher spectral resolution by using AOS-H. The B2 position is located in the downstream of B1, where the outflow is decelerated and the velocity widths of various molecules become narrower than those

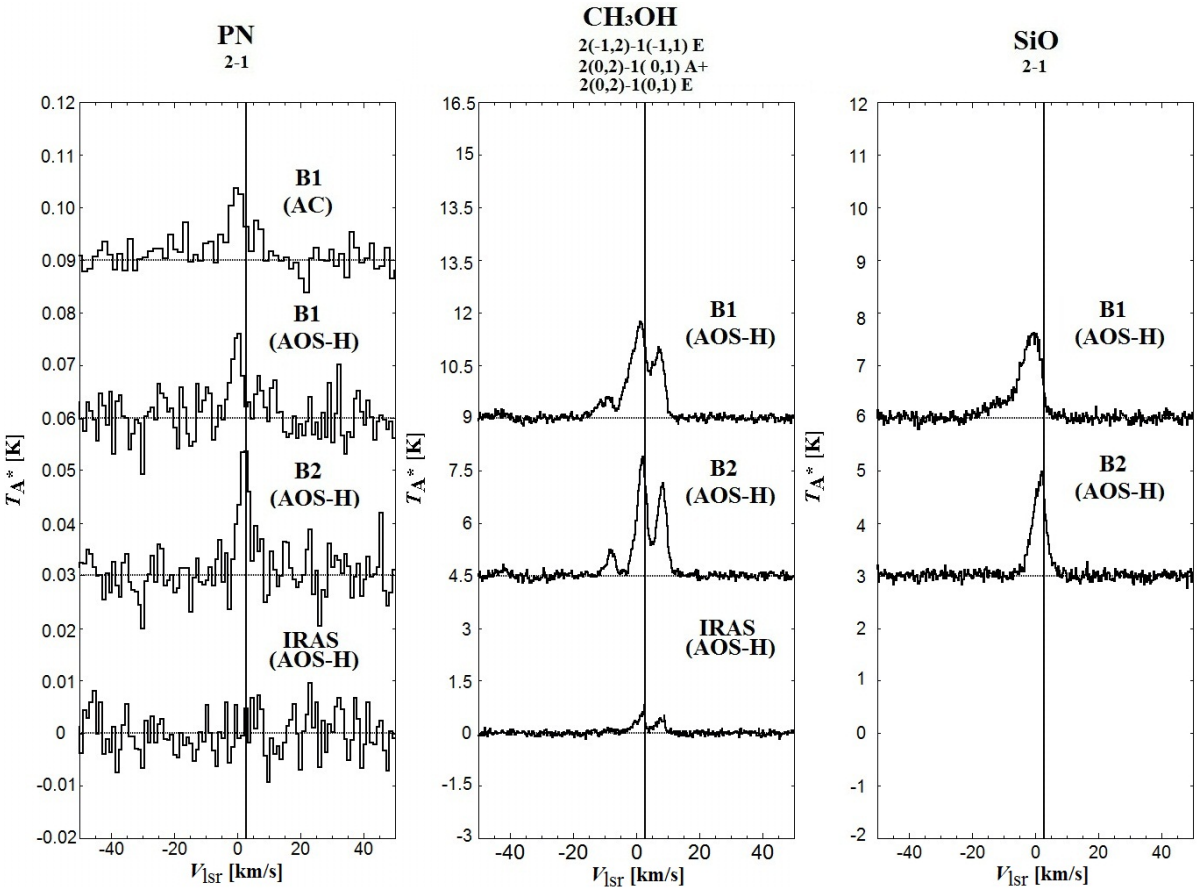

Figure 4.1: Observed spectral line profiles of PN, CH_3OH, and SiO toward L1157 B1, B2, and the protostar position. The IRAS position (L1157 mm) is ($\alpha_{2000.0}$, $\delta_{2000.0}$) = ($20^{\rm h}39^{\rm m}06.2^{\rm s}$, $68°02'15.9''$). The position offsets for B1 and B2 from the IRAS position are ($20''$, $-60''$) and ($45''$, $-105''$), respectively. Vertical lines represent the systemic velocity of the L1157 cloud. As for the AOS-H spectrum of PN, 16 channels are summed up to improve the signal to noise ratio. The resultant velocity resolution is 1.9 km s^{-1}. The $V_{\rm lsr}$ velocity for PN refers to the rest frequency without the hyperfine splitting, and that for CH_3OH refers to the rest frequency of the $2_{0,2}$-$1_{0,1}$ A^+ line. The hyperfine splitting is not resolved in this observation.

in the B1 position (e.g. Bachiller and Pérez Gutiérez 1997). Toward the B2 position, we also detected the PN (J = 2-1) line (Figure 4.1). The $V_{\rm lsr}$ value for the PN line is 1.7 km s^{-1} toward B2, which is close to the systemic velocity of the L1157 cloud. On the other hand, we did not detect the PN line toward the protostar position (Figure 4.1). These results likely suggest that the distribution of PN is localized in the shocked region.

4.3.2 Line Profiles

Here we compare the line profiles of PN (J = 2-1) with those of the shock tracer lines, CH_3OH ($J_K = 2_K$-1_K) and SiO (J = 2-1) (Figure 4.1). The line widths of PN are 3.8 km s^{-1} and 3.7 km s^{-1} toward B1 and B2, respectively, which are narrower than those of SiO, 7.9 km s^{-1} and 5.2 km s^{-1}, respectively (Table 4.3). On the other hand, they are rather close to the line widths of CH_3OH, 6.6 km s^{-1} and 4.2 km s^{-1} toward B1 and B2, respectively (Table 4.3), although toward B1, the line width of PN is still narrower than that of CH_3OH. The CH_3OH molecule in the gas-phase originates from the evaporation of the grain mantle caused by shock (Avery and Chiao 1996), whereas SiO is supplied mainly by disruption of the silicate grains (Mikami et al. 1992). The requirement for the grain disruption under stronger shock conditions is evidenced by the broader SiO line profiles as compared to those of the CH_3OH lines. Hence, it seems that the formation of PN is related to the grain mantle evaporation rather than the disruption of the grains.

4.3.3 Column Densities

We calculate the column density of PN, assuming the local thermodynamic equilibrium (LTE) and optically thin conditions, as summarized in Table 4.4. The excitation temperature is uncertain for PN, and hence, we calculate the column density for three excitation temperatures, $T_{\rm rot}$ = 12 K, 30 K, and 50 K, referring to other molecules observed in this region as in the case of Chapter 3 (Sugimura et al. 2011; Arce et al. 2008; Bachiller et al. 1995). The column density toward the B2 position is almost comparable to that toward the B1 position. These values are lower by one or two orders of magnitude than those reported for Ori KL, W51 and Sgr B2 (Turner and Bally 1987), as shown in Table 5. The fractional abundances of PN relative to H_2 are also evaluated (Table 4.5). Here the $N(H_2)$ value of 2×10^{21} cm^{-2} based on the $C^{18}O$ observation is used for the B1 and B2 positions, whereas 5×10^{21} cm^{-2} is used for the protostar position (Bachiller and Pérez Gutiérrez 1997). The fractional abundances of PN in L1157 B1 and B2 are found to be comparable to or higher than those found in the high-mass star forming regions.

4.3.4 The PN Detection in Another Shocked Region in NGC 1333

After detection of PN in L1157 B1, we intended to explore how ubiquitous this molecule is in shocked regions. For this purpose, we observed the NGC 1333 IRAS 4 region.

NGC 1333 IRAS 4 is a low-mass binary system in Perseus. This region harbors two class 0 protostars, IRAS 4A and 4B, toward which some complex organic molecules such as CH_3CHO and $HCOOCH_3$ are detected (Bottinelli et al. 2004). The high-velocity SiO emission traces the bipolar outflow from IRAS 4A, and blue/redshifted components are well distinguished in the map observed by Lefloch et al. (1998, Figure 4.2). From the extent and the terminal velocity of each component, the typical dynamical ages are estimated to be 3500 and 3200 yr for the

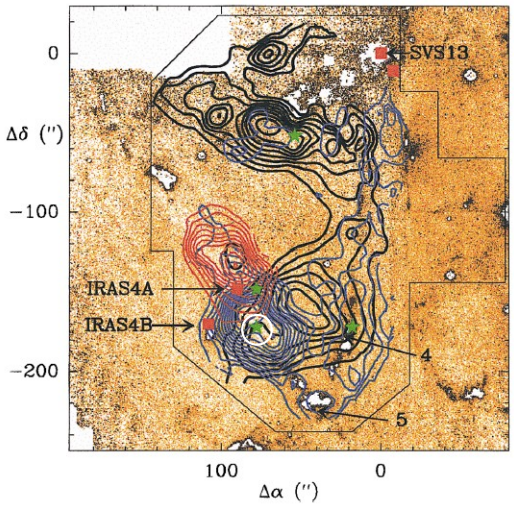

Figure 4.2: SiO ($J = 2 - 1$) map in NGC 1333 IRAS4 (Lefloch et al. 1998). The lowest contour and contour interval are 1 and 0.5 K·km s^{-1}, respectively. The ambient SiO component is indicated in black contours. The white circle indicates the observed position.

blue and red wings, respectively. In this outflow, the average abundance of SiO is calculated to be 3.5 $\times$ 10^{-8}. Apart from this outflow, more extended narrow line emission of SiO was found, whose peak velocity corresponds to that of the ambient gas. Typical line widths range from 0.4 to 1.2 km s^{-1}. SiO abundances in this component are (1-5) $\times$ 10^{-10}, being lower by two orders of magnitude than that of the outflow from IRAS 4A. This component is considered to originate from the outflow of the protostar SVS 13b located at the northwest of IRAS 4 with the separation of 2′, which occurred much earlier than the outflow of IRAS 4[13]. Lefloch et al. (1998) estimated that the ambient component was formed in the timescale of $\sim 10^4$ yr (Figure 4.2).

We conducted the observation of PN ($J = 2 - 1$) toward a shocked region in the outflow of IRAS 4A, which corresponds to the H_2 ($1 - 0$ $S(1)$) peak, CHH16, named by Choi et al. (2006)[14], and tentatively detected its narrow emission (Figure 4.3). The peak velocity is 7.1 km s^{-1}, which is close to that of the ambient gas (7.8 km s^{-1}). The line width is 1.5 km s^{-1}, although it is not resolved.

The peak velocity of the ambient component of SiO line ($J = 2 - 1$) in this region is 8 km s^{-1}, and the line width is 2.4 km s^{-1}. On the other hand, the peak velocity is -3.6 km s^{-1} and the line width is 12 km s^{-1} for the blueshifted component of the outflow from IRAS 4A (Figure 4.3(b)). In comparison, the lack of the blue-shifted component in the PN line ($J = 2 - 1$) seems to indicate that PN is not abundant in the shocked region currently caused by the outflow of IRAS 4A but in the ambient gas affected by the old shock.

4.4 Discussion

Although the ground-state electric structures of the phosphorus and nitrogen atoms are isovalent with each other, their gas-phase chemistry in interstellar clouds is much different. For instance, the P^+ ion and its hydrides (PH_n^+) do not react with H_2, and hence, the ion molecule

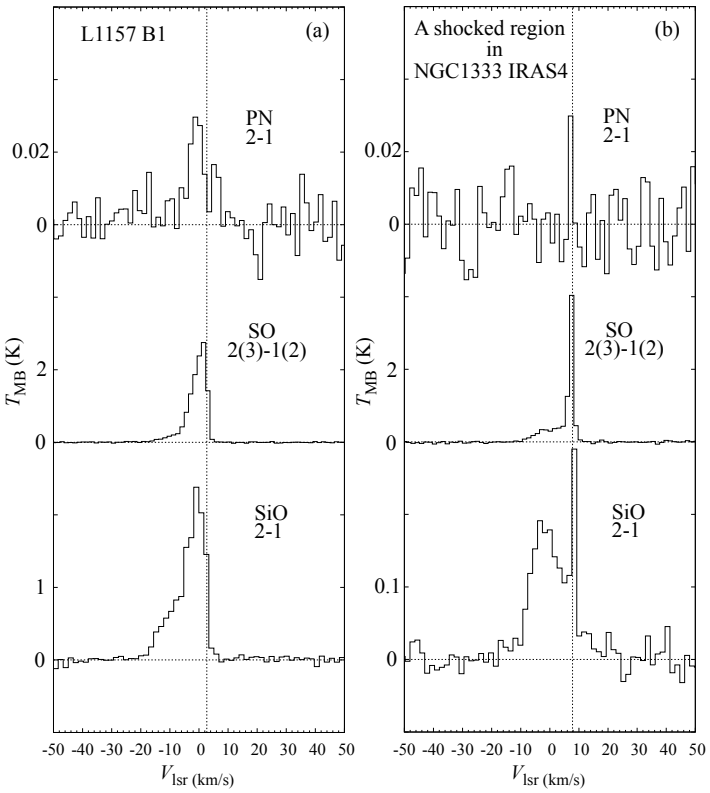

Figure 4.3: Spectral line profiles of PN ($J = 2-1$), SO (2_3-1_2), and SiO (2-1) detected in L1157 B1 (a) and NGC 1333 IRAS 4 (b). Each vertical dashed line indicates the systemic velocity of each cloud, 2.7 km s^{-1} and 7.8 km s^{-1}, respectively.

reaction scheme starting from P^+ is ineffective (Thorne et al. 1984). Therefore, the phosphorus ions and atoms would tend to be depleted onto dust grains before reacting with the gas-phase species.

According to Charnley and Millar (1994), the most abundant phosphorus-bearing molecule on grain mantles is PH_3, which is formed through hydrogenation of the P atom on grain mantles. This molecule is evaporated in the shocked region, which triggers the gas-phase phosphorus chemistry. First, PH_3 reacts with the H atoms to produce PH_2 and PH by abstraction reactions such as

$$H + PH_3 \rightarrow PH_2 + H_2, \tag{4.1}$$

$$H + PH_2 \rightarrow PH + H_2. \tag{4.2}$$

Although these reactions have the activation-energy barriers, they can proceed in warm conditions with the gas temperature greater than 100 K. Then, PH reacts with the oxygen atom to form PO, which further reacts with the nitrogen atom to produce PN as,

$$N + PO \rightarrow PN + O, \tag{4.3}$$

or PH directly reacts with the nitrogen atom to form PN as,

$$N + PH \rightarrow PN + H. \tag{4.4}$$

Note that the following reactions would also contribute to the PH and PO productions, and eventually to the PN production, according to the UMIST database.

$$PH_2 + O \rightarrow PH + OH, \tag{4.5}$$

$$PH_2 + O \rightarrow PO + H_2. \tag{4.6}$$

With the gas kinetic temperature of 100 K and the initial PH_3 fractional abundance of 1.2×10^{-8}, Charnley and Millar (1994) predicted that PN can be formed on a time scale of $\geq 10^4$ yr after mantle evaporation, and can reach an abundance of a few $\times\ 10^{-9}$. This is higher by one order of magnitude than the observed values for L1157 B1 and B2. As they pointed out, the PN abundance directly scales with the adopted PH_3 abundance, which is arbitrarily assumed to be 1.2×10^{-8} in their calculation. This initial abundance of PH_3 may be high, considering that the cosmic abundance of P is 4×10^{-7}. Even if the PH_3 abundance is lower by an order of magnitude than the above assumption, our observational result for L1157 B1 and B2 can be explained.

The model requires the high temperature conditions ($T \geq 100$ K) in order to overcome the activation barriers of the abstraction reactions 4.1-4.2. Indeed, such a high temperature condition is fulfilled in some parts of L1157 B1 and B2, according to the NH_3 observation (Umemoto et al. 1999). The reaction time scale for these initial reactions is estimated to be less than 1000 yr according to the abundance curve of PH_3 in the simulation (Figure 1 of Charnley and Millar 1994). Since the cooling time of the shocked region is from a few 100 to 1000 yr, a substantial part of PH_3 will be converted to PH. The subsequent reactions to form PN are all exothermic without reaction barriers, and hence, they can proceed even after the temperature becomes below 100 K. The model requires the time scale of 10^4 yr for the PN production. Since the timescale of the outflow is reported to be 1.8×10^4 yr (Umemoto et al. 1992), PN can certainly be formed in the shocked region of L1157 B1. Conversely, PN is not abundant in a fresh shock,

Table 4.1: Observed Lines

Molecule	Transitions	ν(MHz)	$S\mu^2$
PN[a]	2-1, F = 3-2	93979.8913	21.1750
	2-1, F = 2-1	93979.7707	11.3438
	2-1, F = 1-0	93978.4749	5.0419
	2-1, F = 2-2	93978.2075	3.7813
	2-1, F = 1-1	93982.3207	3.7813
CH_3OH	$2_{-1,2}$-$1_{-1,1}$ E	96739.362	1.2134
	$2_{0,2}$-$1_{0,1}$ A^+	96741.375	1.6170
	$2_{0,2}$-$1_{0,1}$ E	96744.55	1.6166
SiO	2-1	86846.96	5.8692

[a] The J = 2-1 frequency without the hyperfine structure is 93979.7695 MHz (CDMS). The frequencies listed here are calculated from the molecular constants reported by Cazolli et al. (2006) and Raymonda and Klemperer (1971).

as observed in NGC 1333. However, the model by Charnley and Millar (1994) aims at hot cores, and hence, more detailed simulations including the shock structure would be necessary.

In the above scheme, PH_3 is first released into the gas-phase by the evaporation of grain mantles through sputtering processes, and it is then converted to PN through gas-phase reactions. Thus, the gas-phase phosphorus chemistry and the formation of PN can be triggered by relatively mild shocks, as opposed to the case of SiO, which requires the disruption of the silicate grains due to strong shocks. The narrower line widths observed for PN as compared to that of SiO supports this picture.

For further validating the above formation scenario, it would be very interesting and important to search for other phosphorus-bearing molecules which the model predicts to be abundant. The possible candidates will be PH_3 and PO, which have not been detected in molecular clouds so far. PH_3 and PO are expected to be abundant in the relatively short time scales ($< 10^3$ yr and $< 10^4$ yr, respectively) after the mantle evaporation, according to the model by Charnley and Millar (1994). However, we could not detect PO lines (J = 2.5-1.5) in the observation of L1157 B1 with the rms noise level of $\sim$ 3 mK ($T_{\rm MB}$). The upper limit of the column density is 5.5 $\times$ 10^{11} cm^{-2}. The PO may be consumed for the production of PN in the case of L1157 B1. The production pathway of PN is still to be resolved through the observation.

As mentioned in Section 4.1, the phosphorus chemistry is poorly understood in spite of a relatively high elemental abundance of P. Considering the importance of the phosphorus chemistry in the prebiotic evolution in space, its detailed understanding is required. The present detection of PN in the shocked regions provides us with an important clue to it.

Table 4.2: Observed Positions

Source	α(J2000) h m s	δ(J2000) ° ′ ″
L 1157 B1	20 39 09.8	+68 01 15.9
L 1157 B2	20 39 12.4	+68 00 40.9
L 1157 mm (IRAS)	20 39 06.2	+68 02 15.9

Table 4.3: Line Parameters[a]

Molecules / Sources	Δv (km/s)	$T_{\rm MB}$ (K)	$\int T_{\rm MB} dv$ (K·km/s)	$V_{\rm lsr}$ (km/s)	rms (mK)
PN B1	3.8 ± 0.4	0.035 ± 0.011	0.19 ± 0.03	-0.64 ± 0.17[c]	11
B2	3.7 ± 0.5	0.054 ± 0.012	0.24 ± 0.03	1.7 ± 0.2[c]	12
CH_3OH B1	6.6 ± 0.3[b]	6.2 ± 0.2[b]	–	0.9 ± 0.1[b]	169
B2	4.2 ± 0.2[b]	7.8 ± 0.2[b]	–	1.8 ± 0.1[b]	185
IRAS	4.5 ± 0.4[b]	2.0 ± 0.1[b]	–	1.6 ± 0.2[b]	128
SiO B1	7.9 ± 0.2	3.6 ± 0.2	31.4 ± 0.4	-1.3 ± 0.1	159
B2	5.2 ± 0.1	4.4 ± 0.2	21.9 ± 0.3	1.55 ± 0.05	155

[a] Based on the AOS-H data. Δv, $T_{\rm MB}$ and $V_{\rm lsr}$ are obtained by a single Gaussian fit. The blue wing ($V_{\rm lsr}$ < -10 km s^{-1}) of the SiO emission toward B1 is ignored in the fit.
[b] Obtained only for the $2_{0,2}$-$1_{0,1}$ A$^+$ transition. The overlapping of the other lines is not taken into account.
[c] Calculated on the basis of the rest frequency without the hyperfine splitting. This is close to those of the F = 3-2 and F = 2-1 components.

Table 4.4: Column Densities of PN

Sources	N ($T_{\rm rot}$ = 12 K) (cm^{-2})	N ($T_{\rm rot}$ = 30 K) (cm^{-2})	N ($T_{\rm rot}$ = 50 K) (cm^{-2})
B1	$(4.2\pm0.9)\times10^{11}$	$(7.4\pm1.7)\times10^{11}$	$(1.1\pm0.3)\times10^{12}$
B2	$(5.3\pm1.1)\times10^{11}$	$(9.4\pm2.0)\times10^{11}$	$(1.4\pm0.3)\times10^{12}$
IRAS[a]	$\leq2.9\times10^{10}$	$\leq5.2\times10^{10}$	$\leq7.9\times10^{10}$

[a] Line width is assumed to be 1 km s^{-1}.

Table 4.5: Comparison with Other Sources

Sources	$N_{\rm PN}$ (cm^{-2})	$N_{\rm PN}/N_{\rm H_2}$
L1157 B1	$(4.2\sim11)\times10^{11}$	$(2\sim6)\times10^{-10}$
L1157 B2	$(5.3\sim14)\times10^{11}$	$(3\sim7)\times10^{-10}$
L1157 IRAS	$\leq7.9\times10^{10}$	$\leq1.6\times10^{-11}$
Ori (KL)[a]	4.3×10^{13}	1.7×10^{-10}
W51M[a]	1.1×10^{13}	1.1×10^{-11}
Sgr B2[a]	1.7×10^{12}	1.7×10^{-12}

[a]Turner & Bally (1987)

Chapter 5

L1448 B1/R1

5.1 Internal Shock in Molecular Bullet around L1448 mm

L1448 mm (L1448 C(N)) is a low-mass Class 0 protostar in Perseus, whose mass and dynamical age are 0.03-0.09 $M_\odot$ and (4-12)$\times$ 10^3 yr, respectively (Hirano et al. 2010). This source was discovered by Bachiller et al. (1990) from detection of the high velocity CO outflow emission. By the 350 GHz continuum observation (Hirano et al. 2010), a circumstellar disk with a size of $\sim$90 AU was found, which is elongated perpendicularly to the outflow axis. The mass of the disk is estimated to be $\sim$0.11 $M_\odot$. A well collimated jet from L1448 C(N) along the outflow axis was found through observations of the SiO and CO lines. This jet is extremely energetic (called extremely high velocity (EHV) outflow), and possesses several clumpy structures, called bullets, with almost equal spacing of $\sim$500 AU (Figure 5.1 middle). These bullets are considered to originate from internal bow shocks in the jet beam which were formed as a consequence of the episodic outflow with the period of $\sim$15-20 yr. Particularly, the innermost pairs of bullets (B1, R1) show higher excitation conditions ($n_{\rm H2} \sim 10^6$ cm^{-3}, $T_{\rm kin} \gtrsim$500 K) than L1157 B1 ($n_{\rm H_2}$ $\sim$(1-5)$\times 10^5$ cm^{-3}, $T_{\rm kin}$ $\sim$100-300 K), as shown by the multi-line observation of SiO (Nisini et al. 2007; Figure 5.1 right). In L1448 B1 and R1, the maximum jet velocity reaches $\sim$80 km s^{-1} (Figure 5.1 right), while it is around 20 km s^{-1} toward L1157 B1. Since the distance between L1448 B1 and R1 is $\sim$ 500 AU, their dynamical timescale is $\sim$10 yr, which is much shorter than that toward L1157 B1 ($\sim 10^4$ yr) (Hirano et al. 2010, Nisini et al. 2007, Umemoto et al. 1992). For these reasons, the chemical composition of the B1 and R1 bullets in L1448 will be much different from that in L1157 B1. Only a few molecules like SiO, CH_3OH, and SO have so far been detected in the downstream of the red lobe: ($\Delta\alpha$, $\Delta\delta$) = (16$''$, -34$''$) (Tafalla et al. 2010). In spite of such importance, the molecular line observations have been limited to fundamental species, so far in L1448 B1 and R1. More sensitive and wide range observations are thus necessary for full characterization of the shock chemistry in L1448 B1 and R1, and for comparison with the L1157 B1 shocked region.

5.2 Observation

In order to investigate the shock chemistry in an unbiased way, we conducted the line survey in the 3 mm wavelength with the Nobeyama 45 m telescope toward the protostar position of L1448 C(N) in June 2012. This survey covered the full frequency range of the 3 mm band (79-116 GHz). By observing the protostar position (α(2000) = $3^{\rm h}25^{\rm m}38.8^{\rm s}$, δ(2000) = $68^\circ44'05.0''$),

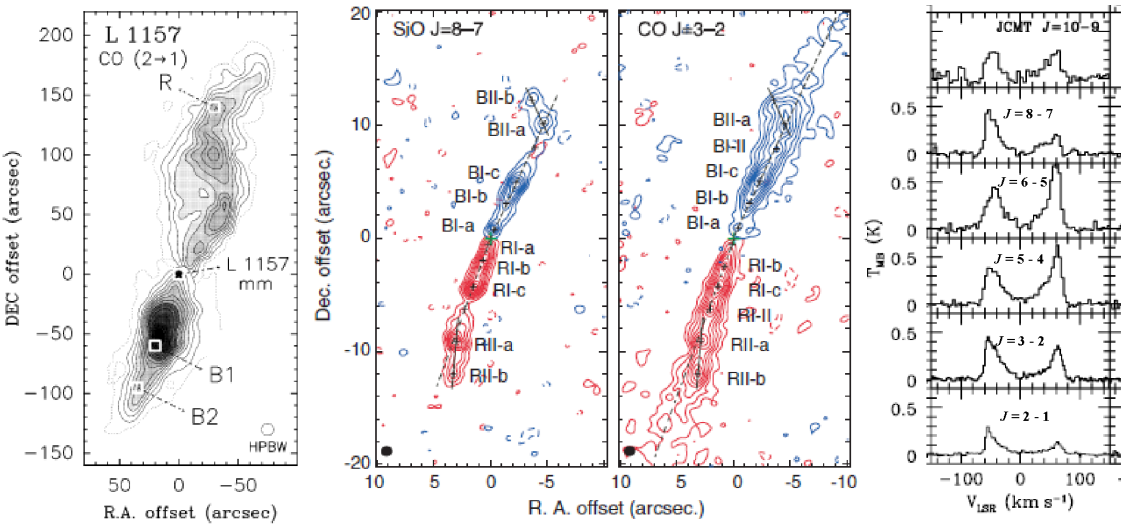

Figure 5.1: Left: CO $(2-1)$ emission from the L1157 outflow (Bachiller and Pérez Gutiérrez 1997). The lowest contour and contour interval are 11 K·km s^{-1}. Middle: High-velocity SiO ($J = 8-7$, left) and CO ($J = 3-2$, right) emissions in L1448 C(N). The velocity ranges are $\pm$(51 to 70) km s^{-1} (Hirano et al. 2010). Blue and red contours represent the blue-shifted and red-shifted emissions, respectively. A well collimmated outflow can be seen, which contains of many bullets. Right: The SiO spectra toward L1448 mm (Nisini et al. 2007). The extremely high velocity (EHV) outflow can be recognized by the double peaked velocity profile.

we covered both the B1 and R1 components within the beam ($\sim 20''$) because the B1 and R1 components are apart from the protostar only by a few arcsecond. We distinguished the spectral line emissions of the shocked region from those of the protostellar core by the line shape and the velocity. The pointing of the telescope was checked by observing the nearby SiO maser source (NML-Tau). The receiver and the backend settings are the same as described in section 3.2.

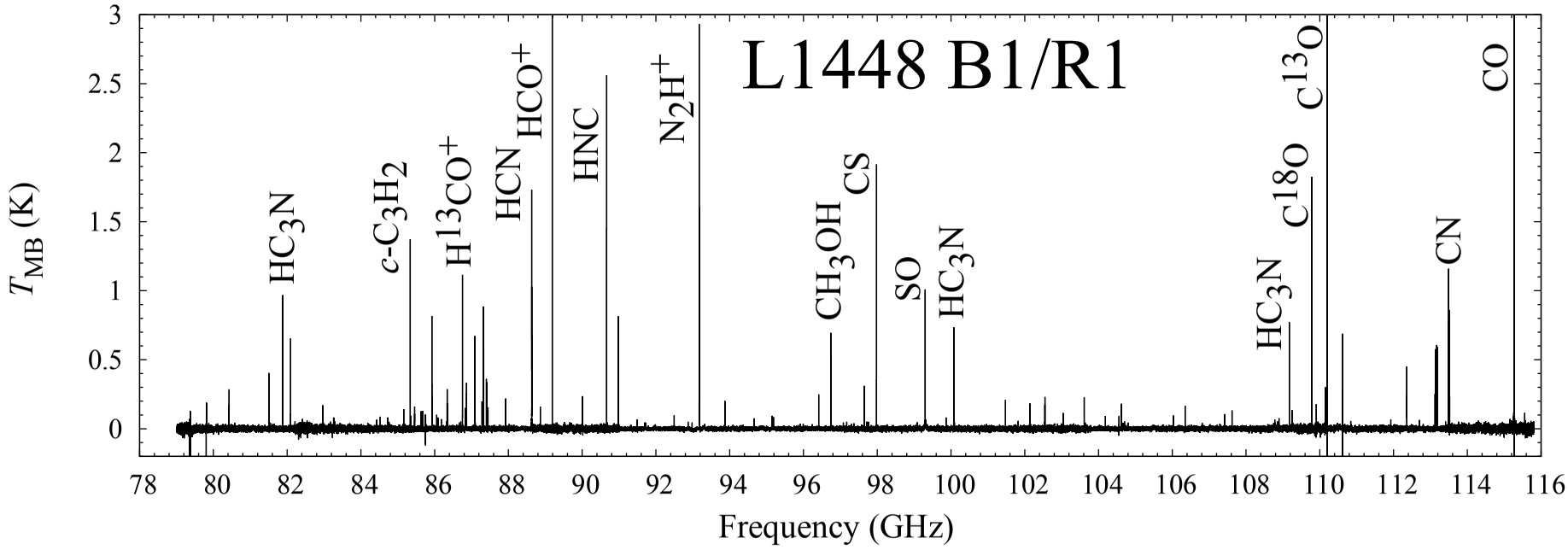

Figure 5.2: The total spectrum of L1448 mm, B1, and R1

Complex Organic Molecules				
CH_3OH				
Nitrile and Other Nitrogen-containing Molecules				
HCN	$H^{13}CN$	$HC^{15}N$	HNC	$HN^{13}C$
HNCO	HC_3N	DC_3N	CH_3CN	NH_2D
Carbon Chain Molecules				
C_2H	C_4H	CCS	CH_3CCH	CH_2DCCH
H_2CCO				
Sulfur-containing Molecules				
CS	^{13}CS	$C^{33}S$	$C^{34}S$	OCS
SO	^{34}SO	SO_2	H_2CS	HDCS
NS				
Molecular Ions				
HCO^+	$H^{13}CO^+$	$HC^{18}O^+$	HCS^+	N_2H^+
Other Molecules				
SiO	^{29}SiO	^{30}SiO	$Si^{18}O$	
CO	^{13}CO	$C^{18}O$	$C^{17}O$	HCO ?
c-C_3H_2	c-C_3HD	c-C_3H	CN	^{13}CN

Table 5.1: Molecules Detected toward L1448 mm.

5.3 Results

In the unbiased spectral line survey observation toward L1448 mm, we covered the frequency range from 79 to 116 GHz, and achieved the typical rms noise level of $\sim$ 10 mK ($T_{\rm MB}$) at the frequency resolution of 488 kHz. The composite spectrum for the whole spectral range is shown in Figure 5.2. We detected 115 lines of 26 species in the observation (Table 5.1). However, the most of the lines show narrow line features whose line width is typically 2$\sim$3 km s^{-1}, as shown in Figure 5.3(b). Since the observation beam involves the L1448 mm protostar, these narrow emissions are thought to come from the protostellar core and its envelope. Note that the protostellar disk ($< 1''$) is much smaller than the observed beam, and hence, its contribution is negligible. On the other hand, the SiO ($J = 2 - 1$) and SO ($J_N = 3_2 - 2_1$) lines show the spectral line feature specific to the EHV component. They show a double-peaked profile with the velocity shift of $\pm$(60-70) km s^{-1} in addition to the narrow component. Furthermore, the HCN line seems to have a weak broad wing component in addition to the narrow component. Hence, the observed beam contains a few different emitting regions. In this chapter, we focus on the EHV component, which is specific to L1448. Although SO, HNCO, HCN, CH_3OH, CS, and SiO reside in the shocked region of L1157 B1, only SO and SiO show the EHV feature. This indicates that the chemical composition of the EHV bullets (R1 and B1) is much different from that of L1157 B1. In particular, the HCN and CH_3OH lines are very bright in L1157 B1, whereas they are almost missing in the EHV bullets. Furthermore, the EHV component of SiO has a different velocity shape from that of SO. This probably originates from the different production mechanisms of the two species in the EHV flow.

Nisini et al. (2007) conducted the SiO multiple-line observation toward L1448 mm, B1, and R1. From the LVG calculation using the RADEX code (Appendix C), they deduced the cloud condition, where $T_{\rm kin} = 300$ K, and $n(H_2) = 8\times10^5$cm^{-3}. With these parameters, we calculated

the SO column densities in L1448 mm, L1448 B1, and L1448 R1 (Table 5.2).

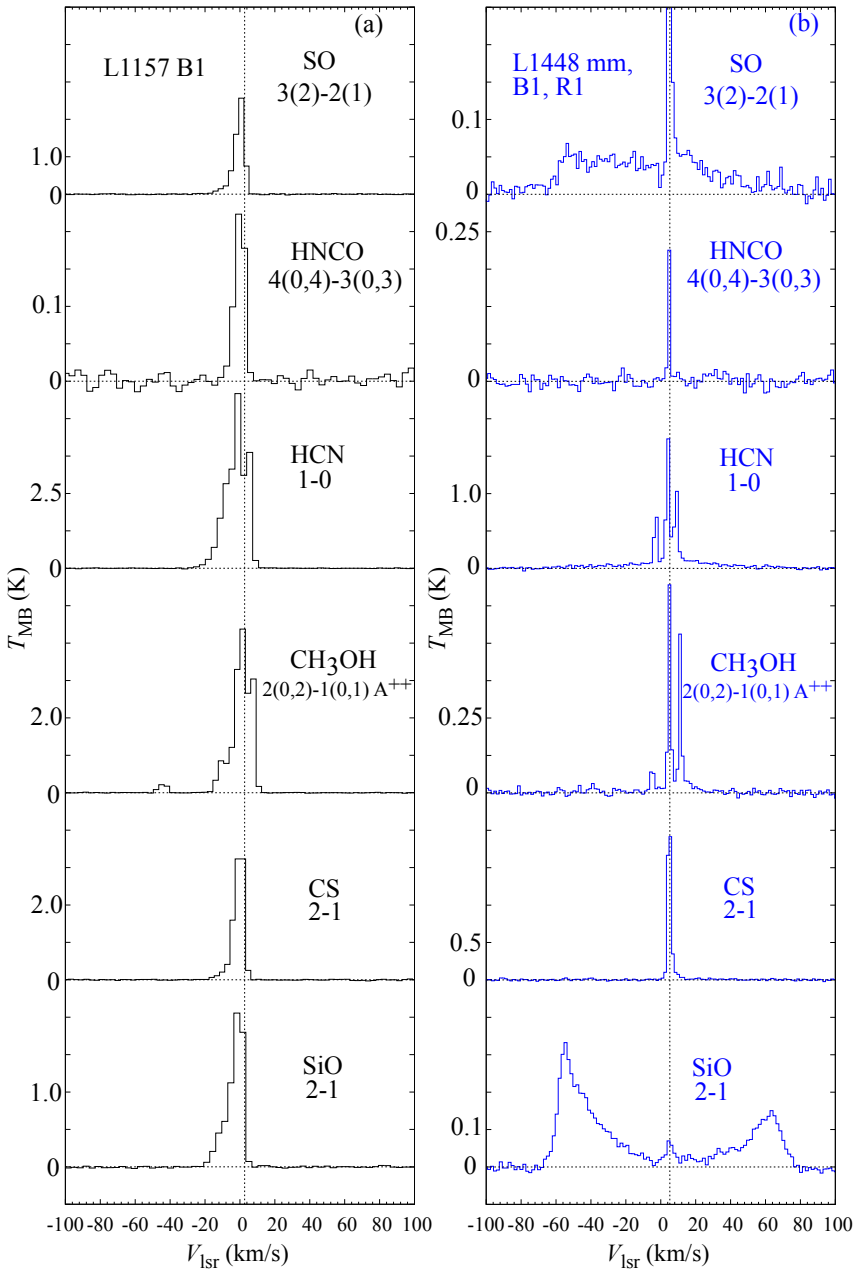

Figure 5.3: Left: Line profiles of several molecules observed in L1157 B1. Right: Line profiles observed in L1448 mm, B1, R1. Only SO (3_2-2_1) and SiO (2-1) lines indicate the broad profiles.

5.4 Discussion

5.4.1 Broad Lines of SiO and SO

As mentioned in Section 3.3.5, SO is considered to be produced through the gas-phase reactions triggered by evaporation of H_2S from grain mantle, while SiO is liberated into the gas-phase by

the disruption of silicate grains. This difference is suggested in the $I(\mathrm{SO})/I(\mathrm{SiO})$ ratio. The ratio is higher in the protostar position than in B1 and R1 shocked regions. If the production processes of SO and SiO were the same (i.e. if both molecules were directly sputtered from the silicate grains), such a clear difference of abundance ratios would not be seen.

In addition, we could not detect the broad component of the SO_2 line from L1448 B1, and R1 (Figure 5.4), while it is seen in the SO line ($J = 3_2 - 2_1$). In contrast, both molecules show similar broad line profiles in L1157 B1. The SO_2/SiO ratio in L1448 B1 is less than 0.2, while that in L1157 B1 is 1.5. Hence, SO_2 is relatively deficient in L1448 B1. In L1157 B1, the jet velocity is $\sim$ 10 km s^{-1}, and the dynamical timescale is estimated to be 1.8 $\times$ 10^4 yr. This is comparable to the production timescale of SO and SO_2, as suggested by Charnley et al. (1997). Hence, SO and SO_2 may efficiently be produced in the gas-phase reactions. On the other hand, the jet velocity is as high as $\sim$ 100 km s^{-1} in L1448 B1 and R1, and the dynamical timescale of L1448 B1 and R1 is only $\sim$ 10 yr. Hence, it seems likely that an observable amount of SO_2 cannot be produced in L1448 B1 and R1 within such a short time scale.

5.4.2 Non-detection of CH_3OH and Other Molecules

We were not able to detect the typical shock tracers CH_3OH, HCN, and CS in the EHV gas of L1448 B1 and R1 regions, although their narrow components are detected. Considering the stronger emission of the SiO (J = 2-1) line in B1 than in R1, we calculated the upper limit of these molecules relative to SiO for B1 (Table 5.3). We assumed the line widths of 40 km s^{-1}, which was estimated from the B1 component of SO (3_2-2_1) line, although the line profile is not appropriately represented by the Gaussian profile.

Tafalla et al. (2010) detected the EHV components of CH_3OH (2_K-1_K, 3_K-2_K; $\sim$ 70 km s^{-1}) as well as of SO, SiO, and H_2CO toward the down stream of the red lobe, where is apart from the protostar by (16″, -34″). At this position, the column density of CH_3OH was reported to be 1.6 $\times$ 10^{13} cm^{-2} for the EHV component. This value is lower by an order of magnitude than our upper limit (2 $\times$ 10^{14} cm^{-2}). Note that this limit may be overestimated by the broad line width of SO (3_2-2_1) line employed for the present estimation. However, the CH_3OH/SiO abundance ratio in B1/R1 is evaluated to be less than 2, which is even smaller than the corresponding ratio (2.5) at the position observed by Taffala et al. (2010). In our obtained S/N ratio, we could not detect a particular EHV component. As far as we focus on B1 and R1 regions, there seems to be a certain difference of the SiO, SO and CH_3OH lines as shock tracers. Although Tafalla et al. (2010) detected various molecular lines with EHV components in the outflow at the downstream of R1, it is not clear whether those molecules directly from the jet from the protostar. Rather, they seem to originate from the interactions with the ambient gas just like the L1157 B1 case. Our result gives important upper limits to the molecular abundances of the shocked bullets at the closest vicinity of the protostar.

Sources	N(SO) (cm^{-2})	$I(\mathrm{SO})/I(\mathrm{SiO})$
L1448 mm	2×10^{14}	6.6±1.9
L1448 B1	2×10^{14}	0.36±0.10
L1448 R1	8×10^{13}	0.33±0.09
L1157 B1	1×10^{14}	0.81±0.22

Table 5.2: SO Column Densities Calculated by RADEX.

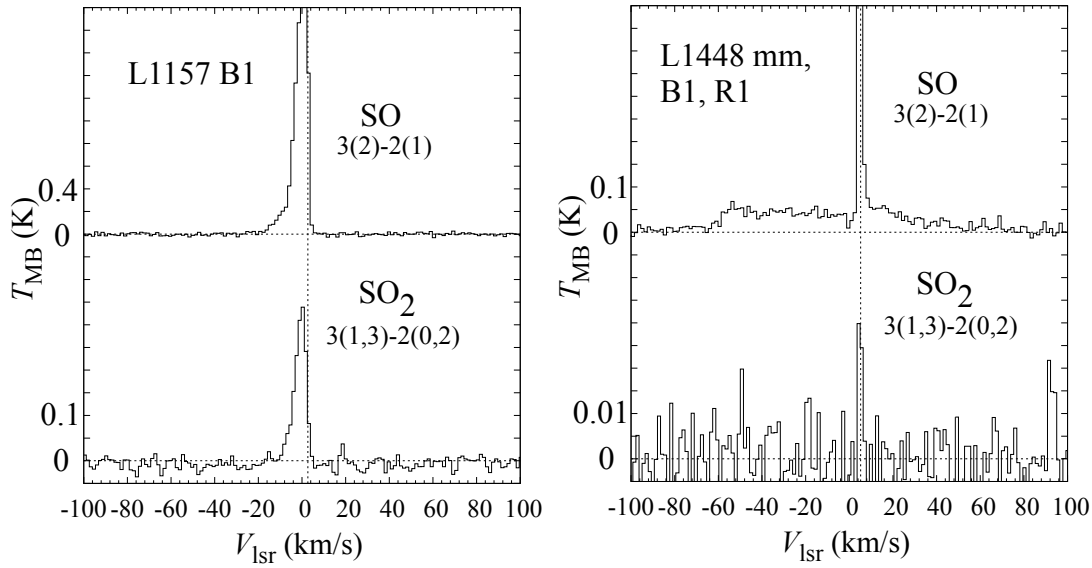

Figure 5.4: Left: SO and SO_2 line profiles in L1157 B1. Right: the same line profiles in L1448 mm.

Molecules	$N(\mathrm{cm}^{-2})$	$N(\mathrm{X})/N(\mathrm{SiO})$ (L1448 B1)	$N(\mathrm{X})/N(\mathrm{SiO})^a$ (Red Lobe)
CH_3OH	$< 2\times10^{14}$	< 5	$(3.3\pm0.5)\times10$
HCN	$< 2\times10^{11}$	$< 5\times10^{-3}$	4.0 ± 0.5
HNC	$< 2\times10^{11}$	$< 5\times10^{-3}$	-
N_2H^+	$< 3\times10^{11}$	$< 8\times10^{-3}$	-
HCO^+	$< 3\times10^{11}$	$< 8\times10^{-3}$	$(3.9\pm0.3)\times10^{-2}$
CS	$< 1\times10^{12}$	$< 3\times10^{-2}$	2.3 ± 0.2
SO_2	$< 8\times10^{12}$	< 0.2	1.4 ± 0.3

Table 5.3: Column density upper limits of molecules undetected in L1448 B1, and the comparison with the result by Tafalla et al. (2010). Our limits and the column density of SiO in B1 are calculated by RADEX.
[a]Tafalla et al. (2010)

While we found the various molecules in L1157 B1, we were not able to detect molecules originating from the shock phenomenon other than SiO, and SO in L1448 B1 and R1. In particular, CH_3OH and other organic molecules are not detected. This indicates the difference of the nature of the grain mantle (See section 1.1) between L1157 B1 and L1448 B1/R1, although we cannot completely rule out the possibility that CH_3OH is completely destroyed in the strong shock. L1448 B1 and R1 are located near the protostar with similar distances ($\sim$ 250 AU). In such a condition, grain mantle would already have evaporated due to the star-forming activities around the protostar. As seen in the discussion in L1157 B1 section, the richness of complex organic molecules in the gas-phase depends on the grain mantle. It is likely that the lack of grain mantle in the pre-shocked gas has made the chemistry very simple in comparison with the

L1157 B1 case. We discuss this point in final chapter.

Chapter 6

IC 443 GI

6.1 Supernova Shock in IC 443

In supernova remnants, we can also expect the shock compression and heating of the gas, resulting in the shock chemistry. However, the physical situation of the supernova shock seems to be much different from the outflow shock. A blast wave of a supernova sweeps up the diffuse interstellar gas during its expansion, producing a shocked shell. It is proposed that the shock is often dissociative (Reach et al. 2002, Wang and Scoville 1992). Furthermore, the pre-shocked gas is a diffuse gas without rich ice mantles on dust grains. These features contrast to the outflow shock case such as L1157 B1, where dust grains are covered with rich ice mantles in a relatively dense region. Hence the chemistry of the supernova shock should be different from that of the outflow shock. The principal purpose of this chapter is to clarify the chemical composition of the supernova shock, and to compare it with that of the outflow shock.

IC 443 is a supernova remnant located in Gemini, which is $\sim$ 1.5 kpc apart from the Solar System. The age is estimated to be $\sim 3 \times 10^4$ yr (Chevalier 1999). It has been observed in various wavelengths from X-ray to radio (Abdo et al. 2010, Fesen and Kirshner 1980, van Dishoeck et al. 1993). All these results indicate several shell-like complex structures of interacting regions. Abdo et al. (2010) observed γ rays from this region with the Fermi Gamma-ray Space Telescope, and found its extended distribution. This is thought to be produced by the cosmic-ray particles accelerated by the supernova. Near the shock front, broad and asymmetric line profiles of CO and OH are observed. From the observations of several rotational transitions of H_2CO, the gas kinetic temperature of the region is estimated to be 100-200 K, while a typical rotation temperature of molecules is around 20 K (van Dishoeck et al. 1993). Ziurys et al. (1989) reported that while the abundances of SO, CS, CN, and NH_3 are not so much different from those in cold dark clouds, the abundances of HCO^+ and SiO seem to be enhanced by the shock. van Dishoeck et al. (1993) detected the submillimeter-wave lines of some simple molecules such as CS, HCN, SO, SiO, and H_2CO toward several positions in this cloud, and found that the G I position (Figure 6.1) is the richest in molecules among the various observed positions.

However, these previous observations focused on the fundamental species. Indeed, they could not detect a typical shock tracer, CH_3OH, and other complex organic molecules, seen in L1157 B1. More sensitive observations for more complex species in the 3 mm wavelength region are necessary for full characterization of the shock chemistry in IC 443, and for its comparison with other shocked regions.

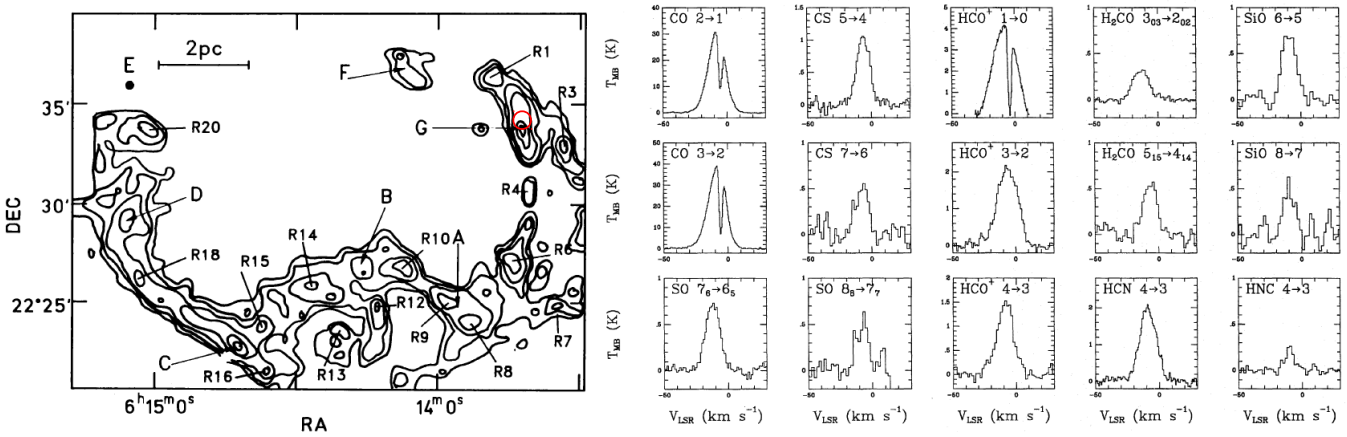

Figure 6.1: Left: Map of the shocked molecular hydrogen emission at 2.1 μm in the IC 443 region (van Dishoeck et al. 1993). G I position is indicated by the red circle. Right: Line profiles of various molecules obtained toward G I position (van Dishoeck et al. 1993). Some lines such as CO ($J = 2 - 1$), CO ($J = 3 - 2$), and HCO^+ ($J = 1 - 0$) show a sharp absorption due to the foreground gas.

6.2 Observation

We chose the position G I (α(J2000) = $06^h16^m43^s.4$, δ(J2000) = $22°32'33.5''$) for the spectral line survey to characterize the chemical composition. Toward this position, many lines had been detected by van Dishoeck et al. (1993). We covered a frequency range from 78 to 116 GHz in the line survey with the Nobeyama 45 m telescope. The off-position is taken at α(J2000) = $06^h20^m01^s.08$, δ(J2000) = $22°18'39.1''$ (van Dishoeck et al. 1993). We used the TZ1 H/V receiver and SAM 45 with the spectral resolution 488 kHz. Two channels of SAM 45 were summed up to enhance the signal-to-noise ratio. The resulting velocity resolution of ~ 3 km s^{-1} at 90 GHz is fine enough for the typical line width of > 10 km s^{-1} in this region. The pointing of the telescope was checked by observing the SiO maser source (U-Ori).

6.3 Results

6.3.1 Detected Molecules

Figure 6.2 is an overview of the observed spectrum toward IC 443 G I in the frequency range from 78.1 to 115.8 GHz, whereas Fig. Appendix B.1 shows its expansion. The rms noise level achieved is 12-20 mK at the frequency resolution of 1 MHz. With this sensitivity, we detected several weak lines in addition to strong lines such as CO, ^{13}CO, HCO^+, HCN, SiO, and CS. We identified the observed lines by using the molecular spectral line databases, CDMS (Muller et al. 2005), JPL (Pickett et al. 1998), and NIST (Lovas et al. 2009). The spectral lines from the image side band are indicated as 'image' in Fig. B.1. A basic criterion for detection is that the line has an integrated intensity with the confidence level higher than 4σ at the expected frequency. All the detected molecules are summarized in Table 6.1. In total, 44 lines of 14 species are detected. Table 6.2 lists the parameters of the detected lines, which are obtained by

the Gaussian fitting. Almost all lines have broad velocity widths (FWHM) ranging from 7 to 22 km s^{-1}. This indicates that these lines do not originate from the ambient gas but from the shocked region. However, the isotopic species of CO exceptionally show narrow velocity widths ranging from 3 to 4 km s^{-1}, which suggests that they are mainly emitted from the ambient gas. The peak velocities of most lines are blue-shifted with respect to the systemic velocity of the ambient gas by about -4 km s^{-1}. Exceptions are the isotopic species of CO, as in the case of the line widths. We will further discuss the relationship between the line width and the peak velocity in Section 6.4.1.

Saturated Organic Molecules				
CH_3OH				
Nitrogen-containing Molecules				
HCN	$H^{13}CN$	$HC^{15}N$	HNC	HC_3N
CN				
Carbon Chain Molecules				
C_2H	c-C_3H_2			
Sulfur-containing Molecules				
CS	$C^{34}S$	SO	^{34}SO	SO_2 ?
Molecular Ions				
HCO^+	$H^{13}CO^+$	N_2H^+		
Other Molecules				
SiO	^{29}SiO	CO	^{13}CO	$C^{18}O$

Table 6.1: Molecules Detected toward IC 443 G I.

Rest Frequency (GHz)	Molecules	Transition	E_u (cm^{-1})	T_{MB} (K)	V_{lsr} (km/s)	Δv (km/s)	$\int T_{MB} dv$ (K·km/s)
82.0935437	c-C_3H_2	2(0,2)-1(1,1)	4.47	0.04±0.01	-5.51±0.72	7.63±1.39	0.33±0.05
83.688093	SO_2 ?	8(1,7)-8(0,8)	25.5	0.02±0.01	-6.81±1.36	12.11±2.69	0.26±0.13
84.521169	CH_3OH	5(-1,5)-4(0,4) E	28.1	0.05±0.01	-7.06±0.63	11.71±1.17	0.62±0.09
85.338894	c-C_3H_2	2(1,2)-1(0,1)	4.48	0.10±0.01	-5.47±0.58	10.82±1.12	1.15±0.09
85.759199	^{29}SiO	2-1	4.29	0.04±0.01	-7.16±0.67	7.20±1.30	0.31±0.06
86.0549664	$HC^{15}N$	1-0	2.87	0.06±0.01	-6.28±0.82	10.05±1.59	0.64±0.10
86.09395	SO	2(2)-1(1)	13.4	0.09±0.01	-8.24±0.45	11.83±0.84	1.13±0.11
86.3399215	$H^{13}CN$	1-0	2.88	0.19±0.01	-7.01±0.36	14.91±0.69	3.02±0.19
86.7542884	$H^{13}CO^+$	1-0	2.89	0.22±0.02	-6.33±0.35	14.84±0.66	3.47±0.56
86.84696	SiO	2-1	4.34	0.54±0.06	-8.09±0.31	14.74±0.59	8.47±0.56
87.284105	C_2H	1-0, J = 3/2-1/2, F = 1-1	2.91	0.06±0.01	-4.28±0.50	6.70±0.98	0.43±0.25
87.316898	C_2H	1-0, J = 3/2-1/2, F = 2-1	2.91	0.46±0.04	-5.60±0.31	9.35±0.58	4.58±0.35
87.328585	C_2H	1-0, J = 3/2-1/2, F = 1-0	2.91	0.25±0.02	-5.05±0.25	7.08±0.48	1.88±0.30
87.401989	C_2H	1-0, J = 1/2-1/2, F = 1-1	2.92	0.30±0.05	-4.86±0.68	6.40±1.11	2.06±0.21
87.407165	C_2H	1-0, J = 1/2-1/2, F = 0-1	2.92	0.12±0.03	-3.46±2.30	16.7±4.2	2.18±0.21
87.44647	C_2H	1-0, J = 1/2-1/2, F = 1-0	2.92	0.06±0.01	-6.28±0.71	16.25±1.39	1.04±0.26
88.6316022	HCN	1-0	2.96	3.17±0.14	-9.02±0.53	19.78±1.06	66.76±3.78
89.1885247	HCO^+	1-0	2.98	4.21±0.36	-8.91±1.07	22.72±2.43	101.81±5.75
90.663568	HNC	1-0	3.02	0.65±0.03	-6.30±0.21	12.08±0.39	8.36±0.50
90.979023	HC_3N	10-9	16.7	0.05±0.01	-9.59±0.80	11.87±1.53	0.63±0.08
93.1733922	N_2H^+	1-0	3.11	0.11±0.01	-6.26±0.36	14.53±0.69	1.70±0.12
95.169463	CH_3OH	8(0,8)-7(1,7) A^{++}	58.1	0.07±0.01	-6.06±0.59	4.86±0.93	0.36±0.06
96.4129495	$C^{34}S$	2-1	4.82	0.06±0.01	-6.55±0.47	11.92±0.90	0.76±0.08
96.739362	CH_3OH	2(-1,2)-1(-1,1)					
96.741375	CH_3OH	2(0,2)-1(0,1) A^{++}	4.84	0.13±0.01	-5.47±0.54	15.35±1.05	2.12±0.14
96.74455	CH_3OH	2(0,2)-1(0,1) E					
97.715317	^{34}SO	3(2)-2(1)	6.32	0.03±0.01	-8.77±0.74	10.33±1.43	0.33±0.06
97.9809533	CS	2-1	4.9	1.55±0.05	-6.53±0.14	11.76±0.26	19.40±1.12
99.29987	SO	3(2)-2(1)	6.41	0.63±0.07	-6.83±0.28	12.66±0.53	8.49±0.52
100.076392	HC_3N	11-10	20	0.07±0.01	-9.12±0.38	9.38±0.73	0.70±0.07
104.0294183	SO_2 ?	3(1,3)-2(0,2)	5.38	0.07±0.01	-9.49±0.66	3.96±0.93	0.30±0.04
104.2392952	SO_2 ?	10(1,9)-10(0,10)	38	0.03±0.01	-7.91±1.19	10.52±2.25	0.34±0.07
108.893963	CH_3OH	0(0,0)-1(-1,1) E	9.12	0.04±0.01	-3.06±1.09	9.89±2.07	0.42±0.09
109.173634	HC_3N	12-11	23.7	0.05±0.01	-8.92±0.94	13.45±1.81	0.72±0.19
109.25222	SO	2(3)-1(2)	14.6	0.19±0.01	-6.87±0.27	10.89±0.52	2.20±0.16
109.7821434	$C^{18}O$	1-0	3.66	0.20±0.01	-4.44±0.15	3.40±0.29	0.72±0.07
110.2013534	^{13}CO	1-0	3.68	2.38±0.14	-4.19±0.11	3.72±0.18	9.43±0.57
113.1233701	CN	1-0, J = 1/2-1/2, F = 1/2-1/2	3.77	0.10±0.01	-6.32±0.55	9.97±1.06	1.06±0.60
113.1441573	CN	1-0, J = 1/2-1/2, F = 1/2-3/2	3.77	0.45±0.02	-6.44±0.26	13.97±0.51	6.69±0.71
113.1704915	CN	1-0, J = 1/2-1/2, F = 3/2-1/2	3.78	0.46±0.02	-6.53±0.34	13.68±0.64	6.70±0.70
113.1912787	CN	1-0, J = 1/2-1/2, F = 3/2-3/2	3.78	0.55±0.02	-6.21±0.19	12.28±0.35	7.19±0.67
113.4881202	CN	1-0, J = 3/2-1/2, F = 3/2-1/2	3.79				
113.4909702	CN	1-0, J = 3/2-1/2, F = 5/2-3/2	3.79				
113.4996443	CN	1-0, J = 3/2-1/2, F = 1/2-1/2	3.79				36±0.7
113.5089074	CN	1-0, J = 3/2-1/2, F = 3/2-3/2	3.79				
113.5204315	CN	1-0, J = 3/2-1/2, F = 1/2-3/2	3.79				
115.2712018	CO	1-0	3.85	17.01±0.78	-6.76±0.39	14.63±0.77	264.98±15.20

Table 6.2: Line Parameters Observed in IC 443 G I.

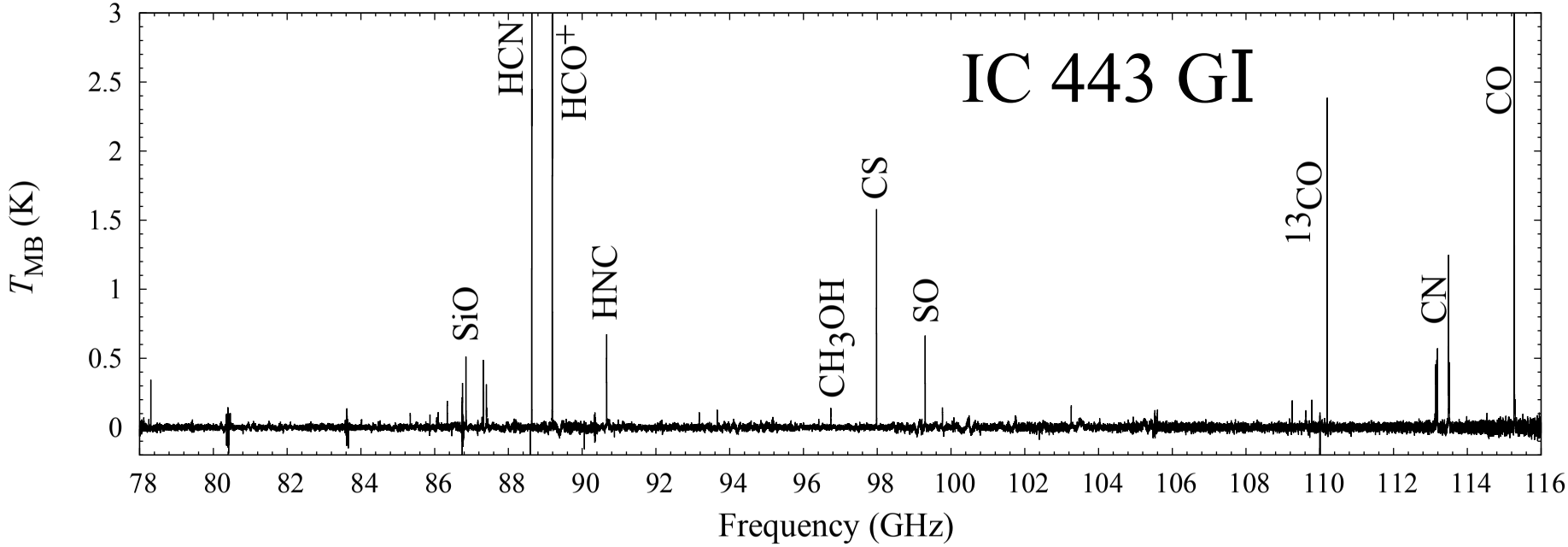

Figure 6.2: The total spectrum of IC 443 G I

6.3.2 Complex Organic Molecules

Although van Dishoeck et al. (1993) reported the non-detection of CH_3OH line in IC 443 clumps, we detected six emission lines of CH_3OH, which are $5_{-1,5} - 4_{0,4}$ E, $8_{0,8} - 7_{1,7}$ A^{++}, $2_{-1,2} - 1_{-1,1}$, $2_{0,2} - 1_{0,1}$ A^{++}, $2_{0,2} - 1_{0,1}$ E, $0_{0,0} - 1_{-1,1}$ E lines. We were unable to detect any absorption line of CH_3OH in contrast to the L1157 B1 case. This is mainly due to the low abundance of CH_3OH in IC 443 G I. The integrated intensity of $2_K - 1_K$ line ($\sim$ 2 K·km s^{-1}) is indeed weaker than that observed toward L1157 B1 ($\sim$ 50 K·km s^{-1}) . van Dishoeck et al. (1993) attributed their non-detection of CH_3OH to the low density of the pre-shocked gas ($\sim$ 10^4 cm^{-3}), where the photo-dissociation effect is significant. With the improved signal-to-noise ratio, we succeeded in detecting the CH_3OH lines in the shocked region ($V_{\rm lsr} \sim$ -6 km s^{-1}, $\Delta v \sim$ 10 km s^{-1}). This result suggests that CH_3OH is formed to some extent on dust grains in diffuse clouds and this molecule can be used as a shock tracer even in some supernova shock cases, although its emissions are not bright. On the other hand, we failed to detect other complex organic molecules such as $HCOOCH_3$, CH_3CHO, CH_3CN, NH_2CHO, and HCOOH observed in L1157 B1. Considering weak intensities of CH_3OH lines, these non-detections seem to be reasonable.

6.3.3 Carbon-chain Molecules

We detected six hyperfine component lines of C_2H ($N = 1 - 0$). As mentioned in Chapter 3, carbon-chain molecules are abundant in young starless cores like TMC-1 and Lupus-1 A (Sakai et al. 2010), or low-mass star-forming regions such as L1527 and IRAS 15398-3359. The total integrated intensity of C_2H lines is $\sim$ 12 K·km s^{-1} while this is $\sim$ 8 K·km s^{-1} in L1157 B1. Considering the $V_{\rm lsr}$ value and the line width, C_2H resides in the shocked gas. On the other hand, we could not detect any CCS line in IC 443 G I. As mentioned in section 3.3.4, we detected CCS lines in the shocked gas of L1157 B1. These results indicate that the chemical processes for productions are different between C_2H and CCS. In addition, we detected the HC_3N lines ($J = 10-9, 11-10, 12-11$), which were previously undetected by van Dishoeck and al. (1993). However, these lines are much weaker than those in L1157 B1 (averaged intensity ratio $I_{\rm IC443GI}$/ $I_{\rm L1157B1} \sim 0.16$).

6.3.4 Sulfur-bearing Molecules

We detected several lines of sulfur-bearing species. They are CS ($J = 2-1$), $C^{34}S$ ($J = 2-1$), SO ($J_N = 2_2 - 1_1, 3_2 - 2_1$, and $2_3 - 1_2$), ^{34}SO ($J_N = 3_2 - 2_1$), and tentatively detected SO_2 lines ($8_{1,7} - 8_{0,8}$, $10_{1,9} - 10_{0,10}$). On the other hand, we were unable to detect OCS, H_2CS, and NS detected in L1157 B1. Sulfur-containing molecules can be produced through gas-phase reactions from H_2S supplied from evaporation of grain mantle, rather than direct evaporation of grain mantle or disruption of the silicate grain through which SiO is considered to be produced. We had already found that the SO and SO_2 abundances in L1157 B1 and L1448 B1 are different from each other (Section 5.4.1 and Table 5.2). This may be caused by the difference of the dynamical timescales of outflows.

6.3.5 Other Molecules

In addition to the above-mentioned molecules, we detected the spectral lines of fundamental molecules such as ^{28}SiO ($J = 2 - 1$), ^{29}SiO ($J = 2 - 1$), 7 fine and hyperfine components of CN

($N = 1 - 0$), HCN ($J = 1 - 0$), $H^{13}CN$ ($J = 1 - 0$), $HC^{15}N$ ($J = 1 - 0$), HNC ($J = 1 - 0$), CO ($J = 1 - 0$), ^{13}CO ($J = 1 - 0$), $C^{18}O$ ($J = 1 - 0$), HCO^+ ($J = 1 - 0$), $H^{13}CO^+$ ($J = 1 - 0$), and N_2H^+ ($J = 1 - 0$). As seen in the L1157 B1 observation, we were able to detect the spectral lines of some isotopic species.

6.3.6 Isotopic Species

The integrated intensity ratio $I(C^{32}S)/I(C^{34}S)$ is evaluated to be 25.5±3.1. This value is similar to that reported for interstellar clouds by Chin et al. (1996) (24.4±5.0), and hence, we can conclude that the $C^{32}S$ and $C^{34}S$ lines are optically thin. Similarly, the $I(^{32}SO)/I(^{34}SO)$ ratio for the $J_N = 3_2 - 2_1$ lines is 25.7±4.9, indicating that the ^{32}SO and ^{34}SO lines are also optically thin in IC 443 G I.

The $I(^{28}SiO)/I(^{29}SiO)$ ratios for the $J = 2 - 1$ lines are evaluated to be 27.1±5.6. This value is similar to the terrestrial isotopic $^{28}Si/^{29}Si$ ratio 19.7. Hence, ^{28}SiO and ^{29}SiO lines are optically thin.

The $I(H^{12}CN)/I(H^{13}CN)$ ratio for the $J = 1 - 0$ lines is calculated to be 22.1±1.9, which is lower than the standard $^{12}C/^{13}C$ ratio in interstellar clouds (60) by a factor of 0.37. The $I(HC^{14}N)/I(HC^{15}N)$ ratio is 104±17, although the interstellar value of $^{14}N/^{15}N$ is 237 (Lucas and Liszt 1998). Hence, the HCN line is slightly optically thick. On the other hand, $I(H^{13}CN)/I(HC^{15}N)$ is calculated to be 4.7±0.8, which corresponds to the interstellar value of 4.0 calculated in Section 3.3.9. Hence, $H^{13}CN$ and $HC^{15}N$ lines can be regarded as optically thin.

6.4 Discussion

6.4.1 Comparison on a V_{lsr}-Δv Diagram

Typical line profiles observed toward IC 443 G I tend to be blue-shifted with respect to the systemic velocity of the quiescent gas (∼ -4 km s^{-1}), and show broad line widths from 5 to 20 km s^{-1}. Because of this, the peak velocity (V_{vlsr}) and the line width (Δv) are expected to show correlation. Hence, we examine this correlation. The peak velocity and the line width are approximately determined by assuming a single Gaussian profile, although the real profile is slightly asymmetric as in the case of L1157 B1. The results are listed in Table 6.2 with the fitting errors. Although the spectral resolution is about 3 km s^{-1}, we can determine the V_{lsr} value much more precisely by the fit, as shown in Table 6.2. The V_{lsr} and Δv values should reflect differences of the distributions of molecules to some extent. As in the case of L1157 B1, we will discuss the relation between V_{lsr} and Δv for various molecules.

We employ the SiO ($J = 2-1$), CH_3OH ($5_{-1,5} - 4_{0,4}$ E) and ^{13}CO (J = 1-0) lines as the standard lines (Fig. 6.3(a)). As seen in the L1157 B1 section, the SiO ($J = 2-1$) line shows the most blue-shifted peak velocity and the broadest line width. Namely, it has V_{lsr} of -8.1 ± 0.3 km s^{-1} and Δv of 14.7±0.6 km s^{-1}, which is located near the upper-left corner of the V_{lsr}-Δv diagram (Fig. 6.3(a)). On the other hand, CH_3OH is produced in grain mantles, and is released into the gas-phase by sputtering. Since CH_3OH is evaporated more easily than SiO, the evaporation of CH_3OH can occur even under weaker shocks. This nature of CH_3OH is reflected in the velocity profile. Namely, the peak velocity is less blue-shifted than the SiO line, and the line width is narrower. For example, the line profile of the $5_{-1,5} - 4_{0,4}$ E line has V_{lsr} = -7.1±0.6

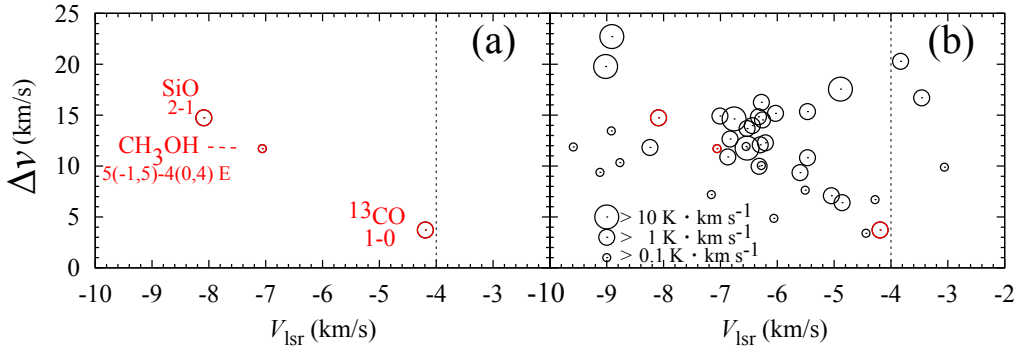

Figure 6.3: (a): $V_{\rm lsr}$-Δv plots for SiO ($J = 2 - 1$) CH_3OH ($5_{-1,5} - 4_{0,4}$), and ^{13}CO (1-0) in IC 443 G I. (b): Those for all spectra. A size of the circle approximately represents the intensity. The vertical dotted line at $V_{\rm lsr}$ = -4 km s^{-1} shows the systemic velocity of the IC 443 G I cloud. The two strong lines in the upper left corner of the right panel are HCO^+ and HCN, which are broad due to the saturation effect.

km s^{-1} and Δv = 11.7±1.2 km s^{-1}. In contrast, the ^{13}CO (J =1−0) line is mainly emitted from the quiescent ambient gas, and hence, the peak velocity and the line width ($V_{\rm lsr}$ = -4.2±0.1 km s^{-1}, Δv = 3.7±0.2) are much different from those of the SiO and CH_3OH lines. This feature can also be seen in the $C^{18}O$ (J = 1−0) line. In fact, the $V_{\rm lsr}$ values of the ^{13}CO (J = 1−0) and $C^{18}O$ (J = 1−0) are -4.2 and -4.4 km s^{-1}, respectively, which are close to the systemic velocity ($\sim$ -4 km s^{-1}). If the line profile reflects the spatial distribution of molecule as seen in the above three molecules, the line width will systematically decrease as the peak velocity becomes closer to the systemic value. The $V_{\rm lsr}$-Δv plot for all the detected lines shows such a trend, as shown in Fig. 6.3(b), although the correlation is not tight. In the following subsections, we will discuss the $V_{\rm lsr}$-Δv plot for each class of molecules.

CH_3OH

Figures 6.4(a) presents the $V_{\rm lsr}$-Δv diagrams of CH_3OH. As mentioned above, the CH_3OH lines have higher $V_{\rm lsr}$ and narrower Δv than the SiO (J = 2−1) line (Fig. 6.4(a)), although the plots are scattered. The higher excitation lines tend to have lower $V_{\rm lsr}$ values and wider line widths. The averaged position in the diagram is ($V_{\rm lsr}$, Δv) = (-5.4 km s^{-1}, 10.45 km s^{-1}).

Sulfur-containing Molecules

Figures 6.4(e) and (f) are the $V_{\rm lsr}$-Δv diagrams for CS and its isotopomers, and SO and its isotopomer, respectively, detected in IC 443 G I. The averaged positions for these molecules in the diagram are also shifted toward the lower-right direction in comparison with that of SiO (J = 2−1) in spite of a large scatter. The difference of the averaged positions in the $V_{\rm lsr}$-Δv diagram reflects the difference of the spatial distributions between these sulfur containing molecules and SiO. As discussed in the L1157 B1 case (Section 3.4.2), these sulfur-containing molecules are thought to be produced by the gas-phase reactions in the high temperature gas from H_2S evaporated from grain mantles (Charnley 1997), whereas SiO is produced through the disruption of the silicate grain. Hence, the averaged positions in their $V_{\rm lsr}$-Δv diagrams

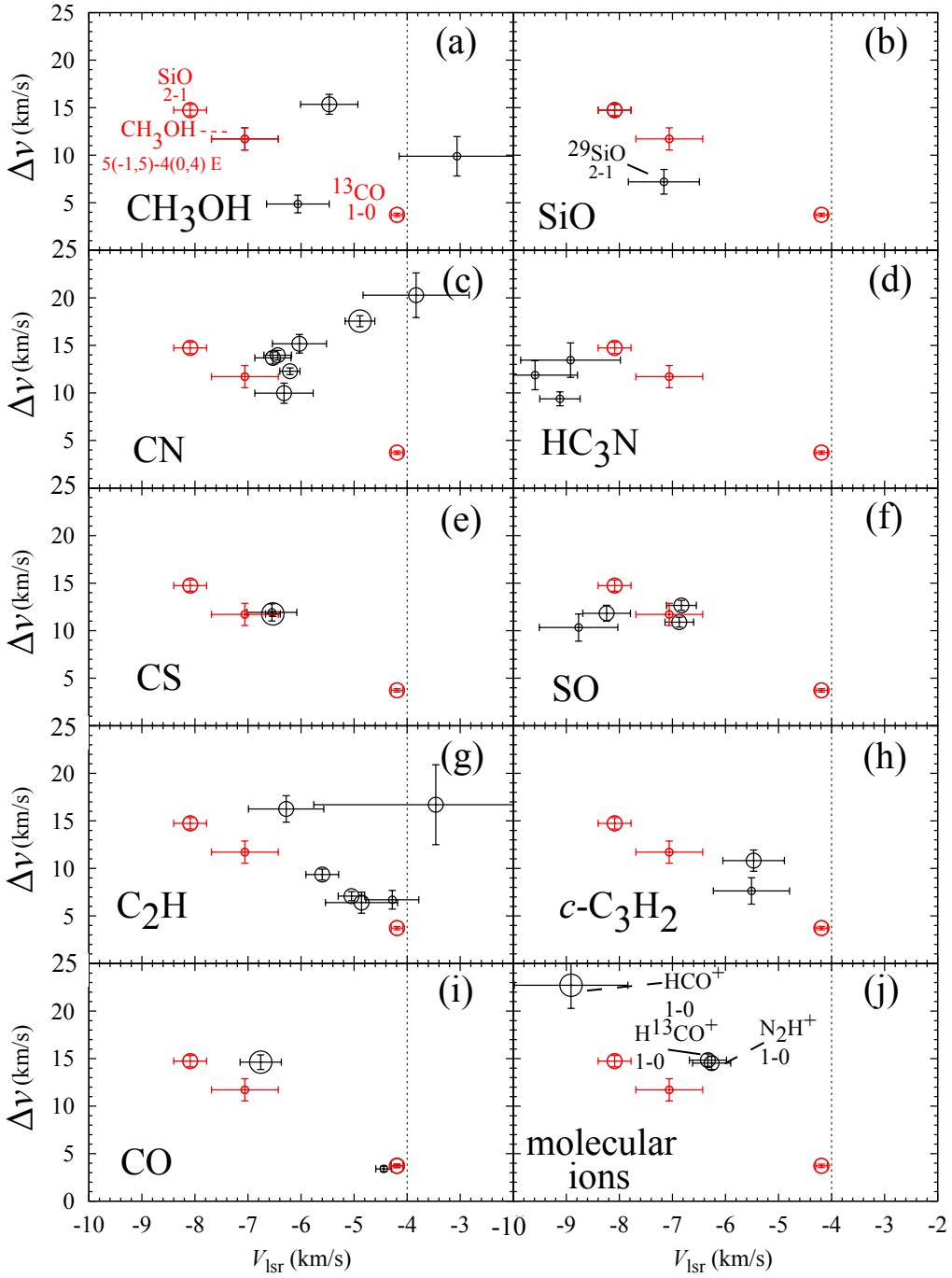

Figure 6.4: $V_{\rm lsr}$-Δv diagrams for various molecules. See Figure 6.3(b) and its caption for the size of the circle. The vertical dotted lines at $V_{\rm lsr}$ = -4 km s^{-1} show the systemic velocity of the IC 443 G I cloud.

are expected to be similar to each other. The diagrams of CS, SO, and their isotopomers are consistent with expectation. It should be emphasized that the position of the sulfur-bearing molecules in the $V_{\rm lsr}$-Δv diagram are similar to that for L1157 B1.

Carbon-chain Molecules

Figures 6.4(g) and (h) are the $V_{\rm lsr}$-Δv diagrams of C_2H and c-C_3H_2, respectively. As in the case of CH_3OH and the sulfur-containing molecules, the averaged positions in the $V_{\rm lsr}$-Δv diagrams for these carbon-chain molecules are shifted toward the lower-right direction in comparison with that of the SiO ($J = 2 - 1$) line. This trend is the same as in L1157 B1. Namely, they have higher peak velocities and narrower line widths than the SiO ($J = 2 - 1$) line. The averaged line widths are from 9 to 10 km s^{-1}. This feature confirms that the lines of carbon-chain molecules mainly come from the shocked regions. It seems likely that the production of these carbon-chain molecules is triggered by the grain mantle evaporation, not by the disruption of grain cores.

Other Molecules

Figures 6.4(c) and (d) are the $V_{\rm lsr}$-Δv diagrams of CN and HC_3N. The average peak velocity of HC_3N lines is -9.2 km s^{-1}, which is slightly lower than that of SiO (-8.1 km s^{-1}), and hence, HC_3N may be produced in the extreme shock in IC 443 G I. This is in great contrast to the behavior of HC_3N in L1157 B1. Figures 3.7(i) and (j) are the $V_{\rm lsr}$-Δv diagrams of CO with its isotopomers and molecular ions, respectively. The ^{12}CO line shows an exceptionally lower peak velocity and broader line width than the other CO isotopomers, because it well traces the outflow and the shocked region due to its high optical depth. The narrow component tends to be saturated, and hence, $V_{\rm lsr}$ tends to shift to the bluer velocity with a broader line width. On the other hand, the rare CO isotopomers mainly trace the ambient gas. Although a similar situation was seen for the molecular ions (HCO^+ and $H^{13}CO^+$) in L1157 B1, the positions of HCO^+ and $H^{13}CO^+$ in the $V_{\rm lsr}$-Δv diagram are (-8.9 km s^{-1}, 22.7 km s^{-1}) and (-6.3 km s^{-1}, 14.8 km s^{-1}), respectively, for IC 443 G I. Hence, both isotopomers of HCO^+ seem to reside in the shocked region. The $V_{\rm lsr}$-Δv diagram of the N_2H^+ line (-6.3 km s^{-1}, 14.5 km s^{-1}) also indicates that this ion exists in the shocked region. . This result is evidently different from that in L1157 B1, where N_2H seems to mainly exist in the ambient gas.

The difference of the line profiles may reflect different distributions of molecules in the shock. It is eventually related to the production mechanism of each molecule. However, the detailed distribution needs to be investigated by interferometric observations.

6.4.2 Comparison of Molecular Abundances with Dark Cloud

We calculated the column densities of detected molecules with the RADEX code except $C^{34}S$, $H^{13}CO^+$, $C^{18}O$, and C_2H, for which the collisional data were unavailable and we employed the LTE approximation (Table 6.3). Referring to the results of LVG calculation by van Dishoeck et al. (1993), we adapted the kinetic temperature $T_{\rm kin}$ = 100 K, the H_2 density = 1×10^6cm^{-3} Assuming the $N({\rm CO})/N({\rm H_2})$ ratio $\sim 10^{-4}$, we also calculated the abundance ratios to H_2, and compared them with those obtained toward a dark cloud, TMC-1.

van Dishoeck et al. (1993) could not detect CH_3OH in IC 443, and obtained an upper limit of the abundance ratio of 1×10^{-10}. However we obtained the abundance ratio of 2.8×10^{-8}. This value is higher than that in TMC-1 by an order of magnitude, though the abundance ratio is

lower than that in L1157 B1 ($\sim 10^{-6}$). It seems that the CH_3OH abundance is enhanced in the shocked region of IC 443 G I to some extent. Non-detection of CH_3OH by van Dishoeck et al. (1993) seems to be due to insufficient excitation of the CH_3OH lines in the submillimeter wave region. Hence, the millimeter wave spectral line survey is essential for chemical characterization.

The fractional abundance of HC_3N relative to H_2 is evaluated to be 3×10^{-10}. This is lower than 6×10^{-9} in TMC-1. This result indicates that HC_3N is not so efficiently produced in IC 443 G I. In the Section 6.4.1, we saw the $V_{\rm lsr}$ values of HC_3N lines are comparatively low ($\sim$ -9 km s^{-1} in average). These results may pose the possibility that HC_3N is produced in the extreme shock because of the high peak velocities of detected lines, although its chemical process is puzzling.

The abundance ratio of C_2H in IC 443 G I is similar to that in TMC-1, which are 4.5×10^{-8} and 5×10^{-8}, respectively. This molecule is often considered as a photodissociation product. However, we detected C_2H with the similar abundance in L1157 B1. It seems that the condition for the C_2H production does not so much depend on the pre-shocked condition. It may be produced in the shock.

The abundance ratio of CS is 2×10^{-8} in IC 443 G I while it is 1×10^{-8} in TMC-1. The SO abundance in IC 443 G I is 2×10^{-8}, which is slightly higher than that in TMC-1 (5×10^{-9}). These results may suggest that SO and CS abundances are enhanced in the shocked region compared with dark clouds.

Molecules	N (cm^{-2})	$N(X)/N(H_2)$	$N(X)_{TMC-1}/N(H_2)_{TMC-1}$
CH_3OH	2.8×10^{14}	2.8×10^{-8}	2×10^{-9}
HCN	1×10^{14}	1×10^{-8}	2×10^{-8}
$H^{13}CN$	6×10^{12}	6×10^{-10}	-
$HC^{15}N$	9×10^{11}	9×10^{-11}	-
HNC	2×10^{13}	2×10^{-9}	2×10^{-8}
HNCO	$< 3\times10^{12}$	$< 3\times10^{-10}$	2×10^{-8}
HC_3N	3×10^{12}	3×10^{-10}	6×10^{-9}
CH_3CN	$< 8\times10^{11}$	$< 8\times10^{-11}$	1×10^{-9}
CS	2×10^{14}	2×10^{-8}	1×10^{-8}
$C^{34}S$	$(4.9\pm1.3)\times10^{12*}$	4.9×10^{-10}	-
OCS	$< 1\times10^{14}$	$< 1\times10^{-8}$	-
SO	2×10^{14}	2×10^{-8}	5×10^{-9}
SO_2	$2\times10^{13\#}$	2×10^{-9}	1×10^{-9}
H_2CS	$< 4\times10^{12}$	$< 4\times10^{-10}$	$< 3\times10^{-9}$
HCO^+	3×10^{14}	3×10^{-8}	8×10^{-9}
$H^{13}CO^+$	$(5.4\pm1.2)\times10^{12*}$	5.4×10^{-10}	2×10^{-10}
N_2H^+	5×10^{12}	5×10^{-10}	5×10^{-8}
SiO	3×10^{13}	3×10^{-9}	$< 2\times10^{-12}$
^{29}SiO	1×10^{12}	1×10^{-10}	-
CO	1×10^{18}	1×10^{-4} (assumed)	8×10^{-5}
^{13}CO	5×10^{16}	5×10^{-6}	-
$C^{18}O$	$(1.0\pm0.2)\times10^{15*}$	1×10^{-7}	-
C_2H	$(4.5\pm1.4)\times10^{14*}$	4.5×10^{-8}	5×10^{-8}
c-C_3H_2	8×10^{12}	8×10^{-10}	1×10^{-8}
CN	5×10^{14}	5×10^{-8}	-

*derived from LTE approximation

#tentative detection

Table 6.3: Column Densities Calculated by RADEX.

Chapter 7

Classification of Shock Chemistry

7.1 Summary of the Three Shocked Regions

In preceding chapters, we described the characteristics of chemical composition in L1157 B1, L1448 B1 and R1, and IC 443 G I. In this chapter, we will focus on the difference among these shocked regions. Although these three sources are shocked regions, their origins are different from one another. L1157 B1 is the shocked region caused by an impact of the molecular outflow on the ambient cloud. L1448 B1 is also a shocked region in the star forming region, but it is an internal shock within the high velocity jet. On the other hand, IC 443 is a molecular cloud clump formed by the shock compression by the supernova explosion. Hence, the physical conditions of these three regions are different, as summarized in Table 7.1

The spectral line survey in the 3 mm band was conducted for these three regions with the Nobeyama 45 m telescope. We detected 29, 3, and 14 molecular species from L1157 B1, L1448 B1, and IC 443 G I, respectively. Apparently, chemical richness is different from source to source. First, we discuss the chemical compositions of L1157 B1, which shows the richest chemistry among the three sources.

	L1157 B1	L1448 B1	IC 443 G I
Shock Origin	Outflow	High Velocity Jet	Supernova
Apparent Shock Velocity	10 km s^{-1}	40 km s^{-1}	15 km s^{-1}
Average Temperature	100 K	300 K	100 K
Average Density	2×10^5 cm^{-3}	8×10^5 cm^{-3}	1×10^6 cm^{-3}
Detected Species	29	3 (EHV)	14
Chemistry	Rich	Poor	Moderate

Table 7.1: Shock Natures of Three Regions.

7.2 Comparison with the Chemical Model

First, we compare the measured chemical compositions in L1157 B1 with the chemical model, which was conducted by Nomura (private communication). This chemical model simulation assumes the pre-shocked gas density of 10^5 cm^{-3}, a temperature of 10 K, and a shock velocity of 20 km s^{-1}, where the shock model by Jiménez-Serra et al. (2008) is used. As for the reaction

rates, the UMIST database for astrochemistry is employed (Nomura and Millar 2009). The initial The initial condition of the chemical compositions is assumed to be those of quiescent molecular clouds at 10 K, where CH_4, CH_3OH, $HCOOCH_3$, and C_2H_5OH are in grain mantle. The result is indicated in Figure 7.1. In all the panels, the vertical axis indicates the abundance ratio relative to H_2, and the horizontal the time elapsed since the shock.

Carbon-chain Molecules

The upper left panel of Figure 7.1 shows the gas-phase production of carbon-chain molecules. We assume that CH_4 and C_2H_2 originate from the grain mantle. According to our observational results, the abundances of C_2H, HC_3N, and CH_3CCH decrease in this order. This order is qualitatively reproduced in the simulation around $t = 10^4$ yr, which corresponds to the dynamical timescale of the outflow from L1157 mm. However, these abundances are lower by two or three orders of magnitude than observed values of C_2H and HC_3N (Figure 7.2). Hence, production of the carbon-chain is not well reproduced quantitatively. In Chapter 3, it is suggested that carbon-chain production triggered by the evaporation of CH_4 (WCCC effect; Sakai et al. 2008, 2009, 2010) may also work in shocked regions. This mechanism is already taken into the model, but the above comparison suggest that it is insufficient to explain the observed abundance of C_2H and HC_3N. Hence, it seems necessary to consider that the carbon-chain molecules reside on grain mantle and are liberated into the gas-phase by shocks. The C_2H abundance relative to H_2 toward the protostar position of L1157 is 3×10^{-9} (Bachiller et al. 1997), which is lower by about two order of magnitude than that toward the B1 position (1.2×10^{-7}). Similarly, the HC_3N abundance toward the protostar position is 4.6×10^{-10}, whereas that toward the B1 position is 5×10^{-9}. Again, the shocked region shows the higher abundance. This clearly indicates necessity of carbon-chain production mechanism specific to shocked regions, which should be production on grain mantle. Although the carbon-chain production on grain mantle has not been considered seriously, the present result suggests that it should be explored theoretically and observationally.

Sulfur-bearing Molecules

The upper right panel of Figure 7.1 indicates temporal abundance variations of sulfur-bearing molecules after the shock. Except H_sS, OCS, and S, almost all molecules are assumed to be produced through gas-phase reactions. Around $t = 10^4$ yr, the abundances of OCS, SO_2, SO, H_2CS, NS, and HCS^+ decrease in this order in the model. However, the observed results are much different. The order is CS, SO_2, SO, H_2CS, OCS, NS, and HCS^+. As indicated in Table 3.4, CS, SO_2, SO, and H_2CS have similar column densities. The calculated abundances of CS and SO in Figure 7.1 are around 10^{-10} at $t = 10^4$ yr, and they are too lower than the observational results (Figure 7.2). This result posts the question of the gas-phase production of sulfur-bearing molecules.

Organic Molecules

For organic molecules, we present two results with different initial conditions. The lower left panel in Figure 7.1 shows temporal abundance variations of HCOOH, CH_3OH, C_2H_5OH, H_2CCO, CH_3CHO, $HCOOCH_3$, and $(CH_3)_2O$, where CH_4, HCOOH, CH_3OH, and C_2H_5OH are assumed to originate from the grain mantle, while H_2CCO, CH_3CHO, $HCOOCH_3$, and $(CH_3)_2O$ abundances are produced in the gas-phase after evaporation of parent molecules (CH_3OH,

HCOOH, C_2H_5OH). In the lower right panel, CH_3CHO is also assumed to originate from the grain mantle. Although the CH_3CHO abundance ratio of $\sim 10^{-8}$ observed in L1157 B1 can be reproduced in both models, $HCOOCH_3$ abundance ratio of $\sim 10^{-8}$ can be attainable only by the grain surface production of $HCOOCH_3$. We detected H_2CCO with the abundance ratio of $\sim 10^{-9}$ in L1157 B1. Since our gas-phase production model for this molecule indicates the abundance ratio lower than 10^{-10}, it may be difficult to produce H_2COO in the gas-phase process after the shock. This molecule may also be produced mainly on the grain surface, and evaporated by the shock. Finally, since the upper limit to the abundance ratio of $(CH_3)_2O$ obtained from our observation is $\sim 10^{-9}$, it is difficult to confirm whether this molecule originates from the gas-phase, or the grain-surface reaction. In our simulation, the abundance ratio of this molecule does not exceed 10^{-10} in the gas-phase reaction.

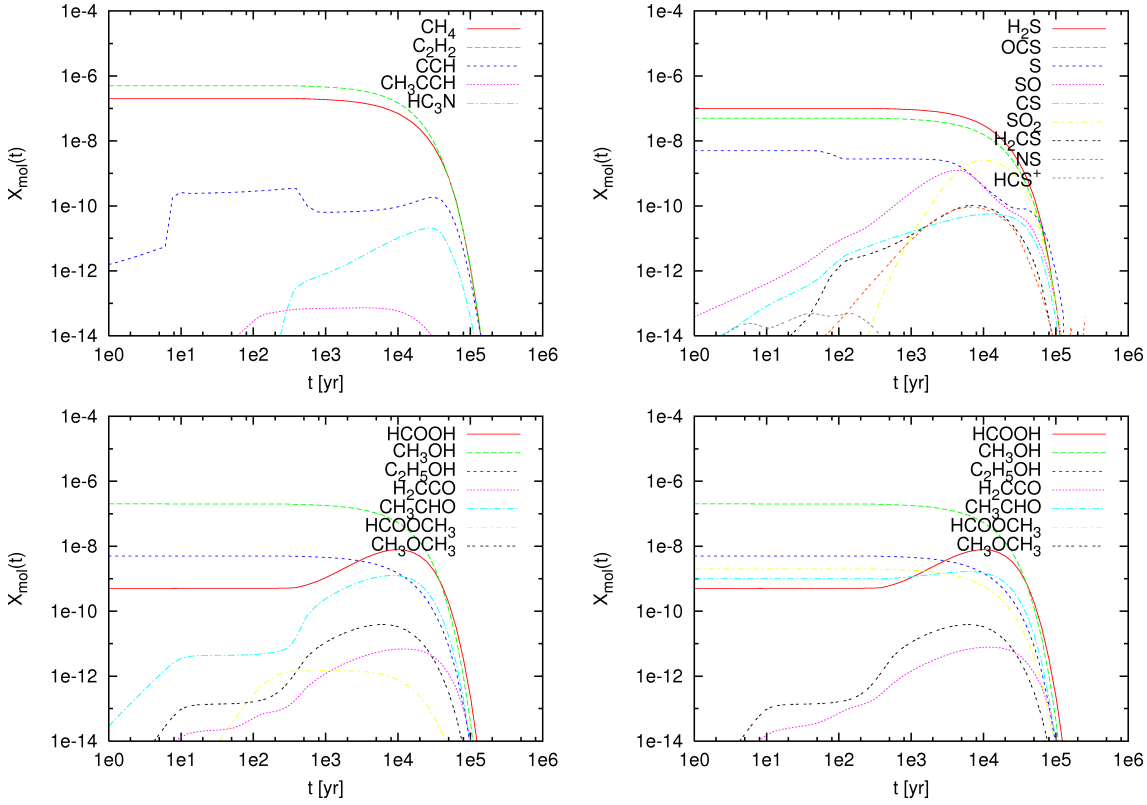

Figure 7.1: The chemical model simulation. The temporal abundance variations of various molecules are shown. The time is measured from the time when the shock occurred (Nomura, private communication).

As seen above, the present chemical model does not fully account for the observed abundances in L1157 B1. There are two reasons for this. First, the model itself is based on many assumptions. For instance, many reaction rate coefficients of the gas-phase reactions still have large uncertainties in spite of many efforts. Furthermore, the initial abundance of grain mantles is completely unknown, and we have to assume it arbitrarily. This seriously affects the molecular synthesis after the shock. Second, the abundances obtained from the observations have their own limitations. They are 'averaged' abundances over the telescope beam size, and hence, small-scale structures in the shock are not considered at all. Chemical differentiation is expected within

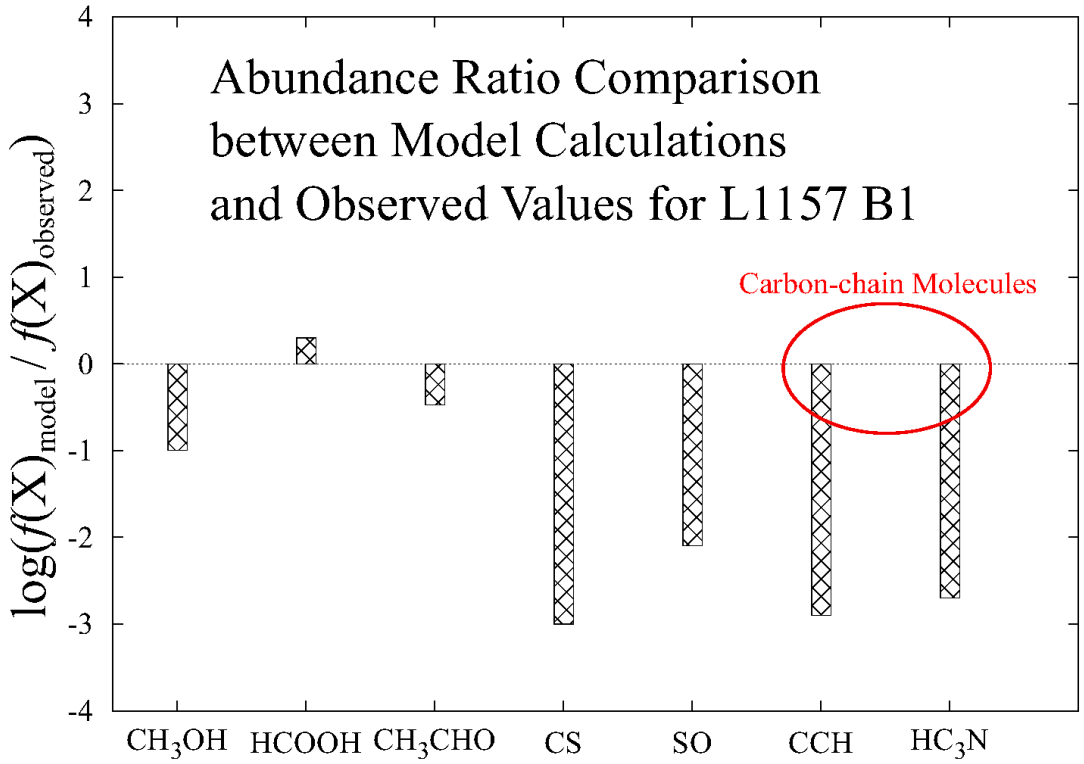

Figure 7.2: The differences between observed and calculated abundaces.

the shock, as partly inferred from the $V_{\rm lsr}$-Δv diagram, while the abundances reported in the previous chapters do not include this effect. Apparently, more detailed physical and chemical modeling is necessary for the shocked region. We can stress that our observed abundances in L1157 B1 can be a good starting point for such efforts.

7.3 Grain Mantle Compositions: A Key to Chemical Difference among Shocked Regions

Here, we can suggest the formation process of molecules on the basis of our observational results (i.e. abundances and $V_{\rm lsr}$-Δv diagram). For simplicity, we classify molecules into four categories: (1) molecules which are produced by disruption of grain cores; (2) molecules which are directly supplied from grain mantle; (3) molecules which are formed by the gas-phase reactions triggered by evaporation of parent molecules from grain mantle; (4) molecules which were already in the ambient cloud (pre-shocked cloud). They are shown in Table 7.3. Note that the classification is sometimes arbitrary, as indicated by '?' marks. Thus, the most important process in the shock chemistry is evaporation of molecules from grain mantle. In other words, the chemical composition of grain mantle mostly governs the gas-phase chemical composition. The chemical composition of grain mantle depends on the physical and chemical state of the pre-shocked gas. For instance, a dense starless core in a molecular cloud has chemically rich grain mantle around grain cores, because atoms and molecules are depleted onto dust grains to proceed a variety of grain-surface reactions. This is accelerated for denser clouds. In contrast, a

diffuse cloud should have a relatively poor grain mantle. The first reason is that the collisional molecules are lower than in molecular clouds because of lower gas density. The second reason is high desorption rate of atoms and molecules due to high temperature (30-100 K). For instance, CO is not well absorbed at this temperature range, and hence, the formation of CH_3OH on grain mantle will not be efficient. From this consideration, the different chemical composition of the different shocked regions mainly originate from the grain mantle compositions, which are determined by the pre-shocked physical conditions. We will discuss the L1448 B1/R1 and IC 443 G I results from this viewpoint.

7.4 Comparison of L1157 B1 with IC 443 G I and L1448 B1/R1

According to van Dishoeck et al. (1993) the pre-shocked gas in IC443 in a photodissociation region (PDR), which has a typical visual extinction A_V of ~ 3, and a gas density of $N(H_2) \sim 10^4$ cm^{-3}. In such a diffuse cloud, the interstellar UV radiation plays a major role in heating. Following the ultraviolet ($h\nu$) absorption by dust grains, a photoelectron is ejected with kinetic energy of $h\nu - W$, where W denotes the work function for the dust grain. The photoelectron collides with H_2 molecules or H atoms, transferring a part of its kinetic energy to the collision partners. Along with the cooling by spectral line emissions of fine structure transitions C^+ and O and CO rotational transitions, the gas kinetic temperature of a diffuse cloud becomes 20 - 100 K. The dust temperature is generally lower than the gas temperature to some degree. The relatively high temperature hinders processes of the grain mantle chemistry. CH_3OH is not produced efficiently in PDRs for lack of enough CO on dust grains. Therefore, other organic molecules produced from CO are not abundant on dust grains in PDRs. When a PDR cloud is affected by the shock, the temperature is temporarily raised, and the organic molecules formed on dust grains are liberated into the gas-phase, as in the case of L1157 B1. However, organic molecules are poor on dust grains and their sublimation does not enhance the gas-phase abundances very much. This trend can actually be seen in the composition of the abundances in the IC 443 region with those in L1157 B1 (Table 7.2 and Figure 7.4). In IC 443 G I, the CH_3OH density is indeed lower by an order of magnitude than that in L1157 B1. This is not due to a difference of the strength of the shock. The abundance ratios are almost independent on the desorption energy, as shown in Figure 7.3. This means that the all molecules contained in grain mantle are released into the gas-phase, regardless of the strength of the shock. Hence, the abundance difference between the two sources represents the difference of grain mantle compositions. As mentioned above, L1157 B1 shows the many lines of complex organic molecules such as HCOOH, $HCOOCH_3$, and CH_3CHO. These observational results also seem consistent with above consideration.

Absence of CH_3OH in L1448 B1/R1 can be understood in the same way. The shock in L1448 B1/R1 is that caused in a high velocity jet just launched from the protostar. Hence, the gas and grains have passed through the vicinity of the protostar, and have experienced a temporary high temperature conditions. It seems likely that most of grain mantle has already evaporated in this process. Silicon and sulfur are much more non-volatile and can survive the high temperature environment around a protostar. They are liberated into the gas-phase in the shock in the jet. In other words, dust grains are covered with little grain mantle.

Molecules	$N(\mathrm{X})_{\mathrm{IC443GI}}/N(\mathrm{H_2})_{\mathrm{IC443GI}}$	$N(\mathrm{X})_{\mathrm{L1157B1}}/N(\mathrm{H_2})_{\mathrm{L1157B1}}$
CH_3OH	2.8×10^{-8}	5×10^{-7}
HCN	1×10^{-8}	1×10^{-7}
$H^{13}CN$	6×10^{-10}	2×10^{-9}
$HC^{15}N$	6×10^{-10}	3.5×10^{-10}
HNC	2×10^{-9}	4.5×10^{-9}
HNCO	$< 3\times10^{-10}$	1×10^{-8}
HC_3N	3×10^{-10}	5×10^{-9}
CH_3CN	$< 8\times10^{-11}$	3.5×10^{-9}
CS	2×10^{-8}	5×10^{-8}
$C^{34}S$	4.9×10^{-10}	$6\times10^{-9*}$
OCS	$< 1\times10^{-8}$	$4\times10^{-8*}$
SO	2×10^{-8}	5×10^{-8}
SO_2	$2\times10^{-9\#}$	4×10^{-8}
H_2CS	$< 4\times10^{-10}$	1×10^{-8}
HCO^+	3×10^{-8}	1×10^{-8}
$H^{13}CO^+$	$5.4\times10^{-10*}$	$2.2\times10^{-10*}$
N_2H^+	5×10^{-10}	1×10^{-10}
SiO	3×10^{-9}	2×10^{-8}
^{29}SiO	1×10^{-10}	2×10^{-9}
CO	1×10^{-4}	1×10^{-4}
^{13}CO	5×10^{-6}	1×10^{-5}
$C^{18}O$	$1\times10^{-7*}$	$8\times10^{-7*}$
C_2H	$4.5\times10^{-8*}$	$1.2\times10^{-7*}$
c-C_3H_2	8×10^{-10}	1×10^{-9}
CN	5×10^{-8}	5×10^{-8}

*derived from LTE approximation

#tentative detection

Table 7.2: Column Density Ratios to H_2 Density Calculated by RADEX.

The Silicate Grain Disruption				
SiO				
Grain Mantle Production and Evaporation by Shock				
CH_3OH	HCOOH	$HCOOCH_3$	HNCO	NH_2CHO
CS	C_2H_5CN	HCN ?	CH_3CN ?	
Gas-phase Production				
CH_3CHO	SO	SO_2	PN	CN
C_2H ?	CCS ?	CH_3CN ?	c-C_3H_2 ?	CS ?
H_2CS				
Ambient Gas				
HCO^+	$H^{13}CO^+$	N_2H^+		

Table 7.3: The classification of production processes of molecules detected in shocked region.

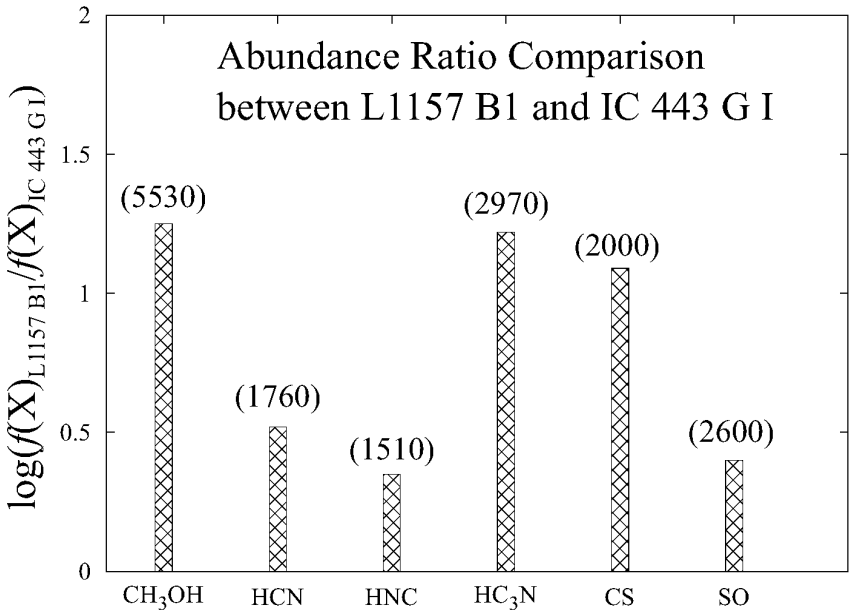

Figure 7.3: Comparison of abundance ratios between L1157 B1 and IC 443 G I. The numbers in parentheses represent the desorption energy in K.

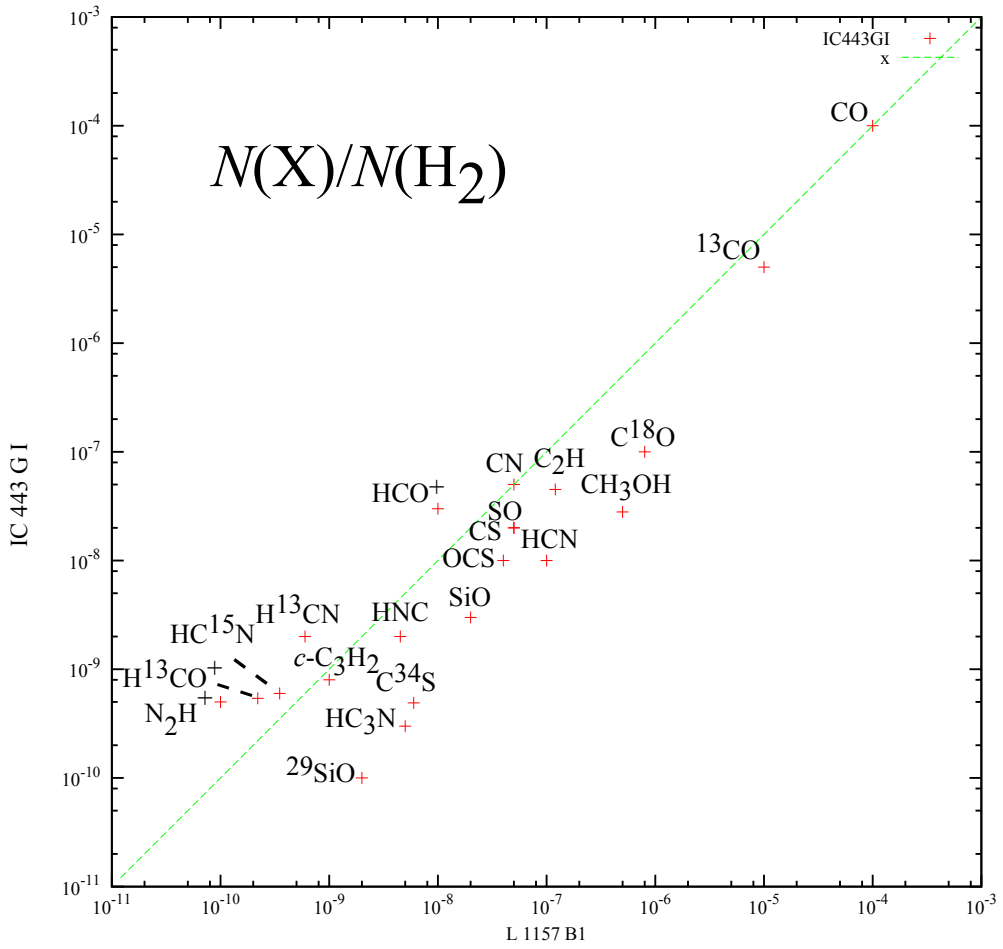

Figure 7.4: Comparison of abundance ratios between L1157 B1 and IC 443 G I

Chapter 8

Conclusion

In this thesis, the unbiased spectral line surveys in the 3 mm wave band have been carried out with the Nobeyama 45 m telescope toward three shocked regions, L1157 B1, L1448 B1/R1, and IC443 GI, which have different origins of shocks. The spectral line survey in the 3 mm band is very useful to grasp chemical compositions of the sources, because rotational spectral lines of many fundamental molecules fall in this band. As the result, we delineated characteristic chemical compositions for these three sources.

L1157B1 is a shocked region formed by an impact of molecular outflows from the low-mass protostar on the ambient cloud. It is found to harbor very rich chemistry. Various saturated organic molecules, sulfur-bearing species, and carbon-chain molecules were detected in addition to the fundamental species such as CO, HCN, HCO^+, and their isotopic species. In particular, we first identified PN, NH_2CHO, and H_2CCO in this source. Rich chemical composition is thought to originate from evaporation of grain mantle in shocked region.

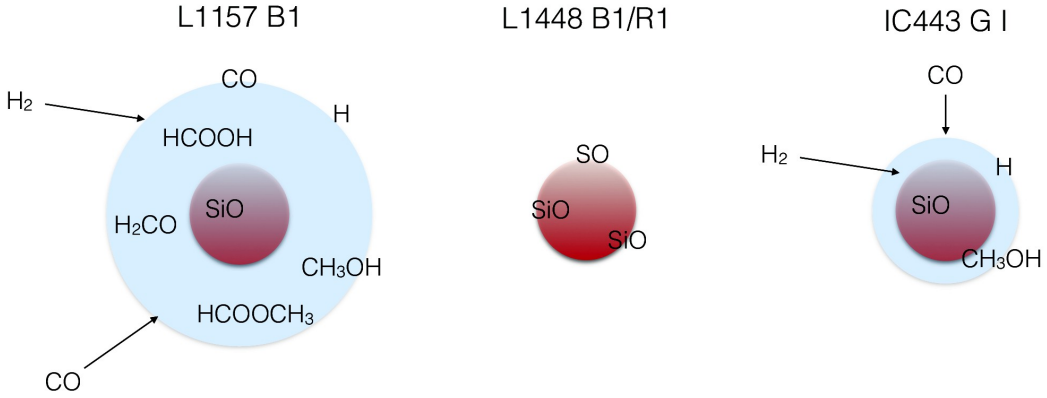

Figure 8.1: Schematic illustration of grain mantle for the three observed sources.

In contrast, L1448 B1/R1 is found to have rather poor chemistry. Only SiO and SO were detected in our observations. Spectral lines of CH_3OH, which is regarded as a shock tracer molecule, have not been observed. This shocked region is formed in the high-velocity jet, and hence, grain mantle surrounding the dust grain is already lost in the pre-shocked gas, because it has already experienced the warm condition around the protostar. This seems to be the main

reason why the CH_3OH and other organic molecules are deficient in this source.

IC443 GI is a shocked region formed by the supernova expansion. This region is found to be chemically rich, but not as rich as L1157 B1. The CH_3OH lines are indeed very weak, and were detected for the first time in the present study. Since this region is formed by compression of a diffuse gas, the pre-shocked gas would be in a higher temperature condition than that for L1157 B1. For this reason, the grain mantle has not been grown up to harbor various organic molecules including CH_3OH.

From these results, the major conclusions are summarized as follows:

(1) The evaporation of grain mantle makes an essential contribution to the gas-phase chemical compositions of shocked regions.

(2) The chemical compositions of shocked regions strongly depend on the pre-shocked conditions, specifically the grain mantle compositions of the pre-shocked gas. The situations for the three sources are schematically illustrated in Figure 8.1.

(3) The chemical model of the shocked region is found to be still infancy. In particular, the production of carbon-chain molecules is not well implemented. Further improvement of the model as well as consideration of the physical structure of shock is indispensable.

These results mean that we can investigate the chemical compositions of grain mantle by observing the gas-phase chemical compositions of shocked regions. Although the chemical composition of grain mantle has been studied by infrared observations (Herbst and van Dishoeck 2009), identification of complex species is very difficult. The radio astronomical approach using shocked regions would open a new window in studying chemical composition of grain mantles. In addition, the present results indicate that it is very dangerous to judge the shock by a single shock tracer, because some shock tracers like CH_3OH do not always appear in all shocked regions. CH_3OH must be formed on dust grain before the shock, if it can be used as a shock tracer. Full chemical analyses by a spectral line survey, as done in the present thesis, are thus indispensable for chemical identification of shocks.

Acknowledgements

First, I am grateful to Professor Satoshi Yamamoto for his invaluable advice and collaboration. I am also grateful to the members of the line survey project, which was conducted as a legacy project of the Nobeyama 45 m telescope, who always give me very insightful advices. I thank the staff of NRO for their support. In particular, I thank Ryohei Kawabe, the ex-director of NRO, for his continuous encouragement and support to this project. I am grateful to Nario Kuno, the director of NRO, for his grate effort of the management. I would like to thank Shuro Takano, the science manager of NRO, for his persevering collaboration.

In the initial instruction of the Nobeyama 45 m telescope operation, I owe much to Nami Sakai, the assistant professor of the University of Tokyo, and Tomoya Hirota, the assistant professor at VERA. Nami Sakai also gives me incessant collaboration and advices. Mika Sugimura relayed me her great achievement of the initial result of the line survey in L1157 B1. Yoshimasa Watanabe, the assistant professor of the University of Tokyo, always helps me with his profound insight about the interstellar physics. I thank all student in Yamamoto Laboratory for their encouragements to me. Without them, I could not achieve this thesis.

References

[1] Abdo, A.A., et al., 2010, ApJ, 712, 459.

[2] Agúndez, M., Cernicharo, J., and Guélin, M., 2007, ApJ, 662, L91.

[3] Agúndez, M., Cernicharo, J., Pardo, J.R., Guélin, M., and Phillips, T. G., 2008, A&A, 485, L33.

[4] Allen, T.L., Goddard, J.D., and Schaefer III, H.F., 1980, J. Chem. Phys., 73, 3255.

[5] Arce, H.G., Santiago-Garcıa, J., Jørgensen, J.K., Tafalla, M., and Bachiller, R. 2008, ApJ, 681, L21.

[6] Avery, L.W., and Chiao, M., 1996, ApJ, 463, 642.

[7] Bachiller, R, Cernicharo, J., Martín-Pintado, J., Tafalla, M., and Lazareff, B., 1990, A&A, 231, 174.

[8] Bachiller, R., Liechti, S., Walmsley, C. M., and Colomer, F., 1995, A&A, 295, L51.

[9] Bachiller, R., Pérez Gutiérrez, M., 1997, ApJ, 487, L93.

[10] Bachiller, R., Pérez Gutiérrez, M., Kumar, M.S.N., and Tafalla, M., 2001, A&A, 372, 899.

[11] Beltrán, M.T., Cesaroni, R., Neri, R., Codella, C., Furuya, R.S., Testi, L., and Olmi, L., 2004, ApJ, 601, L187.

[12] Benedettini, M., Viti, S., Codella, C., Bachiller, R., Gueth, F., Beltrán, M.T., Dutrey, A., and Guilloteau, S., 2007, MNRAS, 381, 1127.

[13] Bisschop, S.E., Jørgensen, J.K., van Dishoeck, E.F., and de Wachter, E.B.M., 2007, A&A, 465, 913.

[14] Blake, G.A., Keene, J., and Phillips, T.G., 1985, ApJ, 295, 501.

[15] Blake, G.A., Sutton, E.C., Masson, C.R., and Phillips, T.G., 1987, ApJ, 315, 621.

[16] Blake, G.A., van Dishoeck, E.F., Jansen, D.J., Groesbeck, T.D., and Mundy, L.G., 1994, 428, 680.

[17] Bottinelli, S., et al., 2004, ApJ, 615, 345.

[18] Brouillet, N., et al., 2013, A&A, 550, A46.

[19] Caux, E., et al., 2011, A&A, 532, A23.

[20] Cazaux, S., Tielens, A.G.G.M., Ceccarelli, C., Castets, A., Wakelam, V., Caux., E., Parise, B., and Teyssier, D., 2003, ApJ, 593, L51.

[21] Cazolli, G., Cludi, L., and Puzzarini, C., 2006, J. Mol. Struct., 780-781, 260.

[22] Cernicharo, J., Guélin, M., and Kahane, C., 2000, A&AS, 142, 181.

[23] Charnley, S.B., and Tielens, A.G.G.M., 1992, ApJ, 399, L71.

[24] Charnley, S.B., and Millar, T.J., 1994, MNRAS, 270, 570.

[25] Charnley, S. B., 1997, ApJ, 481, 396.

[26] Chevalier, R.A., 1999, ApJ, 511, 798.

[27] Chin, Y.-N., Henkel, C., Whiteoak, J.B., Langer, N., and Churchwell, E.B., 1996, A&A, 305, 960.

[28] Churchwell, E., Walmsley, C.M., and Wood, D.O.S., 1992, A&A, 253, 541.

[29] Codella, C., Benedettini, M., Beltrán, M.T., Gueth, F., Viti, S., Bachiller, R., Tafalla, M., Cabrit, S., Fuente, A., and Lefloch, B., 2009, A&A, 507, L25.

[30] Davis, C.J., and Eislöffel, J., 1995, A&A, 300, 851.

[31] Fesen, R.A., and Kirshner, R.P., 1980, ApJ, 242, 1023.

[32] Frerking, M.A., Linke, R.A., and Thaddeus, P., 1979, ApJ, 234, L143.

[33] Garrod, R.T., and Herbst, E., 2006, A&A, 457, 927.

[34] Goldsmith, P.F., Krotkov, R., and Snell, R.L., 1983, ApJ, 274, 184.

[35] Gottlieb, C.A., 1973, "Molecules in the Galactic Environment", ed. M.A. Gordon and L.E. Snyder, Wiley, New York, p.181.

[36] Guélin, M., Cernicharo, J., Paubert, G., and Turner, B.E., 1990, A&A, 230, L9.

[37] Guilloteau, et al., 1992, A&A, 265, L49.

[38] Halfen, D.T., Clouthier, D.J., and Ziurys, L.M., 2008, ApJ, 677, L101.

[39] Halfen, D.T., Ziurys, L.M., Brünken, S., Gottlieb, C.A., McCarthy, M.C., and Thaddeus, P., 2009, ApJ, 702, L124.

[40] Herbst, E., 1978, ApJ, 222, 508.

[41] Herbst, E., and van Dishoeck, E.F., 2009, A&A , 47, 427.

[42] Hirano, N., and Taniguchi, Y., 2001, ApJ, 550, L219.

[43] Hirano, N., Ho, Paul P.T, Liu, S.-Y., Shang, H., Lee, C.-F., and Bourke, T.L., 2010, ApJ, 717, 58.

[44] Ikeda, M., Ohishi, M., Nummelin, A., Dickens, J.E., Bergman, P., Hjalmarson, Å., and Irvine, W.M., 2001, ApJ, 560, 792.

[45] Irvine, W.M. et al., 1988, ApJ, 334, L107.

[46] Jiménez-Serra, I., Caselli, P., Martín-Pintado, J., and Hartquist, T.W., 2008, A&A, 482, 549.

[47] Kahane, C., Ceccarelli, C., Faure, A., and Caux, E., 2013, ApJ, 763, L38.

[48] Kaifu, N, Ohishi, M., Kawaguchi, K., Saito, S., Yamamoto, S., Miyaji, T., Miyazawa, K., Ishikawa, S.I., Noumaru, C., Harasawa, S., Okuda, M., and Suzuki, H., 2004, PASJ, 56, 69.

[49] Kuan, Y.-J. et al., 2004, ApJ, 616, L27.

[50] Lefloch, B., Castets, A., Cernicharo, J., and Loinard, L., 1998, ApJ, 504, L109.

[51] Linsky, J. L., Brown, A., Gayley, K., Diplas, A., Savage, B., Ayres, T., Landsman, W., Shore, S.N., and Heap, S. R., 1993, ApJ, 402, 694.

[52] Liu, S.-Y., Girart, J.M., Remijan, A., Snyder, L.E., 2002, ApJ, 576, 255.

[53] Lovas, F.J., Bass, J.E., Dragoset, R.A., Olsen, K.J., 2009, NIST Recommended Rest Frequencies for Observed Interstellar Molecular Microwave Transitions - 2009 Revision (version 3.0) (`http://physics.nist.gov/restfreq`), National Institute of Standards and Technology, Gaithersburg, MD.

[54] Lucas, R., and Liszt, H., 1998, A&A, 337, 246.

[55] Martín, S., Mauersberger, R., Martín-Pintado, J., Henkel, C., García-Burillo, S., 2006, ApJS, 164, 450.

[56] Martín-Pintad, et al., 1992, A&A, 254, 315.

[57] Matthews, H.E., Friberg, P., and Irvine, W.M., 1985, ApJ, 290, 609.

[58] Matthews, H.E., Feldman, P.A., and Bernath, P. F., 1987, ApJ, 312, 358.

[59] Mikami, H, Umemoto, T., Yamamoto, S., and Saito, S., 1992, ApJ, 392, L87.

[60] Millar, T.J., Bennett, A., and Herbst, E., 1987, MNRAS, 229, 41.

[61] Muller, H.S.P., Schlöder, F., Stutzki, J., and Winnewisser, G., 2005, J. Mol. Struct., 742, 215.

[62] Nakajima, T., et al., 2008, PASJ, 60, 435.

[63] Nisini, B., Codella, C., Giannini, T., Santiago Garcia, J., Richer, J.S., Bachiller, R., and Tafalla, M., 2007, A&A, 462, 163.

[64] Nisini, B., et al., 2010, A&A, 518, L120.

[65] Nisini, B., Giannini, T., Neufeld, D.A., Yuan, Y., Antoniucci, S., Bergin, E.A., and Melnick, G.J., 2010, ApJ, 724, 69.

[66] Nomura, H., and Millar, T.J., 2009, in Potostellar Jets in Context, ed. K.Tsiganos et al., Springer, 593.

[67] Nummelin, A., et al., 1998, ApJ, 117., 427.

[68] Nummelin, A., et al., 2000, ApJ, 128., 213.

[69] Ohishi, M., Irvine, W.M., and Kaifu, N., 1992, in Astrochemistry of Cosmic Phenomena, ed. P.D.Singh (Dordrecht: Kluwer), 171.

[70] Parise, B., et al., 2002, A&A, 393, L49.

[71] Pickett, H.M., Poynter, R.L., Cohen, E.A., Delitsky, M.L., Pearson, J.C., and Muller, H.S.P., 1998, J. Quant. Spectrosc. &Rad. Transfer, 60, 883.

[72] Pineau des Forêts, G., Roueff, E., Schilke, P., and Flower, D.R., 1993, MNRAS, 262, 915.

[73] Plambeck, R.L., and Menten, K.M., 1990, ApJ, 364, 555.

[74] Quade, C.R. and Suenram, R.D., 1980, J. Chem. Phys. 73, 1127.

[75] Raymonda, J., and Klemperer, W., 1971, J. Chem. Phys., 55, 232.

[76] Reach, W.T., Rho, J., Jarret, T.H., and Lagage, P.-O., 2002, ApJ, 564, 302.

[77] Requena-Torres, M.A., Marcelino, N., Jiménez-Serra, I., Martín-Pintado, J, Martín, S., and Mauersberger, R., 2007, ApJ, 655, L37.

[78] Sakai, N., Sakai, T., and Yamamoto, S., 2006, PASJ, 58, L15.

[79] Sakai, N., Sakai, T., Hirota, T., and Yamamoto, S., 2008, ApJ, 672, 371.

[80] Sakai, N., Sakai, T., Hirota, T., Burton, M., and Yamamoto, S., 2009, ApJ, 697, 769.

[81] Sakai, N., Shiino, T., Hirota, T., Sakai, T., and Yamamoto, S., 2010, ApJ, 718, L49.

[82] Schilke, P., Groesbeck, T.D., Blake, G.A., and Phillips, T.G., 1997, ApJ, Suppl., 108, 301.

[83] Schilke, P., Benford, D.J., Hunter, T.R., Lis, D.C., and Phillips, T.G., 2001, ApJS, 132, 281.

[84] Sheffer, Y., et al., 2008, ApJ, 687, 1075.

[85] Sugimura, M., et al., 2011, PASJ, 63, 459.

[86] Suzuki, H., Yamamoto, S., Ohishi, M., Kaifu, N., Ishikawa, S., Hirahara, Y., and Takano, S., 1992, ApJ, 392, 551.

[87] Ohishi, M., Irvine, W.M., and Kaifu, N., 1992, in The Astrochemistry of Cosmic Phonomena, IAU Symposium 150, ed. P.D.Singh (Kluwer, Dordrecht),p.171.

[88] Schilke, P., Groesbeck, T.D., Blake, G.A., and Phillips, T.G., 1995, ApJ., 108, 301.

[89] Schilke, P., Benford., D.J., Hunter, T.R., Lis, D.C., and Phillips, T.G., 2001, ApJ, 132, 281.

[90] Sutton, E.C., Peng, R., Danchi., W.C., Jaminet., P.A., Sandell, G., and Russell., A.P.G., 1995, ApJ., 97, 455.

[91] Tafalla, M., Santiag-García, J., Hacar, A., and Bachiller, R., 2010, A&A, 522, A91.

[92] Tenenbaum, E. D., Woolf, N. J., and Ziurys, L. M., 2007, ApJ, 666, L29.

[93] Tenenbaum, E.D., and Ziurys, L.M., 2008, ApJ, 680, L121.

[94] Tercero, B., Cernicharo, J., Pardo, J.R., 2005, In Astrochemistry: Recent Success and Current Challenges, IAU Symp., 231, Poster 57, ttp://asilomar.caltec.edu

[95] Thorne, L.R., Anicich, V.G., Prasad, S.S., Huntress, W.T., Jr., 1984, ApJ, 280, 139.

[96] Tielens, A.G.G.M., and Hegen, W., 1982, A&A, 114, 245.

[97] Turner, B.E., and Bally, J., 1987, ApJ, 321, L75.

[98] Turner, B.E., Tsuji, T., Bally, J., Guelin, M., and Cernicharo, J., 1990, ApJ, 365, 569.

[99] Umemoto, T., Iwata, T., Fukui, Y., Mikami, H., Yamamoto, S., Kameya, O., and Hirano, N., 1992, ApJ, 392, L83.

[100] Umemoto, T., Mikami, H., Yamamoto, S., and Hirano, N., 1999, ApJ, 525, L105.

[101] van der Tak, F.F.S., Black, J.H., Schöier, F.L., Jansen, D.J., and van Dishoeck, E.F., 2007, A&A, 468, 627.

[102] van Dishoeck, E.F., Jansen, D.J., and Phillips, T.G., 1993, A&A, 279, 541.

[103] van Dishoeck, E.F., Blake, G.A., Jansen, D.J., and Groesbeck, T.D., 1995, ApJ, 447, 760.

[104] Viotti, R., 1969, Mem. Soc. Astron. Ital., 40, 75.

[105] Wang, Z., and Scoville, N.Z., 1992, ApJ, 386, 158.

[106] Wannier, P.G., and Linke, R.A., 1978, ApJ, 226, 817.

[107] Yamaguchi, T., et al., 2011, PASJ, 63, L37.

[108] Yamaguchi, T., et al., 2012, PASJ, 64, 105.

[109] Ziurys, L.M., 1987, ApJ, 321, L81.

[110] Ziurys, L.M., Snell, R.L., and Dickman, R.L., 1989, ApJ, 341, 857.

Appendix A

Spectrum of L1157 B1

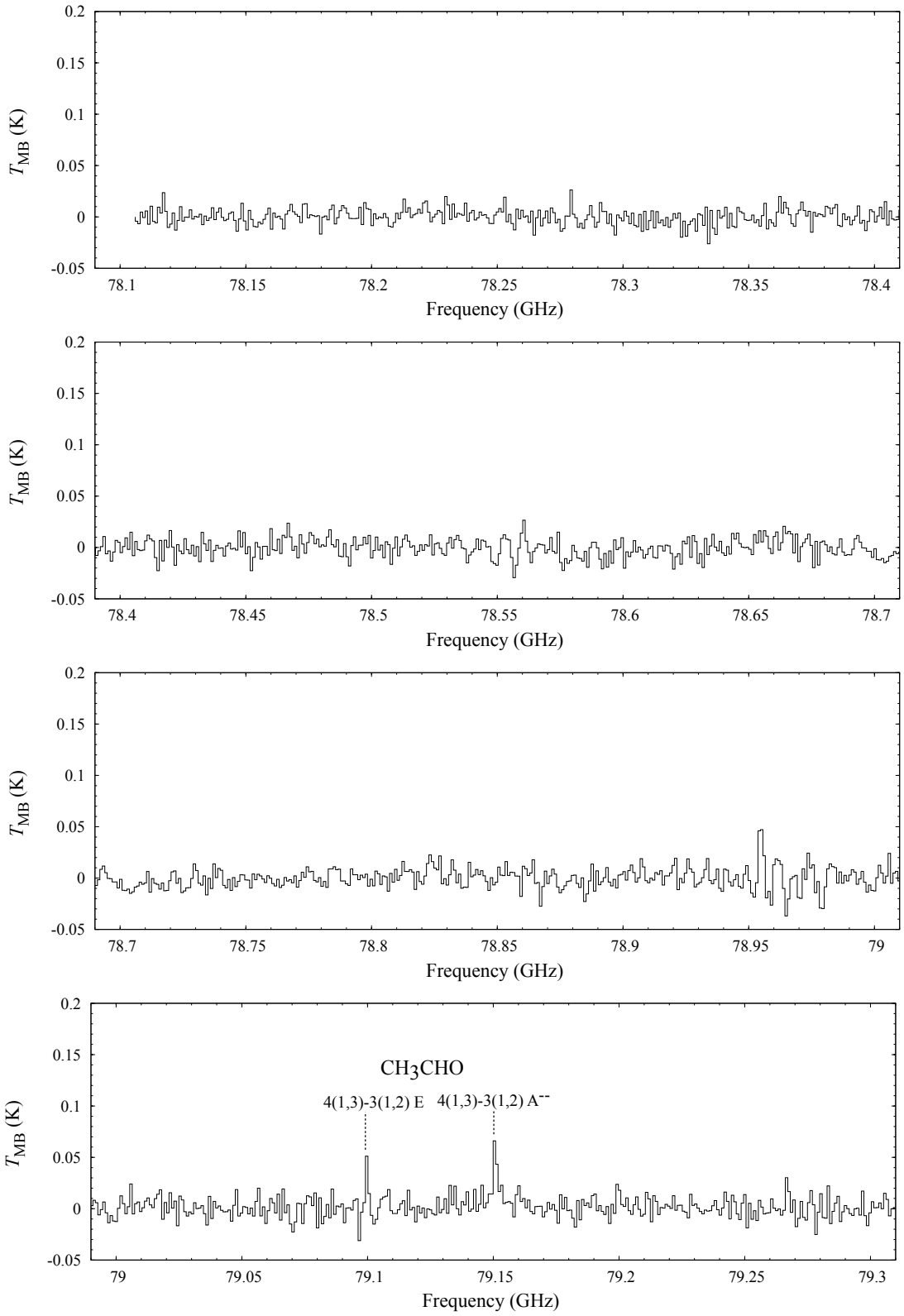

Figure A.1: Spectrum of L1157 B1

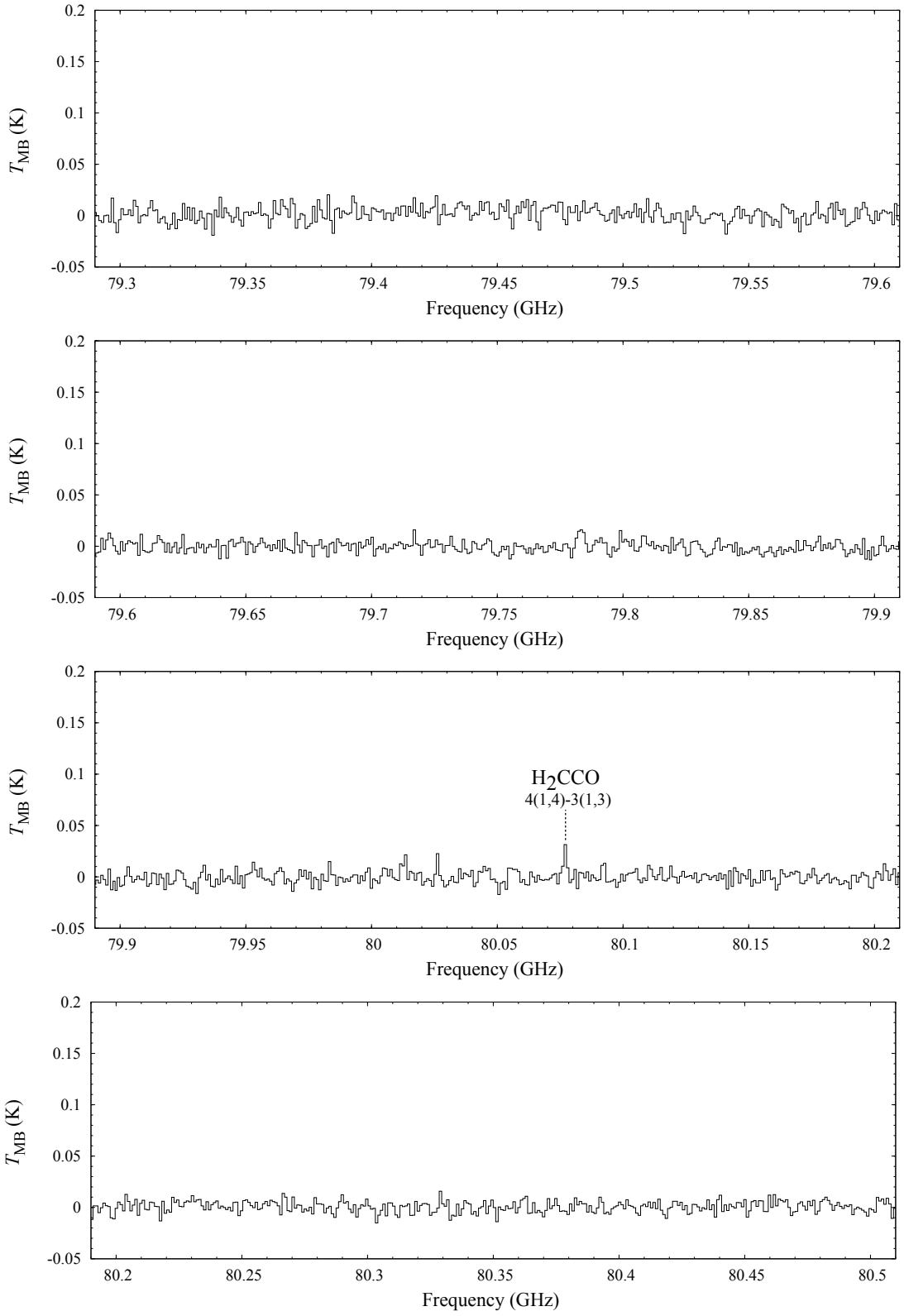

Figure A.1: continued

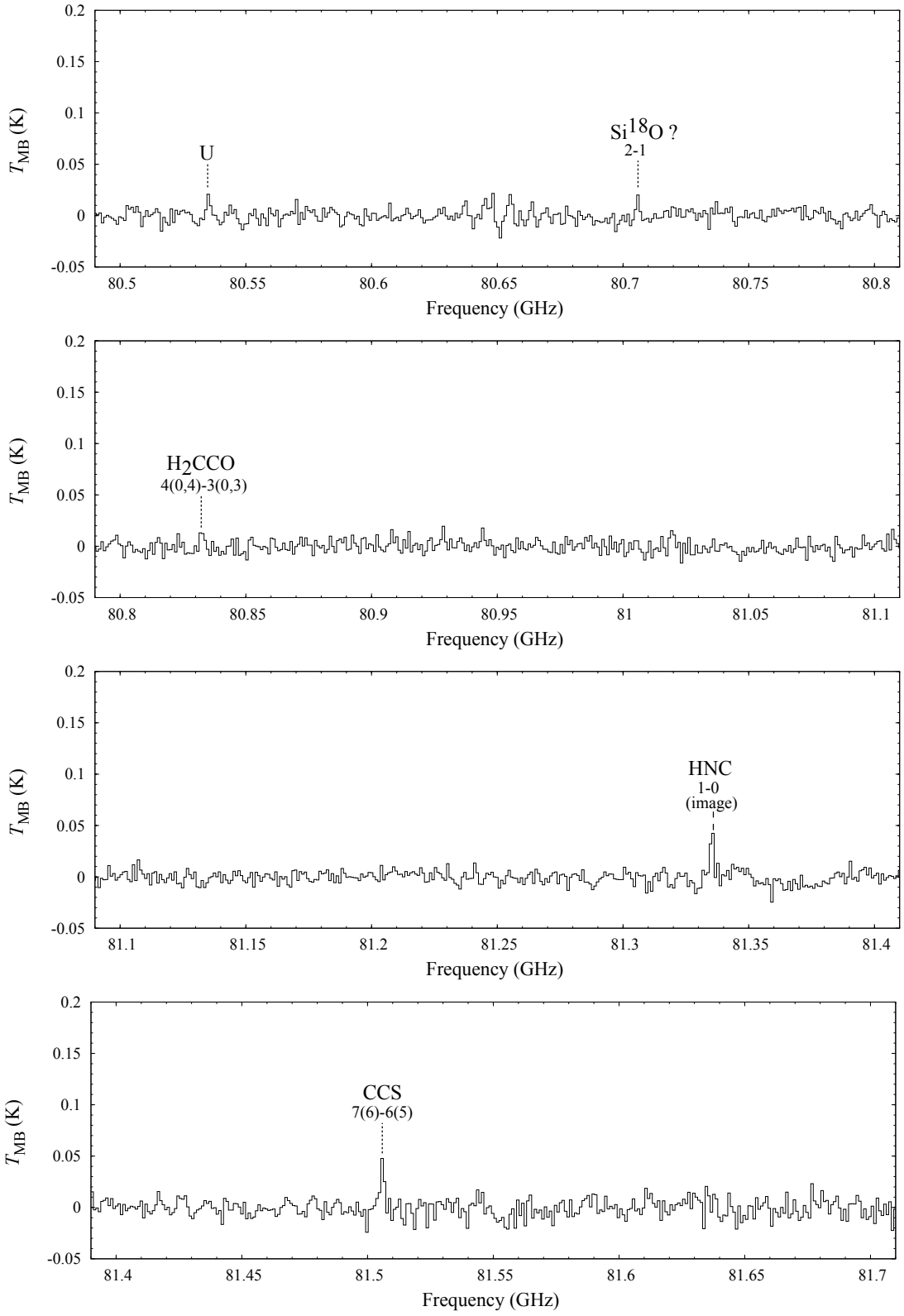

Figure A.1: continued

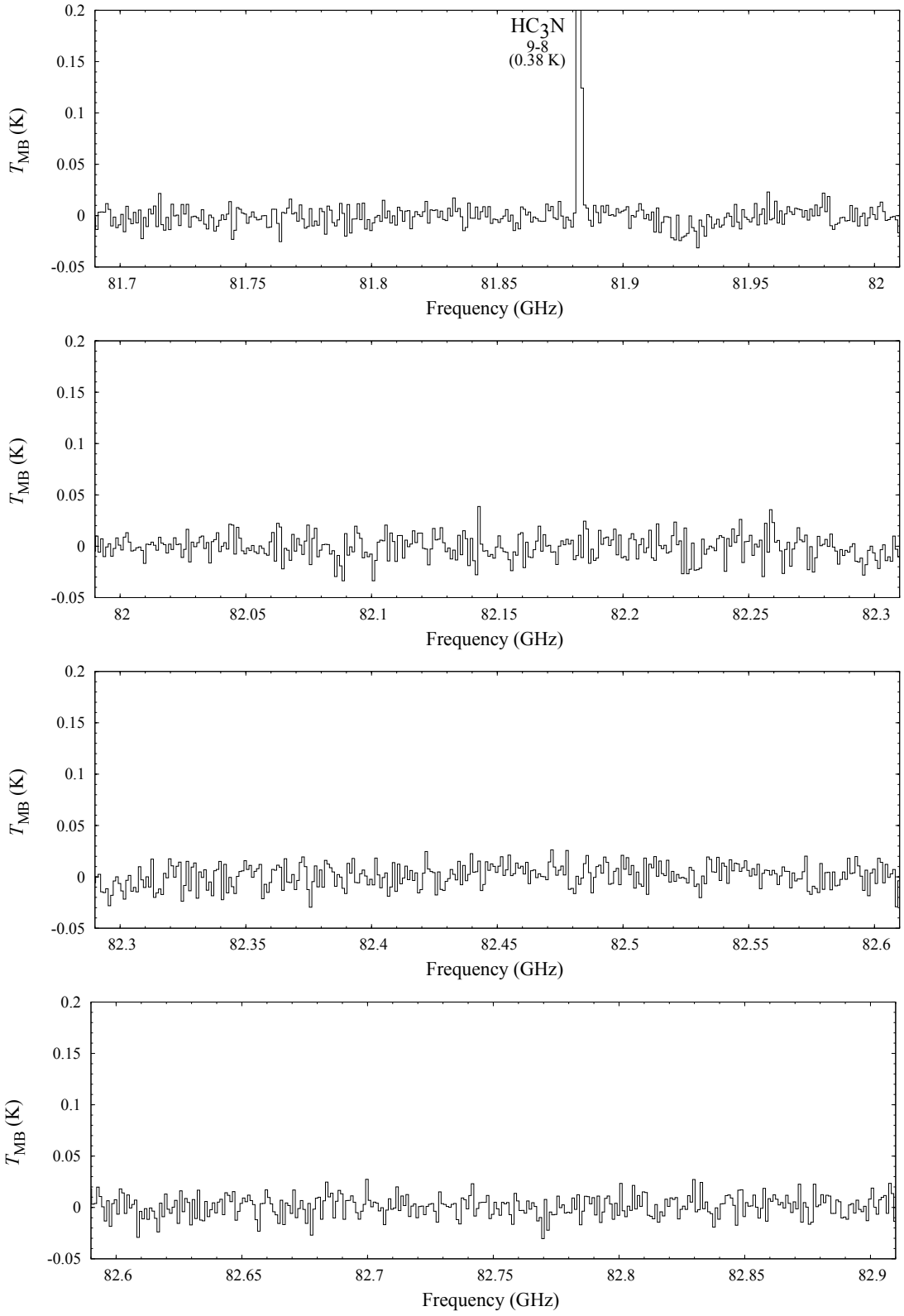

Figure A.1: continued

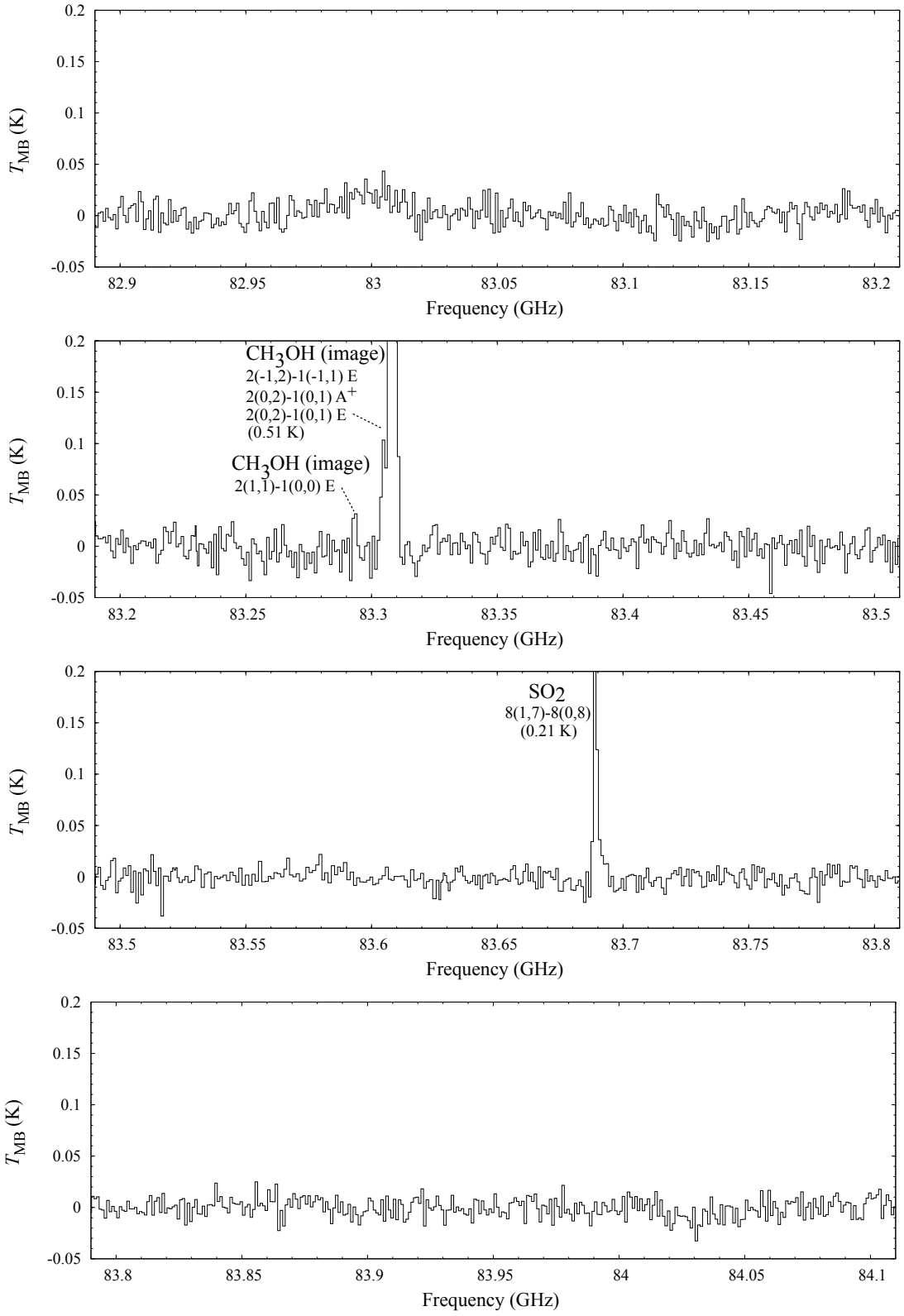

Figure A.1: continued

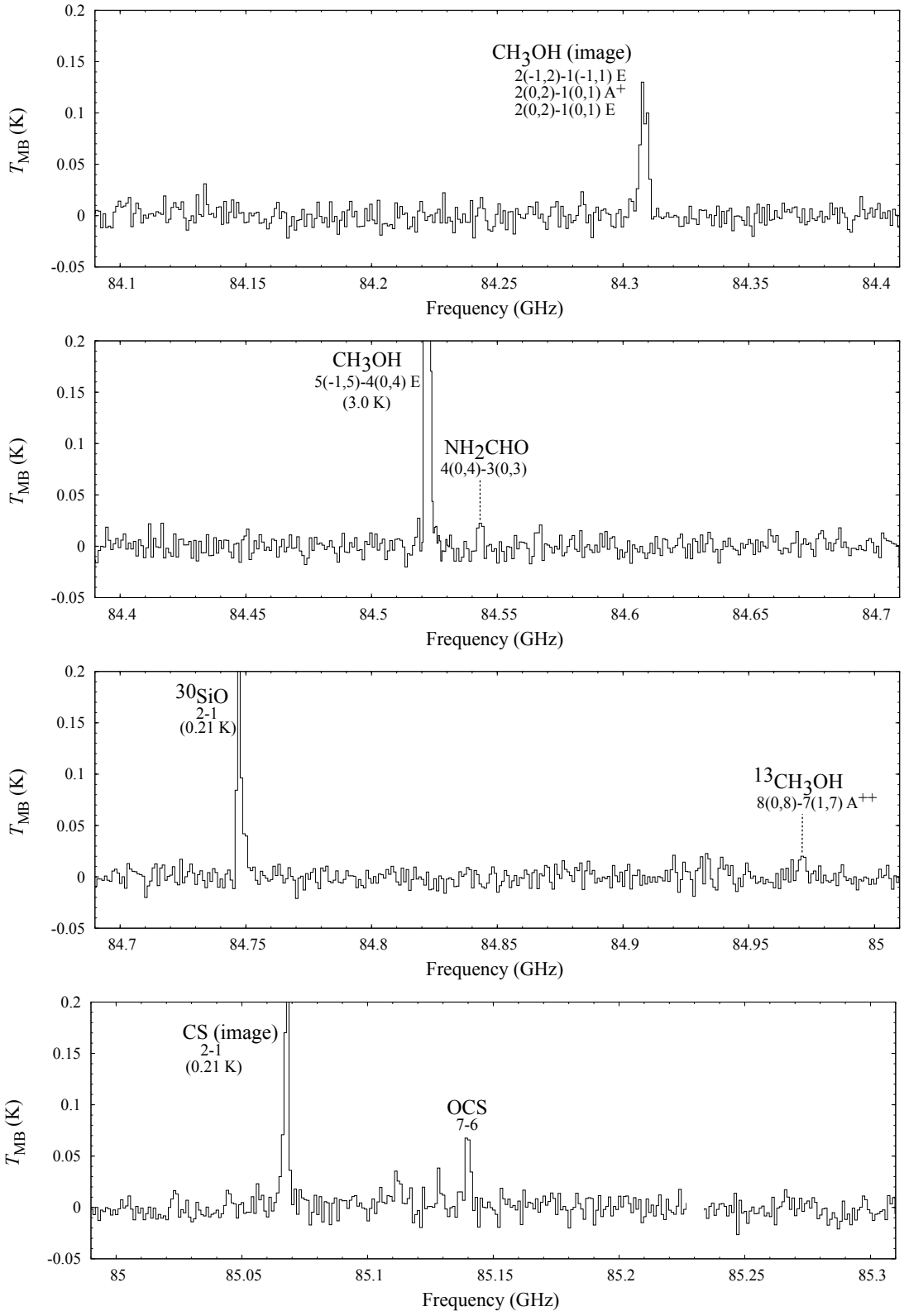

Figure A.1: continued

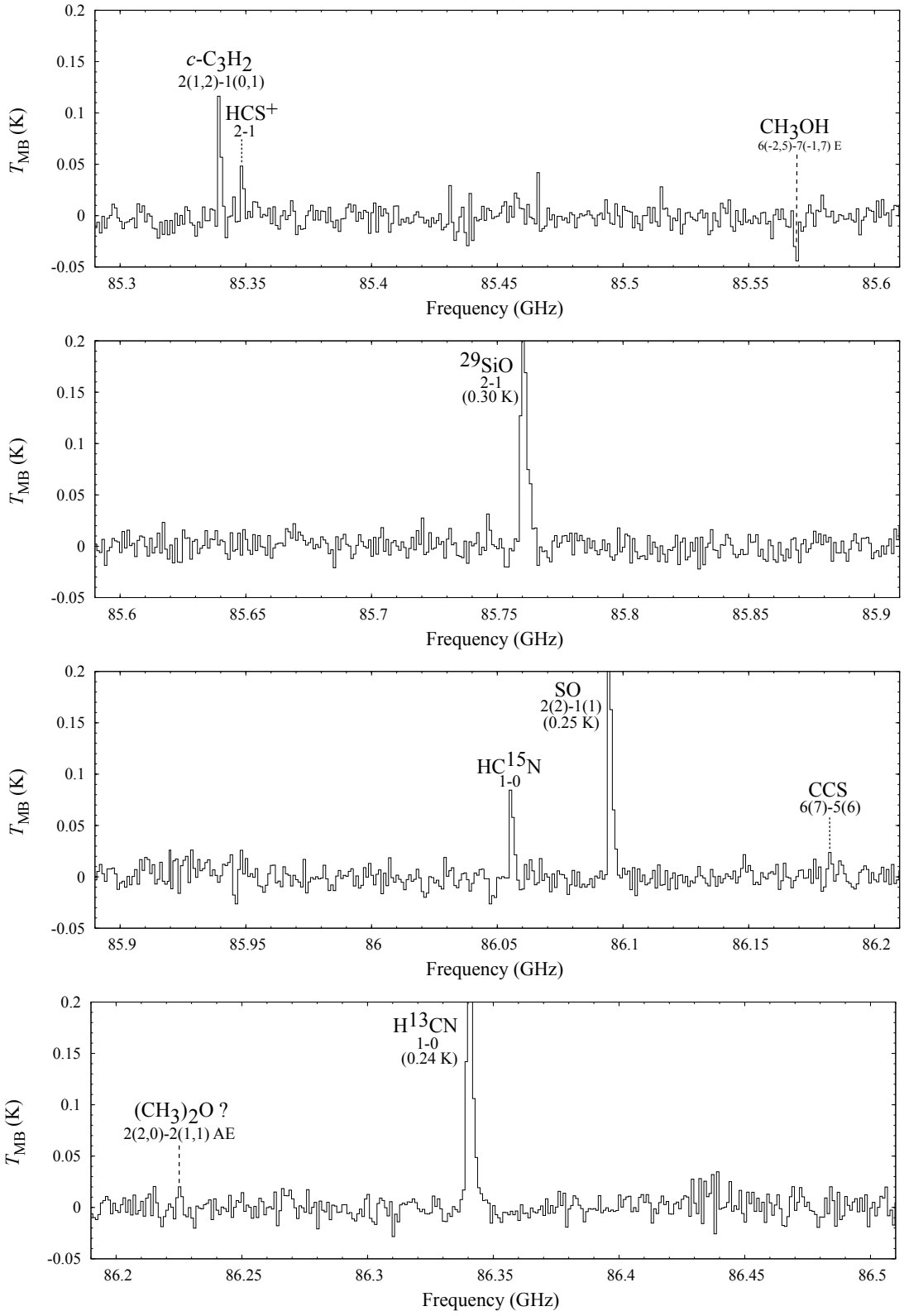

Figure A.1: continued

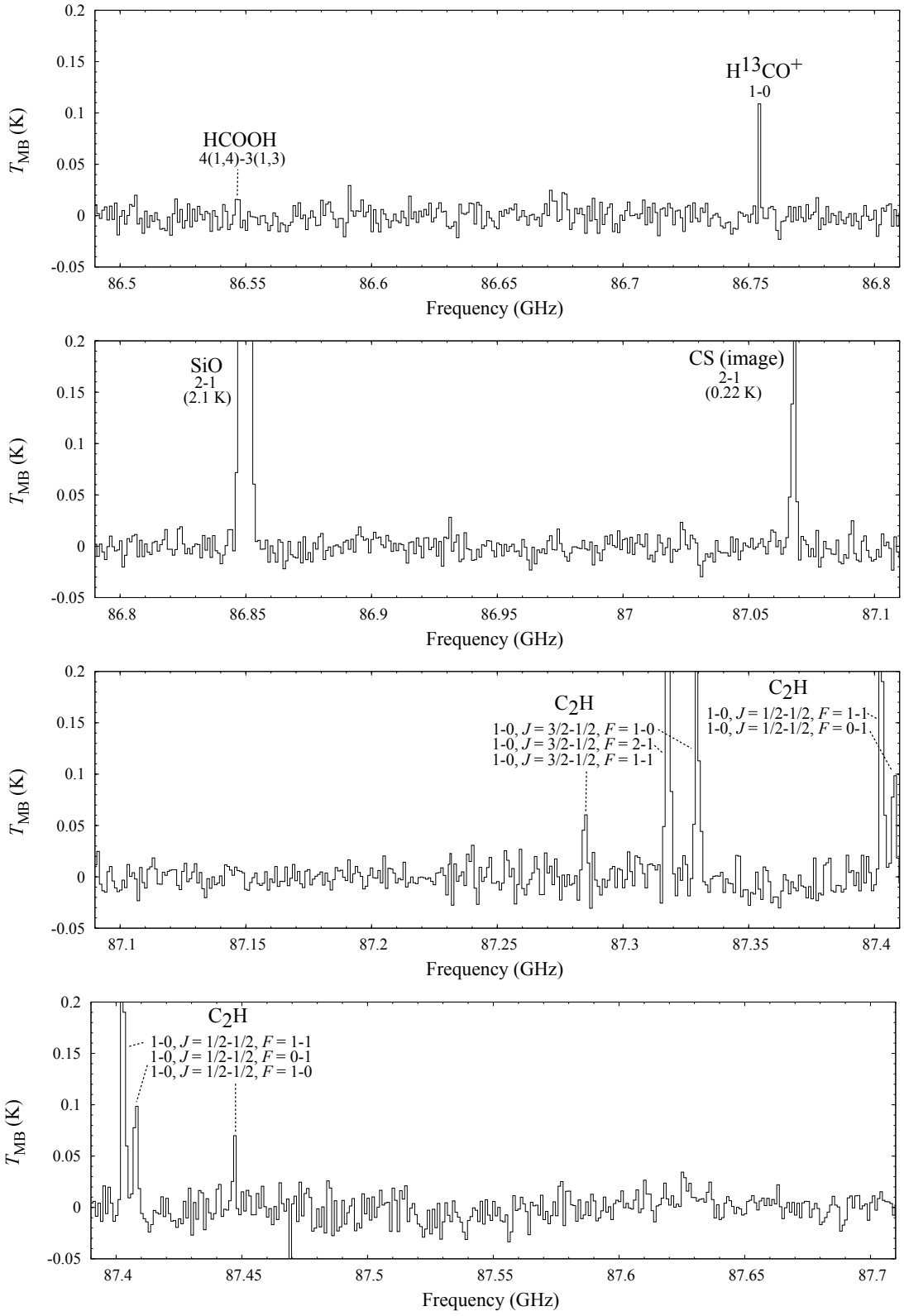

Figure A.1: continued

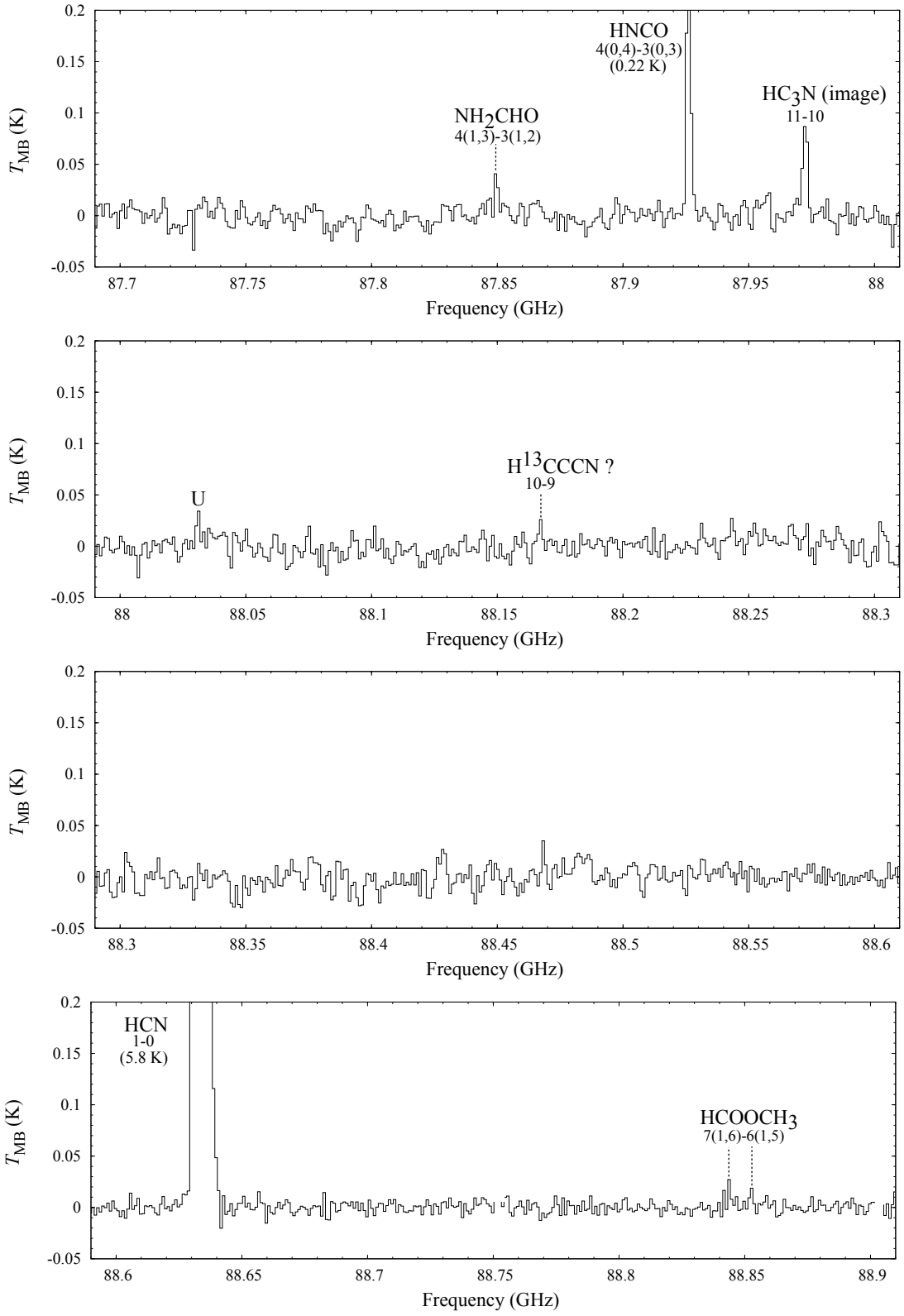

Figure A.1: continued

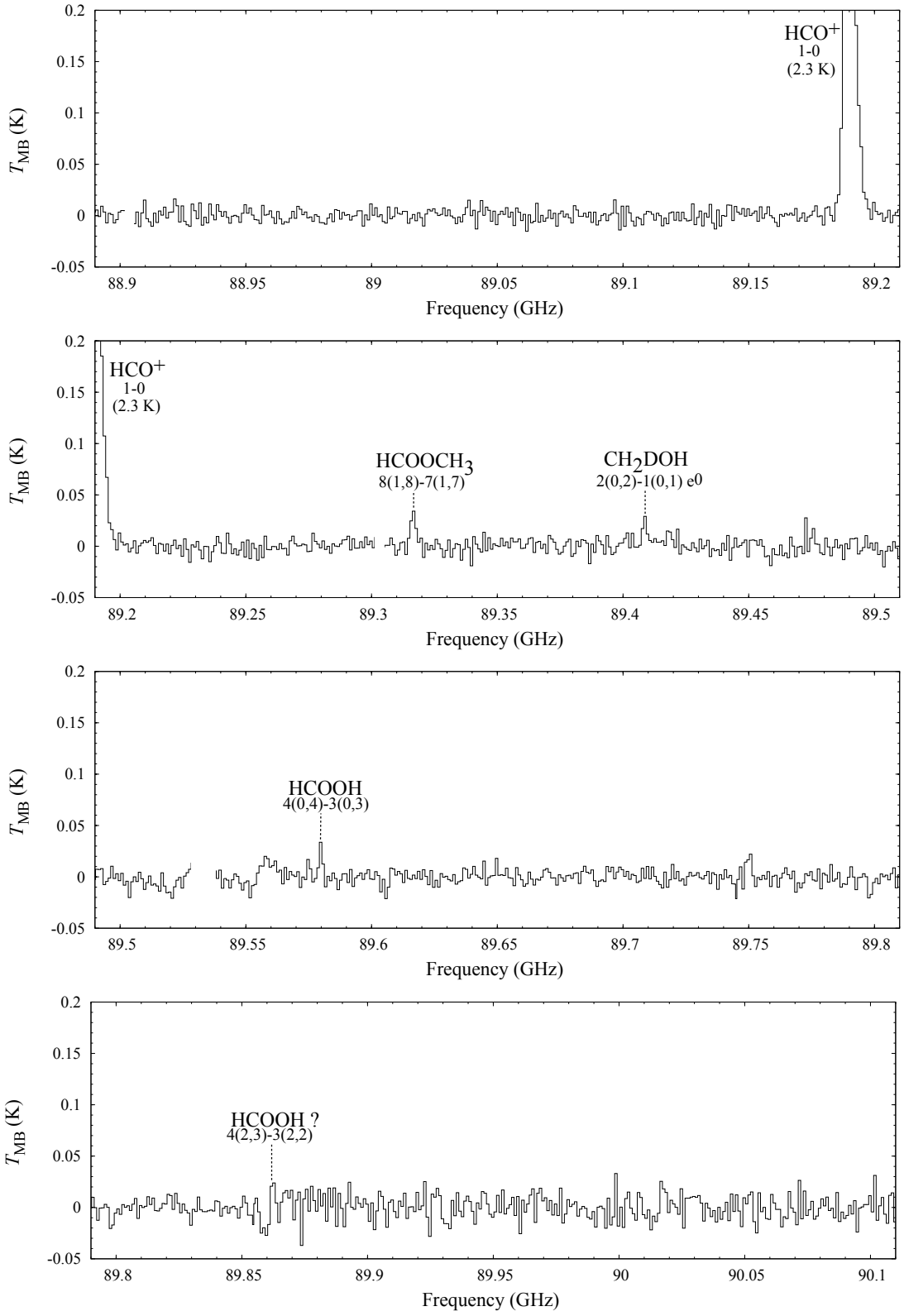

Figure A.1: continued

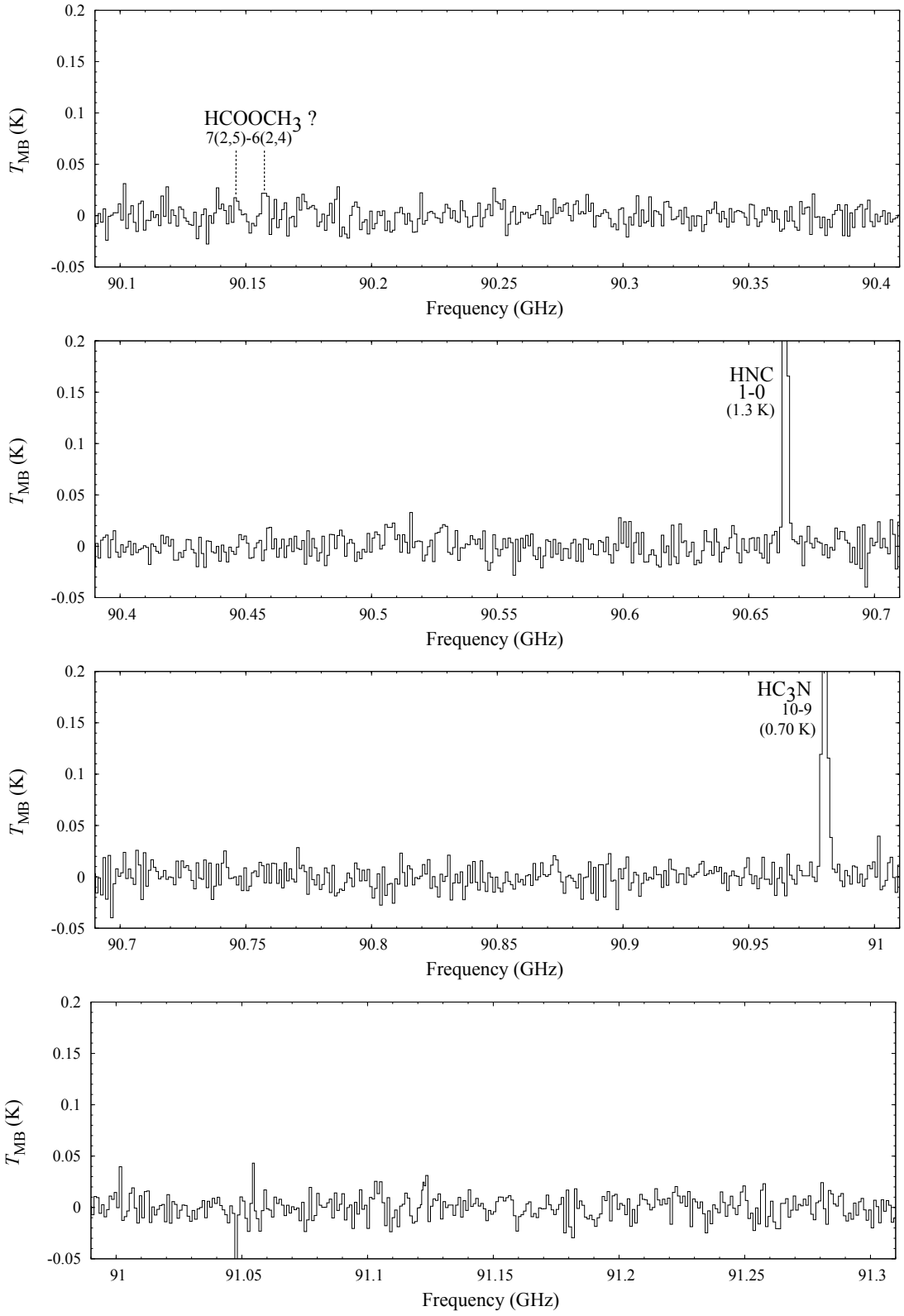

Figure A.1: continued

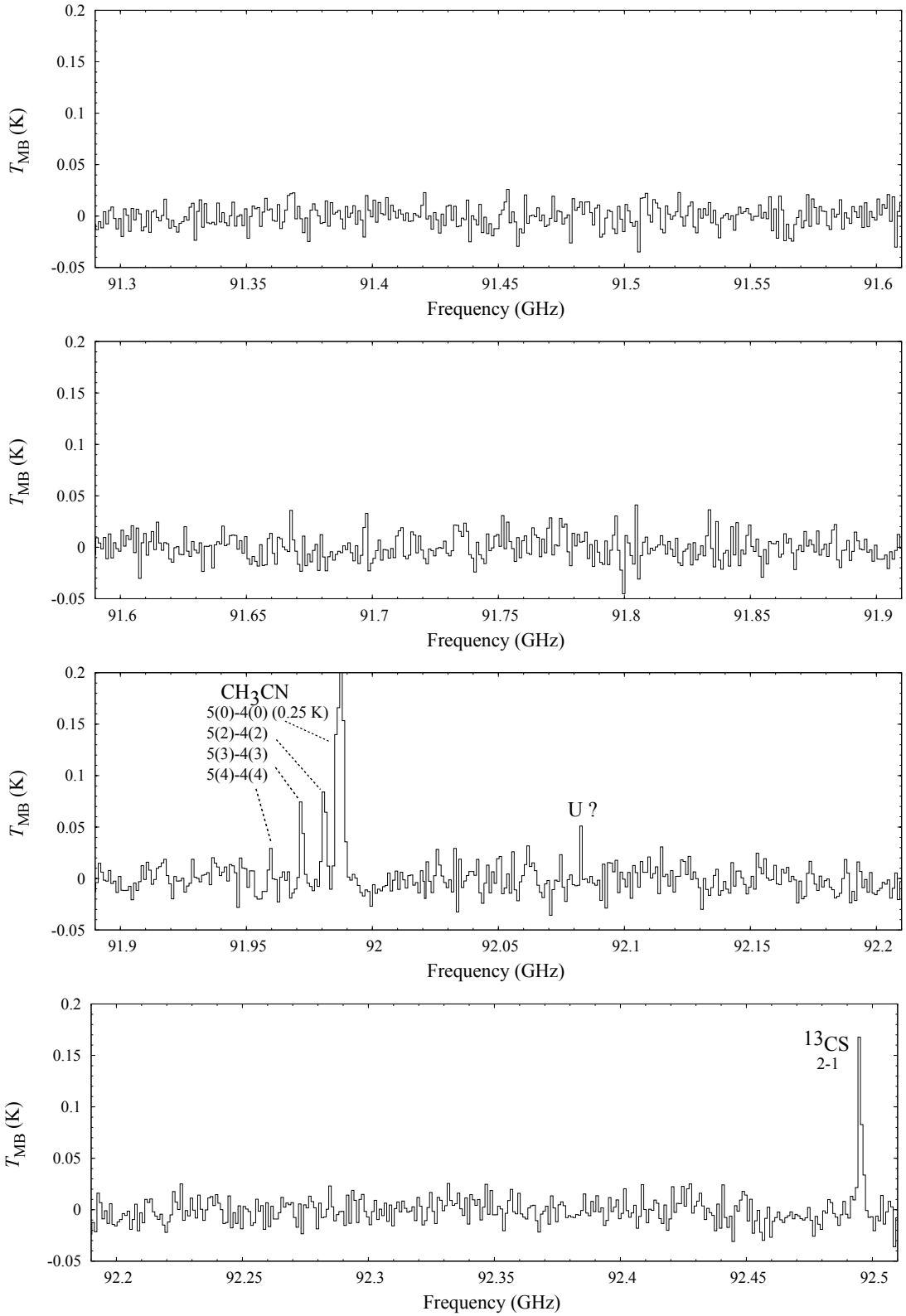

Figure A.1: continued

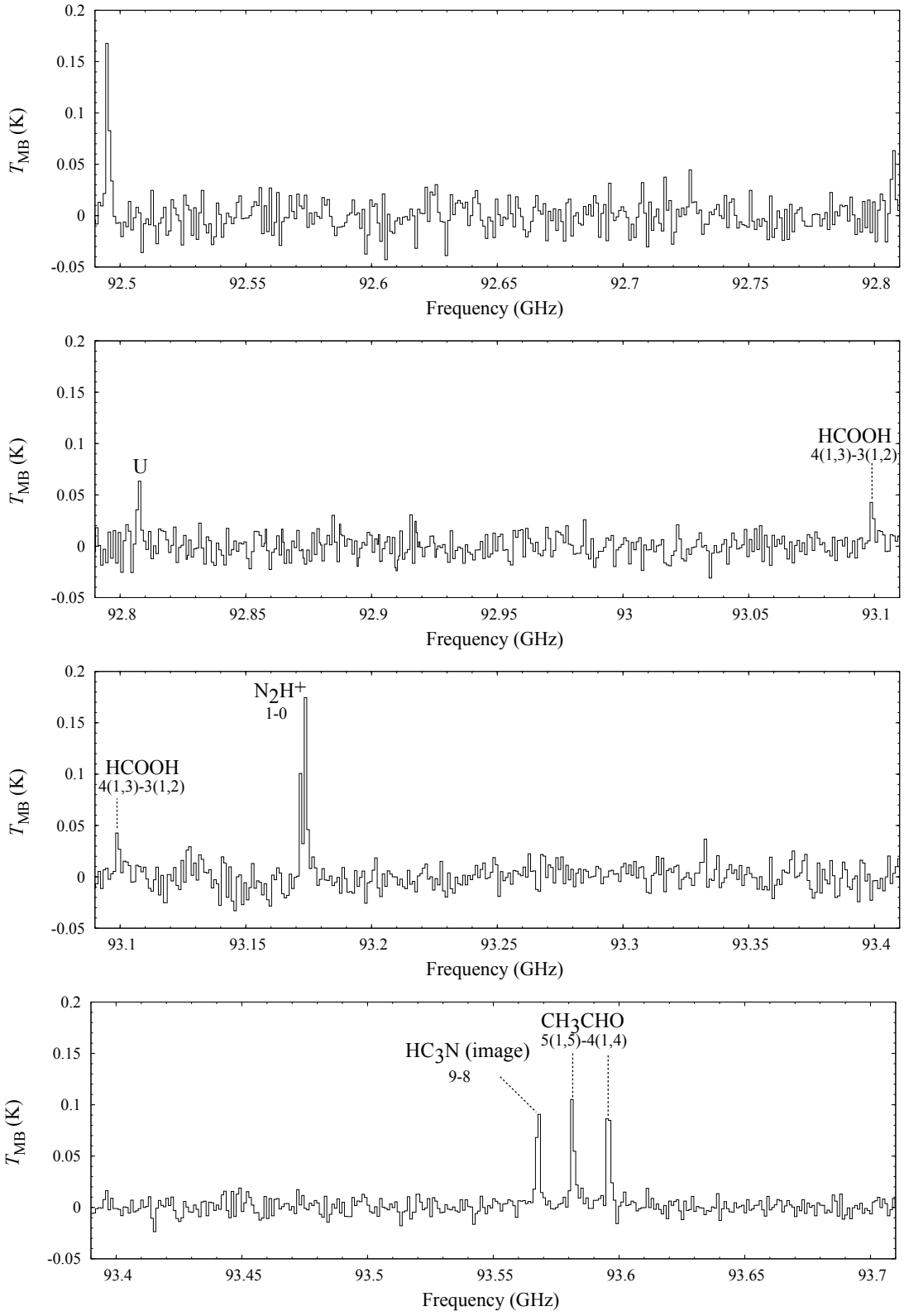

Figure A.1: continued

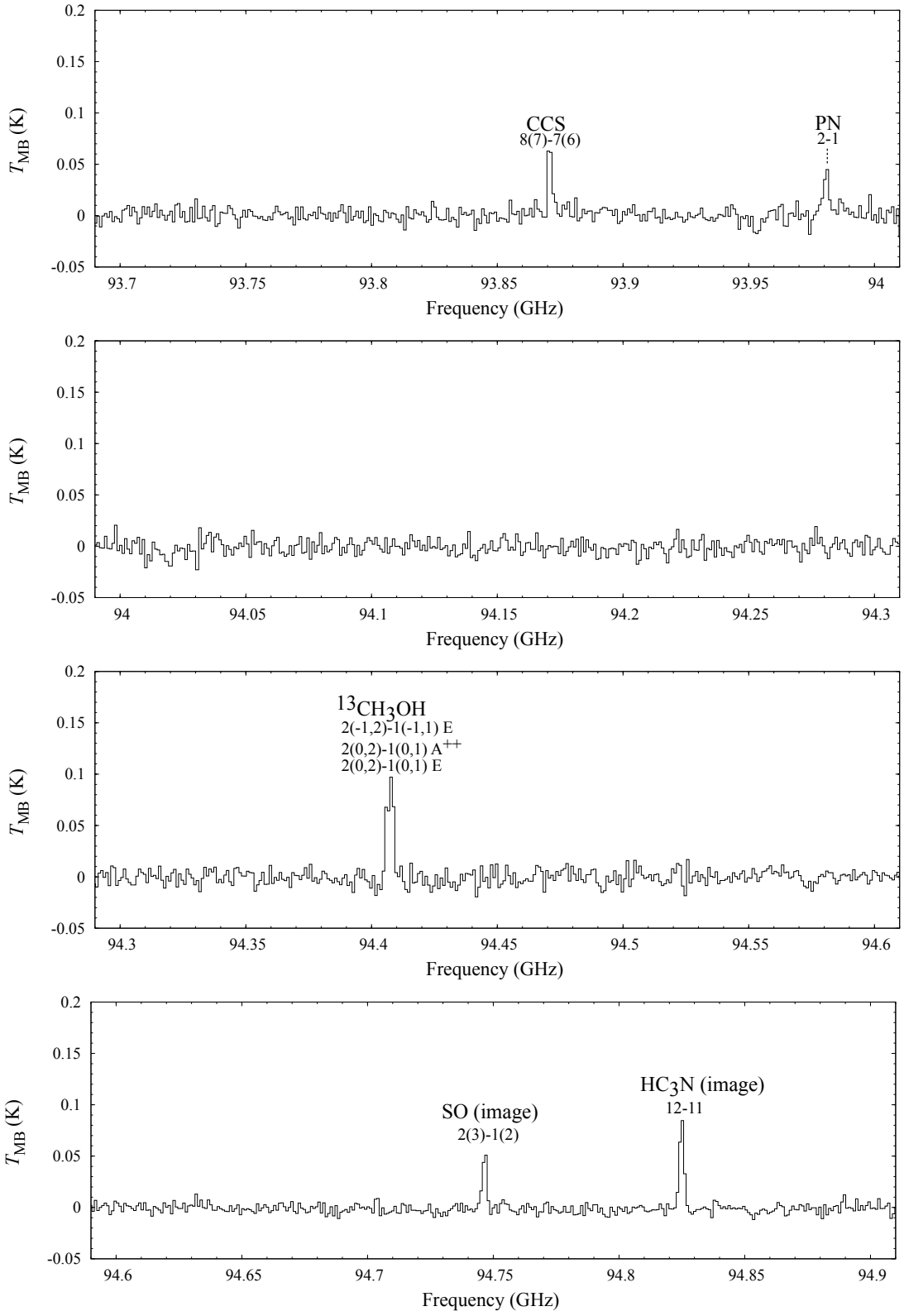

Figure A.1: continued

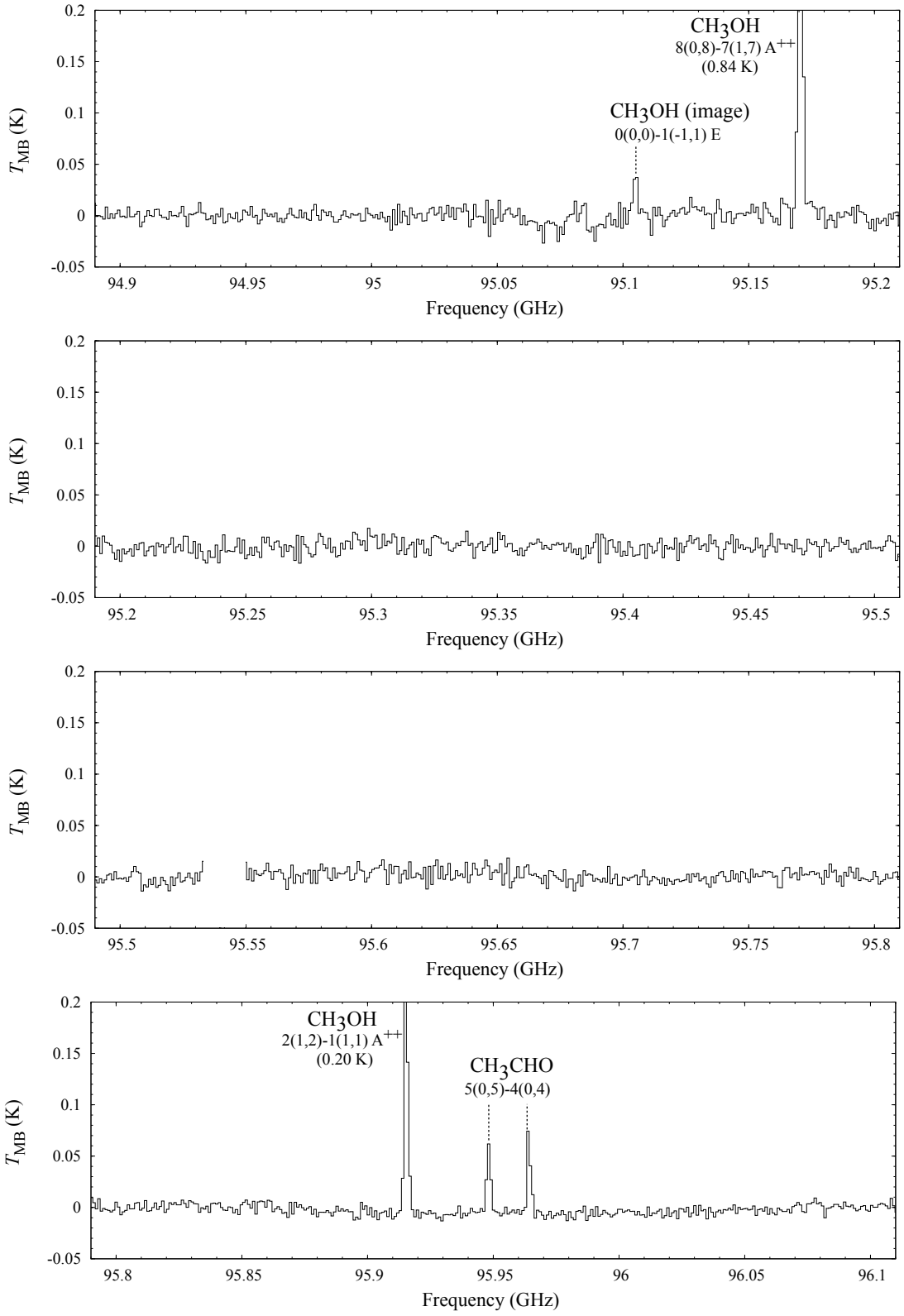

Figure A.1: continued

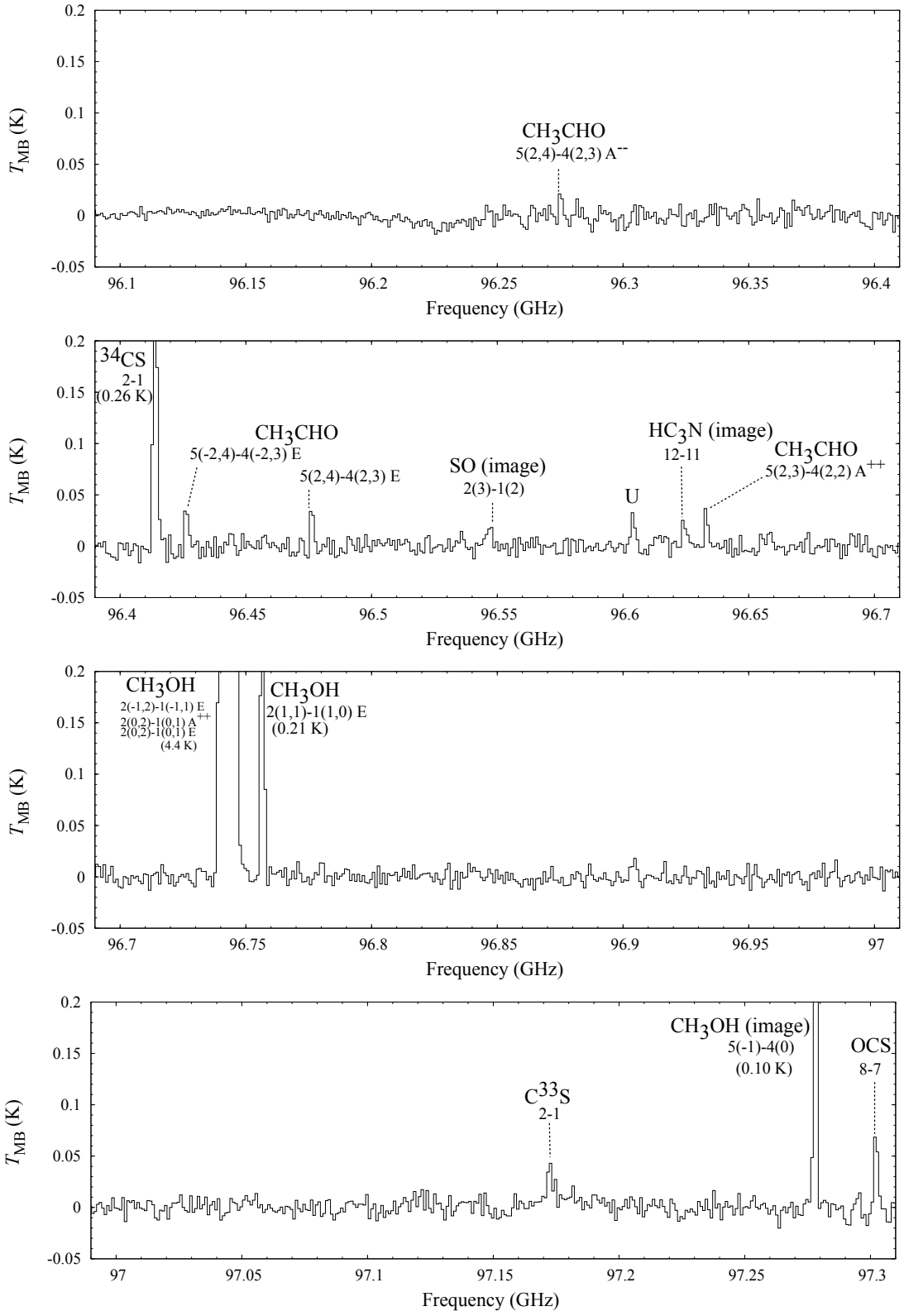

Figure A.1: continued

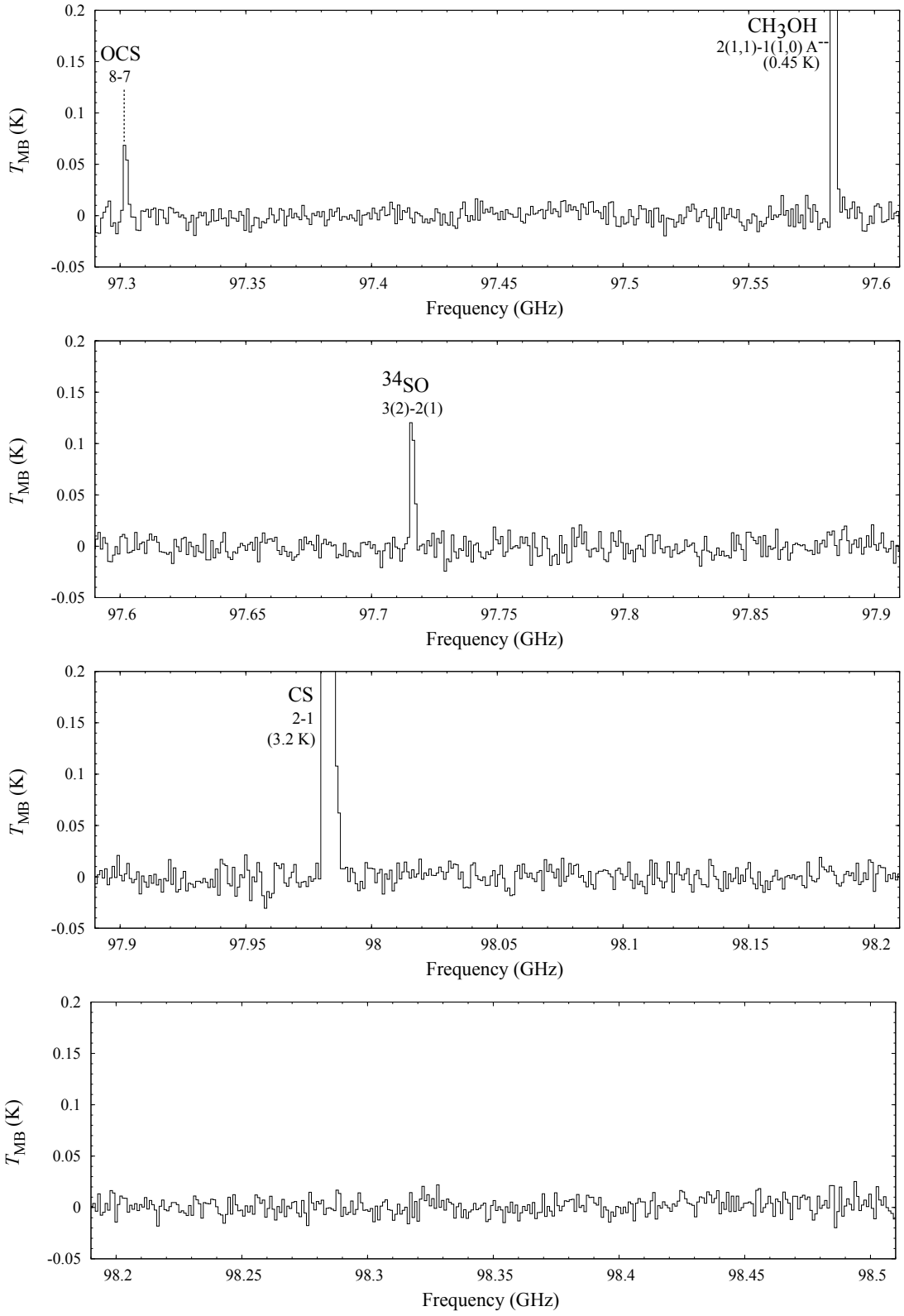

Figure A.1: continued

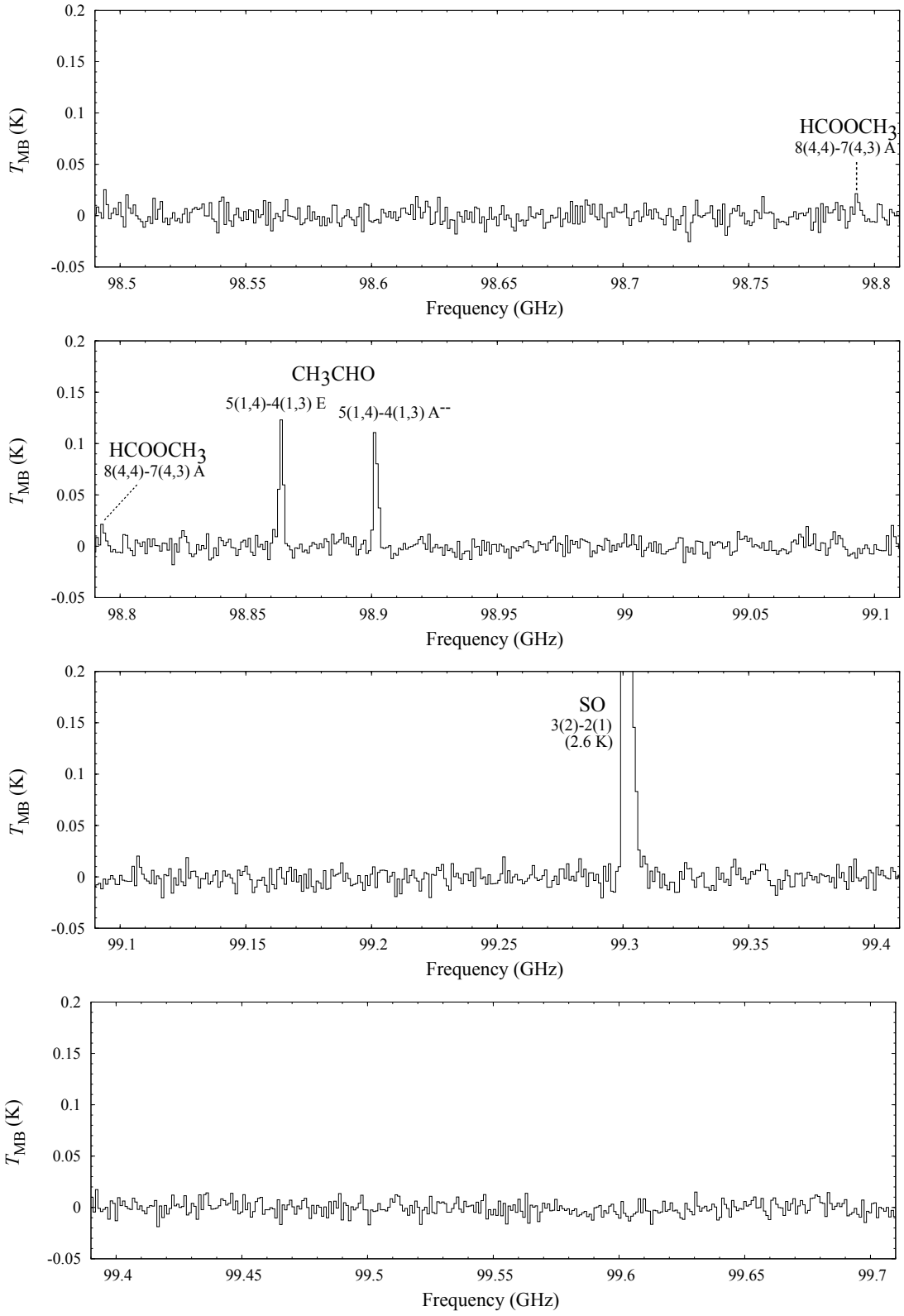

Figure A.1: continued

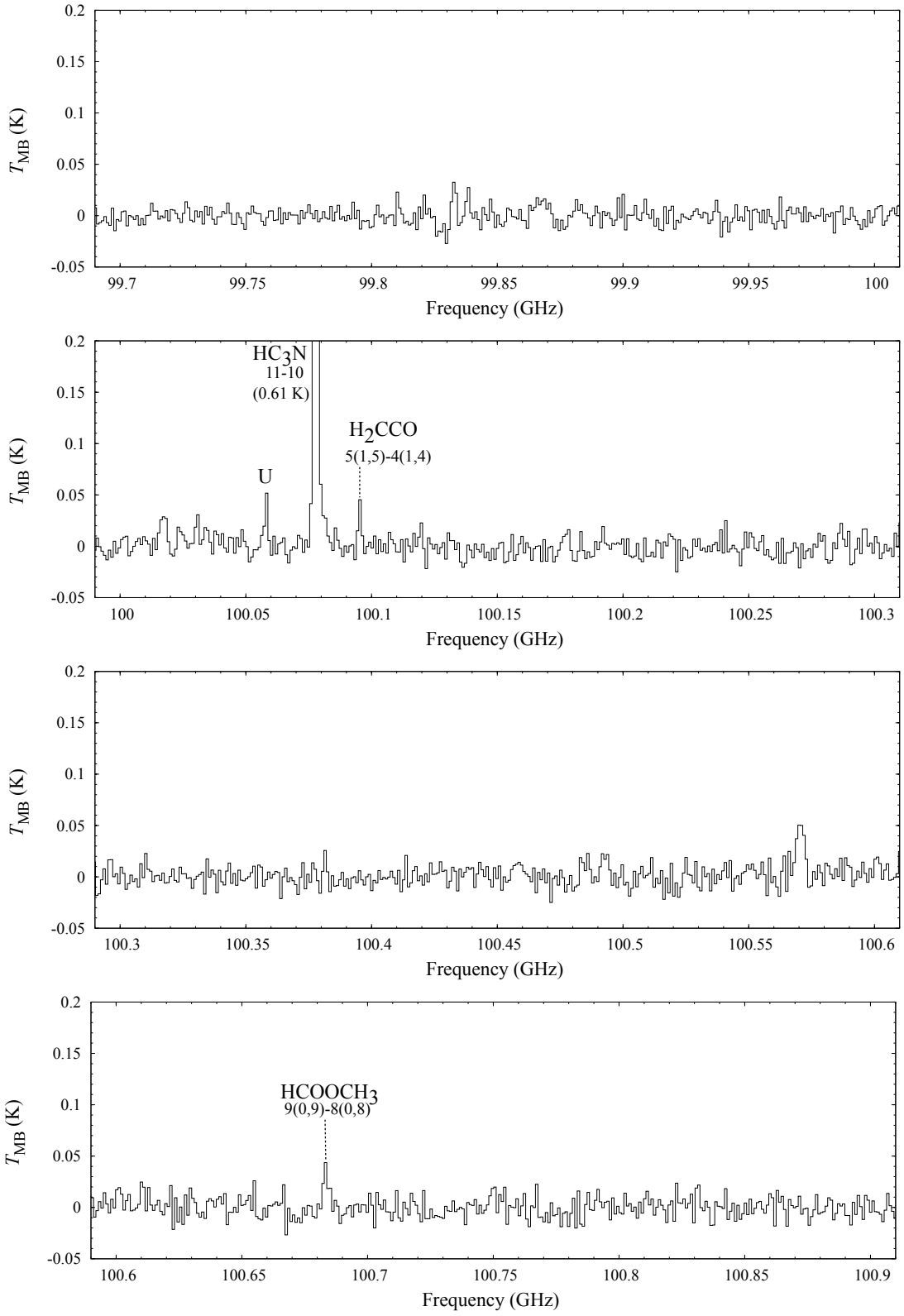

Figure A.1: continued

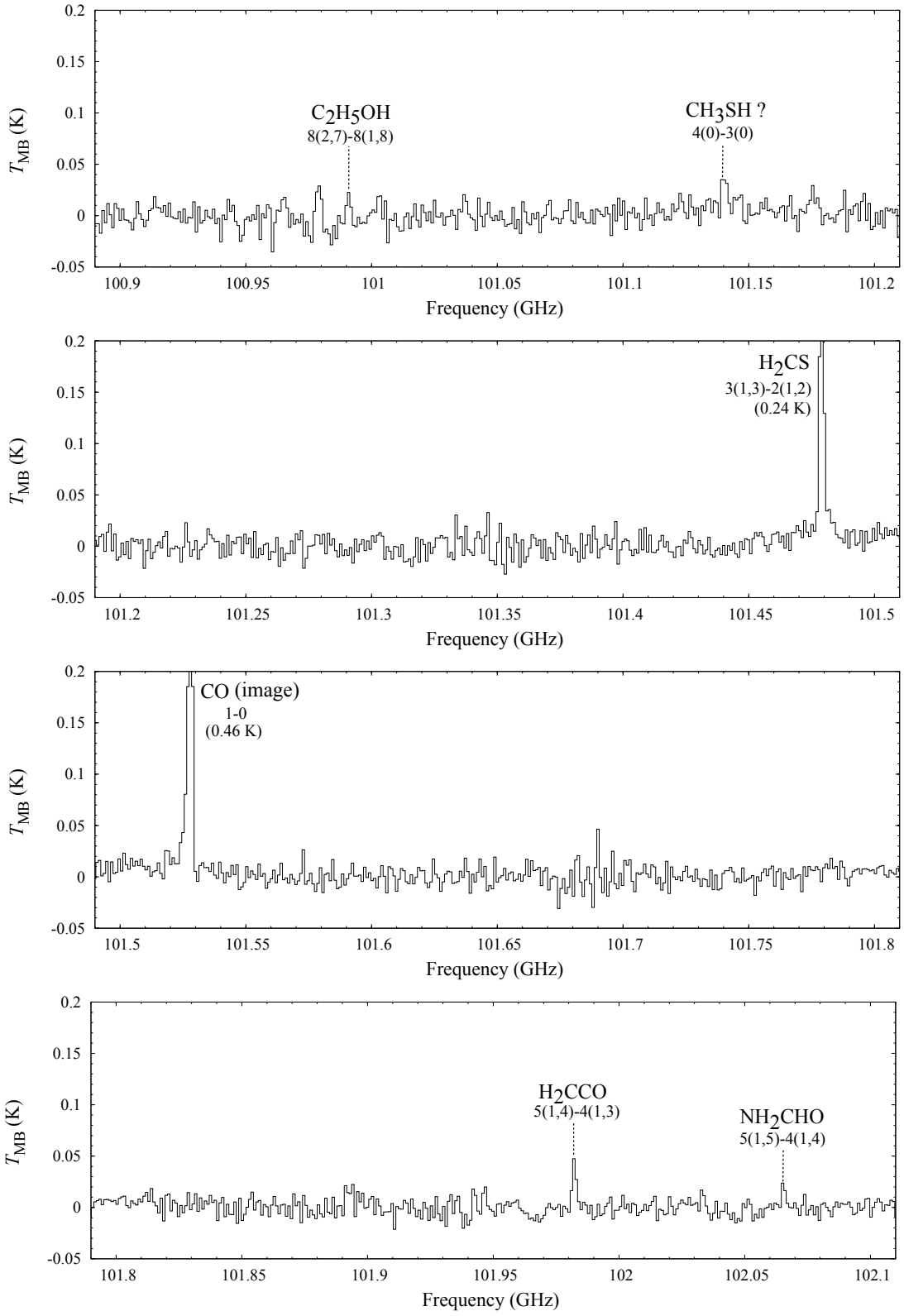

Figure A.1: continued

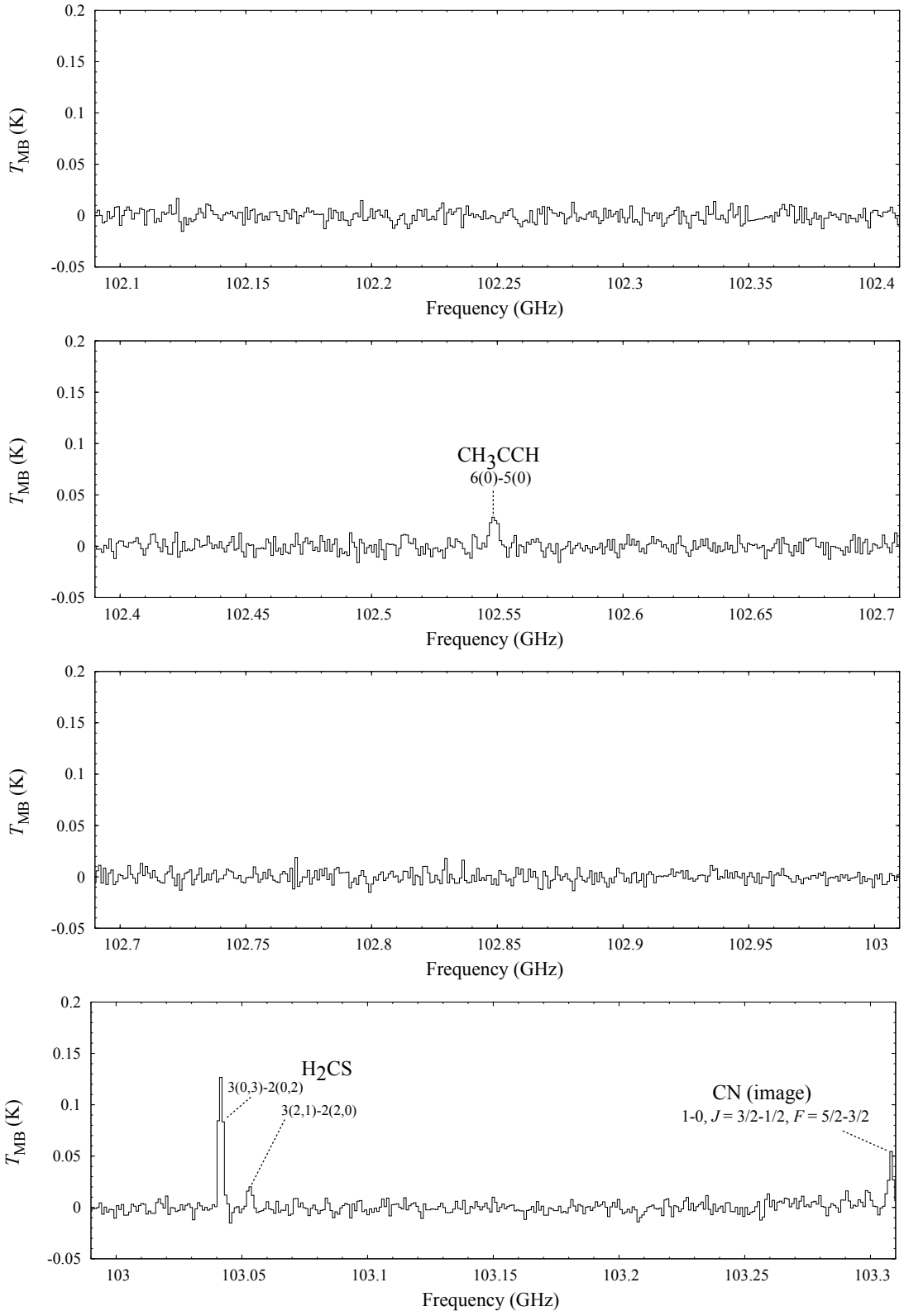

Figure A.1: continued

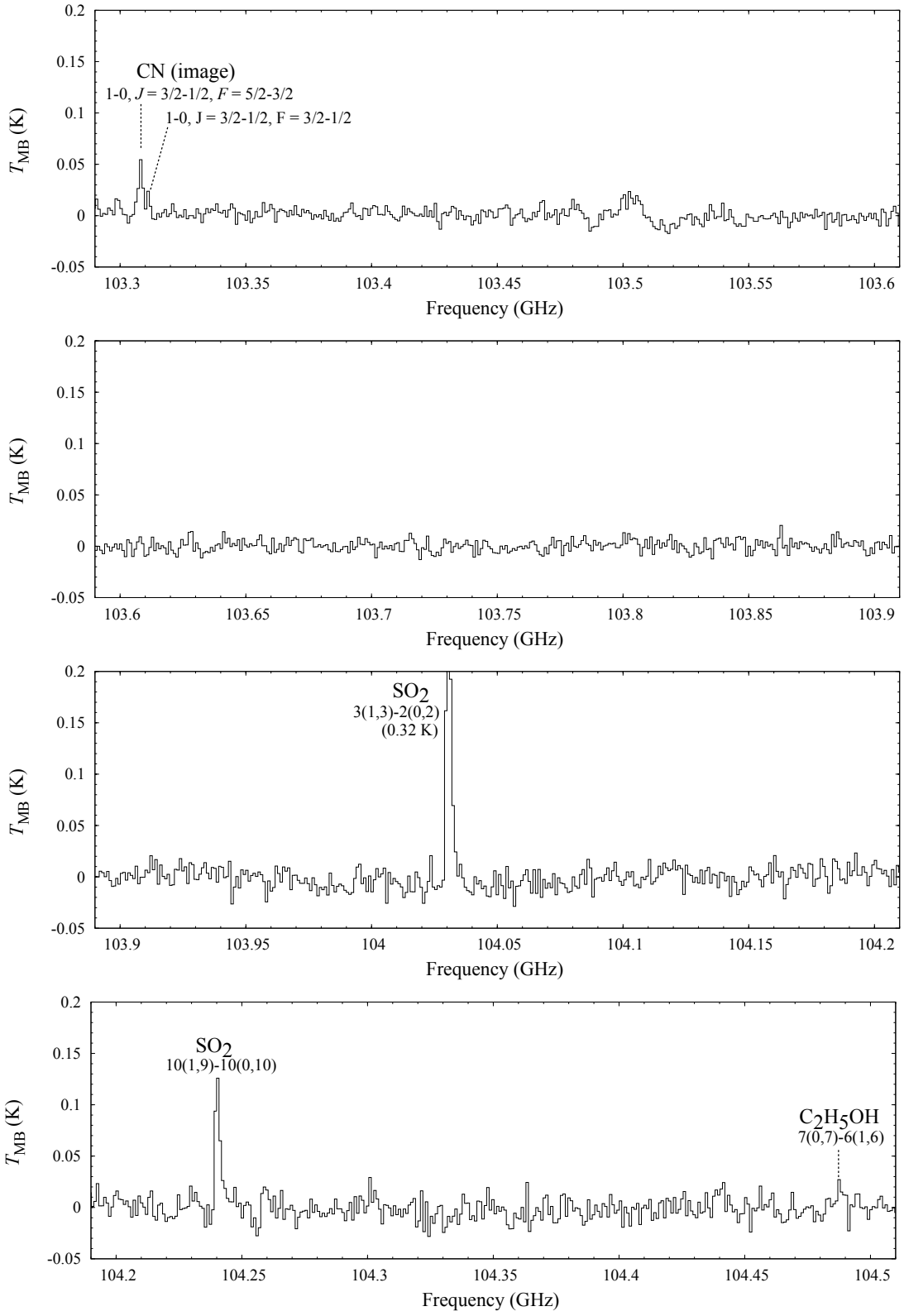

Figure A.1: continued

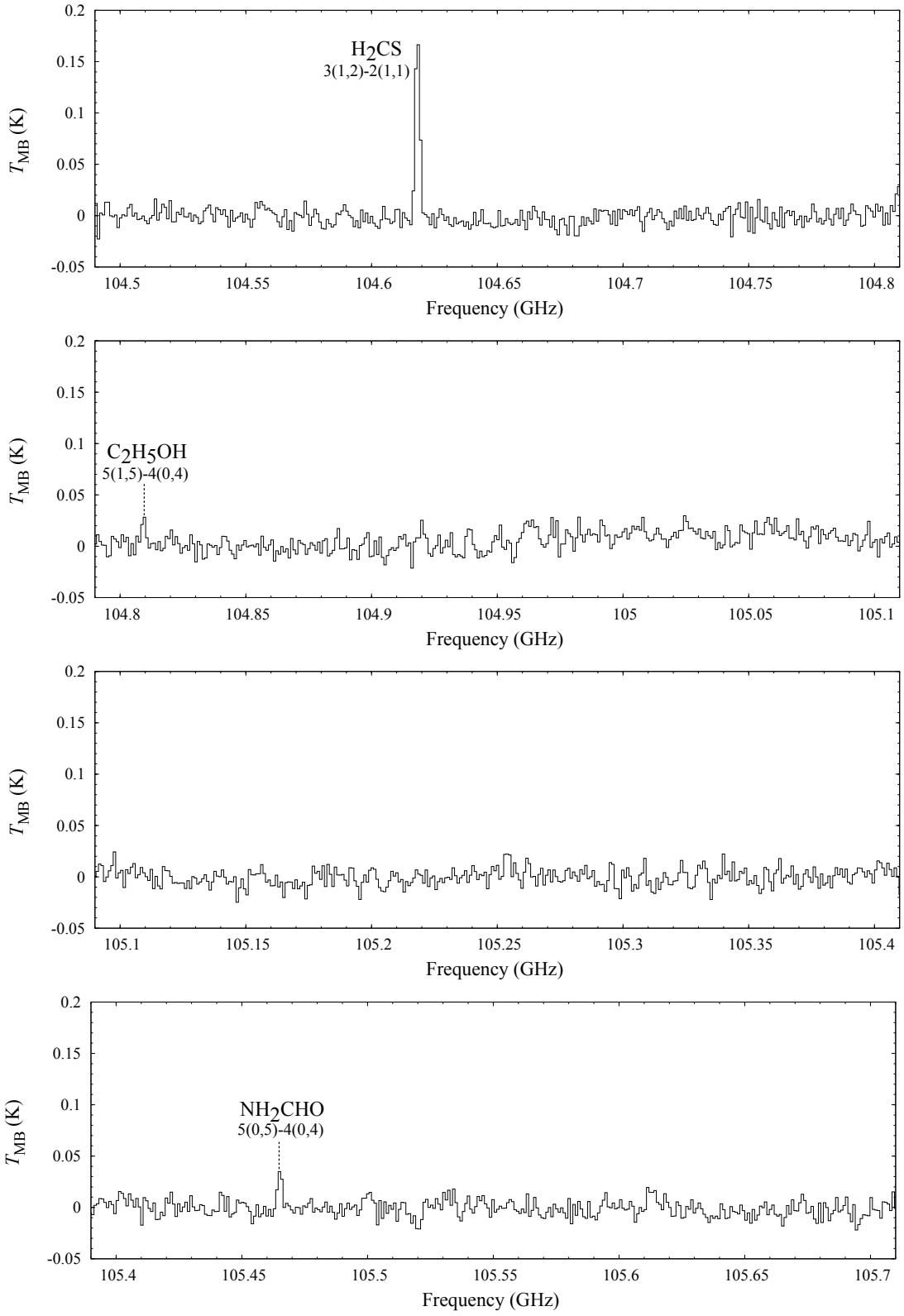

Figure A.1: continued

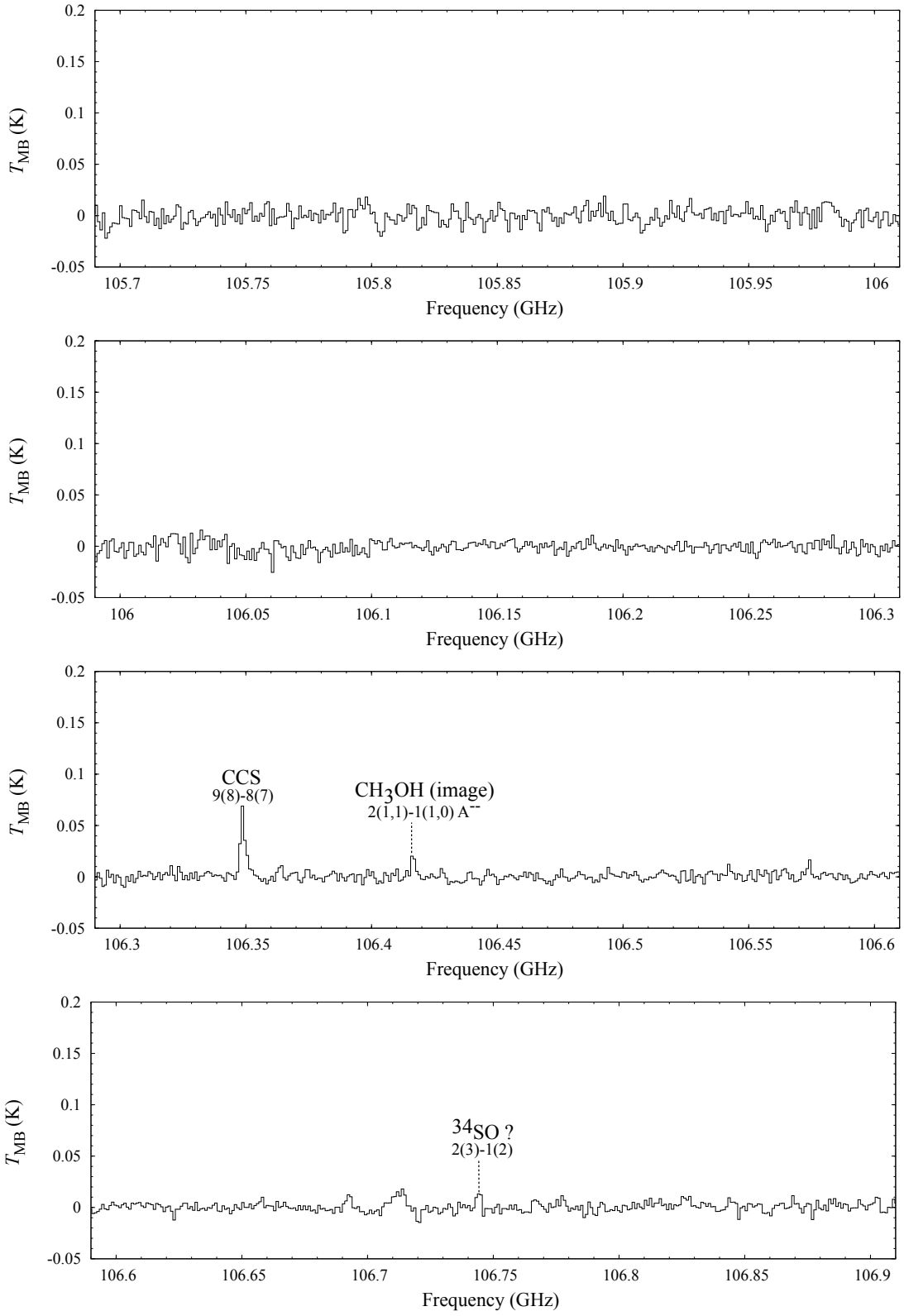

Figure A.1: continued

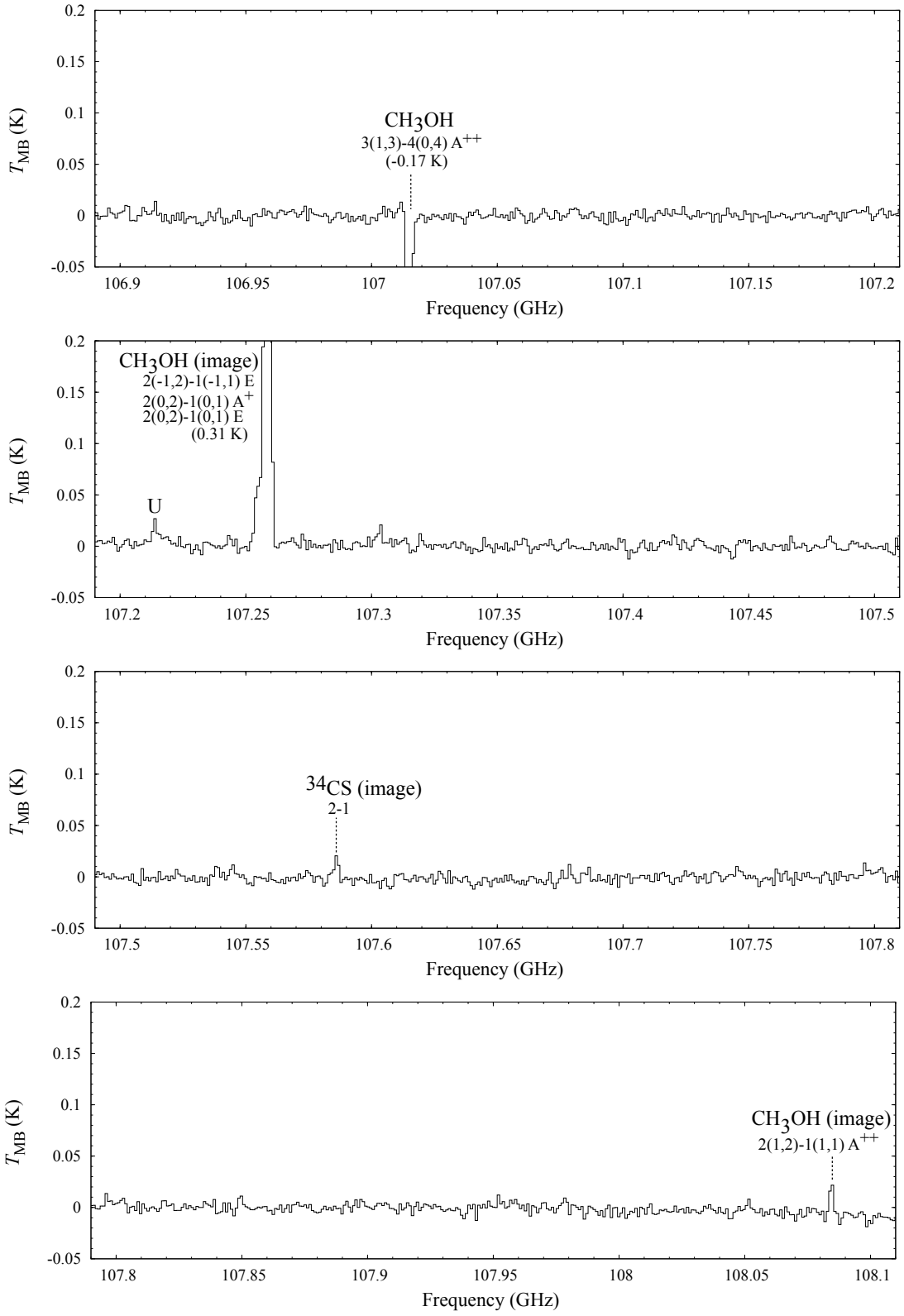

Figure A.1: continued

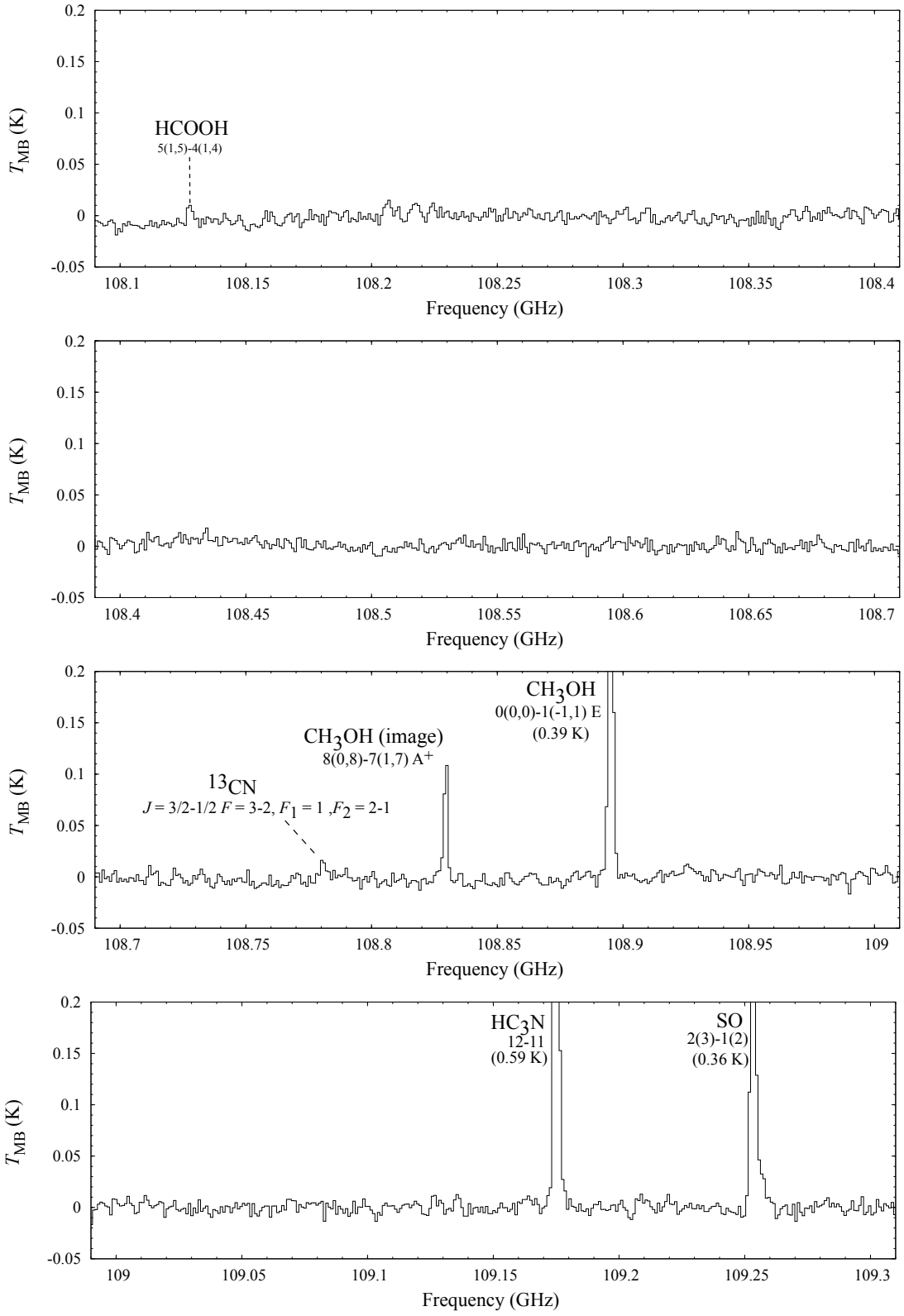

Figure A.1: continued

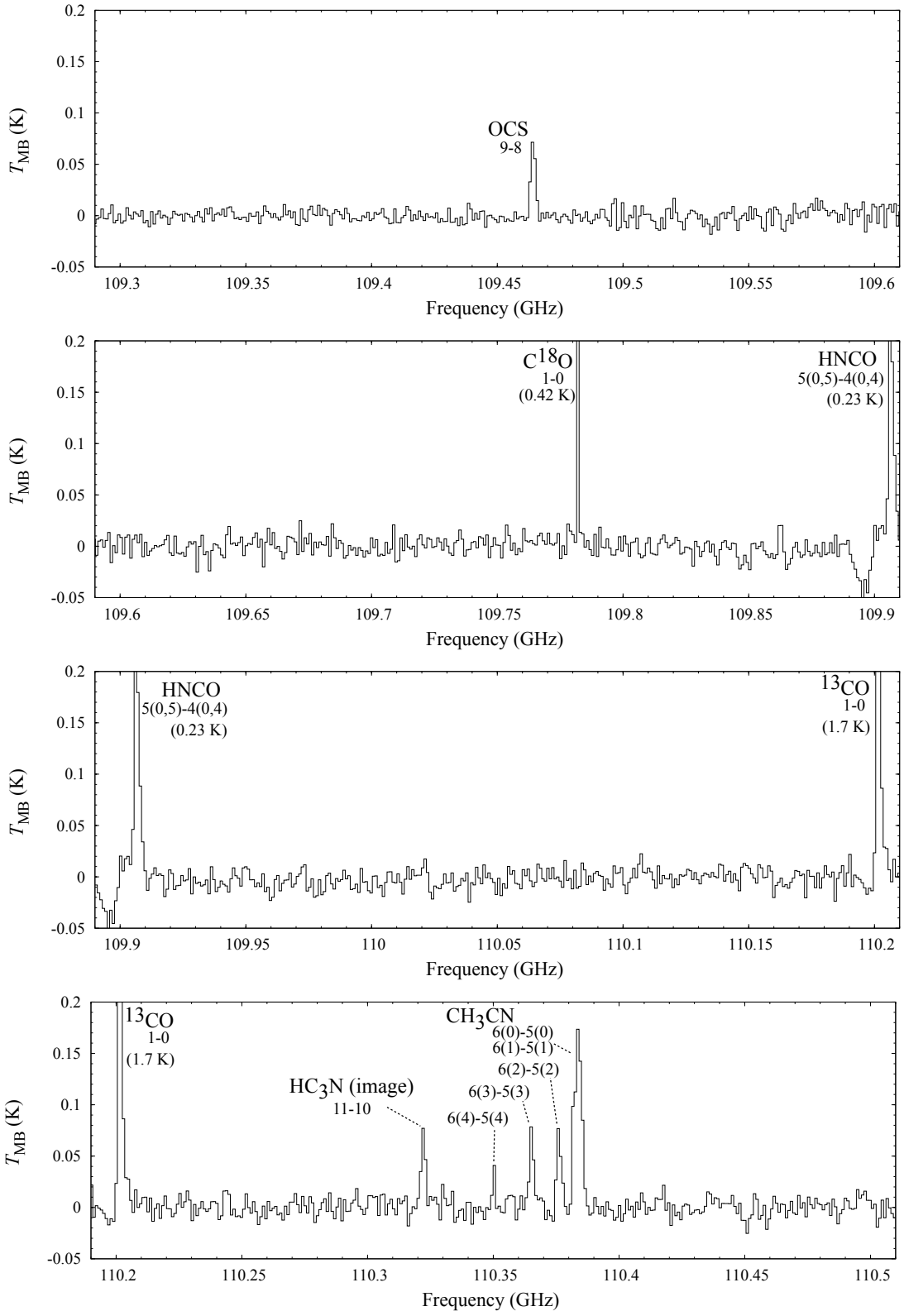

Figure A.1: continued

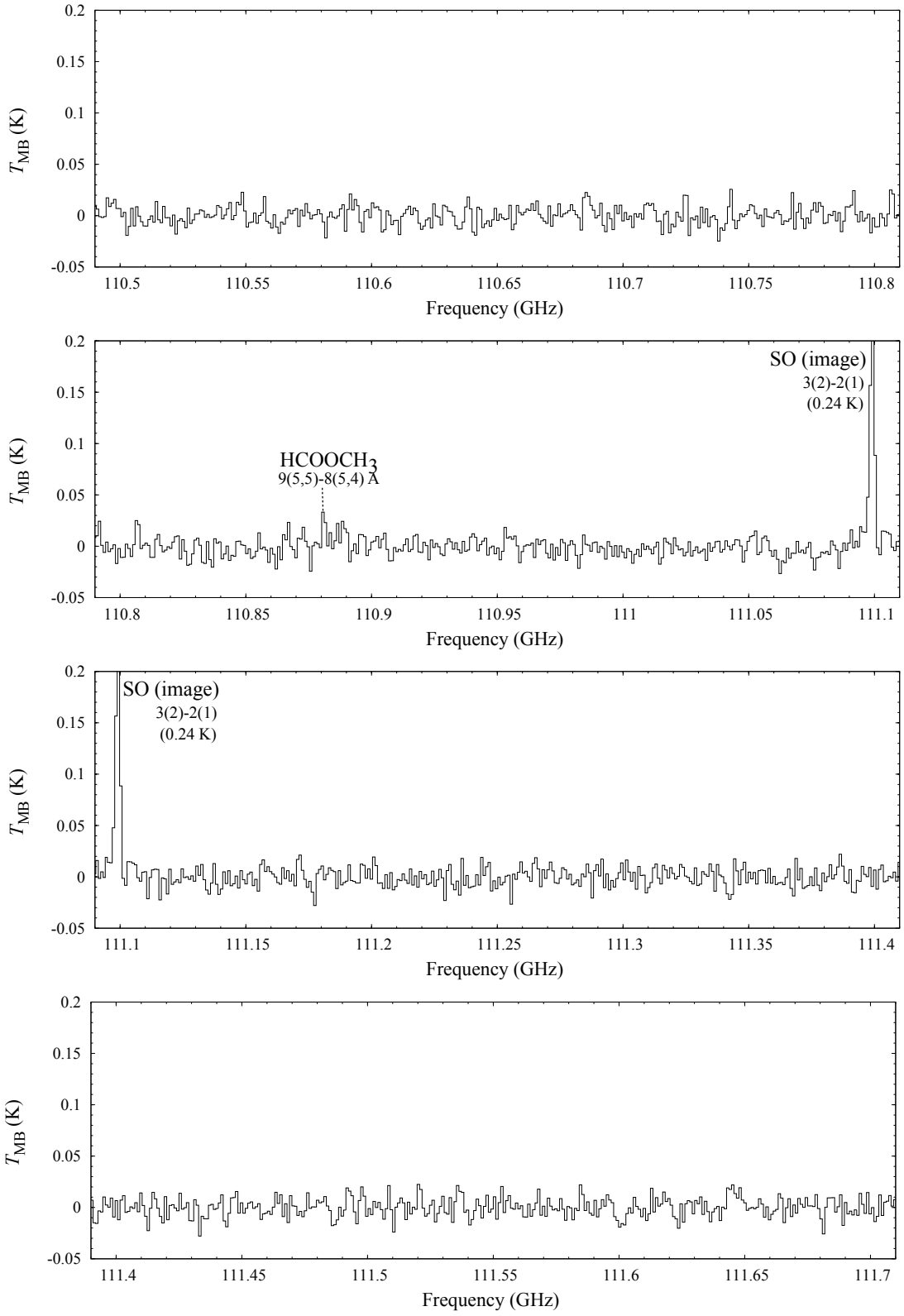

Figure A.1: continued

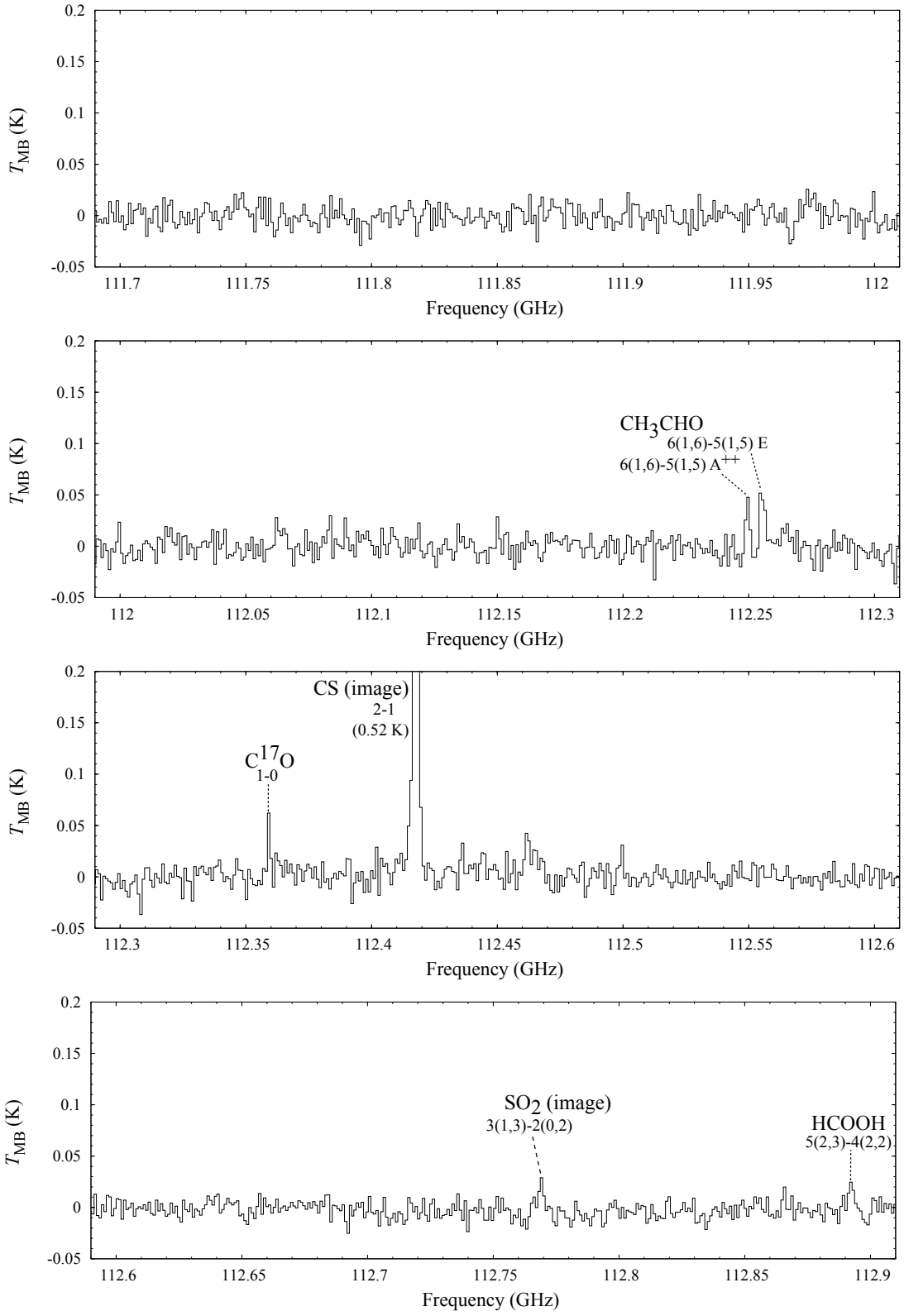

Figure A.1: continued

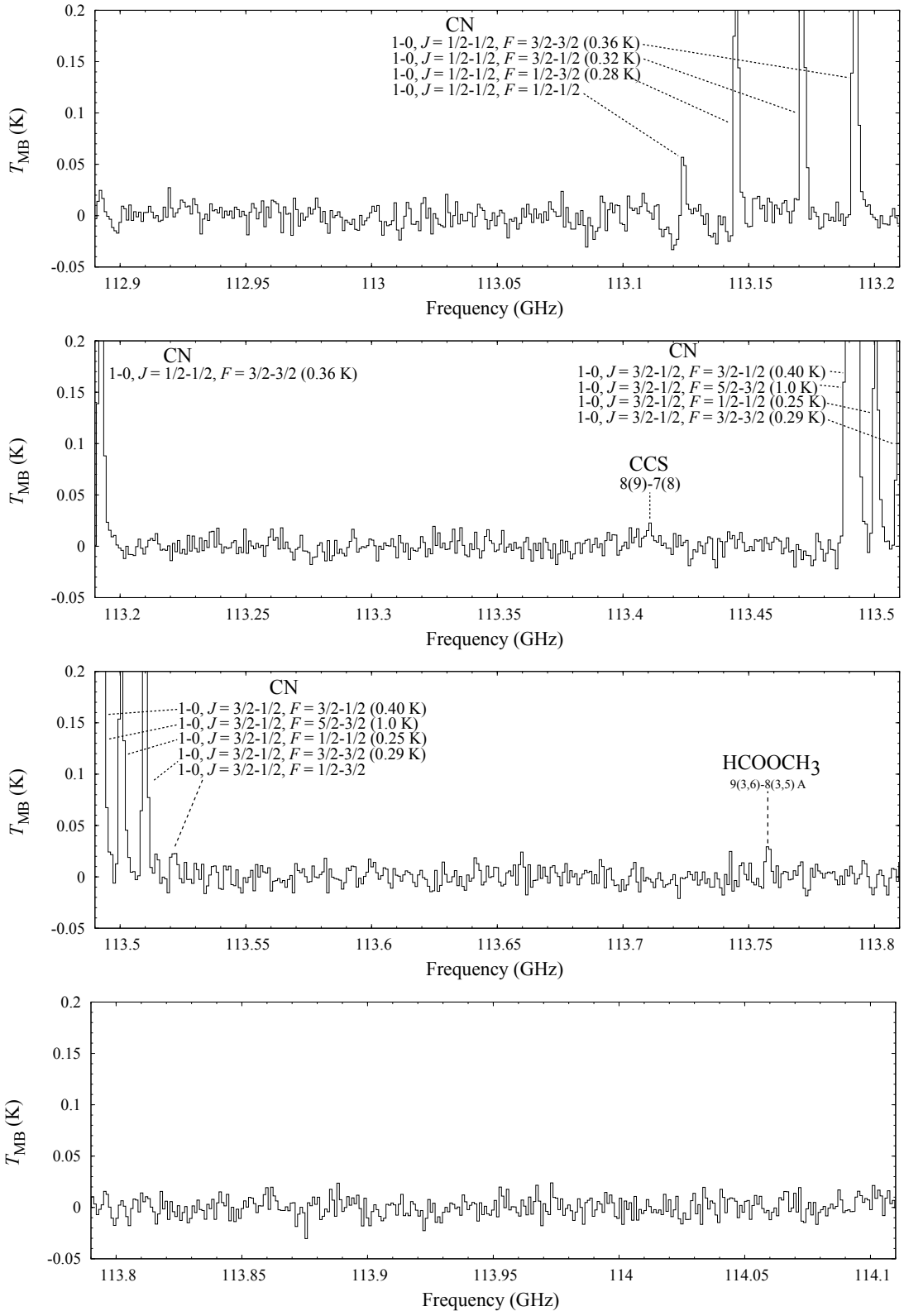

Figure A.1: continued

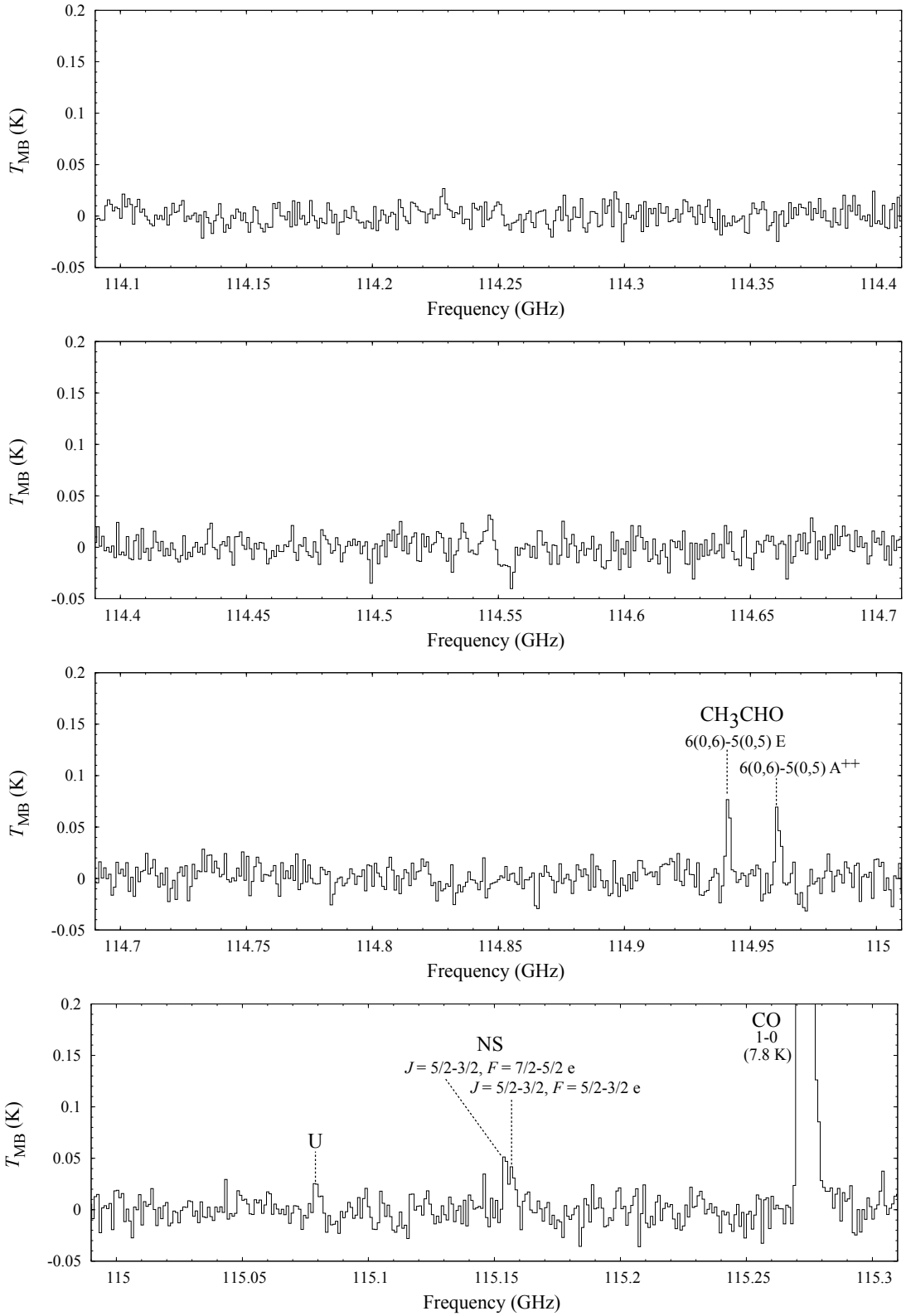

Figure A.1: continued

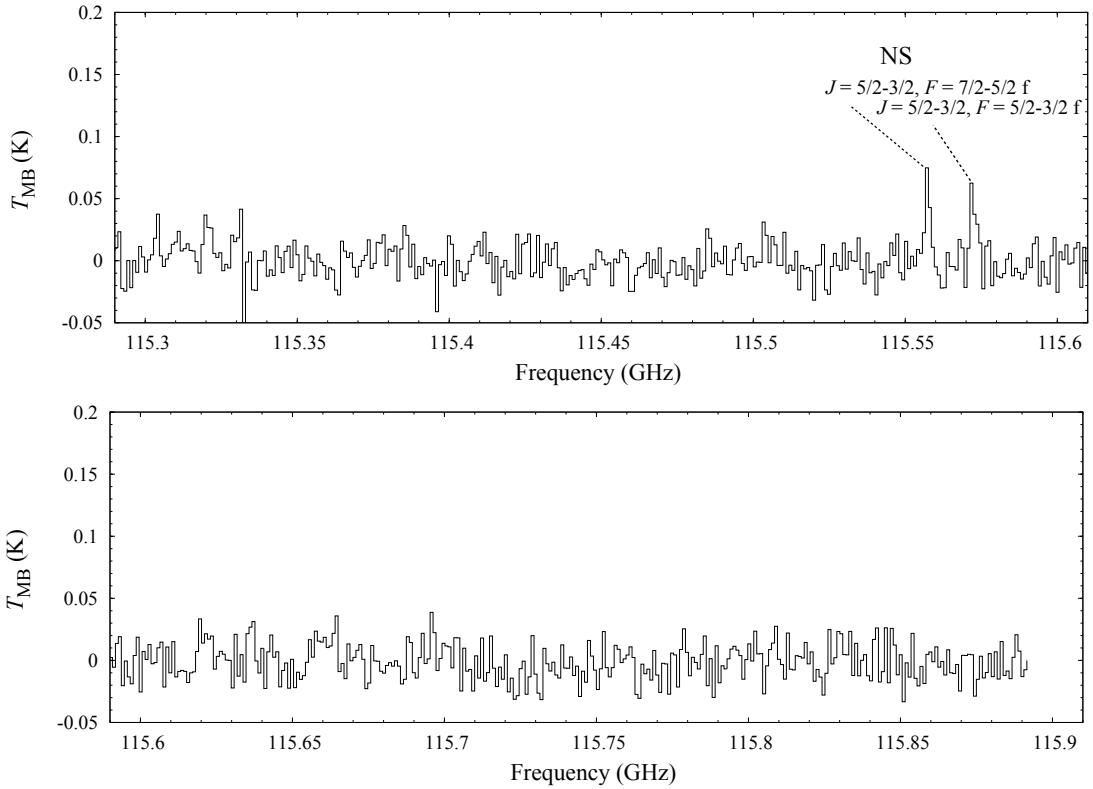

Figure A.1: continued

Appendix B

Spectrum of IC 443 G I

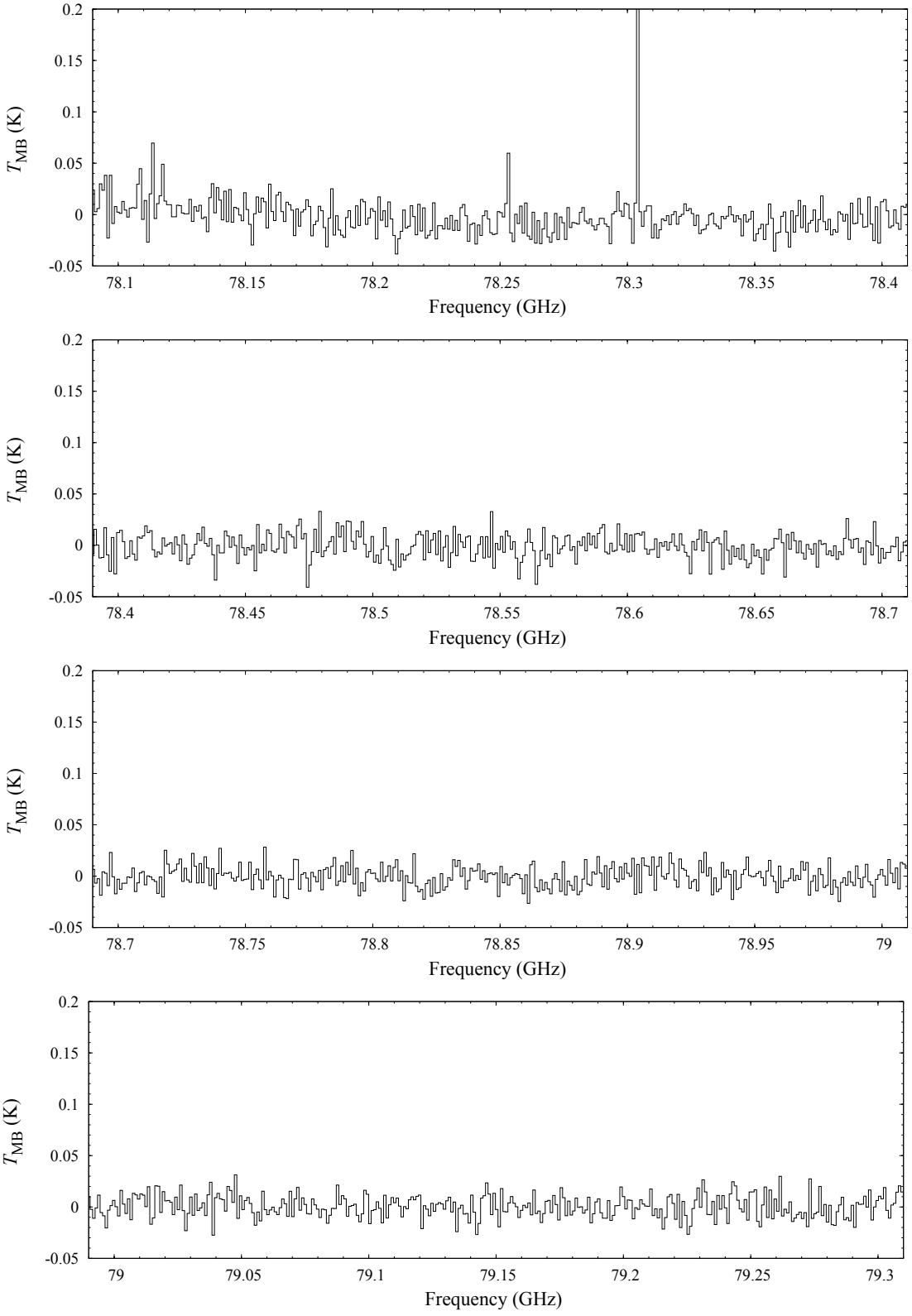

Figure B.1: continued

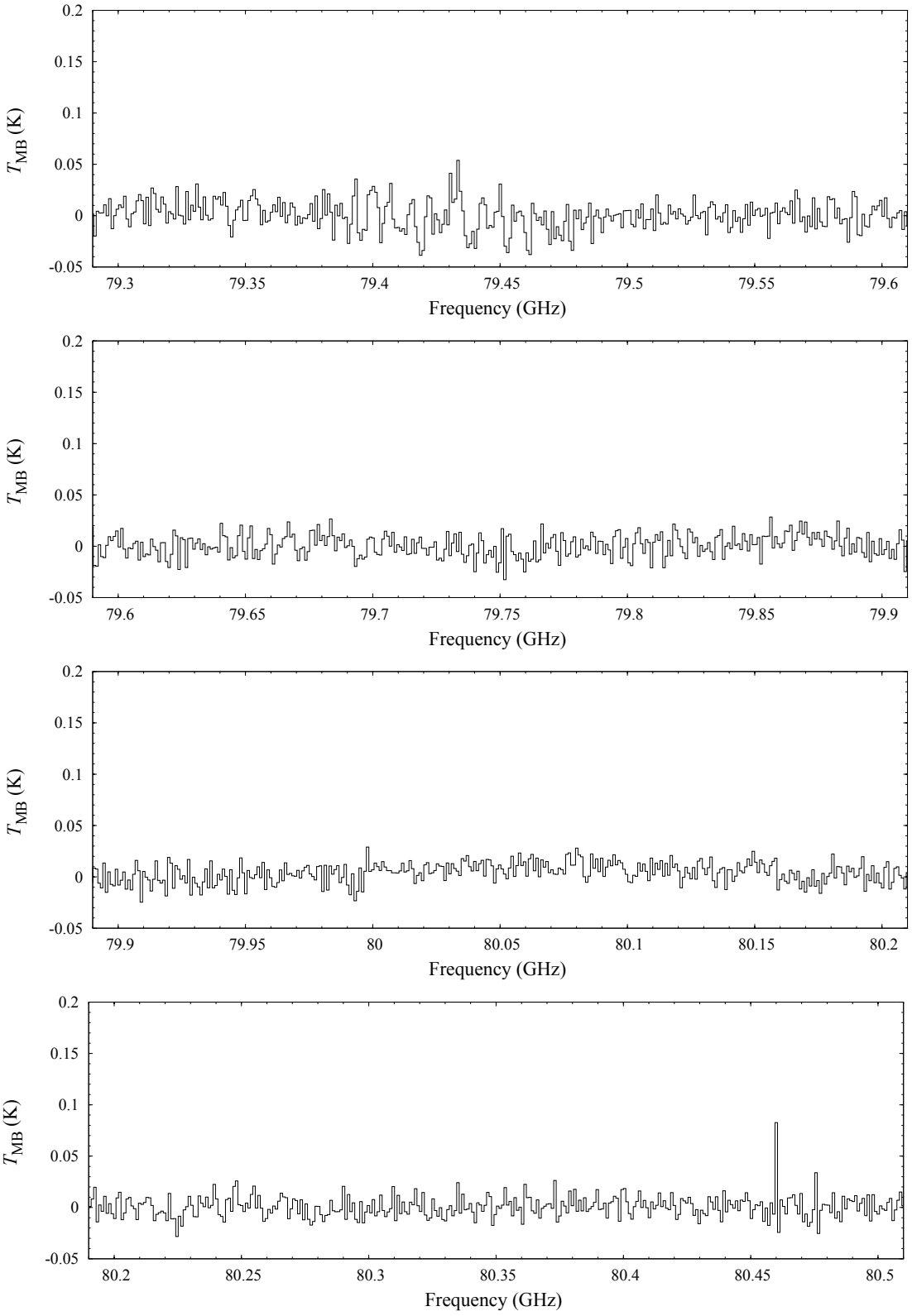

Figure B.1: continued

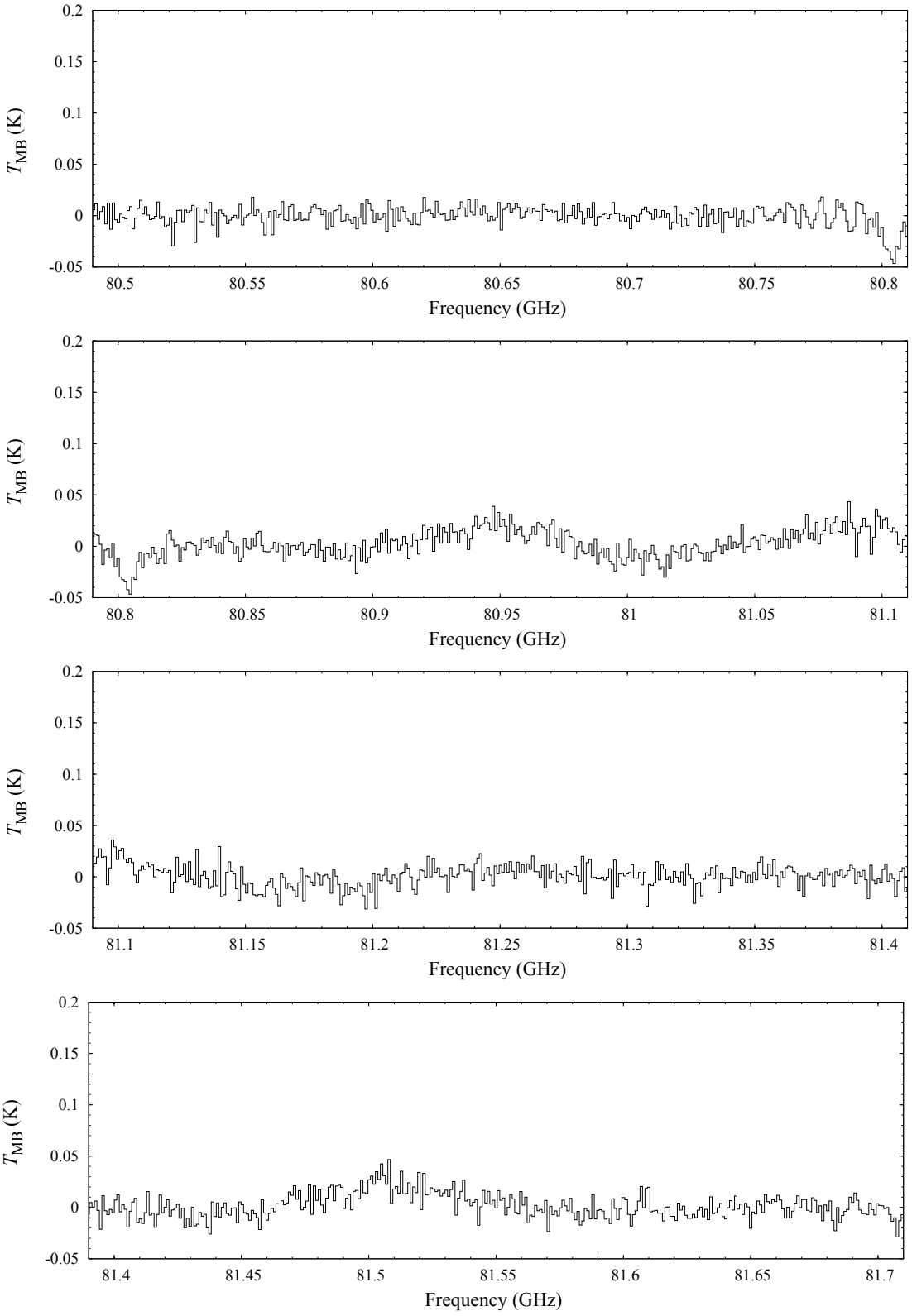

Figure B.1: continued

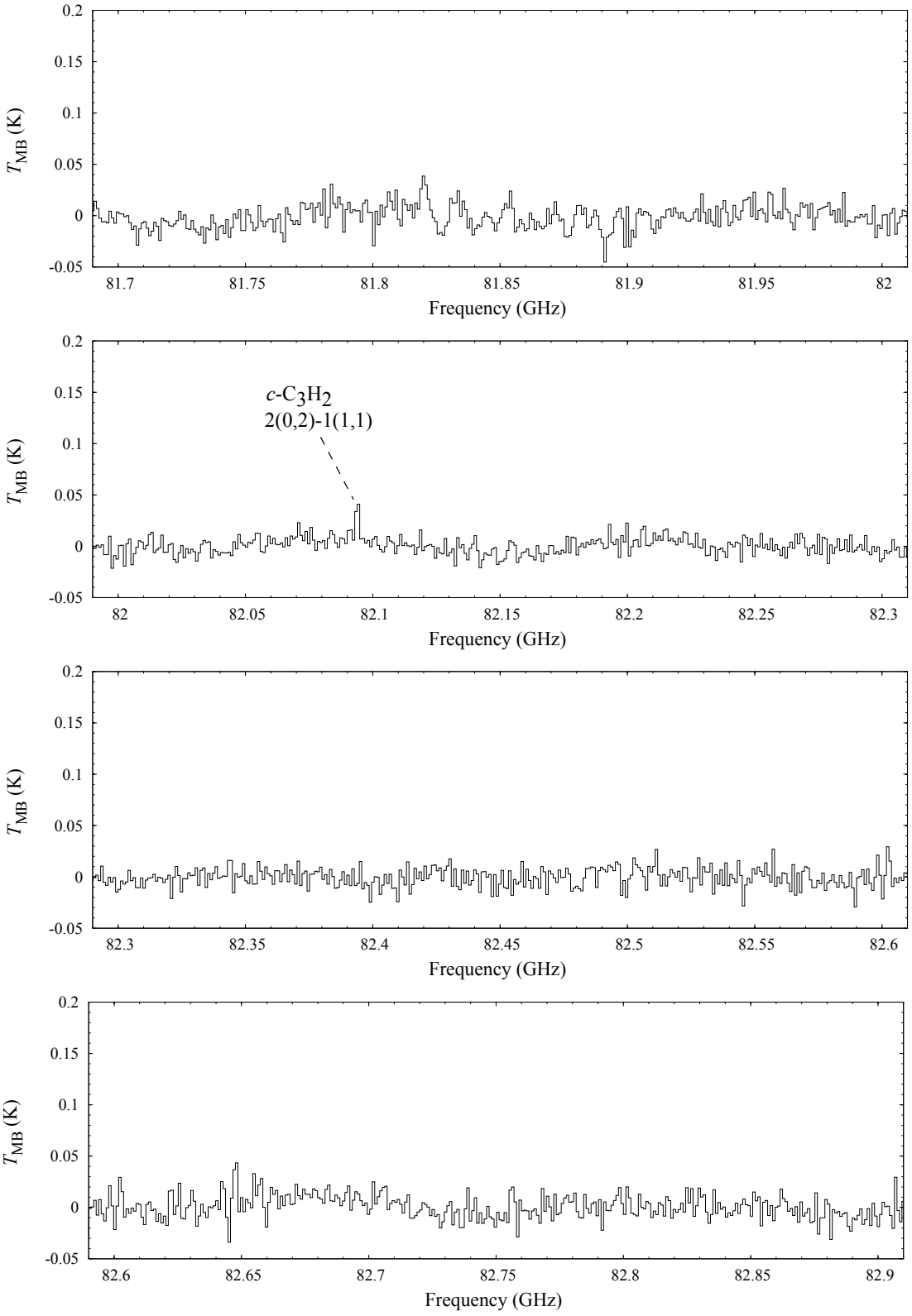

Figure B.1: continued

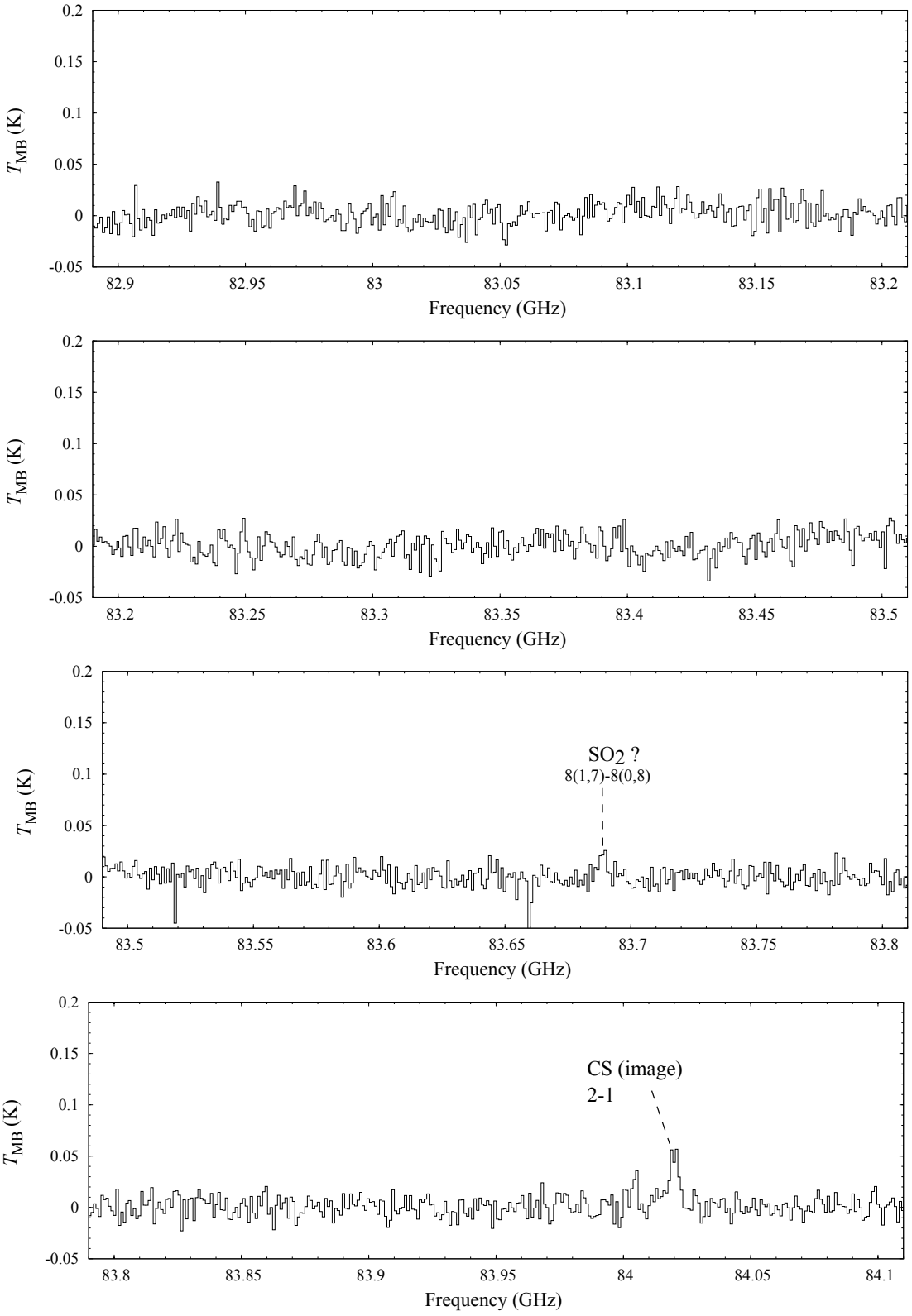

Figure B.1: continued

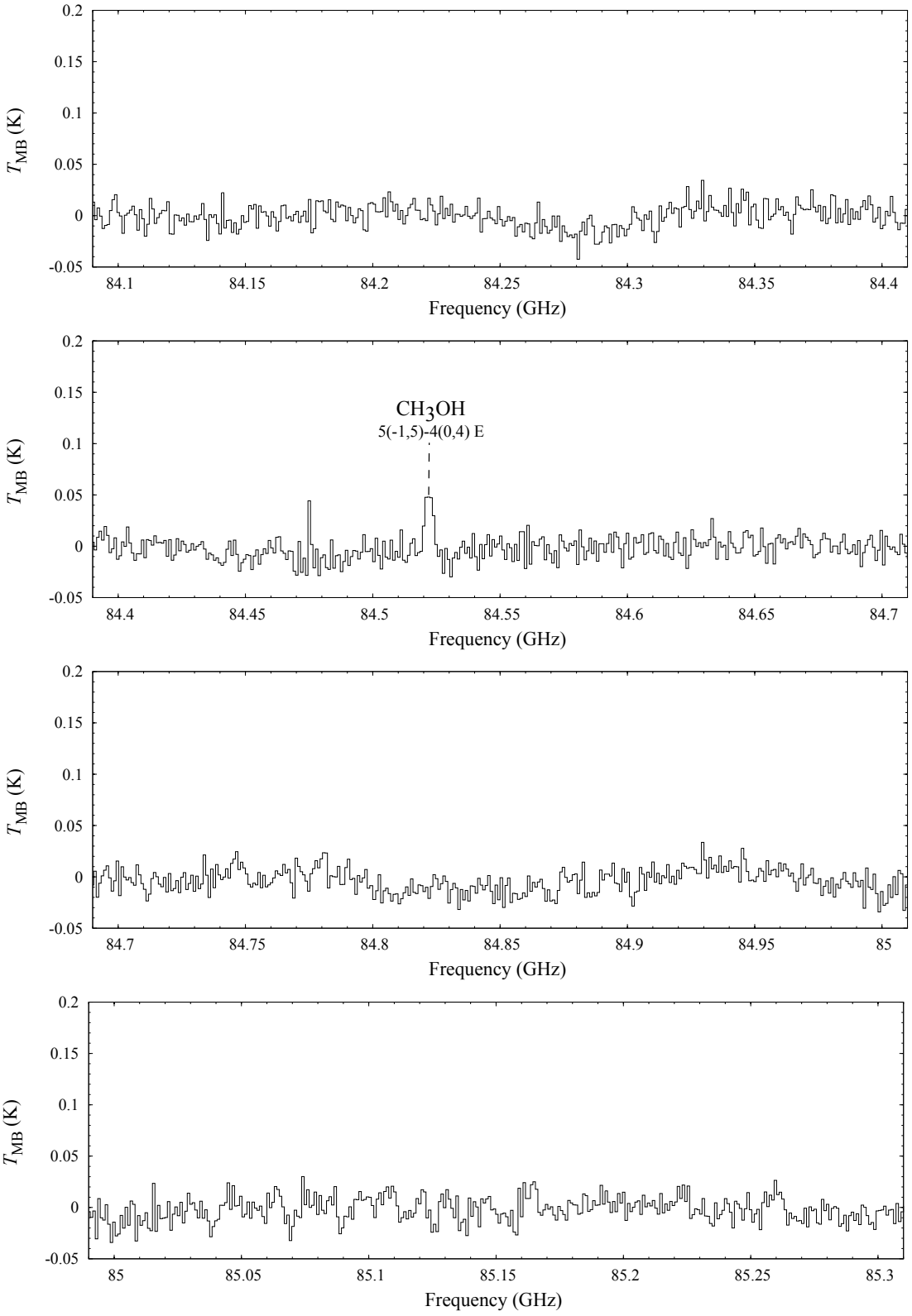

Figure B.1: continued

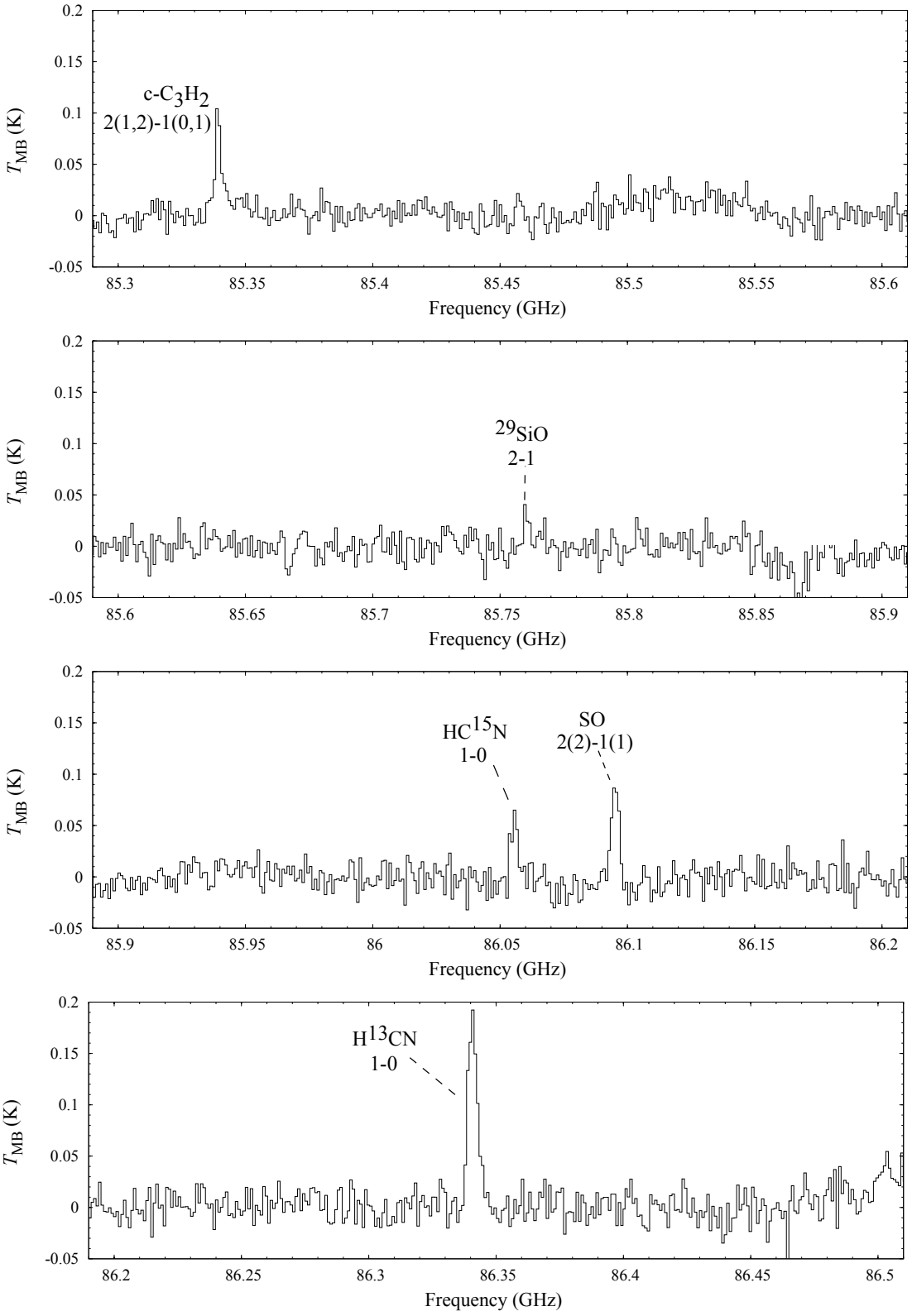

Figure B.1: continued

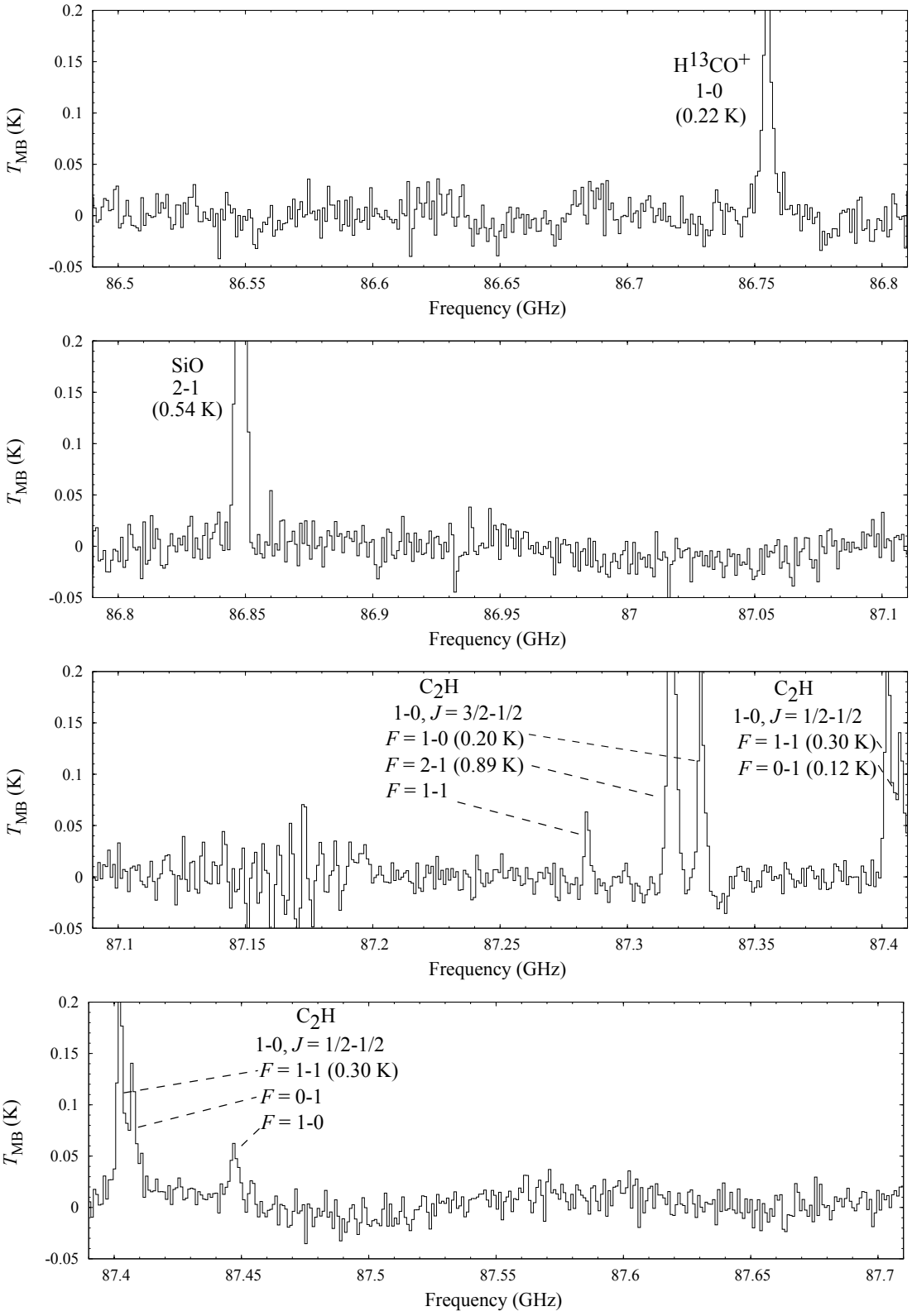

Figure B.1: continued

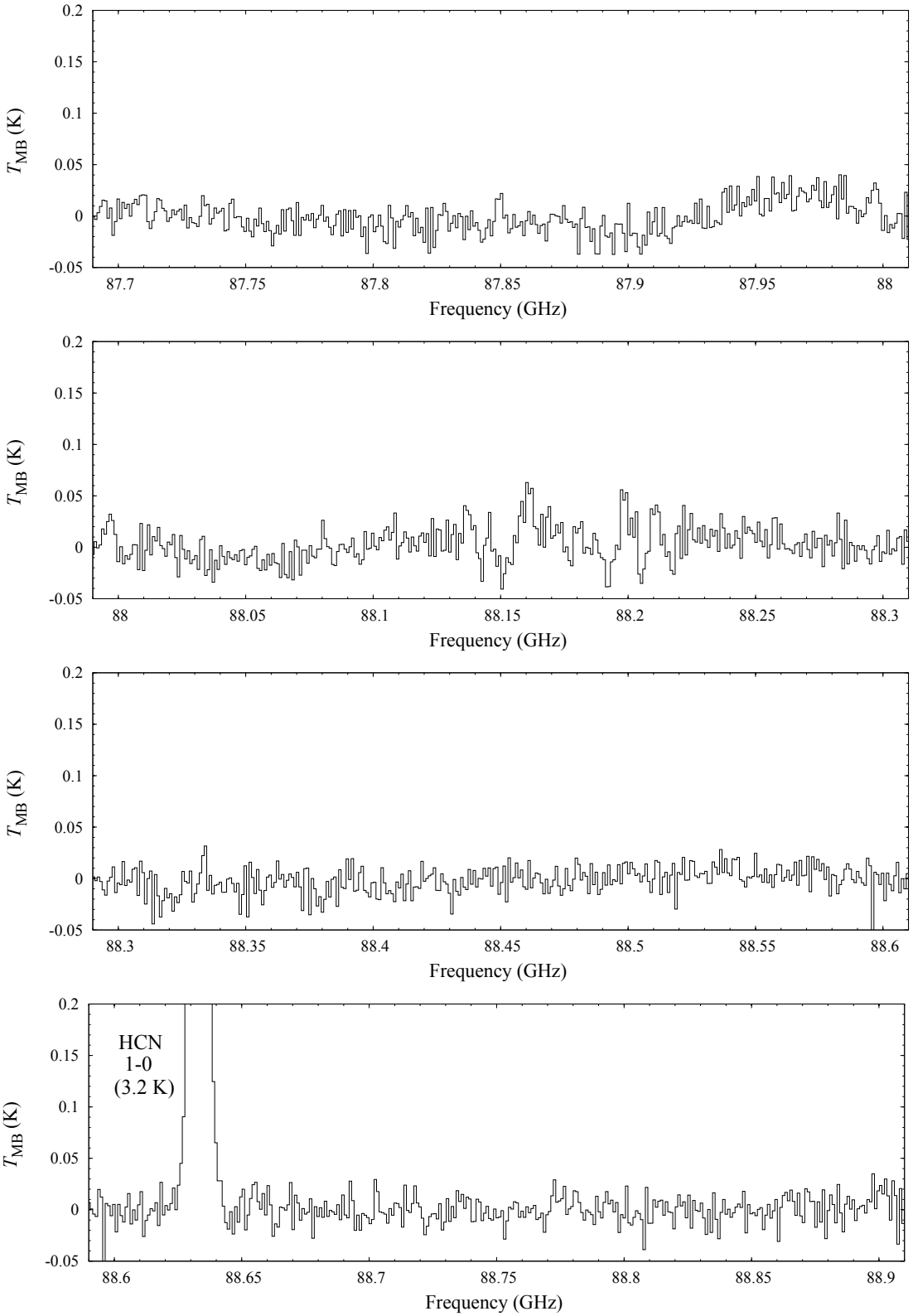

Figure B.1: continued

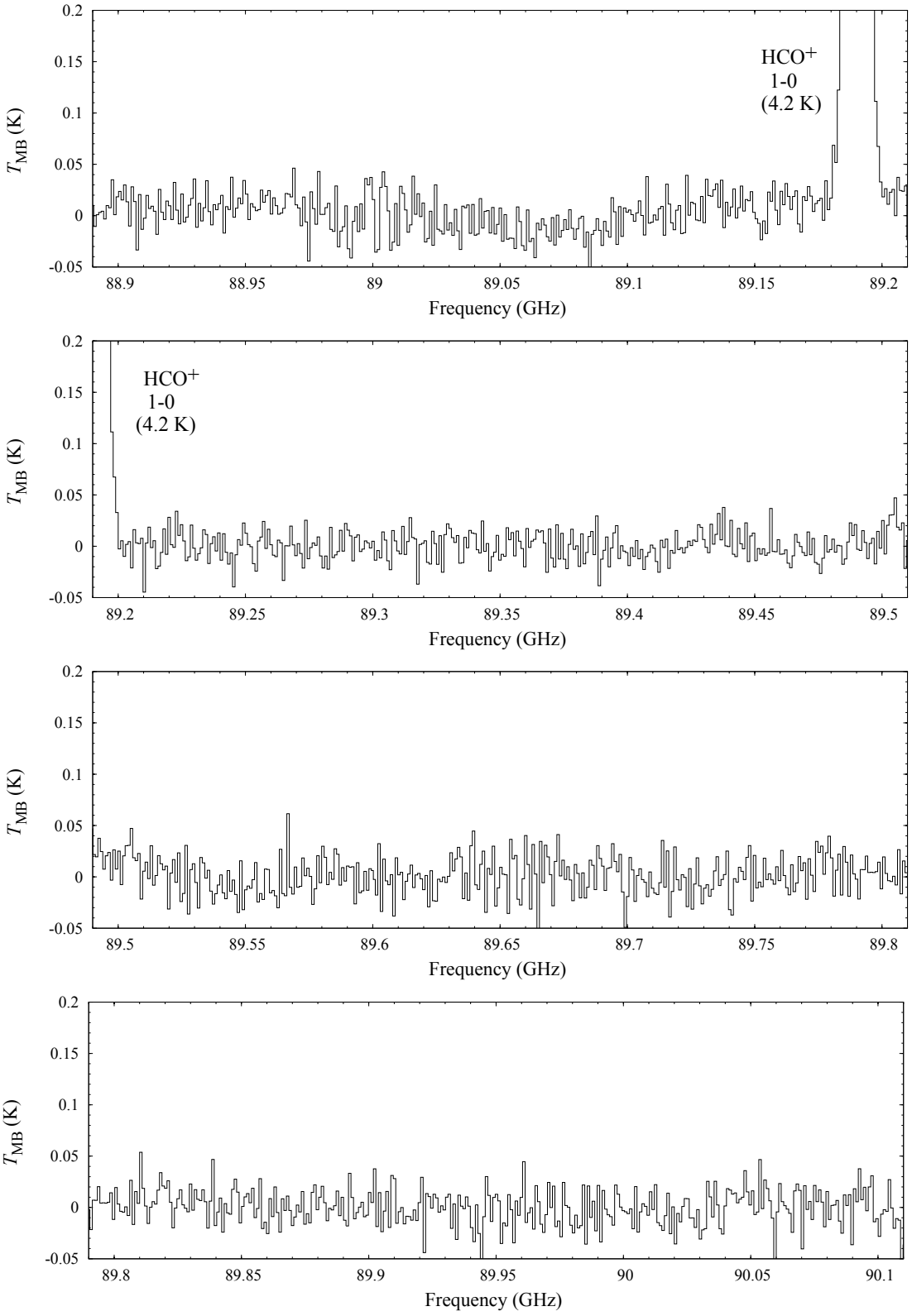

Figure B.1: continued

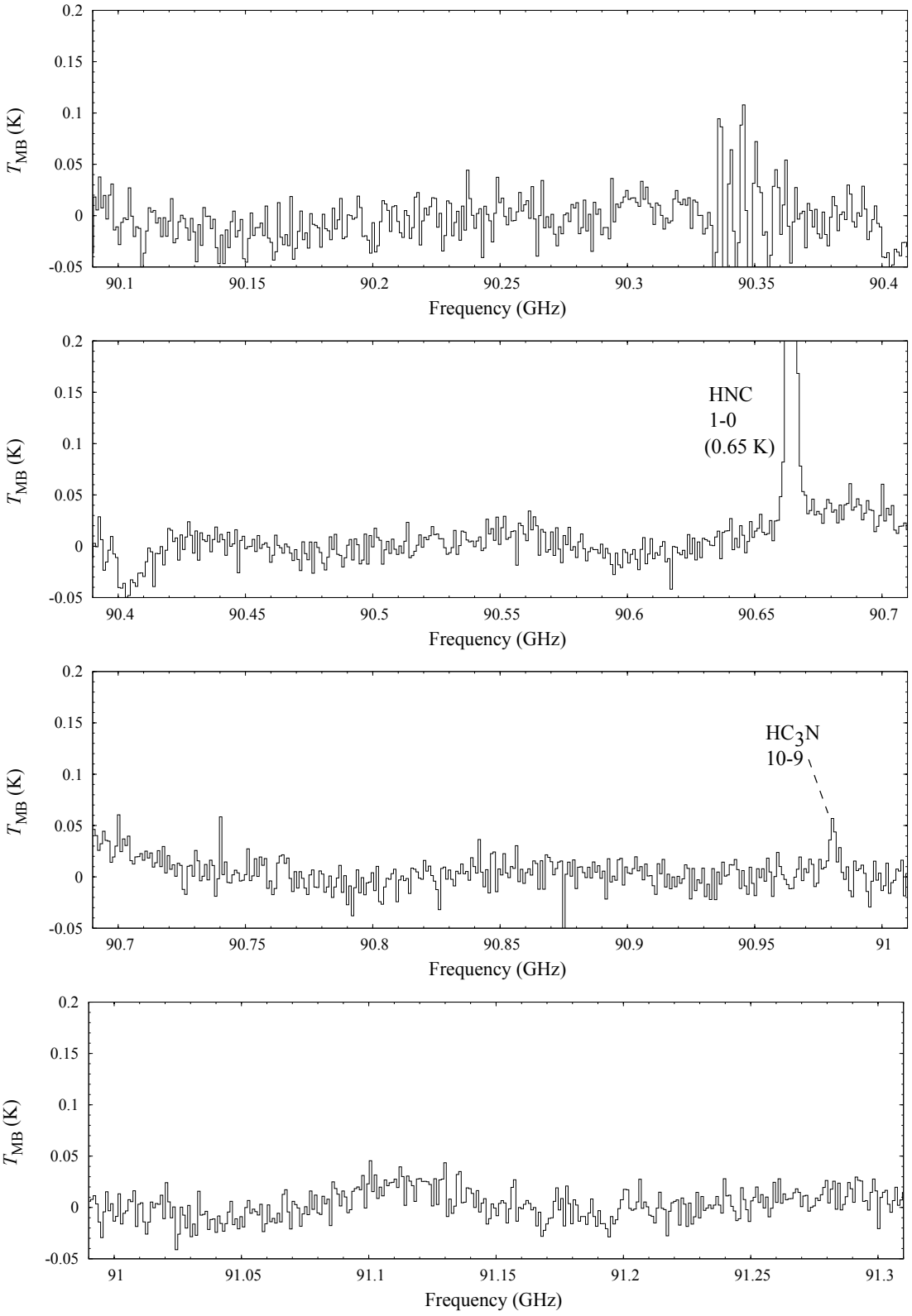

Figure B.1: continued

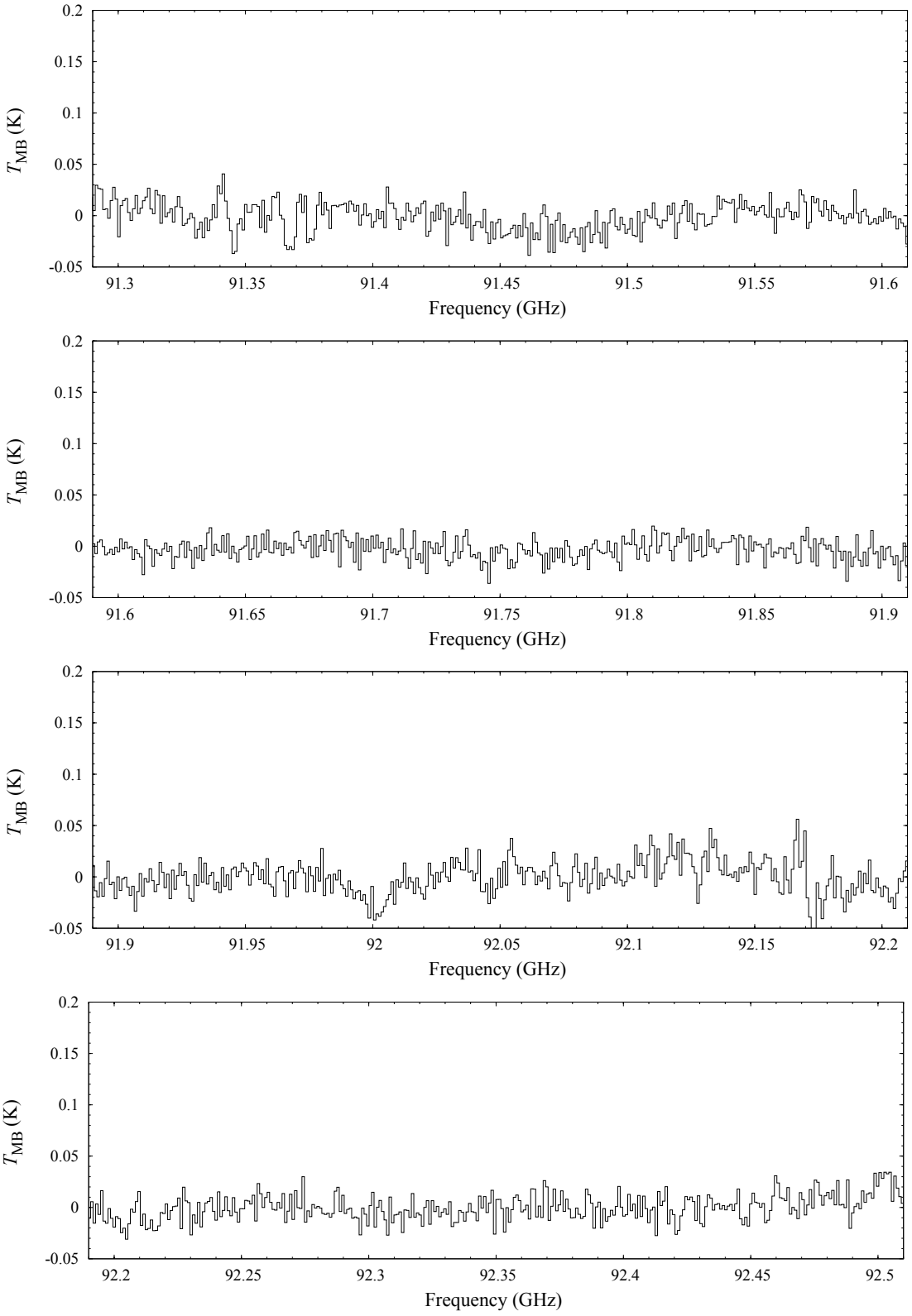

Figure B.1: continued

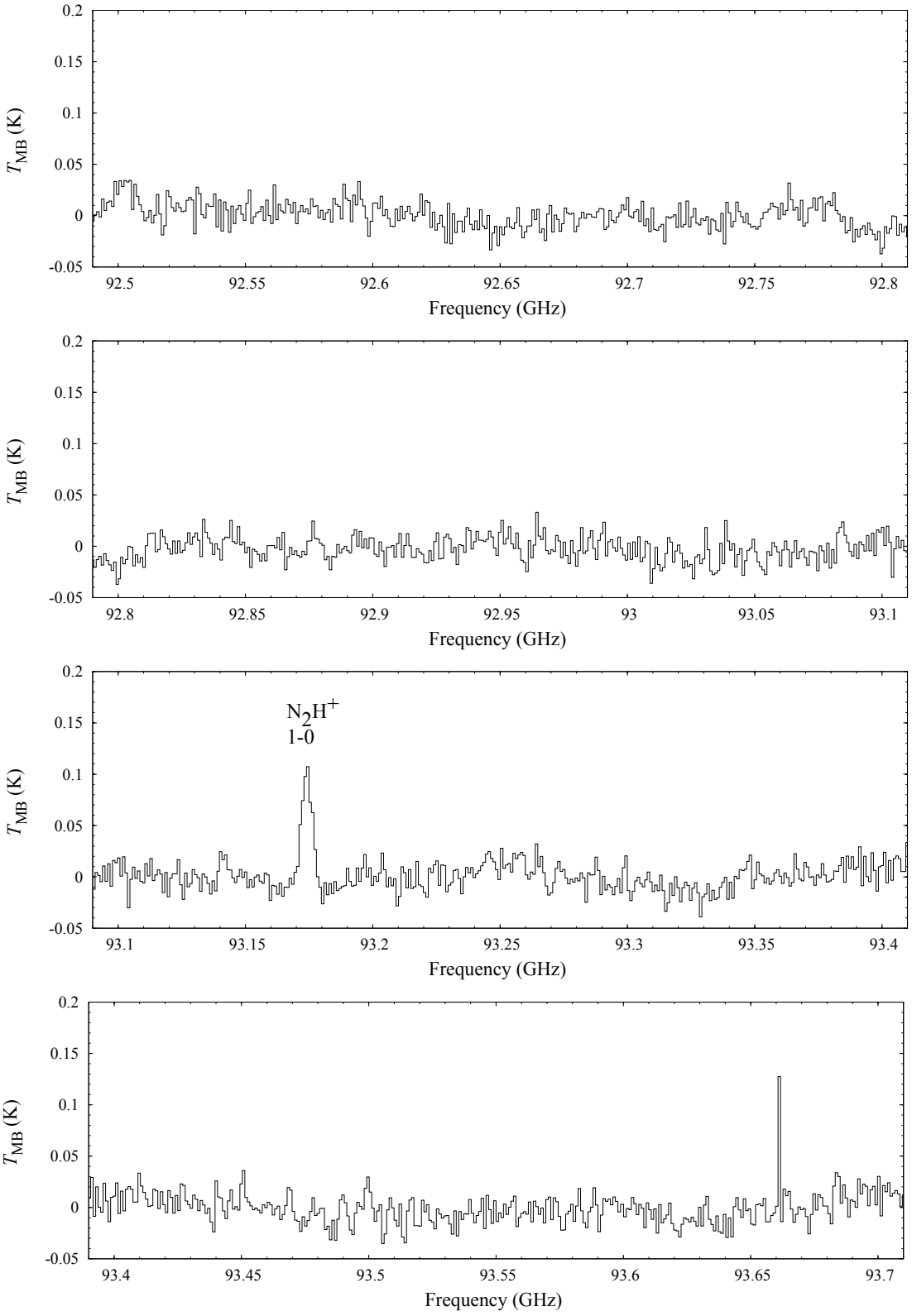

Figure B.1: continued

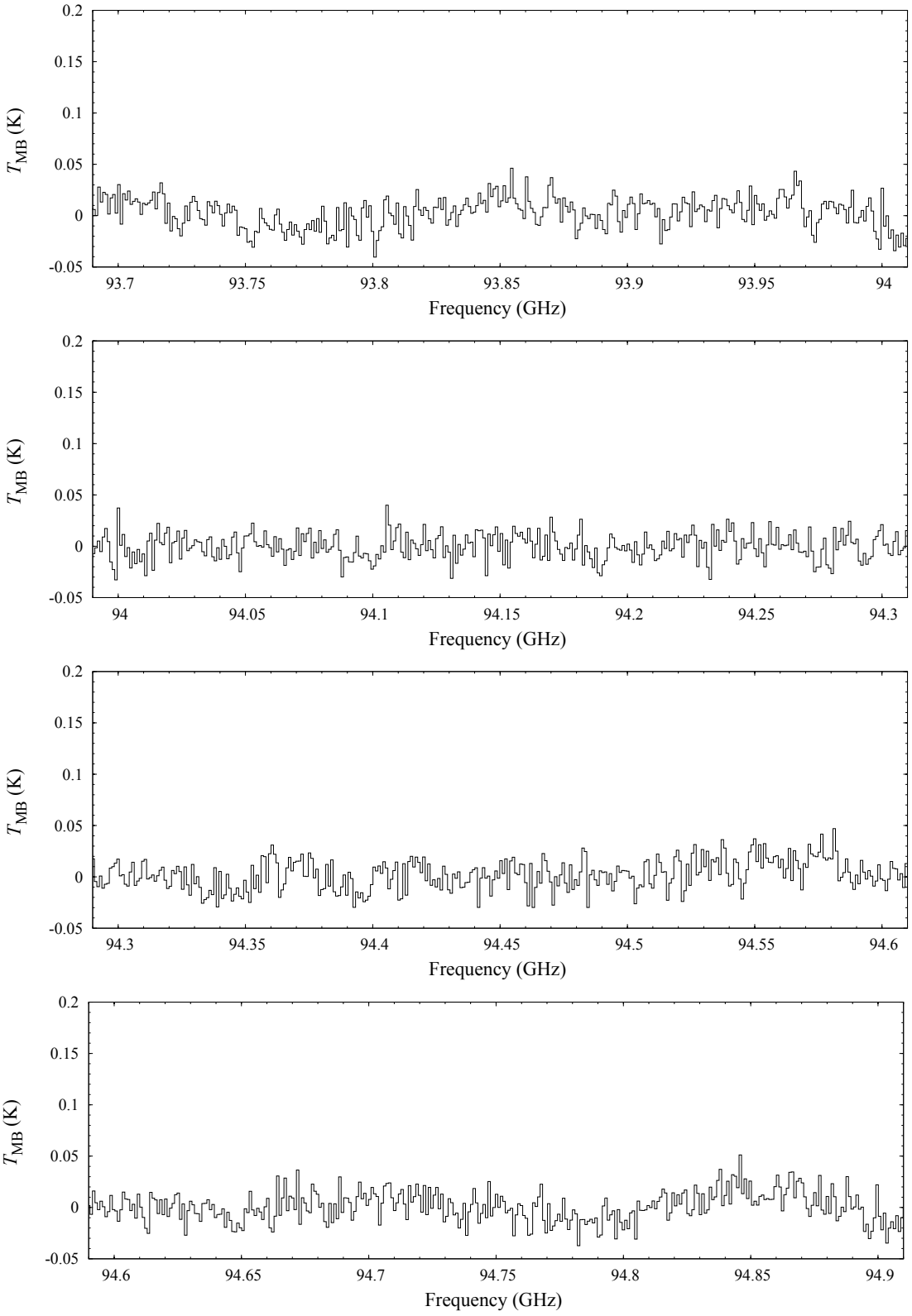

Figure B.1: continued

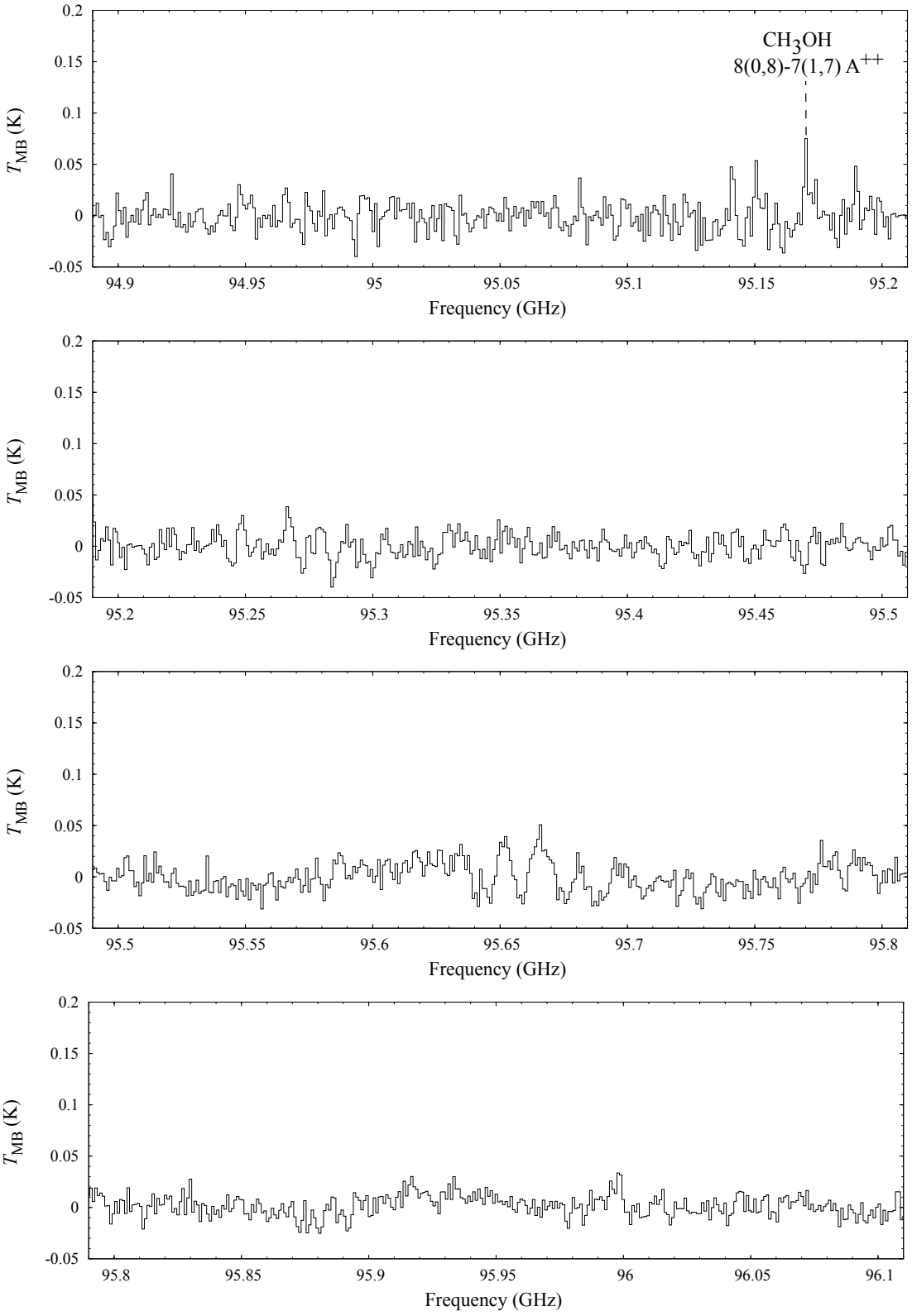

Figure B.1: continued

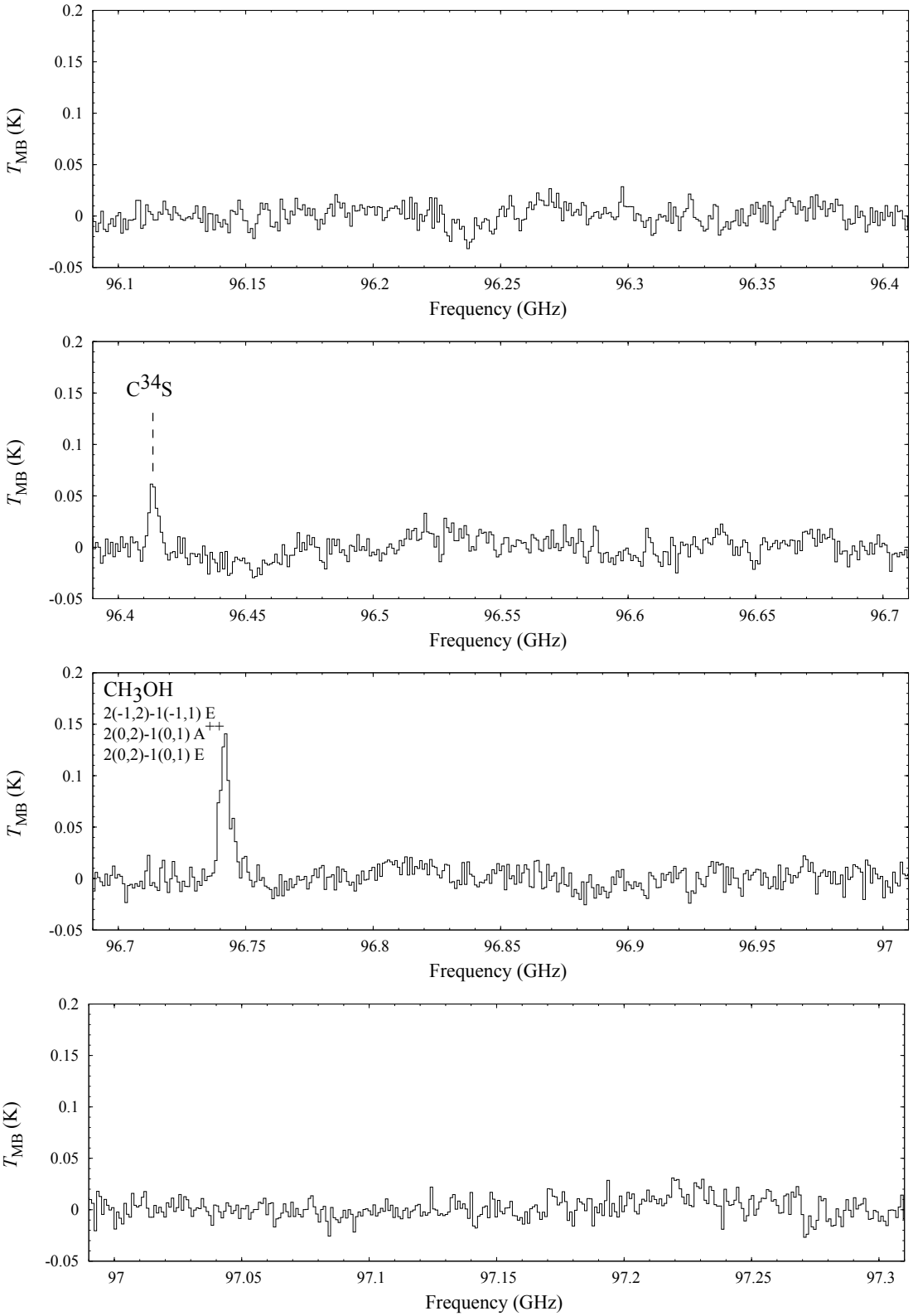

Figure B.1: continued

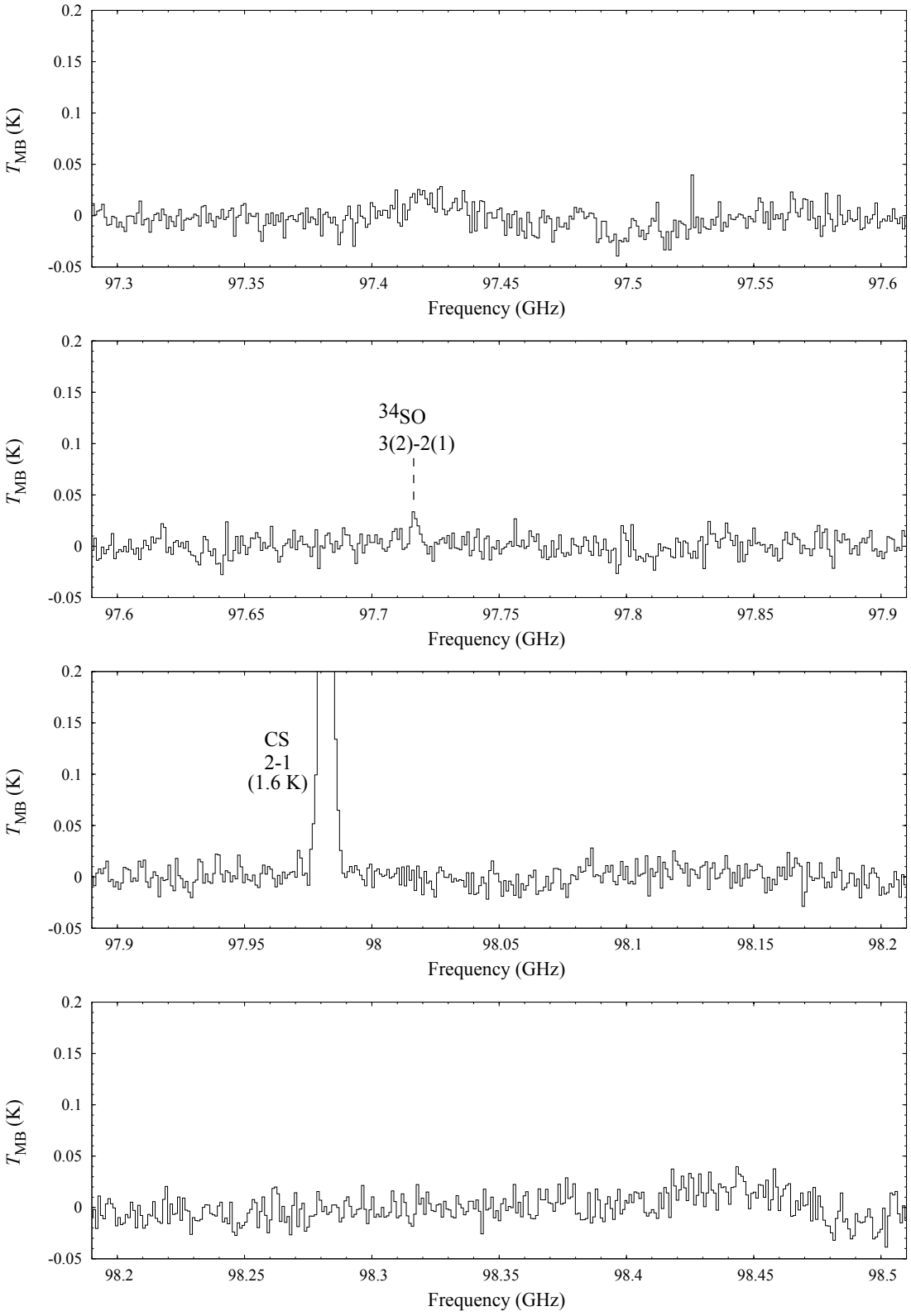

Figure B.1: continued

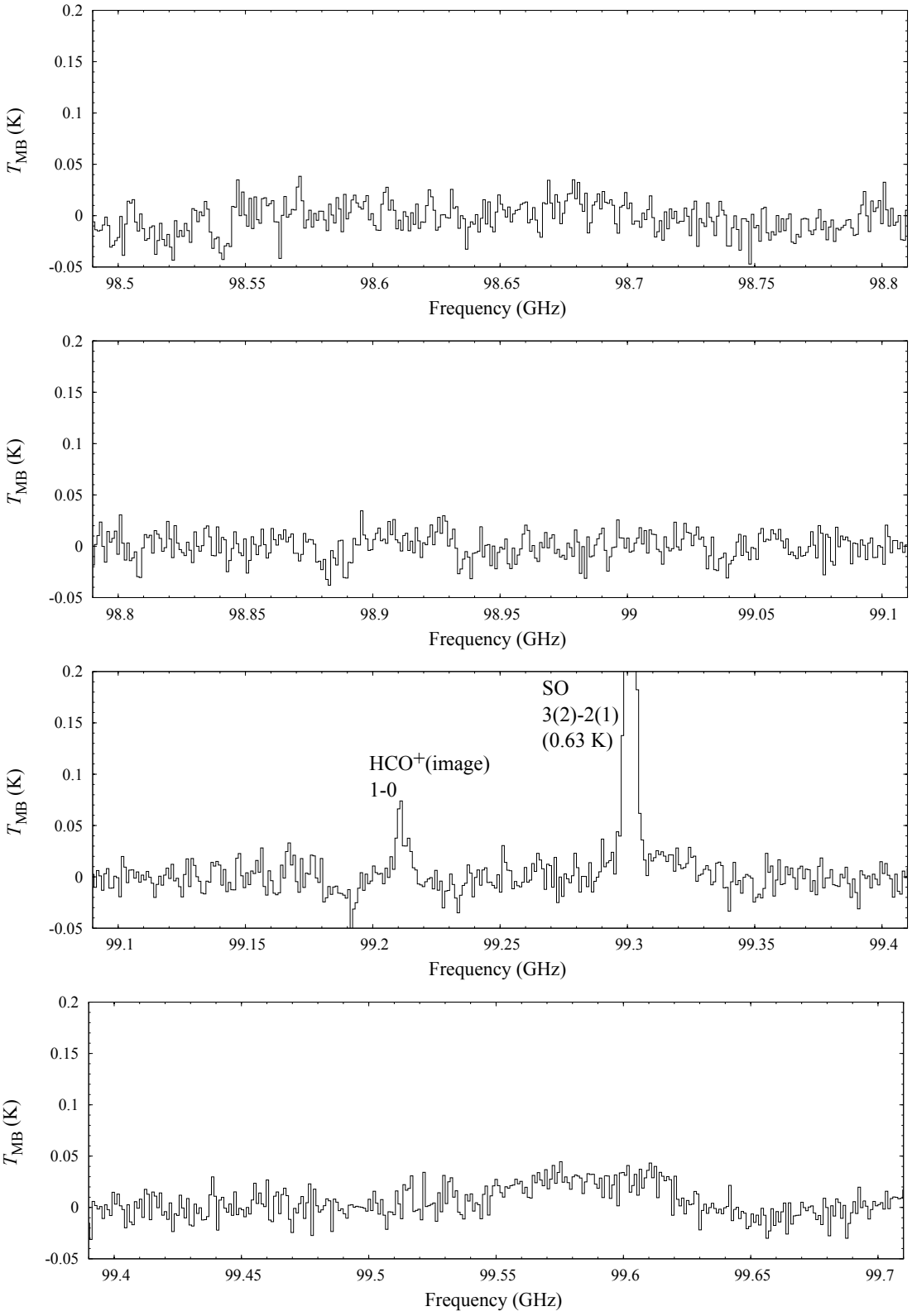

Figure B.1: continued

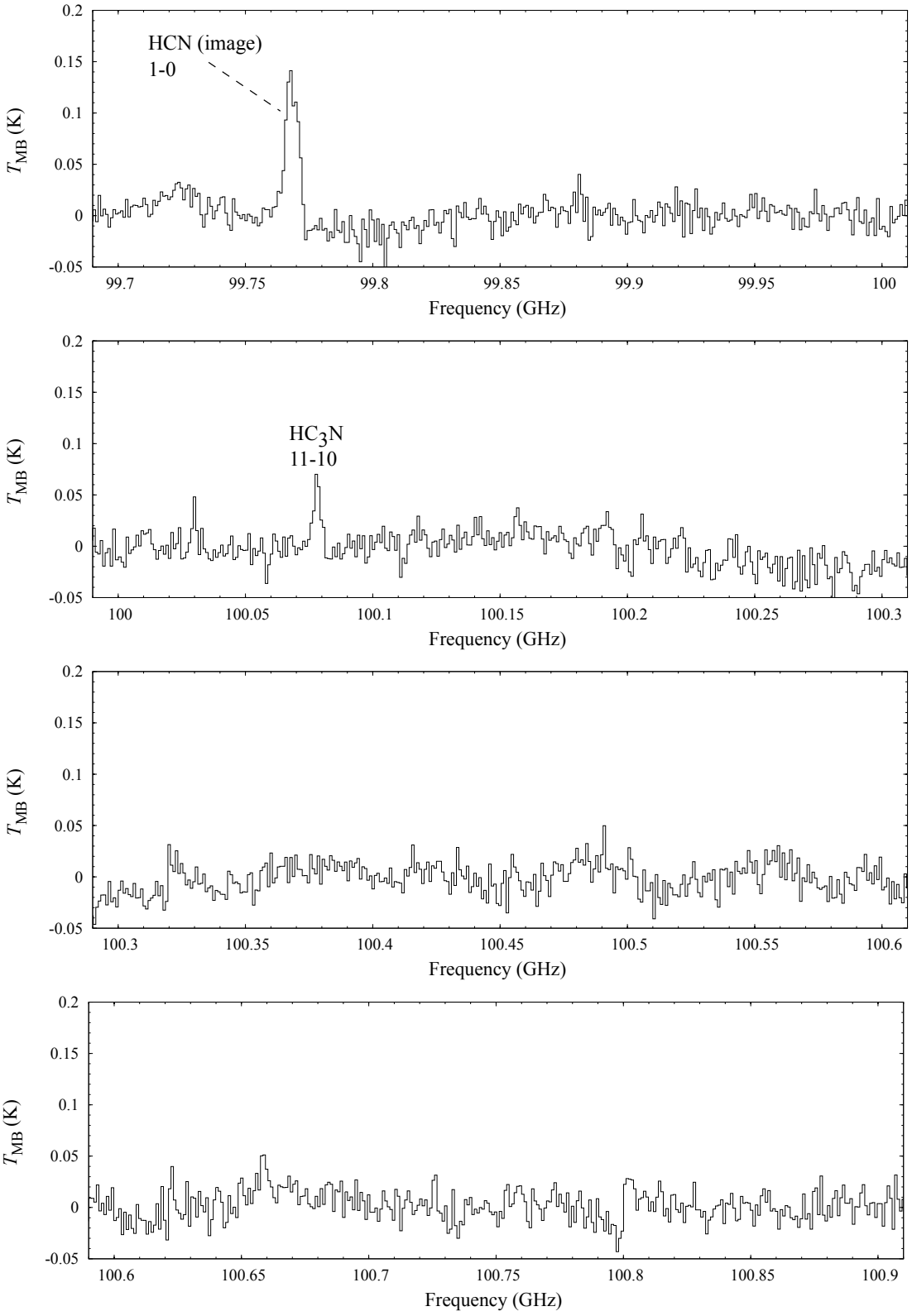

Figure B.1: continued

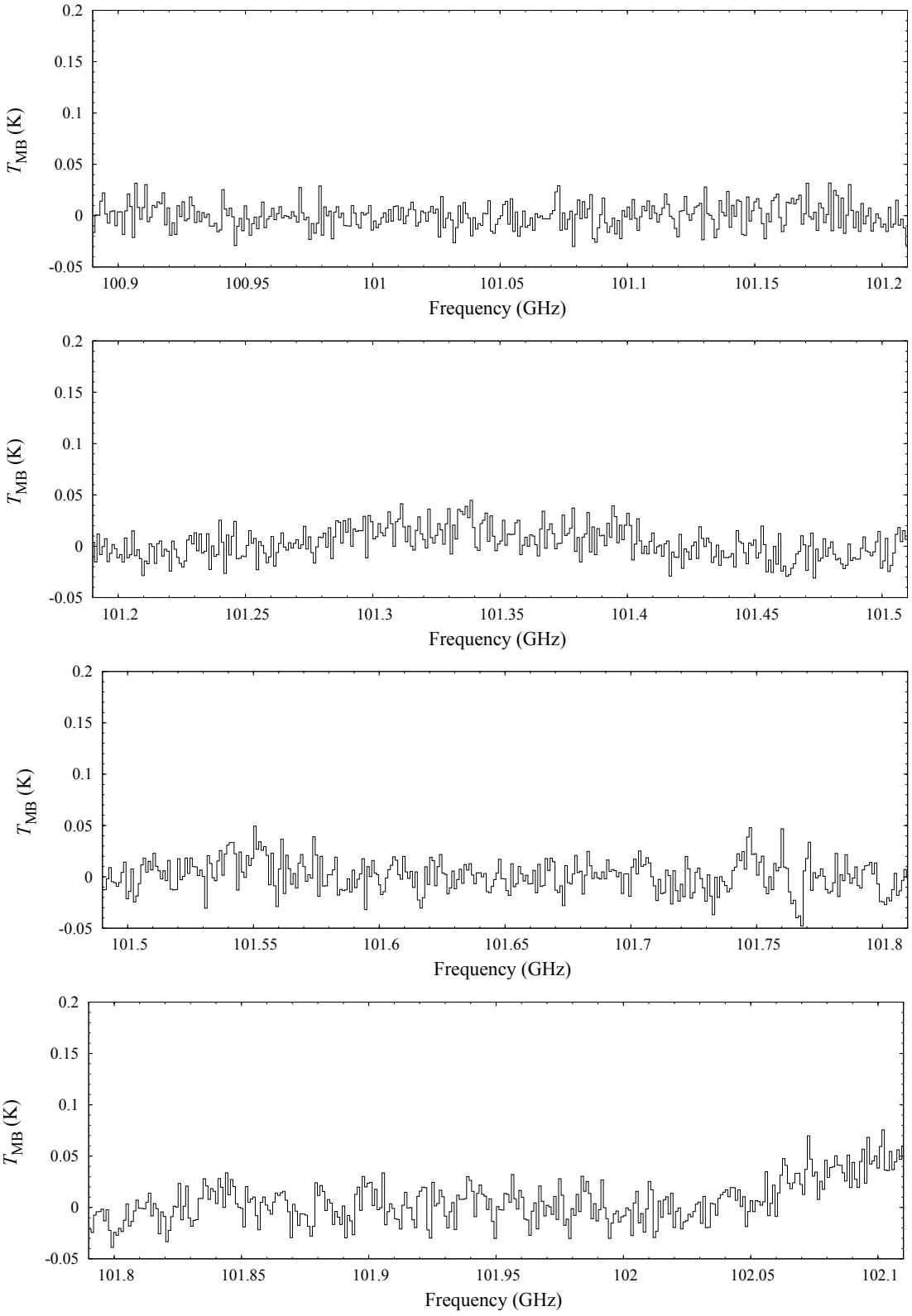

Figure B.1: continued

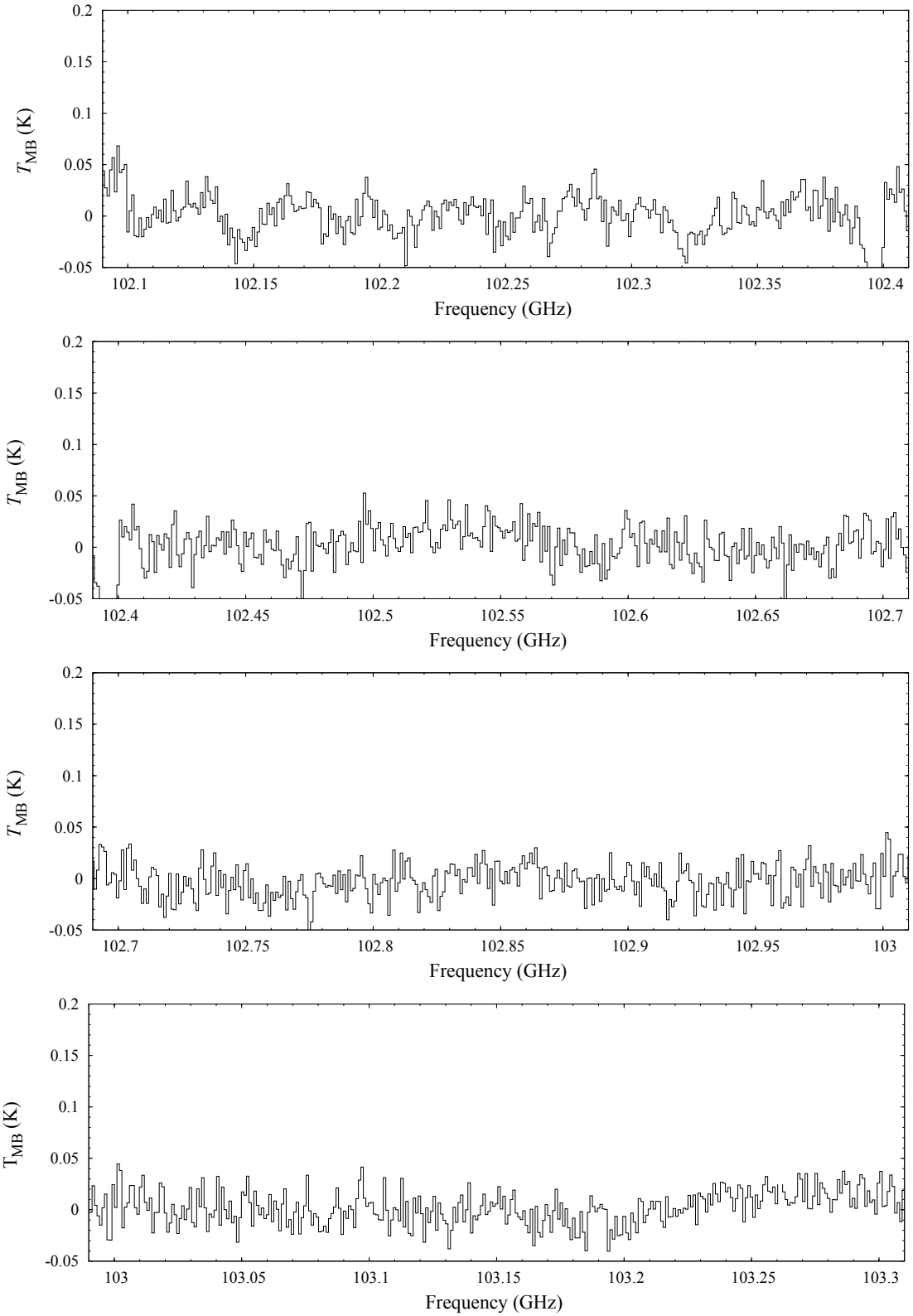

Figure B.1: continued

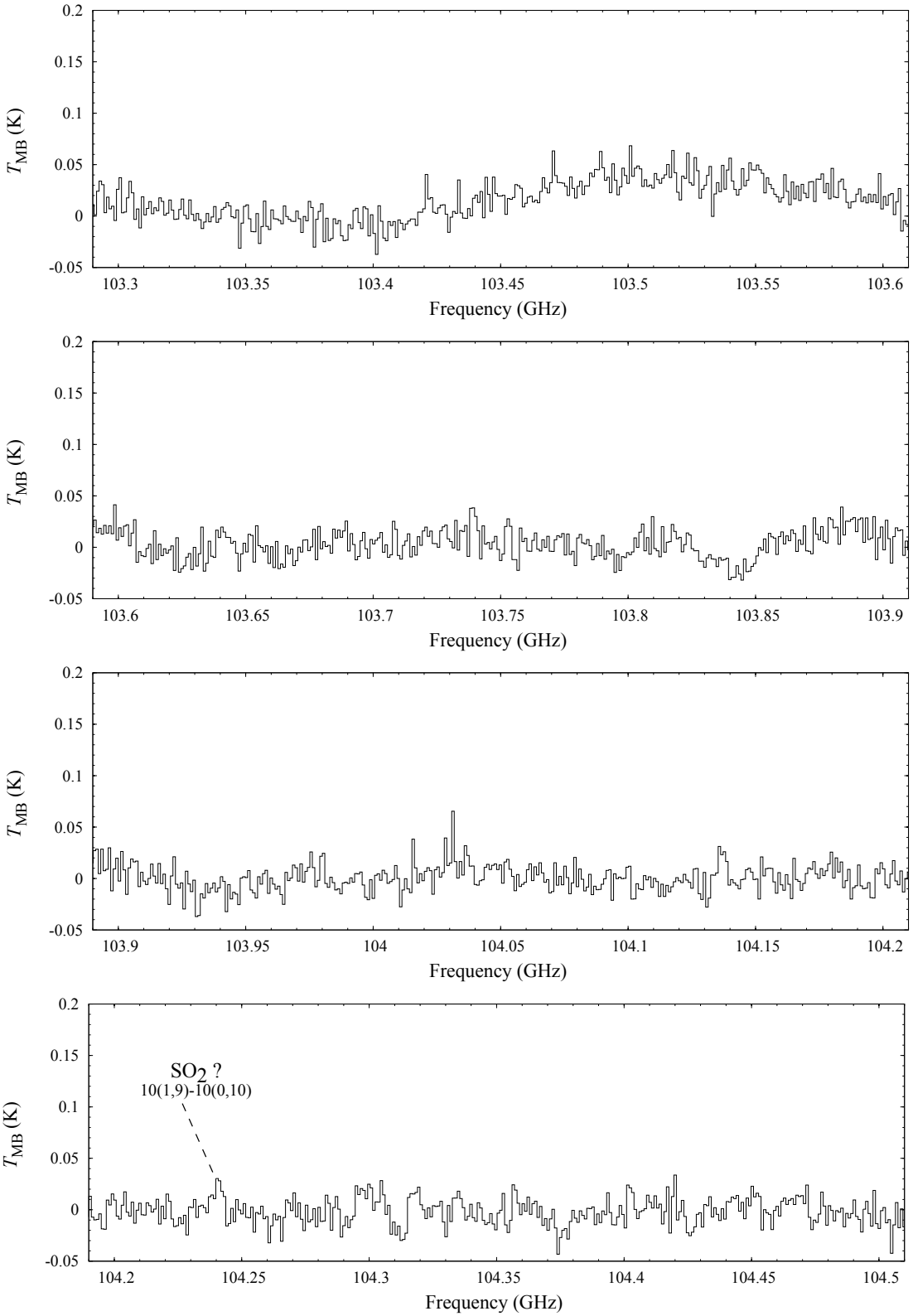

Figure B.1: continued

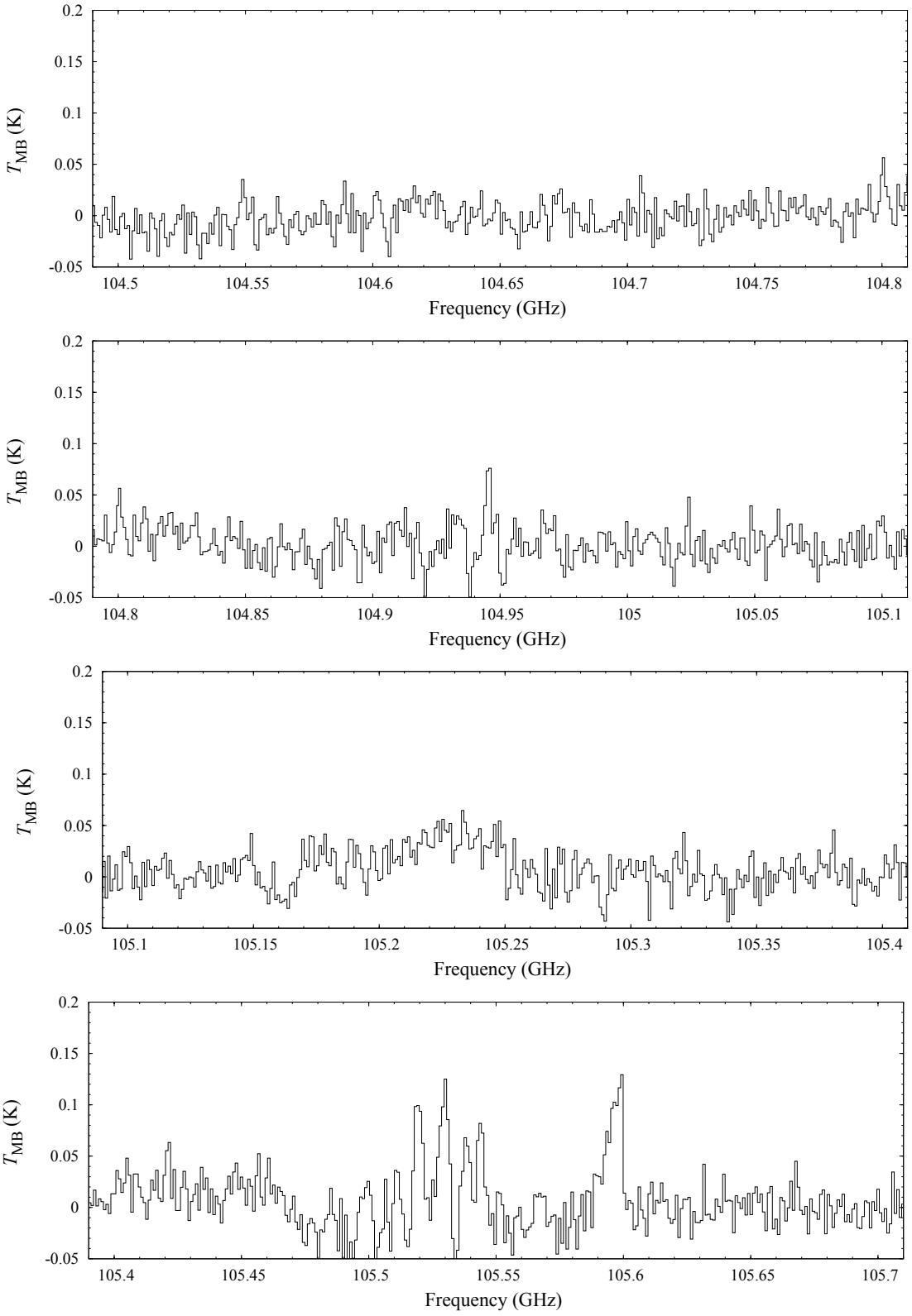

Figure B.1: continued

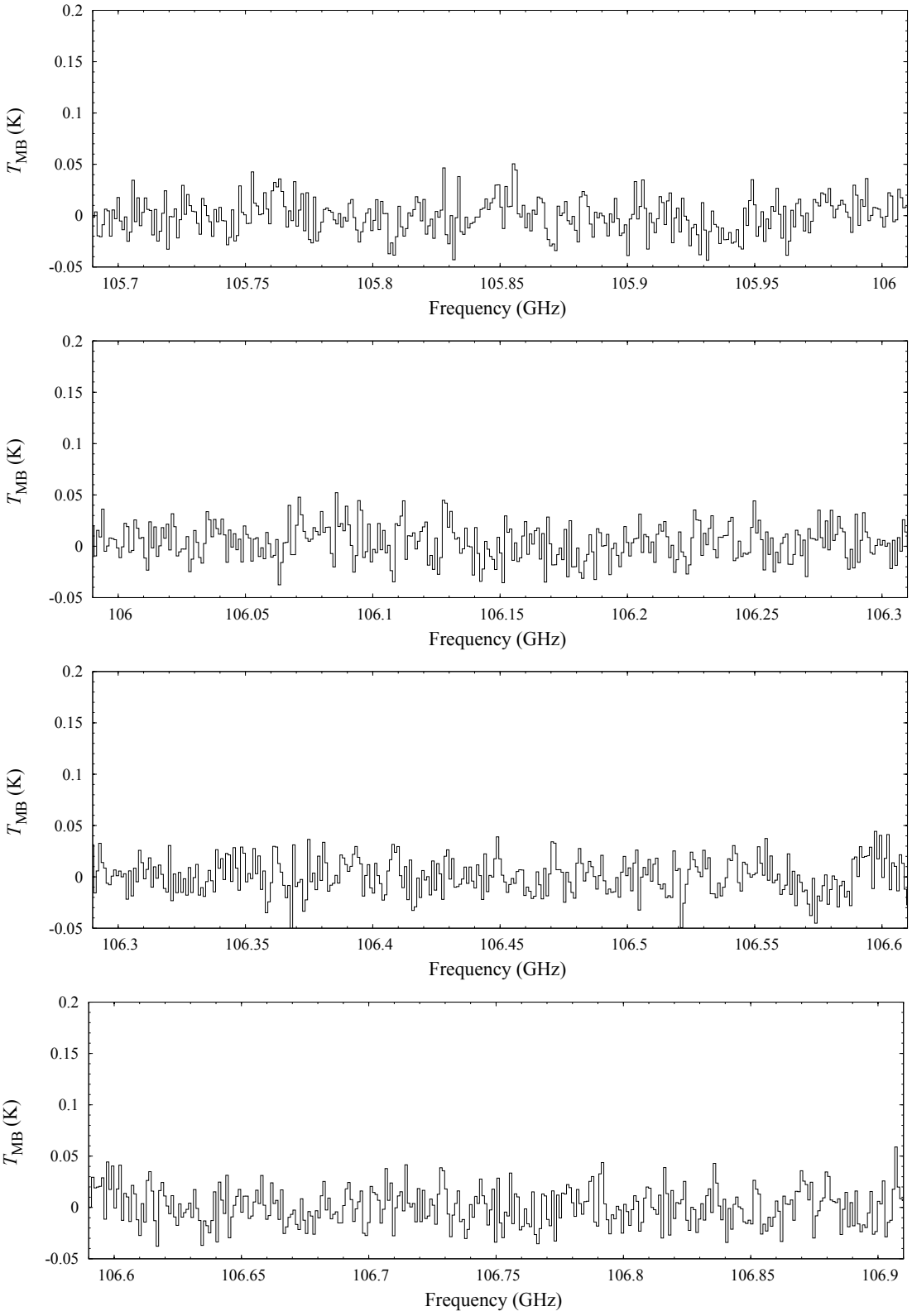

Figure B.1: continued

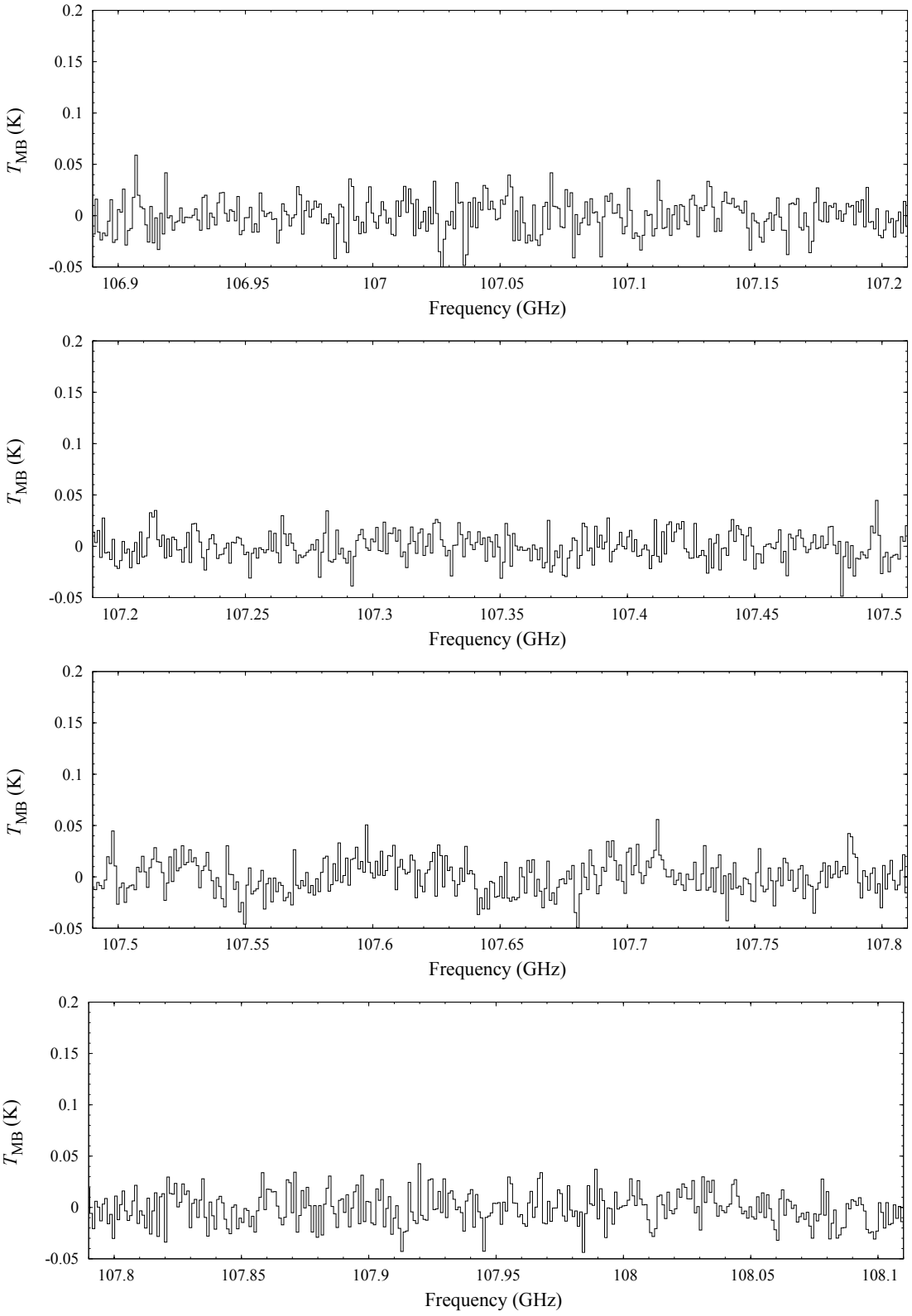

Figure B.1: continued

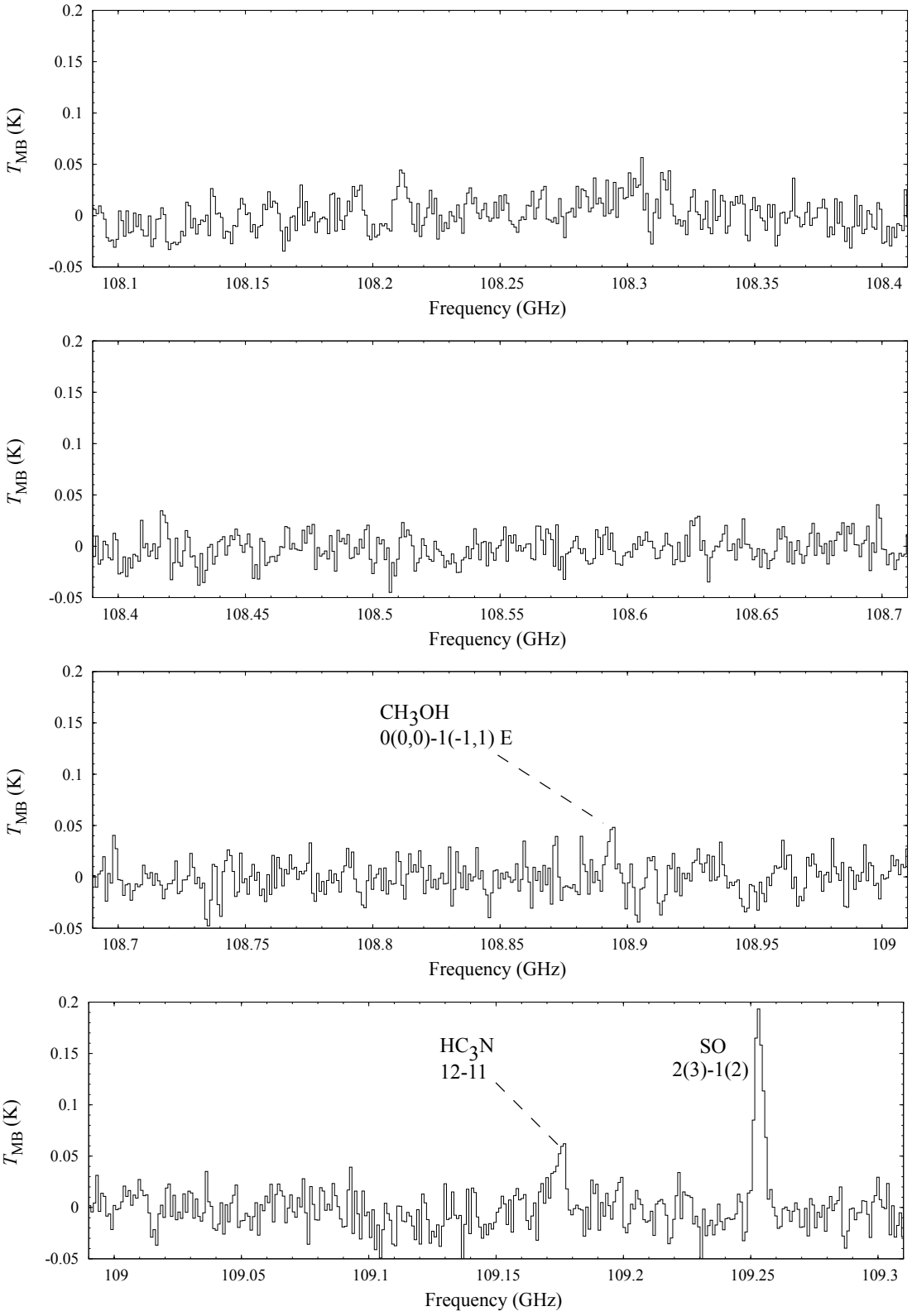

Figure B.1: continued

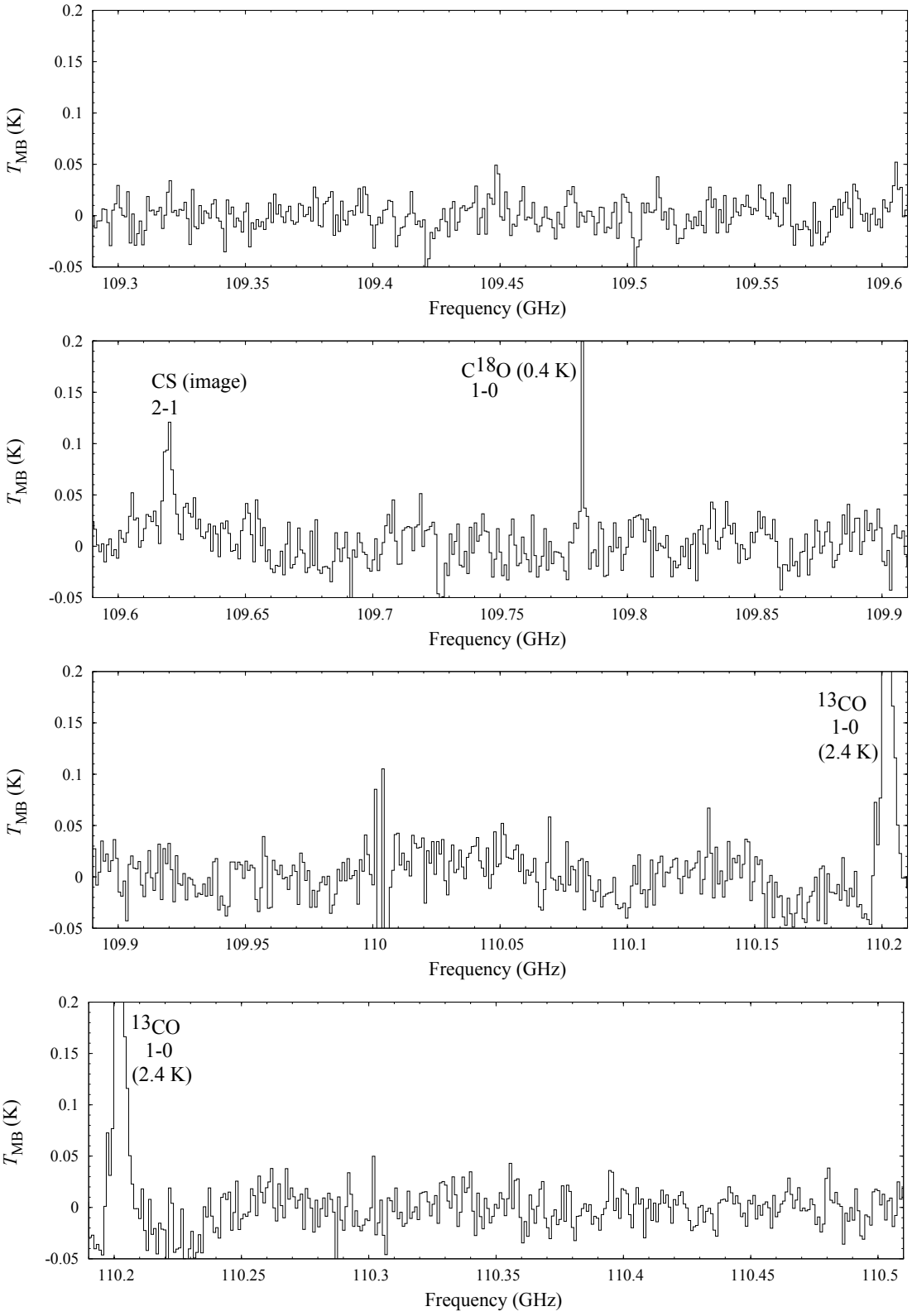

Figure B.1: continued

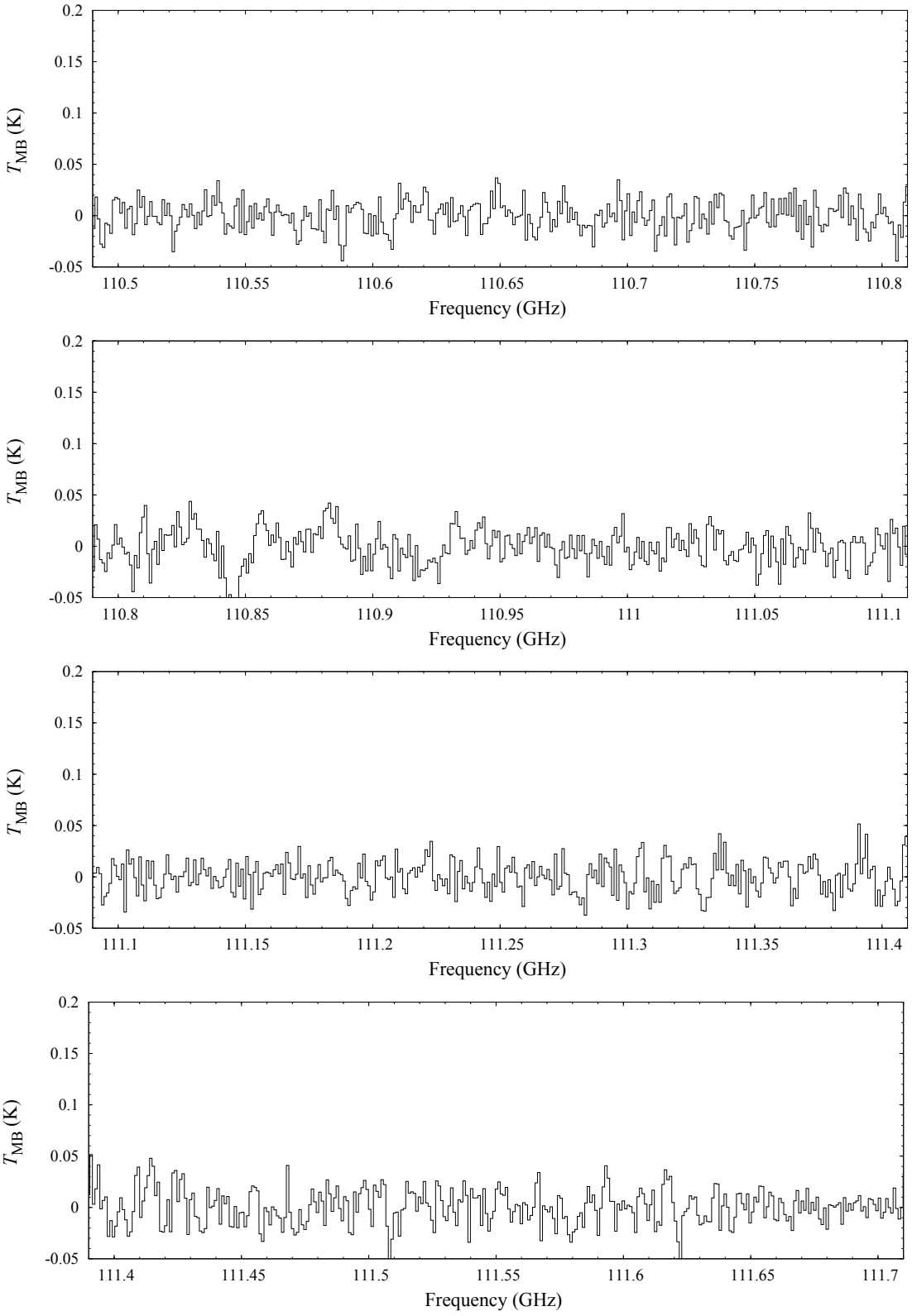

Figure B.1: continued

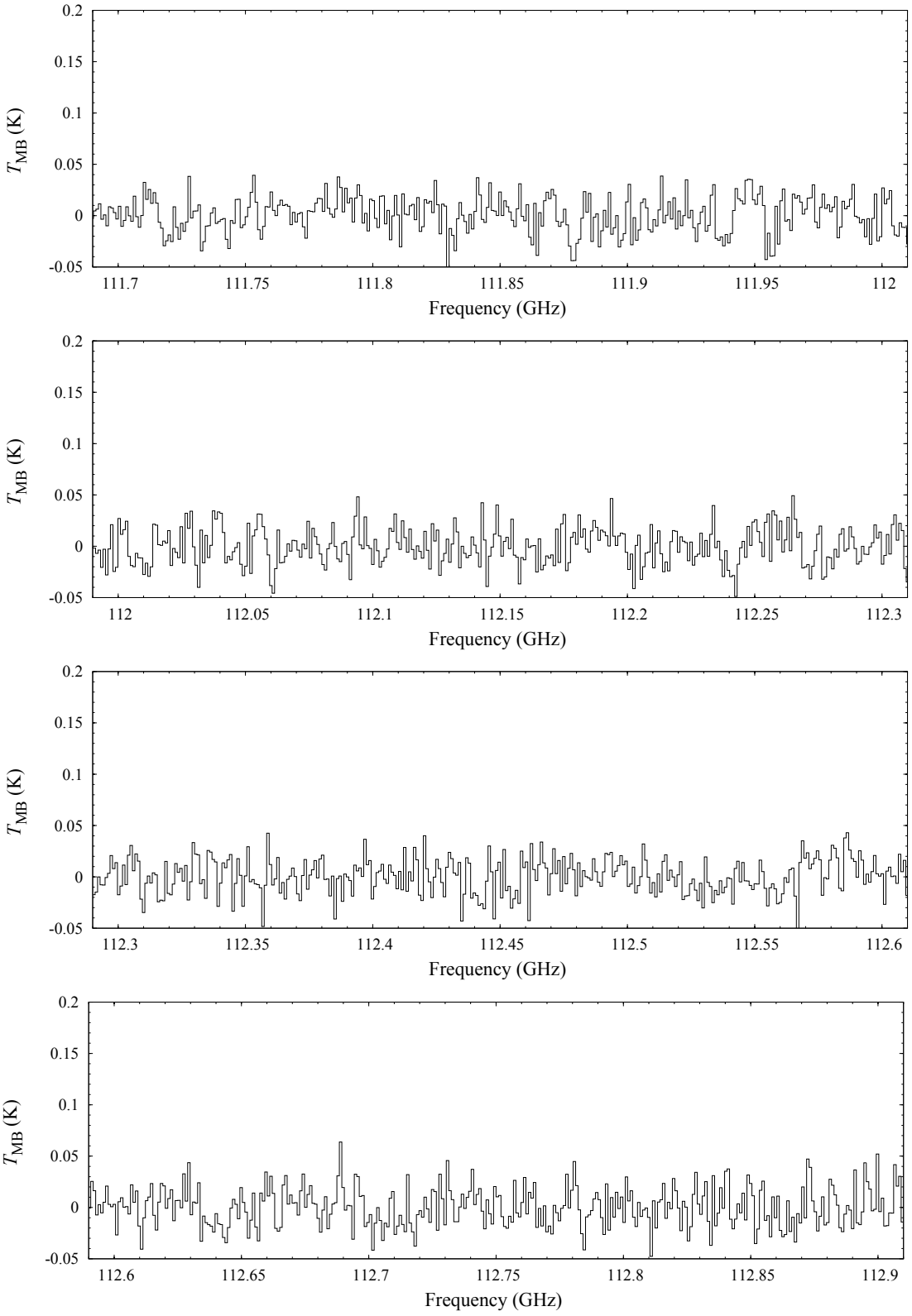

Figure B.1: continued

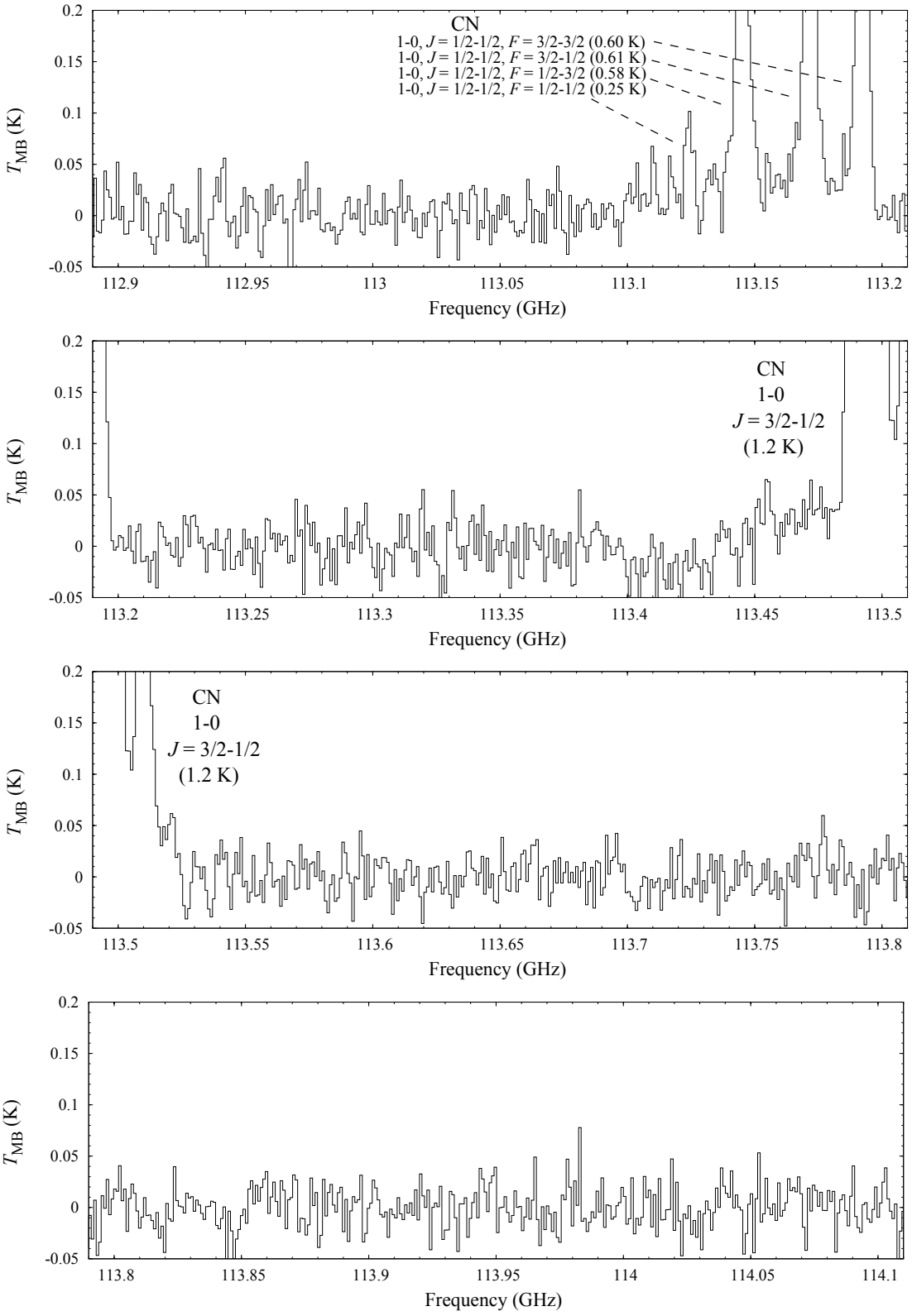

Figure B.1: continued

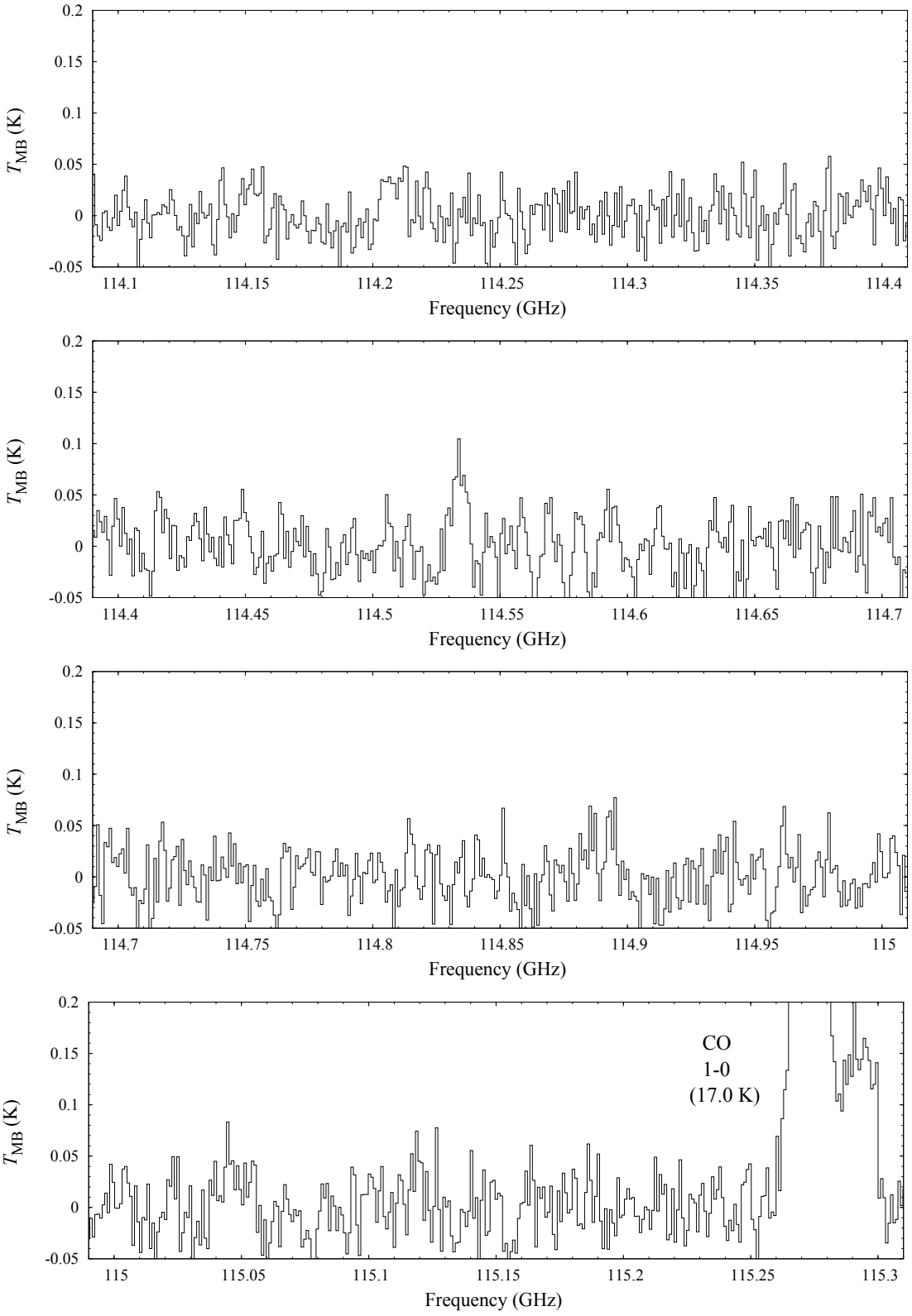

Figure B.1: continued

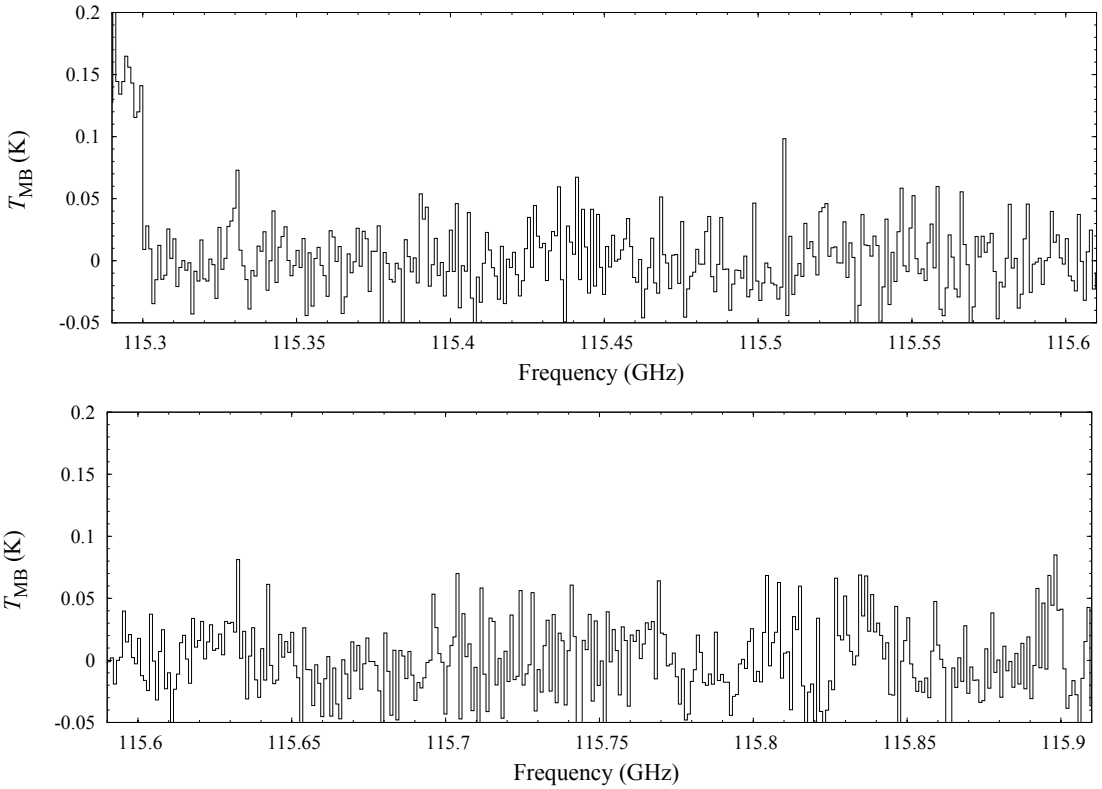

Figure B.1: continued

Appendix C

RADEX Calculation

In order to investigate the physical and chemical conditions of molecular clouds, the LTE assumption cannot always be applied. The rotation diagram method assumes a single excitation temperature fitted to the line intensities as a function of upper level energy. We found out from rotation diagram that rotation temperatures of many species are not comparable to the kinetic temperature deduced from CH_3CN. Hence, the excitation temperature cannot be approximated by kinetic temperature. LTE method is only valid in such a case as high-density clouds as seen in star-forming regions.

Statistical equilibrium method is applied on the assumption of a local excitation, which includes the balance of excitation and de-excitation rates. Radex method is summarized as follows.

The transfer equation for radiation propagating a distance ds is

$$dI_\nu ds = j_\nu - \alpha_\nu I_\nu, \tag{C.1}$$

where j_ν and α_ν express the local emission and extinction coefficients, respectively. The source function combines these two terms as

$$S_\nu \equiv \frac{j_\nu}{\alpha_\nu}. \tag{C.2}$$

With the transport equation in its integral form and the definition of the optical depth, $d\tau_\nu \equiv \alpha_\nu ds$, the radiation from the medium, I_ν can be written as

$$I_\nu = I_\nu(0)\mathrm{e}^{-\tau_\nu} + \int_0^{\tau_\nu} S_\nu(\tau'_\nu)\mathrm{e}^{-(\tau_\nu - \tau'_\nu)} d\tau'_\nu \tag{C.3}$$

$$\tag{C.4}$$

where $I_\nu(0)$ is the background radiation entering into the medium.

Radex program focuses on transitions of a molecule consisting of N levels with spontaneous downward rates A_{ul}, Einstein coefficients for stimulated transitions B_{ul} and B_{lu}, and collisional rates C_{ul} and C_{lu}, between upper levels u and lower levels l.

The downward collisional rate is written as

$$C_{ul} = n_{\mathrm{col}}\gamma_{ul}, \tag{C.5}$$

where n_{col} is the number density of the collision partner (H_2 molecule in cm^{-3}) and γ_{ul} is the downward collisional rate coefficient (in $\mathrm{cm}^{-3}\mathrm{s}^{-1}$). The rate coefficient is defined as Maxwellian

average of the collision cross section, σ,

$$\gamma_{ul} = \left(\frac{8kT_{\rm kin}}{\pi\mu}\right)^{-1/2}\left(\frac{1}{kT_{\rm kin}}\right)^2\int \sigma E {\rm e}^{-E/kT_{\rm kin}}dE, \tag{C.6}$$

where E is the collision energy, k is the Boltzmann constant, $T_{\rm kin}$ is the kinetic temperature, and μ is the reduced mass of the system. The upward rates comes through detailed balance as:

$$\gamma_{lu} = \gamma_{ul}\frac{g_u}{g_l}{\rm e}^{-h\nu/kT_{\rm kin}}, \tag{C.7}$$

where g_i is the statistical weight of level i. For a transition $u \to l$ with the rest frequency ν_{ul}, the local emissivity is written as:

$$j_\nu = \frac{h\nu_{ul}}{4\pi}n_u A_{ul}\phi_\nu, \tag{C.8}$$

in which n_u is the number density of molecules in level u and ϕ_ν is the frequency-dependent line emission profile. The absorption coefficient is expressed as

$$\alpha_\nu = \frac{h\nu_{ul}}{4\pi}\left(n_l B_{lu}\varphi_\nu - n_u B_{ul}\chi_\nu\right), \tag{C.9}$$

where φ_ν and χ indicate the line profiles of absorption and stimulated emission, respectively.

On the assumption of complete angular and frequency re-distribution of emitted photons, $\phi_\nu = \varphi_\nu = \chi_\nu$, so that the source function is expressed as

$$S_{\nu_{ul}} = \frac{n_u A_{ul}}{n_l B_{lu} - n_u B_{ul}} = \frac{2h\nu_{ul}^3}{c^2}\left(\frac{g_u n_l}{g_l n_u} - 1\right)^{-1}, \tag{C.10}$$

using the relations between Einstein's A and B coefficients. The excitation temperature $T_{\rm ex}$ is defined through the Boltzmann equation

$$\frac{n_u}{n_l} = \frac{g_u}{g_l}\exp\left[-\left(E_u - E_l\right)/kT_{\rm ex}\right], \tag{C.11}$$

where E_i is the energy of level i, resulting in the specific intencity of a black body radiation at $T_{\rm ex}$ as $S_{\nu_{ul}} = B_\nu(T_{\rm ex})$. In the interstellar cloud, the line broadening mainly occurs from Doppler effect. Line widths are much larger than expected from the kinetic temperature unless observed in very cold and dark cloud cores. Considering random macroscopic gas motions or turbulence, a Gaussian line profile is represented as:

$$\phi_\nu = \frac{1}{\nu_{\rm D}\sqrt{\pi}}\exp\left[-\left(\nu - \nu_{ul} - \boldsymbol{v}\cdot\boldsymbol{n}\frac{\nu_{ul}}{c}\right)/\nu_{\rm D}^2\right], \tag{C.12}$$

where $\nu_{\rm D}, \boldsymbol{u}, \boldsymbol{n}$, and c denote the Doppler width, the velocity vector of the moving gas at the position of the scattering, a unit vector in the direction of the propagating beam of radiation, and the light speed, respectively. The Doppler width is the $1/e$ half-width of the line profile, which is $\Delta V/2\sqrt{\ln 2}$ where ΔV is full width at half-maximum (FWHM).

The knowledge of the level populations n_i enables us to solve the radiative transfer equation exactly. Though the density in molecular clouds is often too low to attain LTE, statistical equilibrium (SE) can be assumed as

$$\frac{{\rm d}n_i}{{\rm d}t} = 0 = \sum_{j\neq i}^{N} n_j P_{ji} - n_i\sum_{j\neq i}^{N} P_{ij} = \mathcal{F}_i - n_i\mathcal{D}_i, \tag{C.13}$$

where P_{ij}, the destruction rate coefficient of level i, and the formation rate coefficient P_{ji} are defined as

$$P_{ij} = \begin{cases} A_{ij} + B_{ij}\bar{J}_\nu + C_{ij} & (i > j) \\ B_{ij}\bar{J}_\nu + C_{ij} & (i < j). \end{cases} \tag{C.14}$$

In Eq. C.14,

$$B_{ij}\bar{J}_\nu = B_{ij}\int_0^\infty J_\nu \phi(\nu) d\nu \tag{C.15}$$

expresses the number of induced radiative (de-)excitations from state i to state j per second per particle in state i, and

$$J_\nu = \frac{1}{4\pi}\int I_\nu d\Omega \tag{C.16}$$

is the specific intensity I_ν integrated over solid angle $d\Omega$ and averaged over all directions, which means that SE equations take into the calculation the effects of non-local radiation.

Appendix D

A List of Names of Chemical Species

CO Carbon-monoxide

HCN Hydrogen Cyanide

HNC Hydrogen Isocyanide

HCO^+ Formyl Cation

N_2H^+ Protonated Nitrogen

C_2H Ethynyl Radical

HCOOH Formic Acid

CH_3CHO Acetaldehyde

HC_3N Cyanoacetylene

CH_3CN Acetonitrile (Methyl Cyanide)

$HCOOCH_3$ Methyl Formate

C_2H_5CN Ethyl Cyanide

CH_3OH Methanol

C_2H_5OH Ethanol

c-**C_3H_2** Cyclopropenylidene

SiO Silicon Monoxide

SO Sulfur Monoxide

SO_2 Sulfur Dioxide

OCS Carbonyl Sulfide

NH_2CHO Formamide

H_2CO Formaldehyde

H_2CS Thioformaldehyde

HNCO Isocyanic Acid

CH_3CCH Methyl Acetylene

H_2CCO Ketene

CH_3SH Ethanethiol

SiS Silicon Monosulfide

PN Phosphorus Nitride